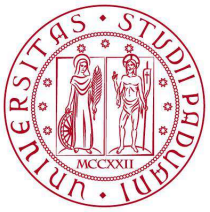

UNIVERSITÀ
DEGLI STUDI
DI PADOVA

Sede Amministrativa: Università degli Studi di Padova
Dipartimento di Ingegneria Civile Edile e Ambientale
Scuola di dottorato in Scienze dell'Ingegneria Civile e Ambientale
Ciclo XXVII

STUDY OF LARGE DEFORMATION GEOMECHANICAL PROBLEMS WITH THE MATERIAL POINT METHOD

Studio di problemi geotecnici a grandi deformazioni con il Material Point Method

Direttore della Scuola: Ch.mo Prof. STEFANO LANZONI
Supervisore: Ch.mo Prof. PAOLO SIMONINI
Co-supervisore: Ch.mo Emer. Prof. PIETER A. VERMEER

Dottorando/a: FRANCESCA CECCATO

"Data! Data! I need data!", cried Holmes impatiently,
"I can't make bricks without clay".
– Sir Arthur Conan Doyle

Summary

The numerical simulation of real geomechanical problems often entails an high level of complexity; indeed they are often characterized by large deformations, soil-structure interaction and solid-fluid interaction. Moreover, the constitutive behavior of soil is highly non-linear. Landslides, dam failure, pile installation, and undrground excavation are typical examples of large deformation problems in which the interaction between solid a fluid phase as well as the contact between bodies are essential.

This thesis addresses the challenging issue of the numerical simulation of large deformation problems in geomechanics. The standard lagrangian finite element methods are not well suited to treat extremely large deformations because of severe difficulties related with mesh distortions. The need to overcome their drawbacks urged researchers to devote considerable effort to the development of more advanced computational techniques such as meshless methods and mesh based particle methods.

In this study, the Material Point Method (MPM), which is a mesh based particle method, is exploited to simulate large deformation problems in geomechanics. The MPM simulates large displacements with Lagrangian material points (MP) moving through a fixed mesh. The MP discretize the continuum body and carry all the information such as mass, velocity, acceleration, material properties, stress and strains, as well as external loads. The mesh discretizes the domain where the body move through; it is used to solve the equations of motion, but it does not store any permanent information.

In undrained and drained conditions the presence of water can be simulated in a simplified way using the one-phase formulation. However, in many cases the relative movement of the water respect to the soil skeleton must be taken into account, thus requiring the use of the two-phase formulation.

The contact between bodies is simulated with an algorithm specifically developed for the MPM at the beginning of the century. This algorithm was originally formulated for the frictional contact. It extension to the adhesive contact is considered in this thesis, which is well suited to simulate soil-structure interaction in case of cohesive materials.

In this thesis typical geomechanical problems such as the collapse of a submerged slope and the simulation of cone penetration testing are considered. Numerical results are successfully compared with experimental data thus confirming the capability of the MPM to simulate complex phenomena.

Sommario

La simulazione numerica di molti problemi geotecnici é spesso caratterizzata da un elevato grado di complessitá, infatti tipici fenomeni come frane, collasso di rilevati e installazione di pali necessitanto di tener conto delle grandi defromazioni del materiale, dell'accoppiamento meccanico tra fase solida e fase liquida e dell'interazione terreno-struttura. Questa tesi si occupa della simulazione numerica di tali problemi attraverso il Material Point Method, in particolare vengono considerati il collasso di un pendio sommerso e la penetrazione del piezocono.

I classici metodi lagrangiani agli elementi finiti, ampiamente utilizzati da decenni, non sono adatti alla simulazione di grandi deformazioni per i severi problemi conseguenti le estreme defromazioni della mesh. La necessitá di superare i limiti dei classici FEM, diversi gruppi di ricerca si sono impegnati, negli ultimi anni, a sviluppare nuovi metodi numerici tra cui si ricorda SPH (Lucy 1977), MPM (Sulsky et al. 1994) e PFEM (Idelsohn et al. 2004). Nel Material Point Method il continuo deformabile é rappresentato da un insieme di punti materiali che si spostano attraverso una mesh fissa di elementi finiti. I punti materiali trasportano tutte le informazioni del corpo come velocitá, tensioni, deformazioni, proprietá del mateiale e carichi, mentre la mesh é utilizzata solo per risolvere le equazioni del moto, ma non memorizza alcuna informazione permamente; in questo modo si evitano problemi di distorsione degli elementi finiti.

L'interazione con l'acqua o altri fluidi interstiziali é determinante nel comportamento del terreno nella maggior parte delle condizioni di carico. In condizione drenate e non drenate, la presenza dell'acqua puó essere tratta in modo semplificato cosí che gli spostamenti del terreno possono essere calcolati con l'uso delle equazioni del continuomo monofase. In molti casi é essenziale tener conto del movimento relativo tra lo scheletro solido e l'acqua, questo necessita dell'uso della formulazione bifase. Entrambe queste possibiltá di simulare il terreno saturo vengono utilizzate nello studio dei problemi oggetto di questo studio.

Nel MPM problemi caratterizzati dal contatto fra corpi possono essere simulati con un algoritmo sviluppato specificatamente per l'MPM all'inizio del secolo (Bardenhagen et al. 2000c); tale algoritmo viene ripreso in questa tesi ed esteso al caso dei terreni coesivi per la simulazione dell'interazione terrno-struttura.

Contents

Acknowledgments

I am grateful to many people who had a part in my grow up as a young researcher and a woman. This PhD experience has been a process of emotional and scientific maturation which made me a somehow different, and hopefully better, person than I was three years ago.

I would like to express my gratitude to my supervisor Professor Paolo Simonini who supported, guided and encouraged me in my engineering study since a was a bachelor student at the University of Padova.

I wish to thanks all the people working in the MPM group at Deltares (Delft, The Netherlands), first of all Professor Pieter Vermeer, who gave me the opportunity to be part of the team, Dr. Lars Beuth and Dr Issam Al-Kafaji for their patience and for having introduced me to the MPM, Dr. Alex Rohe, Dr. Mario Martinelli and the PhD students Alba Yerro, Shuhong Tan, Phuong Nguyen and James Fern for their always present and kind support. Working at Deltares has been an exciting experience during which I learnt a lot from the scientific and personal point of view.

Thank also to my friends and colleagues in Padova Dr. Fabio Gabrieli, Alberto Bisson, Silvia Bersan and in Delft Dr. Ana Teixeira, Almar Joling, Maria Varini who made my hard working days enjoyable with their smiles, talks, coffee and cakes.

Special thanks to all my family and to my boyfriend who cheered me up in the difficult moments, without them this thesis would not be completed. My final thanks to all the people who believed in me and my ability and encouraged me to be the best that I could be.

1 Introduction

Many geomechanical problems such as landslides, dam and embankment failure, pile driving and underground excavation involve large deformations; despite the considerable evolution of numerical methods, the simulation of this kind of phenomena is still challenging.

The standard Lagrangian Finite Element Method (UL-FEM) has been successfully applied for decades in engineering and science, however severe mesh distortions, which accompany large deformations, lead to inaccurate results. In some cases it is even impossible to complete the simulation, as illustrated in Figure 1.1.

Although remeshing techniques and Arbitary Lagrangian-Eulerian (ALE) formulations can overcome the problem, the remapping of state variables arises difficulties with history dependent materials and the accuracy of results is questionable. The necessity to solve this problem has encouraged the development of several alternative methods such as the Discrete Element Methods (DEM), where the soil is represented as a collection of grains, and meshless or mesh-based particle methods, which are based on the continuum theory, such as the Smoothed Particles Hydrodynamics (SPH), the Material Point Method (MPM), and many others.

This thesis deals with advanced numerical modeling of geotechnical problems at large deformations by mean of the MPM. The attention is focused on the response of water-saturated soil in drained, partially drained and undrained conditions.

With the MPM, the body is discretized with a set of material points (MP) which store all the properties of the continuum such as state variables, material properties, loads and so on. The domain, where the body is moving through, is discretized with a fixed mesh, which is only used to solve the equations of motion. It simulates large deformations by MP moving through a background mesh, thus overcoming problems

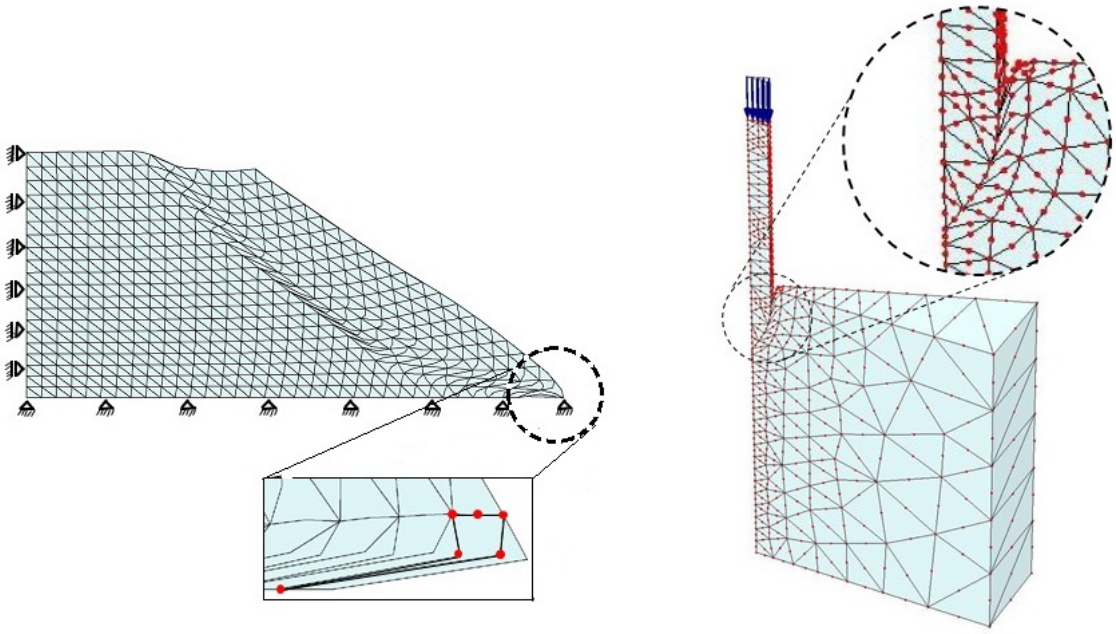

Figure 1.1: Examples of extreme mesh distorsion using the Updated Lagrangian Finite Element Method to simulate large deformation problems (Rohe and Vermeer 2014).

of mesh distortion, while keeping the advantage of a Lagrangian description of the motion.

The MPM appears one of the most promising methods to simulate large deformation problems. Indeed, it can be viewed as an extension of the UL-FEM; hence, the experience on this method can be applied. Moreover, it is computationally less expensive than other meshless methods. For these reasons it is favored in this thesis.

The method was introduced in the nineties by Sulsky et al. (1994) and has been considerably improved by several research groups since then. It has been applied in many field of engineering and science to simulate large deformations and extreme loading conditions such as explosions and impacts (Hu and Chen 2006, Lian et al. 2011), failure and fracture evolution (Nairn 2003), metal forming and processing (Chen et al. 1998), just to name a few. It has also been used in geomechanics to simulate problems of granular flow (Wieckowski et al. 1999, 2001), anchors placed in soil (Coetzee et al. 2005), excavator bucket filling (Coetzee et al. 2007), soil penetration (Beuth and Vermeer 2013, Elkadi and Nguyen 2013), landslides (Andersen 2009a) and dam failure (Alonso and Zabala 2011).

Geotechnical problems generally have a very high level of complexity. Indeed, soil

is a multiphase porous medium whose response is highly dependent on the mutual interaction between solid, fluid and gas. Its mechanical behavior is difficult to model and, to capture most of its features, constitutive models become very complex. In addition to this, typical geotechnical problems are characterized by dynamic loading and often involve the interaction with structures such as a foundation or a wall.

The generation and dissipation of pore pressure under loading can be captured thanks to the recently implemented dynamic two-phase formulation (Jassim et al. 2013). One of the innovative element of this study is the consideration of partially drained conditions within a threedimensional numerical model able to simulate large deformations. To the author knowledge, up to now numerical analyses of large strain problems considered almost always drained and undrained conditions.

The MPM implementation used in this thesis can simulate the soil-structure interaction. It is modeled with an algorithm specifically developed for the MPM by Bardenhagen et al. (2001). The original contact algorithm considers only frictional contact, but it has been extended to the adhesive contact in the frame of this thesis.

This thesis applies the two-phase MPM to the study of typical geomechanical problems such as the collapse of a submerged slope and the penetration of a cone into the soil.

Submerged landslides, as well as mud-flows and debris-flows, are often simulated with hydromechanical models because the soil behaves more like a fluid than a solid in part of the slide. These models are suitable to study the propagation phase, but requires the definition of the rheologic characteristics of the material, which may be difficult to estimate. On the contrary, geotechnical FE models incorporates advanced constitutive relation to describe soil behavior, but are suitable to simulate the slope up to the trigger of its failure. The MPM can simulate the soil flow while the material is described by constitutive models developed in soil mechanics. The possibility of simulating the initiation, the propagation and the deposition of the landslide with a single model is of great interest in geotechnics.

The cone penetration test is a common in-situ soil testing technique, used to characterize the soil profile and to estimate soil parameters. It has been deeply studied for decades. However, to the author knowledge, at the moment there are no truly threedimensional numerical simulations of the penetration process which use a realistic constitutive model, consider the effect of pore pressure dissipation during loading and the cone rougness. The study described in this thesis gives a contribution in the understanding of the penetration process, investigating the effect of partial drainage

and cone roughness on the measured tip resistance.

1.1 Layout of the thesis

Chapter 2 discusses the basis of the numerical modeling process and briefly presents the most popular numerical methods. The soil is a collection of grains but can be regarded as a continuum material at a macro-scale. Following this intrinsic duality of soil, numerical methods can be classified in discontinuous models and continuum models. The methods based on the continuum theory are characterized by the way the body is discretized: the mesh-based methods use a grid or mesh, while the particle-based methods use a set of material points, also called particles. The latter overcome problems of mesh distortions and tend to be more suitable to simulate large deformations.

After an overview of the most recently used numerical methods, a literature study on the Material Point method is provided. The numbers and quality of publications about MPM shows that the method is very powerful and promising. It can be applied in many fields of engineering and science especially for problems involving large deformations.

Chapter 3 presents the details of the one-phase MPM formulation. First the mathematical model is derived; second the governing equations are discretized in time and space; finally the solution procedure is discussed in detail. Despite the soil is a multiphase material, this simple formulation can be used in case of undrained and drained conditions, indeed in these cases the presence of water can be treated in a simplified way as shown in Section 3.5.

The two-phase formulation is discussed in **Chapter 4**. The governing equations of the fluid and solid phase are solved for the velocities of the two phases. This formulation can simulate the generation and dissipation of pore pressures as encoutered in partially drained conditions. Moreover, it is very well suited to model the behavior of saturated soil under dynamic loading conditions (van Esch et al. 2011a). The solution of the governing equations follows Verruijt (1996). The saturated soil is discretized with one layer of MP which moves according to the solid velocity as explained in Section 4.2.

The constitutive modeling of soil is one of the most challenging issues in geomechanics; this theme is discussed in **Chapter 5**. The most popular elastoplastic models such as the Mohr-Coulomb, Tresca and Modified Cam Clay are included in this

chapter. To the author's knowledge this study is one of the first application of the Modified Cam Clay model within the MPM.

Chapter 6 treats special numerical techniques used to overcome specific problems such as the volumetric locking typical of low order element, the dissipation of dynamic waves, the computational cost of quasi-static simulation, the contact between bodies and the application of non-zero traction and velocity. Section 6.4 is dedicated to the contact algorithm, which has a considerable importance for the application of the MPM to problems involving soil-structure interaction. The original frictional algorithm (Bardenhagen et al. 2001) is presented and extended to the adhesive contact type. The new implementation is validated with the problem of the sliding block.

Chapter 7 is dedicated to the validation of the two-phase formulation. The method is capable of simulating the propagation of one-dimensional dynamic waves and the consolidation of a 1D-column for small and large deformations. The use of energy-dissipation techniques such as viscous boundary and local damping is investigated too.

A first application of the two-phase MPM to typical large deformation geotechnical problem is found in **Chapter 8**. The numerical model simulates the collapse of a submerged slope in a small-scale laboratory experiment. The complex soil-water interaction has been taken into account by mean of the two-phase formulation. The MPM simulation is in excellent agreement with the experimental result.

Chapter 9 shows the possibility to simulate with the MPM the highly complex problem of the penetration of a cone into the soil, considering partial consolidation under loading. Simulating the cone penetration for various drainage conditions requires to model the generation and dissipation of pore pressure during penetration, the constitutive behaviour of soil and the soil-cone contact. The cone penetration test is a common in-situ soil testing technique; it has been deeply studied for decades, but numerical simulations of the penetration process in different drainage conditions are rare. This thesis contributes to achieve a deep understanding of penetration process in partially drained conditions. Numerical results are compared with experimental data founding good agreement.

This work confirms that MPM is a very promising methods and is very well suited to geomechanical problems involving large deformations, a summary of the conclusions and future developments can be found in **Chapter 10**.

The thesis has two appendices: **Appendix A** contains the basis of continuum me-

chanics, while **Appendix B** gives and introduction on the damped vibrating systems. Despite the reader is supposed to be familiar with the concepts of continuum mechanics and oscillatory systems, the appendices provide a basic knowledge which can be useful for the understanding of this work.

2

Numerical modeling in geomechanics

The purpose of this chapter is to introduce the matter of numerical modeling in geomechanics and present the state of the art of the Material Point Method (MPM). An introduction on the numerical modeling process is presented in Section 2.1; followed by an overview of the most popular numerical methods in Sections 2.2 and 2.3. For the sake of clarity, the considered numerical methods are distinguished on the basis of the mathematical model on which are based (continuous or discontinuous) and the discretization method which is applied.

Among the various methods, the MPM has been chosen in this thesis to study large deformation problems in geomechanics. The number of publications related to the MPM is growing fast, demonstrating the intense research activity on this subject. The most important contributes are considered in the literature review discussed in Section 2.5.

2.1 Introduction

Engineering is fundamentally concerned with modeling; however the use of models to study reality is common in many fields such aseconomics, anthropology, biology, chemistry, physics ecc..

> 'Scientific understanding proceeds by way of constructing and analyzing models of the segments or aspects of reality under study. The purpose of these models is not to give a mirror image of reality, not to include all its elements in their exact sizes and proportions, but rather to single out and make available for intensive investigation those elements which are decisive. We abstract from non-essentials, we blot out the unimportant to get an unobstructed view

> of the important, we magnify in order to improve the range and accuracy of our observation. A model is, and must be, unrealistic in the sense in which the word is most commonly used. Nevertheless, and in a sense, paradoxically, if it is a good model it provides the key to understanding reality.'

This extract from the Baran and Sweezy's essay (1968) gives a good idea of what a model is:

- A model is a simplification of the reality. It is important to recognize the decisive elements which must be included and those which are unessential; this depends on the purpose of the study.
- A model is an instrument to understand reality and lead decisions to solve a specific problem.

Engineering is concerned with finding solutions to real problems and this requires to be able to recognize the essence of the problem and identify the key features which need to be modeled. One aspect of engineering judgment is the identification of those features which we believe it is safe to ignore and those which should be taken into account.

Engineers can use empirical, analytical or numerical models to find practical solutions for their problems. Empirical solutions come from the direct observation of the physical reality. They are developed to provide satisfactory answers even though the logical thread cannot always be continuously traced. Analytical solutions seem the most desirable ones because they usually look very elegant, come from a scientific theory and are easy to compute; however exact, closed-form solutions are in general restricted to a limited set of conditions. Numerical models have become more and more popular thanks to the recent developments in computer technology. They are based on mathematical models which are solved using specific numerical schemes. Numerical models are currently the most advanced. Considerable effort has been put so far to improve them; however they still contain limitations and drawbacks that encourage further study on this field.

A flow-chart of the numerical modeling process in geomechanics is shown in Figure 2.1. The real physical system is firstly idealized in a mathematical model. This model contains the principles of mechanics (conservation's laws) and the constitutive models of materials. The mathematical model is based on certain assumptions which lead to the so called idealization error. Secondly the governing equations are discretized in order to solve a finite system of equations; here the discretization

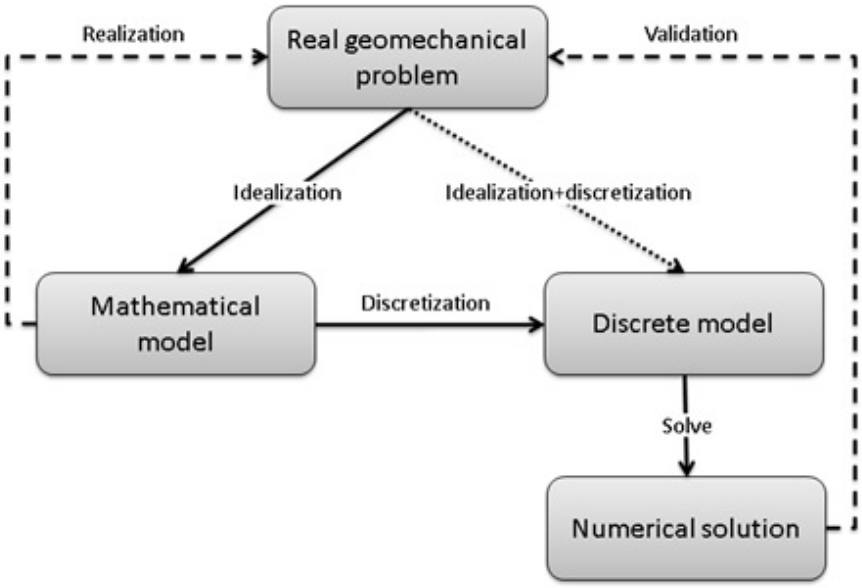

Figure 2.1: The phases of the numerical modelling (C. Tamagnini)

error is introduced. Thirdly the approximate solution of the discretized equations is achieved numerically. In this process the approximation error enters the solution. Finally, an essential step of numerical modeling is the validation; Section 2.4 is dedicated to this phase.

Discretization can be done together with the mathematical idealization, as carried out in the methods belonging to the Discrete Element family. In this case the granular material is discretized as a collection of particles representing single soil grains and micromechanical interactions between particles are modeled.

The soil has an intrinsic duality in the sense that it can be modeled as a continuum at a macroscopic level or as a particle collection at a micro-meso scale.

For a very long time soil has been modeled according to the continuum theory. The governing laws are the conservation of mass, the conservation of momentum, the conservation of energy and the Clausius-Duhem inequality (second principle of thermodynamic). The constitutive equations of the material are based on its macroscopic behavior, which is usually easy to investigate by standard testing procedures.

Only with the arrival of advanced computer technology, modeling soil particles became possible and the methods have been improving fast both from the computational and theoretical point of view. To follow this approach the knowledge of soil characteristics at microscopic level is necessary and this is often difficult to achieve in practice.

Sections 2.2 and 2.3 provide an overview of the most popular numerical methods in geomechanics. Recalling the discrete-continuum soil duality, it is clear that we can firstly distinguish geomechanical computational methods between discontinuous models and continuum models. In this frame discontinuous models indicate those which the material is assumed to be made of discrete entities. On the other hand, the continuum models are based on the assumption of continuity, i.e. the material conserves its properties regardless the scale. For soil this assumption is not true, but is acceptable at a macroscopic level.

Discontinuous models differentiate mainly by the way the interactions between individual particles (and eventually fluids) are modelled. Among continuum models different approaches can be choosen to discretize the domain and solve the equations; the main difference lies between mesh-based methods and particle-based methods. In this thesis mesh-based methods are those in which the discretization and the solution are based on a grid or mesh, like the finite difference methods (FDM) and finite element methods (FEM). Particle-based methods are those in which the discretization is based on a cloud of material points or particles, like smoothed particle hydrodynamics (SPH), the Material Point Method (MPM), the Particle Finite Element Method (PFEM).

2.2 Discontinuous models

Discrete models are suitable for those materials which consist in a set of particles, for example granular materials (cereals, sands ecc.), industrial or chemical powders, biological solutions (blood, proteins, ecc.), blocky rock masses. Since the late 50s, when the Molecular Dynamic method was developed by Alder and Wainwright (1959) and Rahman (1964) independently, discrete methods have been growing in popularity. Several discrete modelling techniques have been developed, including Monte Carlo method, cellular automata and discrete element method (DEM). The last one is the most popular in geomechanics. It was originally applied to rock mechanics by Cundall and Strack in 1979. Figure 2.2 shows possible applications of DEM to the study of the behavior of granular material.

The macroscopic behaviour of a particulate matter is determined by the interactions between individual particles as well as interactions with surrounding fluids and wall. Understanding the microscopic mechanisms which governs these interactions is therefore the key point of the methods. This leads to a truly interdisciplinary research into particulate matter at particle scale. In recent years, such research has

been rapidly developed worldwide, mainly as a result of the rapid development of discrete particle simulation technique and computer technology.

The most common DEM formulations are the so-called soft-particle and hard-particle. The soft-sphere method originally developed by Cundall and Strack (1979) was the first granular dynamics simulation technique published in the open literature. In such an approach, particles are permitted to experience minute deformations, and these deformations are used to calculate elastic, plastic and frictional forces between particles. The motion of particles is described by the well-established Newton's laws of motion. A characteristic feature of the soft-sphere models is that they are capable of handling multiple particle contacts which are of importance when modelling quasi-static systems. By contrast, in a hard-particle simulation, a sequence of collisions is processed; often the forces between particles are not explicitly considered. Therefore, typically, hard-particle method is most useful in rapid granular flows.

The particle flow is often coupled with a fluid (gas and/or liquid) flow. To describe this two-phase flow, DEM has been coupled with computational fluid dynamics (CFD). The CFD-DEM approach was firstly proposed by Tsuji et al. (1992, 1993), followed by many others. By this approach, the motion of discrete particles is described by DEM on the basis of Newton's laws of motion applied to individual particles and the flow of continuum fluid by the traditional CFD based on the local averaged NavierStokes equations (Zhu et al. 2007).

DEM simulations can provide dynamic information, such as the trajectories and transient forces acting on individual particles. It is well suited to study fundamental soil behavior during loading, develop and validate constitutive relationships for soil.

The main disadvantage of the DEM is its enormous computational expense. The maximum number of particles and duration of a virtual simulation is limited by computational capacity. Typical flows contain billions of particles, but contemporary DEM simulations on large cluster computers have only recently been able to approach this scale for sufficiently long simulated time. When modeling full-scale problems a method which minimizes the number of particles is necessary to keep the problem computationally feasible.

A second issue involves the input parameters, which refer to particle properties rather than aggregate properties. The DEM parameters must be chosen such that realistic soil behaviour is modelled (Ting et al. 1989).

By use of a proper averaging procedure, a discrete particle system can be transferred

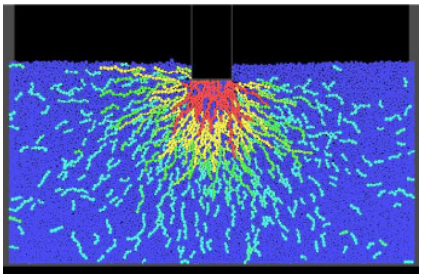

(a) Determination of force chains during punching of granular material

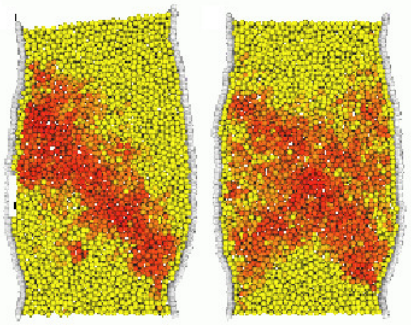

(b) Localization of shear band in a triaxial sample.

Figure 2.2: Examples of DEM applications.

into a corresponding continuum system. Macroscopic variables in the continuum approach can be linked to the microscopic variables in the discrete approach by means of local averaging. The procedure offers a convenient way to link fundamental understanding generated from DEM-based simulations to engineering application often achieved by continuum modelling. Extensive research has been carried out to develop such averaging methods, but a general theory is still missing.

The Discrete Element methods appear to be very promising to study granular materials, however they seem more suitable to scientific application than to engineering practice because of their microscopic approach and high computational cost.

2.3 Continuous models

In engineering applications, soil is often modeled as a continuum. Soil is a porous medium and its governing equations are derived assuming that each phase present in the system fills up the entire domain, forming an overlapping continuum. The representative variables are average values over a representative elementary volume (REV). The size selected for the REV should remove the effect of the microscopic inhomogeneity without eliminating the effect of macroscopic inhomogeneity (Lewis and Schrefler 1998).

The governing equations can be expressed according to the Lagrangian or Eulerian approach. The Lagrangian specification of the flow field is a way of looking at fluid motion where the observer follows an individual fluid parcel as it moves through space and time. Plotting the position of an individual parcel through time gives

the pathline of the parcel. This can be visualized as sitting in a boat and drifting down a river. The Eulerian specification of the flow field is a way of looking at fluid motion that focuses on specific locations in the space through which the fluid flows as time passes. This can be visualized by sitting on the bank of a river and watching the water pass the fixed location (Batchelor 2000).

It is always possible to switch from Eulerian to Lagrangian formulation by means of basic rules. A first classification can distinguish between the numerical models based on the Eulerian formulation and those based on the Lagrangian formulation. The Eulerian formulation is mostly used in fluid dynamics, while the Lagrangian formulation is dominant when the material behavior is history dependent.

Once the governing laws have been derived, the equations have to be discretized. Here it was decided to distinguish the methods on the basis of the discretization procedure:

- methods where the domain is discretized with a mesh. This mesh is necessary to write the approximate solution and solve the problem at each time step. The mesh stores important information and cannot be changed very easily.
- methods where the deformable body is discretized with a cloud of particles. Among them a second distinction is possible:
  - methods in which the mesh is eventually required to write the approximate solution and/or to calculate numerically the integrals characterizing the governing law, but can be destroyed at each time step. The number of these methods is very large;
  - methods in which no mesh is needed in any phase of the solution process. These methods are rare.

In this thesis the first family of methods is called mesh-based methods and the second particle-based methods. The main features of some of them are summarized in the following.

The use of the words meshless and meshfree methods is deliberately avoided since their use is popular in the literature, but their definition is still confuse. Indeed Atluri et al (1999):

> To be a truly meshless method, the two characteristics should be guaranteed: One is a non-element interpolation technique, and the other is a non-element approach for integrating the weak form.

for De Borst et al.(2012):

> meshless or meshfree methods do not require an explicitly defined connectivity between nodes for the definition of the shape function. Instead, each node has a domain of influence which does not depend on the arrangement of the nodes. The domain of influence of a node is the part of the domain over which the shape function of that specific node is non-zero.

while for Idelshon et al (2003):

> A meshless method is an algorithm that satisfies both of the following statements:
>
> - the definition of the shape functions depends only on the node positions.
> - the evaluation of the nodes connectivity is bounded in time and it depends exclusively on the total number of nodes in the domain.

moreover Oñate et. al (2004) use these terms in a generalized way for their PFEM method, where a finite element mesh does exist and connects the nodes defining the discretized domain where the governing equations are solved in the standard FEM fashion as well as the boundary of the continuum body.

2.3.1 Mesh-based methods

The most popular mesh methods are the finite difference methods (FDM) and the finite element methods (FEM).

The finite difference approximation for derivatives is the oldest approach to solve differential equations. It was already known by L. Euler ca. 1768, for the one dimensional space and was probably extended to dimension two by C. Runge ca. 1908. The advent of finite difference techniques in numerical applications began in the early 1950s and their development was stimulated by the emergence of computers.

It consists in approximating the differential operator by replacing the derivatives in the equations using differential quotients. The domain is partitioned in space and time. Approximations of the solution are computed at the space or time points.

It is difficult to name a date for the invention of **the finite element methods**, they originated from the need to solve complex elasticity problems in civil and

aeronautical engineering. Their developments can be traced back to the work by A. Hrennikoff (1941) and R. Courant (1943). Although the approaches used by these pioneers are different, they share one essential characteristic: mesh discretization of a continuous domain into a set of discrete sub-domains, usually called elements.

FEM its real impetus in the 1960s and 70s by the developments of J.H. Argyris and co-workers at the University of Stuttgart, R.W. Clough and co-workers at UC Berkeley, O.C. Zienkiewicz and co-workers at the University of Swansea, and Richard Gallagher and co-workers at Cornell University. Further impetus was provided in these years by available open source finite element software programs. NASA sponsored the original version of NASTRAN, and UC Berkeley made the finite element program SAP IV widely available. A rigorous mathematical basis to the finite element methods was provided in 1973 in the publication of Strang and Fix. The method has since then been generalized for the numerical modeling of physical systems in a wide variety of engineering disciplines, e.g., electromagnetism, heat transfer, and fluid dynamics(Robinson and Przemieniecki 1985); see e.g. Zienkiewicz and Taylor (2005) and Bathe (2006) for an overview.

In Lagrangian FEM, the mesh moves with the material (Fig. 2.3). Hence, the nodes located at the boundary of the continuum will always remain on the boundary throughout the computations. This means that the free surface of the continuum is well defined, allowing easy track of the interface between different materials and simple imposition of the boundary conditions. Another advantage of Lagrangian FEM is that, by definition, it does not allow the material to flow between elements and hence history dependent material behavior can be easily handled as the quadrature points remain coincident with the material points. However, the mesh distortion problem makes the method cumbersome in modeling very large deformations.

In Eulerian FEM the computational mesh is fixed while the material is deforming in time (Fig. 2.3). Large deformation are handled without the problem of mesh distortion that appears in the Lagrangian FEM. As the computational mesh is completely decoupled from the material, convective terms appear in Eulerian FEM, introducing numerical difficulties with history-dependent materials.

The most attractive feature of the FEM is its ability to handle complicated geometries and boundaries with relative ease. While FDM in its basic form is restricted to handle rectangular shapes and simple alterations thereof, the handling of geometries in FEM is theoretically straightforward. On the other hand FDM are easier to implement.

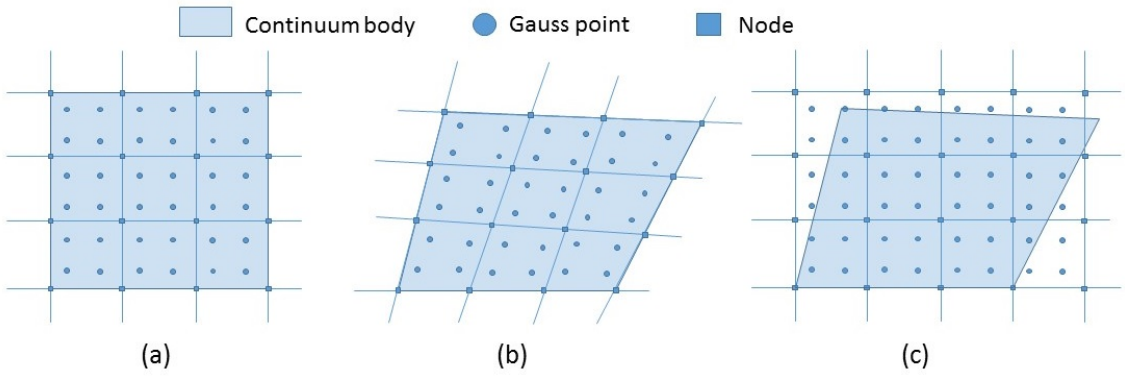

Figure 2.3: (a) Initial configuration in FEM, (b) deformed confitugation in Lagrangian FEM, (c) deformed configuration in Eulerian FEM.

The quality of an FEM approximation is often higher than the corresponding FDM approach, but this is extremely problem-dependent and several examples of the contrary can be provided. Generally, FEM is the most used method in all types of analysis in structural mechanics while computational fluid dynamics (CFD) tends to use FDM or other methods like finite volume method (FVM). Both FDM and FEM are widely used in geomechanics, both for scientific research purposes and professional applications, thanks also to the large availability of commercial codes.

One of the main shortcomings of Lagrangian FEM, common to other mesh-based methods, is the inaccuracy generated by big mesh distortions, then the limitations in modeling large deformations. This can be prevented by remeshing techniques or using **the Arbitray Lagrangian Eulerian** (ALE) formulation, but with a significative increase of computational requirements.

The key difference between ALE formulation and Lagrangian or Eulerian formulations is that in ALE the reference computational domain can move arbitrarily and independently of the material. The movement of the reference domain is represented by a set of grid points, which may be interpreted as the movement of a finite element mesh. Therefore, in an ALE formulation, the finite element mesh does not need to adhere to the material during the course of deformation as in Lagrangian descriptions, and thus the problems of mesh distortions may be avoided (Gadala and Wang 1998).

Penetration problems in geomechanics are sometimes solved with **the Coupled Eulerian-Lagrangian** (CEL) method. In CEL, one material is discretized with Eulerian mesh (usually the soil), whereas the other is discretized with Lagrangian mesh. The interaction between the two meshes is modeled using contact algorithm selected by the user. See e.g. Henke and Grabe (2010), Qiu and Grabe (2011),

Qiu and Henke (2011), Qiu et al. (2011) for CEL applications in geotechnical engineering.

2.3.2 Particle-based methods

Particle Methods discretize a continuum body with a collection of particles, also called material points. All the physical properties are attached to the particles and not to the elements as in the FEM. For the methods presented in this section a particle represents part of the continuum (Oñate et al. 2004).

A large number of mesh-based methods has been developed, however an extensive discussion of them exceed the purpose of this thesis. This section provides a short overview of the most popular particle-based methods which have also been applied in geomechanics.

The considered methods follow a Lagrangian approach of the governing equations. Their main advantage is the possibility to deal with large deformations overcoming the drawbacks associated with mesh distortion encountered in mesh-based methods. The complexity and computational cost are highly dependent on the specific method; in general they are higher than FEM and FDM.

The Material Point Method (MPM) has its origin in the Fluid-Implicit Particle method (FLIP) (Brackbill and Ruppel 1986) and the Particle-In-Cell method (PIC) (Harlow et al. 1957) developed during the 90s at the Sandia National Laboratories. The first publication dates back to 1994 by Sulsky et al.. Since then the method has been applied in many fields where large deformations are of relevance. A literature review on the method can be found in Section 2.5.

In the MPM, the continuum is represented by Lagrangian points, called material points (MP) or particles. The domain in which the body is expected to move into is discretized by a finite element mesh. Large deformations are modeled by material points moving through an Eulerian fixed mesh. The MP carry all physical properties of the continuum such as mass, momentum, material parameters, strains, stresses as well as external loads, whereas the Eulerian mesh and its Gauss points carry no permanent information. At the beginning of the time step, all the relevant quantities are transferred from the MP to the computational mesh (Fig. 2.4a). The integrals characterizing the discretized equations of motion are computed. The mesh is then used to determine the incremental solution of the governing equations (Fig. 2.4b). This nodal solution is mapped back to the MP to update their position, velocity

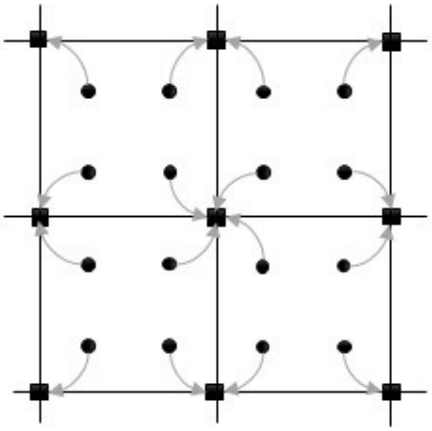

(a) Quantities are mapped from the MP to the mesh nodes.

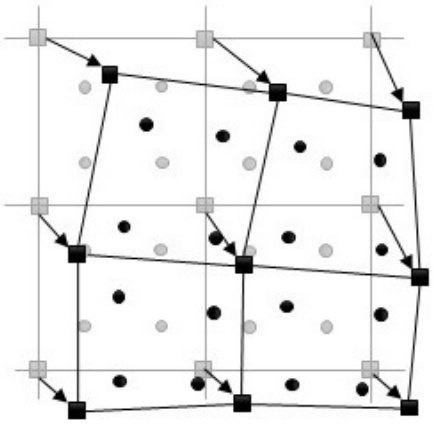

(b) The governing equations are solved at the background mesh which deforms.

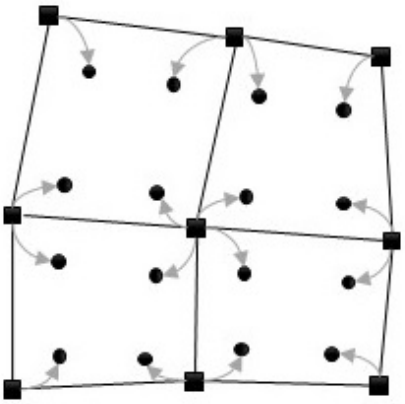

(c) Quantities are mapped from the nodes to the MP.

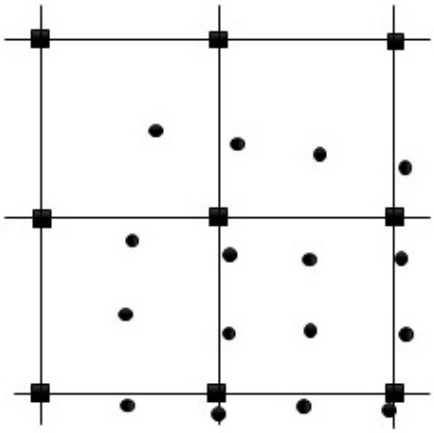

(d) The background mesh can be redefined.

Figure 2.4: Calculation steps of MPM

and all the other quantities (Fig. 2.4c). Afterward, the mesh can be reset to the initial configuration or changed arbitrarily (Fig. 2.4d).

The Lagrangian Integration Point Finite Element Method (FEMLIP) was first developed for geophysical problems (Moresi et al. 2003), but has been successfully applied in geomechanics (Cuomo et al. 2012).

It appears to be very similar to the MPM; indeed material points are used to track history variables and deformations and the essence of the formulation is the use of particles as integration points. The difference between MPM is that in FEMLIP the integration weight is recomputed at each time step in order to obtain the best approximation of the integral for a given element. Recomputing the particle weights is a computationally expensive step not required in the Material Point Method. The

method seems to be well suited for simulating viscoelastic-brittle materials in fluid-like deformation (Moresi et al. 2003).

The Particle Finite Element Method (PFEM) was presented at the beginning of this century (Idelsohn et al. 2004, Oñate et al. 2004) to solve fluid-structure interaction problems and has been later applied to geotechnical engineering.

This numerical method uses a Finite Element mesh to discretize the physical domain and to integrate the differential governing equations. In contrast to classical Finite Element approximations, the nodes transport their momentum together with all their physical properties, thus behaving as particles. Their location is updated according to the equations of motion in a Lagrangian fashion. At the end of each time step the mesh is regenerated. A fast and robust algorithm, based on the Delaunay Tessellation is used to generate the new mesh. The mesh not only serves for the integration of the differential equations, but it is also used to identify the contacts and to track the free surface.

The Smoothed Particle Hydrodynamics (SPH) was originally developed for astronomic applications by Lucy (1977) and Gingold and Monaghan (1977). Since its invention, SPH has been widely applied to many problems in engineering practice such as quasi-incompressible fluid flow (Monaghan 1994), viscous fluid flow (Takeda et al. 1994; Morris et al. 1997), high velocity impact of solid (Allahdadi et al. 1993), geophysical flows (Gutfraind and Savage 1998; Oger and Savage 1999).

Bui et al. (2007, 2008) were the first to apply SPH to elasto-plastic geomaterials. Since then, the method has been extended to a wide range of applications in computational geomechanics such as granular flows, bearing capacity of shallow foundations, slope failure, soil-structure interaction, seepage flows. An overview of the developments of the method and its application can be found in Liu and Liu (2010) and Monaghan (2012)

The computational domain is discretized by a finite number of particles (or points) while the definition of a mesh is not required. These particles, which carry all the material properties, have a spatial distance, known as the smoothing length, over which their properties are smoothed by a kernel function. This means that a physical quantity, at the location of the particle, is obtained by summing the contributions of all the particles which lie within the range of the kernel. The contribution of each particle is weighted according to the distance and the density. Mathematically, this is governed by the kernel function (Fig. 2.5). Kernel functions commonly used include the Gaussian function and the cubic spline.

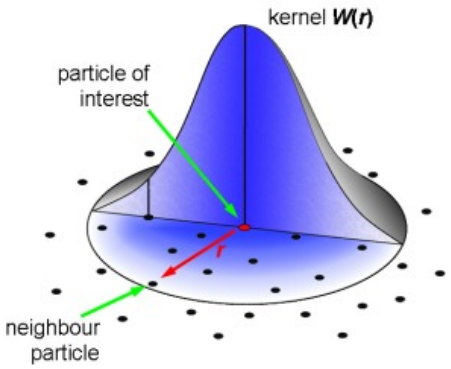

Figure 2.5: Simplified representation of a kernel function.

A detailed comparison between MPM and SPH can be found in Ma et al. (2009). The MPM is found to have some advantages compared to SHP, e.g. in MPM spatial derivatives are calculated based on a regular computational grid, so that the time consuming neighbor searching is not required, the boundary conditions can be applied in MPM as easily as in FEM, and contact algorithms can be efficiently implemented.

The Element Free Galerkin (EFG) method (Belytschko et al. 1994) and **the Meshless Local Petrov-Galerkin** (MLPG) method (Atluri and Zhu 1998) are both based on the idea of discretizing a problem domain by a particle distribution and a boundary definition. The field variable is approximated by interpolants to particle values. Construction of these interpolants requires only points and no mesh of elements, and is based on a least squares approach. The main difference between the EFG method and the MLPG method lies in the way the integrals, of the discretized equations, are calculated. In the former the test and shape functions are identical (hence the use of Galerkin) and therefore the integrations must be carried out over the entire domain for each particle. The latter uses different test and shape functions, which then restrict non-zero terms in the integrals to a zone around each particle.

These methods can provide smooth solutions, using shape functions of any desired order of continuity, in contrast to finite element shape functions which hit problems beyond C^1. However several difficulties must be addressed such as the imposition of essential boundary conditions and the calculation of the integrals.

In the field of geomechanics the EFG method has been applied to model fluid flow in porous media (Kim 2007; Praveen Kumar et al. 2008) while MLPG has been used by Ferronato et al. (2007) for predicting subsidence of reservoirs.

From this brief review of particle based method it can be concluded that although

their introduction in the engineering field is quite recent, they appear very promising in particular for the ability to handle large deformations. Works on further developments of these methods and new challenging applications are in progress.

2.4 Validation

Because of the idealization, discretization and numerical errors which inevitably afflict the analisys, the numerical prediction never completely matches the "real" world behavior. The numerical solution can only be a good approximation of reality. Validation is the process by which the quality of the numerical simulation is assured. In other words, the correspondence between reality and simulation is quantified.

All validation is done through a comparison of a pattern or a reference model with the model under study. There are many ways to make a validation, but in general they are usually classified according to the pattern used in the comparison (Godoy and Dardati 2001, Aad et al. 2008):

Validation using other numerical solutions. This technique compares the results to be validated with the results obtained through other numerical methods previously validated.

Validation using analytical solutions. This type of comparison can be used when the analytical theory behind the problem is known and direct comparison of the results with the analytical solution is possible. One of the main problems of this technique is that it can only be used in extremely simple cases.

Validation using experimental results. With this technique the consistency of the model with the reality is proved.

2.5 The Material Point Method: literature review

After the first publication about MPM by Sulsky et al. (1994), the method has been widely applied to many fields of engineering and science and extended with advanced features. Some of the most important contributions to the development of the MPM and its applications are discussed in this section. In order to keep the presentation clear, this survey has been divided in topics.

2.5.1 Historical developments

The roots of the MPM lie in a more general class of numerical schemes known as Particle-in-cell methods (PIC). The first PIC technique was developed in the 1950s (Harlow et al. 1957) and was used primarily for applications in fluid mechanics. Early implementations suffered from excessive energy dissipation, rendering them obsolete when compared to other, more valid methods.

Many problems affecting early PIC methods were solved developing the Fluid-Implicit Particle (FLIP) formulation (Brackbill and Ruppel 1986, Brackbill et al. 1988) in which the particles carry all the information of the continuum, e.g. mass, momentum, energy and constitutive properties.

In the 90's Sulsky et al. (1994) considerably extended the FLIP method to the application for solid mechanics. The weak formulation and the discrete equations were casted in a form that is consistent with the traditional finite element method. Furthermore, they applied the constitutive equation at each single particle, avoiding the interpolation of history-dependent variables, as the particles are tracked throughout the computation. Through this considerable extension, the method was able to handle history-dependent material behavior. Elements having material with different parameters or different constitutive equations were automatically treated; this is a clear advantage over Eulerian FEM. They considered numerical examples with large rigid body rotation and showed that the energy dissipation which tends to occur in Eulerian approach did not occur in their approach. This extension was then applied to different impact problems in plane-strain condition with elastic and strain hardening plastic material behaviors (Sulsky and Schreyer 1993a).

In the same year (1993), Sulsky and Schreyer extended the application of PIC to incorporate constitutive laws expressed in terms of Jaumann rate of stress. Further applications of PIC method to solid mechanics are given in Sulsky et al. (1995).

In 1996, Sulsky and Schreyer named the method as the Material Point Method and presented its axisymmetric formulation. They applied MPM to upsetting of billets and Taylor impact problems. They also incorporated the thermal effect in the constitutive equation.

Most MPM implementations are dynamic codes which employ an explicit time integration scheme, however implicit time integration has been used by several researchers (Guilkey and Weiss 2001, Guilkey and Weiss 2003, Sulsky and Kaul 2004, Beuth et al. 2008).

Although it is possible to use explicit dynamic programs also for the analysis of quasi-static problems, this is computationally inefficient as explicit integration requires very small time steps and can lead to long computation times.

Beuth et al. (2008) proposed an implicit time integration scheme for MPM using quasi-static governing equations. The virtual work equation obtained from the internal and external static equilibrium of continuum was used as the main governing equation in the proposed method. This method has been applied to slope failure and retaining wall problems (Beuth 2011) and numerical simulation of cone penetration in clay (Beuth and Vermeer 2013).

Bardenhagen and Kober (2004) generalized the discretization procedure of the original MPM. Element shape functions together with particle characteristic functions are introduced in the variational formulation, similarly to other meshless methods. Different combinations of the shape functions and particle characteristic functions resulted in a family of methods named the Generalized Interpolation Material Point Method (GIMP).

The MPM and its extensions have been used for many problems involving extreme deformations, such as explosion and impact (Hu and Chen 2006, Lian et al. 2011), failure and fracture evolution (Nairn 2003), biological and cellular materials (Ionescu et al. 2005, Guilkey et al. 2006), metal forming and processing (Chen et al. 1998), ice dynamics (Sulsky et al. 2007).

The first attempt in the field of geotechnical engineering can be considered the simulation of granular flow (Wieckowski et al. 1999, 2001) and subsidence of landfill covers that include geomembranes (Zhou et al. 1999). Konagai and Johansson (2001) applied the method to plane-strain compression test, failure of a cliff and mass flow through a trapdoor. It has been applied to the modeling of anchors placed in soil (Coetzee et al. 2005), excavator bucket filling (Coetzee et al. 2007), retaining wall failure (Wickowski 2004), the simulation of experiments related to induced ground deformations (Johansson and Konagai 2007) and geomembrane response to settlement in landfills (Zhou et al. 1999). The MPM demonstrated to be suitable for soil penetration problems such as simulation of the cone penetration test (Beuth and Vermeer 2013) and pile installation (Elkadi and Nguyen 2013). Numada and Konagai (2003) were the first to apply the method to soil flows in order to study the run-out of earthquake-induced slides. The MPM has been also used to model landslides (Andersen 2009a) and dam failure (Alonso and Zabala 2011).

2.5.2 Contact algorithms

The MPM is capabe of simulating non-slip contact between different bodies without a special algorithm. However, in many engineering problems a contact algorithm is required to model the relative motion at the interface between the contacting bodies.

A simple contact algorithm was proposed by York et al. (1999) to allow the release of no-slip contact constraint in the standard MPM. In York's method, if two bodies are approaching each other, the impenetrability condition is imposed as in standard MPM. If the bodies are moving away from one another, they move in their own velocity fields to allow separation.

Hu and Chen (2003) presented a contact/sliding/separation algorithm in the multi-mesh environment. In their contact algorithm, the normal component of the velocity of each material particle at the contact surface is calculated in the common background grid, whereas the tangential component of the velocity is found based on the respective individual grid. Although aforementioned contact algorithms are efficient to simulate separation, the friction between contact bodies is not considered.

Bardenhagen et al. (2000c) developed a frictional contact algorithm to model interaction between grains in granular materials. The algorithm allows sliding and rolling with friction as well as separation between grains, and correctly prohibits interpenetration. The strength of the algorithm is the automatic detection of the contact nodes, i.e. a predefinition of the contact surface is not required. It was further improved by Bardenhagen et al. (2001) and applied to simulate stress propagation in granular materials. This algorithm is the most used in MPM literature (Andersen 2009a, Bardenhagen et al. 2000a, Bardenhagen et al. 2000b, Coetzee 2003, Al-Kafaji 2013).

Huang and Zhang (2011) focused on the problem of impact and penetration, such as the perforation of a plate by a projectile. The no-slip contact condition in the standard MPM creates a great penetration resistance, so that the target absorbs more impact energy and decreases the projectile velocity. To accurately simulate the projectile-target interaction improvement of the impenetrability condition was necessary.

In conventional small-deformation finite element analyses, contact problems are solved with interface elements; this can be done with the MPM too (Vermeer et al. 2009). Interface elements were used for slope stability problems and to solve the cone-soil contact in simulation of cone penetration testing with the quasi-static MPM

(Beuth and Vermeer 2013).

Lim et al. (2014) applied a level-set based contact algorithm (Andreykiv et al. 2012) to simulate soil-penetration problems such as the installation of offshore foundations. The idea of the method is to describe the soil and the inclusion with two fully independent, overlapping domains and use a distributed Lagrange multiplier and a level set function to provide the necessary contact interaction. This approach is specific for penetration problems and the extension to other type of applications seems not straightforward.

Ma et al. (2014) implemented in the GIMPM a new contact algorithm to facilitate large deformation analysis with smooth, partially rough or rough contact in geotechnical engineering. They recognize that the Bardenhagen contact algorithm has two limitations:

- The accuracy of the contact algorithm becomes questionable when the stiffness of the contacting materials is very different, such as in the case of interaction between soft clay and penetrometer or foundation. Unrealistic oscillations of the velocity and acceleration are observed.

- In the Coulomb friction model, as modelled by Bardenhagen et al. (2001), the shear stress along the interface is always proportional to the normal stress, that is, the shear stress can be increased indefinitely with the normal stress. This mechanism might be reasonable for elastic materials in contact, but it is unrealistic for cohesive soils under undrained conditions because the shear stress cannot exceed the undrained shear strength of the soil.

A penalty function is introduced to avoid non-physical oscillation, moreover a maximum shear stress, irrespective of the normal stress, is incorporated into the Coulomb friction model for modelling common geotechnical contact conditions. The key concept of the penalty approach is to allow limited interpenetration between the contacting materials. The method showed to be able to reduce numerical oscillations in the contact force, moreover with an optimal selection of the penalty function properties, the interpenetration is limited to a very low level, while the accuracy of the computation is effectively improved.

2.5.3 Multi-phase formulations in MPM

Many problems that are of interest for geotechnical engineers involve fluid-saturated soil. The application of MPM to such multiphase problems is recent (Zhang et al. 2007, Zhang et al. 2008, Zhang et al. 2009, Higo et al. 2010, Jassim et al. 2013, Abe et al. 2013) and the research is in progress.

Zhang et al. (2007) modeled fluid-saturated soil by using two sets or layers of material points. One set of MP moves according to the solid governing equations, while a different set of MP moves according to the fluid governing equations. Such a formulation allows for modeling changes in the water table with time by computing the movements of the fluid particles in the soil. However, their formulation assumed only a small deformation of soil because the same interpolation function was used for both the solid and the fluid layers.

Zhang et al. (2008) proposed a new formulation based on the Eulerian form of the equation in which they modeled solid grains and compressible fluid material. Volume fractions, particle densities, and pressures are directly solved at each step without using time-integrated solutions. They did not use the time-integrated values of pressures because the volume fractions were calculated using a background mesh as the control volume and, for most of the time, the control volume is not fully occupied with material. This leads to errors in pressure increments and an accumulation of errors in the pressure values.

Zhang et al. (2009) introduced a contact algorithm for the coupled MPM based on the u-p formulation, i.e. soil displecement (u) and pore water pressure (p) are the primary variables. They applied the method to predict the dynamic responses of saturated soil subject to contact/impact. In this formulation only one set of material points is used; the material points move with the same velocity of the solid and carry also the information of the liquid.

Higo et al. (2010) proposed a coupled MPM-FDM to model fluid saturated soil. The MPM was used to represent soil particles and the fluid was calculated using an Eulerian approach with FDM (due to the availability of the background grid). The momentum balance equation for the mixture was solved using MPM formulation, and the continuity equation for the water phase was solved using FDM formulation.

Although the u-p formulation can capture the dynamic response for various scenarios, it has been shown that such a formulation cannot accurately capture two-phase dynamic behaviour that involves, for example, the propagation of a compression

wave followed by a second one that is associated with the consolidation process (van Esch et al. 2011a). The full set of equations including all acceleration terms is required to capture both waves. Jassim et al. (2013) implemented a velocity-velocity (v-w) formulation based on the integration steps suggested by Verruijt (2010).

Abe et al. (2013) proposed a soil-pore fluid coupled MPM algorithm based on Biots mixture theory (1962). The continuum is discretized with two layers of particles, i.e., a solid soil skeleton layer and a pore water layer. The water layer is used for calculating the pore-water pressure distribution derived from the equation of state and the velocities of the water particles based on Darcys law. The solid layer is used for calculating the effective stress, velocity, and deformation of the soil skeleton. For demonstrating the applicability of the proposed MPM to geotechnical engineering problems, a large-scale levee-failure experiment conducted by Iseno et al. (2004) was simulated. The numerical model showed to be adequate for simulating the deformation observed after rapid levee failure due to the seepage and migration of water.

A similar two-layer implementation, with advanced featured to increase the numerical stability, has been proposed by (Bandara and Soga 2015). The method has been validated by comparing results with those predicted by analytical solutions and applied to model a levee failure problem using a strain-softening MohrCoulomb model.

2.5.4 Coupling with other methods

One of the prominent trends in recent years is coupling the MPM with other numerical methods. Such an approach allows analysts to reap the benefits of multiple solution types and exploit each method's strengths in multiphysic simulations.

Due to the similarities between MPM and FEM, the combination of these methods comes naturally. The efficiency of MPM is lower than that of FEM due to the mapping between background grid and MP, while the accuracy of calculating the integral with the MP quadrature, used in MPM, is lower than that of Gauss quadrature, used in FEM. FEM is, in general, optimal for small deformations, while MPM is

Zhang et al. (2006) developed an explicit Material Point Finite Element Method (MPFEM) to combine the advantages of both FEM and MPM. In MPFEM, the user is required to identify a large deformation region which is discretized with a computational grid. The material domain is discretized by a mesh of finite elements.

In the large deformation zone, the momentum equations are solved on the computational grid as in the standard MPM. Elsewhere, they are solved on the FE mesh as in the traditional Lagrangian FE method. The finite element nodes covered by the background grid, i.e. in the large deformation zone, are automatically converted into MPM particles.

Similarly, Lian et al. (2011) proposed a Coupled Finite Element Material Point (CFEMP) method, in which the body with mild deformation is discretized by finite elements, while the body with extreme deformation is discretized by MPM particles. The interaction between them is implemented by contact method carried out on the back-ground grid. However, the user is required to identify the body which will experience extreme deformation.

The technique has been further improved in the Adaptive Finite Element Material Point (AFEMP) method (Lian et al. 2012). With this technique, bodies are initially discretized by finite elements, and then the distorted elements are automatically converted into MPM particles when their plastic strain or distortion degree exceeds a user prescribed value during the simulation process. The interaction between the remaining finite elements and MPM particles is implemented based on the background grid. Hence, the material region with mild deformation is modeled by finite elements, while the material region with extreme deformation is modeled by MPM particles automatically.

In order to solve problems of multiphase flow, the MPM has been also coupled with purely Eulerian finite difference or finite volume schemes, e.g., the works presented by Zhang et al. (2008) and Higo et al. (2010). The soil skeleton and the pore fluid are discretized by the MPM and FDM, respectively. In this way the governing equations of different materials or phases are solved by methods well suited to do so.

3

Formulation of the one-phase MPM

As already pointed out, this thesis focuses on the application of the MPM to geomechanical problems. Although the soil is a multi-phase material, characterized by solid particles and fluid or gas filling the pores, in many cases it can be regarded as an homogeneous single-phase material. With this simplified approach only the soild velocity field is considered.

The governing equations of the problem are presented in Section 3.1. The formulation is general, not specific for geomechanical problems, therefore it can be applied to any kind of solid material.

Sections 3.2 and 3.3 explain how the governing equations are discretized in space and time within the MPM; finally the solution procedure is presented in Section 3.4. Possible applications of the one-phase formulation in geotechnical engineering are discussed in section 3.5.

3.1 Governing equations

The analysis of engineering systems requires the idealization of the system, i.e. the formulation of the mathematical model. One group of fundamental equations of continuum mechanics arises from the conservation laws. These equations must always be satisfied by physical systems. Four conservation laws, relevant to thermomechanical systems, are considered here: the conservation of mass, the conservation of linear momentum, often called conservation of momentum, the conservation of angular momentum and the conservation of energy.

A detailed derivation of these equations exceed the purpose of this thesis; for more

details the reader should refer to continuum mechanics books. The definition of the main kinematic and dynamic quantities is in Appendix A.

Conservation of mass. When sources and sinks are neglected, i.e. no mass entering or leaving the domain occupied by the material, the change of mass with time is zero. The mathematical form of the conservation of mass can be written as

$$\frac{\partial \rho}{\partial t} + \rho \frac{\partial v_i}{\partial x_i} = 0 \tag{3.1}$$

with ρ being the mass density of the material, v_i is the i-th component of the velocity and t the time. Equation 3.1 is also referred to as the continuity equation.

Conservation of momentum. Conservation of momentum implies both, conservation of linear and angular momentums. The conservation of linear momentum represents the equation of motion of a continuum, i.e. Newtons second law of motion. It relates the motion or the kinetic of a continuum to the internal and external forces acting upon it. Without going into details of development and derivation of the equation, we give the mathematical form of the conservation of linear momentum as

$$\rho \frac{dv_i}{dt} = \frac{\partial \sigma_{ij}}{\partial x_j} + \rho g_i \tag{3.2}$$

in which the term ρg_i represents the forces due the self weight of the continuum, which are the only body forces considered in this thesis and g_i stands for the components of gravitational acceleration, σ_{ij} is the stress tensor.

The conservation of angular momentum implies that the stress tensor is symmetric,i.e.,

$$\sigma_{ij} = \sigma_{ji} \tag{3.3}$$

As the conservation of angular momentum adds no new equation, most literature calls the conservation of linear momentum as the momentum equation.

Conservation of energy. In this thesis heat effects and any source of thermal energy are disregarded and the mechanical work is considered as the only source of energy, therefore the conservation of energy takes the form

$$\rho \frac{dr}{dt} = \dot{\epsilon}_{ij} \sigma_{ij} \tag{3.4}$$

with r being the internal energy per unit mass and $\dot{\epsilon}_{ij}$ the deformation rate.

The equations given so far apply equally to all material, but they are insufficient to describe the mechanical behavior of any particular material. To complete the specification of the mechanical properties of a material additional equation are required, which are called constitutive equations.

The mechanical constitutive equation of a material specifies the dependence of the stress in a body on kinematic variables such as the strain tensor or the rate-of-deformation tensor. In general the stress rate can be a function of the stress state σ_{ij}, the temperature T and a vector of internal variables $\boldsymbol{\chi}$. For example:

$$\dot{\sigma}_{ij} = f(\dot{\epsilon}_{ij}, \sigma_{ij}, T, \boldsymbol{\chi}) \tag{3.5}$$

Here the thermal effects are neglected. The stress response of a body to a deformation is not affected by rigid motion, therefore the constitutive equations should be invariant under translation and rotation of the frame of reference. This study adopt the Jaumann stress rate tensor, however different definition of the stress rate are possible such as the Truesdell rate and the Green-Naghdi of the Cauchy stress tensor.

An incrementally linear constitutive model assumes the form:

$$\dot{\sigma}_{ij} = D_{ijkl}\dot{\epsilon}_{kl} \tag{3.6}$$

where D_{ijkl} represents the constitutive tensor. Constitutive modeling of soil behavior is one of the most challenging issue in geo-science. A brief overview of the most popular constitutive models is given in chapter 5, however is not in the purpose of this thesis to discuss this issue into details.

3.1.1 Boundary and initial conditions

Let $\partial\Omega$ represents the boundary of the domain; two classes of boundary conditions can be identified: the essential and the natural boundary conditions. The essential boundary conditions are also called Dirichlet or geometric boundary conditions and correspond to prescribed displacements or velocities. The part of the boundary where these conditions are applied is called $\partial\Omega_u$. The natural boundary conditions are also called Neumann or force boundary conditions and corresponds to prescribed boundary forces. $\partial\Omega_\tau$ denotes the part of the boundary where the traction is applied as indicated in Figure 3.1.

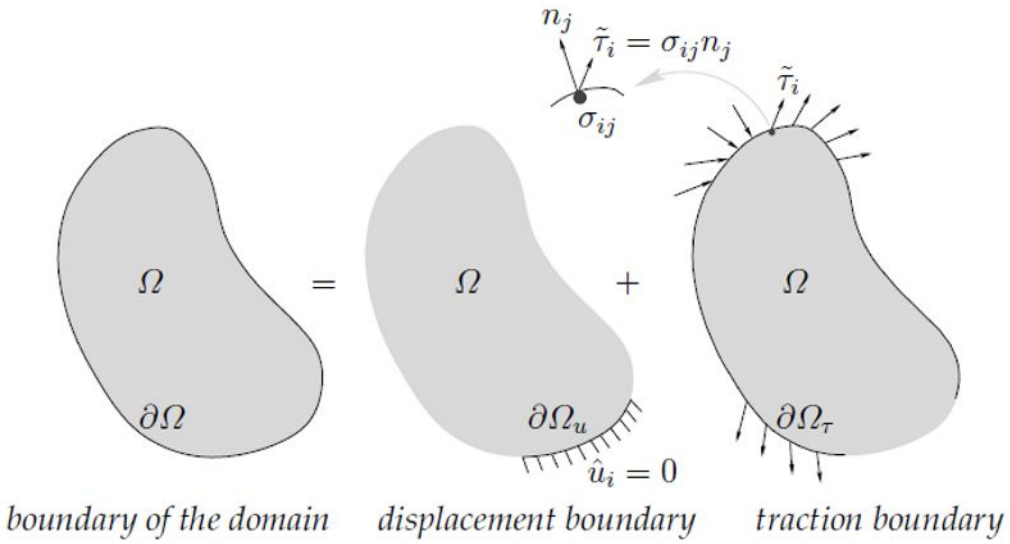

Figure 3.1: Displacement and traction boundary conditions (Al-Kafaji 2013)

The displacement boundary conditions can be written as

$$u_i(\boldsymbol{x}, t) = U_i(t) \quad \text{on} \quad \partial\Omega_u(t) \tag{3.7}$$

The surface traction vector $\tilde{\tau}_i(\boldsymbol{x}, t)$ can be written as a multiplication of a space vector of traction $\tau_i(\boldsymbol{x})$ and a time function $T(t)$, i.e.

$$\tilde{\tau}_i(\boldsymbol{x}, t) = \tau_i(\boldsymbol{x}) T(t) \tag{3.8}$$

Hence, the traction boundary conditions are defined by the Cauchy's formula as

$$\sigma_{ij}(\boldsymbol{x}, t) n_j = \tau_i(\boldsymbol{x}) T(t) \quad \text{on} \quad \partial\Omega_\tau(t) \tag{3.9}$$

with n_j indicating the unit vector normal to the boundary Ω_τ and pointing outward. The vector τ_i represents the prescribed traction at a boundary material point located at $\boldsymbol{x}$.

At the boundary $\partial\Omega$, either displacement or traction must be prescribed, but not both of them, i.e.

$$\partial\Omega_u \cap \partial\Omega_\tau = \emptyset \quad \text{and} \quad \partial\Omega_u \cup \partial\Omega_\tau = \partial\Omega \tag{3.10}$$

It should be realized that the above conditions should be satisfied for each of the three directions.

The initial conditions are written as

$$u_i(\boldsymbol{x}, t_0) = U_{0i}, \quad v_i(\boldsymbol{x}, t_0) = V_{0i} \quad \text{and} \quad \sigma_{ij}(\boldsymbol{x}, t_0) = \sigma_{0ij} \tag{3.11}$$

3.1.2 Weak form of the momentum equation

Equation 3.2 is the strong form of the momentum equation, i.e. strong continuity is required for the field variables. Obtaining the solution for a strong system of equation is usually very difficult for practical engineering problems.

The weak form is usually an integral form and requires weaker continuity on the field variables. For this reason a formulation based on the weak form produces a discrete system of equations that is easier to solve and gives better results, therefore it is preferred in FE formulations (Quek and Liu 2003).

The momentum equation is now multiplied by a test function or a virtual velocity t_i and is integrated over the current domain occupied by the continuum Ω:

$$\int_\Omega t_i \rho \frac{dv_i}{dt} d\Omega = \int_\Omega t_i \frac{\partial \sigma_{ij}}{\partial x_j} d\Omega + \int_\Omega t_i \rho g_i d\Omega \tag{3.12}$$

The test function t_i must be kinematically admissible, i.e. it satisfies the essential boundary conditions and is continuous over the domain.

The use of the Gauss's theorem, also called the divergence theorem, and the Cauchy's formula leads to:

$$\int_\Omega t_i \rho \frac{dv_i}{dt} d\Omega = \int_{\partial\Omega_\tau} t_i \tau_i dS + \int_\Omega t_i \rho g_i d\Omega - \int_\Omega \frac{\partial t_i}{\partial x_i} \sigma_{ij} d\Omega \tag{3.13}$$

which represents the weak form of the momentum equation and will be used in the formulation of the discrete equations.

It should be noted that the first term in Equation 3.13 represents the inertia; the second and the third represent the external surface and body forces; the last one represents the internal force.

3.2 Space discretization

The current section presents the details of the space discretization adopted in the MPM.

Two kinds of space discretization are used in the MPM. Firstly the initial configuration of the analysed body is represented by a cloud of material points (MP). Secondly the entire region where the body is expected to move is discretized by a finite element mesh.

Taking advantage of the symmetry of the strain tensor, the strain and its rate can be represented in a vector form as

$$\dot{\boldsymbol{\epsilon}}(\boldsymbol{x},t) = \frac{d}{dt}\boldsymbol{\epsilon}(\boldsymbol{x},t) \tag{3.14}$$

where

$$\epsilon(\boldsymbol{x},t) = \begin{bmatrix}\epsilon_{11} & \epsilon_{22} & \epsilon_{33} & \gamma_{12} & \gamma_{23} & \gamma_{31}\end{bmatrix}^T \tag{3.15}$$

with ϵ_{ij}, $i = j$ being the normal strain in the direction of the x_i coordinate and $\gamma_{ij} = 2\epsilon_{ij}$, $i \neq j$ being the shear strain in $x_i x_j$ plane.

Similarly, the stress rate vector is

$$\dot{\boldsymbol{\sigma}}(\boldsymbol{x},t) = \frac{d}{dt}\boldsymbol{\sigma}(\boldsymbol{x},t) \tag{3.16}$$

whith

$$\boldsymbol{\sigma}(\boldsymbol{x},t) = \begin{bmatrix}\sigma_{11} & \sigma_{22} & \sigma_{33} & \sigma_{12} & \sigma_{23} & \sigma_{31}\end{bmatrix}^T \tag{3.17}$$

where $\sigma_{ij}, i = j$ is the normal stress in the direction of the x_i coordinate and $\sigma_{ij}, i \neq j$ is the shear stress in $x_i x_j$ plane.

The displacement and eventually the velocity and acceleration are approximated by means of shape functions as:

$$\boldsymbol{u}(\boldsymbol{x},t) \approx \boldsymbol{N}(\boldsymbol{x})\boldsymbol{u}(t) \tag{3.18}$$

$$\boldsymbol{v}(\boldsymbol{x},t) \approx \boldsymbol{N}(\boldsymbol{x})\boldsymbol{v}(t) \tag{3.19}$$

$$\boldsymbol{a}(\boldsymbol{x},t) \approx \boldsymbol{N}(\boldsymbol{x})\boldsymbol{a}(t) \tag{3.20}$$

where $\boldsymbol{N}$ is the matrix of the shape functions, which are identical to the one use in the FEM. The vectors $\boldsymbol{u}(t)$, $\boldsymbol{v}(t)$ and $\boldsymbol{a}(t)$ contain the nodal values of displacement, velocity and acceleration respectively. The test function is approximated in the same way.

The kinematic relation can be written using matrix notation as

$$\dot{\boldsymbol{\epsilon}}(\boldsymbol{x},t) = \boldsymbol{L}\boldsymbol{v}(\boldsymbol{x},t) \tag{3.21}$$

with $\boldsymbol{L}$ being a linear differential operator, that has the following form:

$$\begin{bmatrix} \frac{\partial}{\partial x_1} & 0 & 0 \\ 0 & \frac{\partial}{\partial x_2} & 0 \\ 0 & 0 & \frac{\partial}{\partial x_3} \\ \frac{\partial}{\partial x_2} & \frac{\partial}{\partial x_1} & 0 \\ 0 & \frac{\partial}{\partial x_3} & \frac{\partial}{\partial x_2} \\ \frac{\partial}{\partial x_3} & 0 & \frac{\partial}{\partial x_1} \end{bmatrix} \tag{3.22}$$

Subsituting Equation 3.19 into 3.21 yelds

$$\dot{\boldsymbol{\epsilon}}(\boldsymbol{x}, t) = \boldsymbol{B}\boldsymbol{v}(\boldsymbol{x}, t) \tag{3.23}$$

in which $\boldsymbol{B}$ is the strain-displacement matrix and has the form:

$$\begin{bmatrix} \frac{\partial N_i}{\partial x_1} & 0 & 0 \\ 0 & \frac{\partial N_i}{\partial x_2} & 0 \\ 0 & 0 & \frac{\partial N_i}{\partial x_3} \\ \frac{\partial N_i}{\partial x_2} & \frac{\partial N_i}{\partial x_1} & 0 \\ 0 & \frac{\partial N_i}{\partial x_3} & \frac{\partial N_i}{\partial x_2} \\ \frac{\partial N_i}{\partial x_3} & 0 & \frac{\partial N_i}{\partial x_1} \end{bmatrix} \tag{3.24}$$

Now the virtual work equation 3.13 can be written in matrix form:

$$\int_{\Omega} \boldsymbol{N}^T \rho \boldsymbol{N} \boldsymbol{a} d\Omega = \int_{\partial\Omega_\tau} \boldsymbol{N}^T \boldsymbol{\tau} dS + \int_{\Omega} \boldsymbol{N}^T \rho \boldsymbol{g} d\Omega + \int_{\Omega} \boldsymbol{B}^T \boldsymbol{\sigma} d\Omega \tag{3.25}$$

Closed-form integrations in Equation 3.25 are difficult, or even impossible. Numerical integration is adopted to evaluate these integrals.

In FEM, standard Gauss integration is adopted, which means, e.g. for the last term of Equation 3.25:

$$\int_{\Omega_e} \boldsymbol{B}^T \boldsymbol{\sigma}_e d\Omega \approx \sum_{q=1}^{n_{eq}} W_q \boldsymbol{B}^T(\boldsymbol{x}_q) \boldsymbol{\sigma}_e(\boldsymbol{x}_q, t) \tag{3.26}$$

where the pedix e denotes the element; W_q is the global integration weight associated with the quadrature point q and n_{eq} is the number of quadrature points in the element.

The MPM method is characterized by the so-called Material Point integration, which means that the quadrature points coincide with the MP and the weight associated

to the MP is its volume Ω_p. Therefore Equation 3.26 becomes:

$$\int_{\Omega_e} \boldsymbol{B}^T \boldsymbol{\sigma}_e d\Omega \approx \sum_{p=1}^{n_{ep}} \Omega_p \boldsymbol{B}^T(\boldsymbol{x}_p)\boldsymbol{\sigma}_p \tag{3.27}$$

where now the pedix p refers to the MP, i.e. n_{ep} is the number of MP inside the element, $\boldsymbol{x}_p$ and σ_p are the position and the stress associated to the MP respectively.

At this step, it is important to emphasized that one of the difference between FEM and MPM lies on the integration method used to assemble the equation of motion.

The discretized equation of motion, in matrix notation, assumes the form:

$$\boldsymbol{M}\boldsymbol{a} = \boldsymbol{F}^{ext} + \boldsymbol{F}^{grav} - \boldsymbol{F}^{int} \tag{3.28}$$

Where $\boldsymbol{M}$ is the mass matrix, i.e.

$$\boldsymbol{M} = \sum_{p=1}^{n_p} m_p \boldsymbol{N}^T(\boldsymbol{x_p})\boldsymbol{N}(\boldsymbol{x_p}) \tag{3.29}$$

which depends on the position of the MP, of mass m_p, with respect to the computational mesh. In order to improve the efficiency of the algorithm, a diagonal form of the mass matrix, called lumped mass matrix, is used.

The external forces $\boldsymbol{F}^{trac}$ and $\boldsymbol{F}^{grav}$ are calculated as:

$$\boldsymbol{F}^{trac} \approx \sum_{p=1}^{n_{ebp}} \boldsymbol{N}^T(\boldsymbol{\xi}_p)\boldsymbol{f}_p^{trac} \tag{3.30}$$

$$\boldsymbol{F}^{grav} \approx \sum_{p=1}^{n_{ep}} \boldsymbol{N}^T(\boldsymbol{\xi}_p)\boldsymbol{f}_p^{grav} \tag{3.31}$$

where $\boldsymbol{f}_p^{trac}$ and $\boldsymbol{f}_p^{grav}$ are the traction and the gravity assign to the MP; details of MP initialization are in Paragraph 3.4.1.

The internal force $\boldsymbol{F}^{int}$ is calculated according to Equation 3.27.

3.3 Time discretization

Equation 3.28 is discretized in space, but still continuous in time. It represents a series of second-order ordinary differential equations (ODE) in time. To get a full

discrete system of algebraic equations, Equation 3.28 has to be discretized in time.

A common procedure to do that is by replacing the differentials in the ODE by finite difference quotients on a discretized time domain, which is the independent variable in our ODE. In the present study the explicit Euler-Cromer scheme is used. This means that the acceleration is calculated explicitly and the velocity is updated implicitly, i.e.:

$$\boldsymbol{a}^t = \boldsymbol{M}^{t,-1}(\boldsymbol{F}^{ext,t} + \boldsymbol{F}^{grav,t} - \boldsymbol{F}^{int,t}) \tag{3.32}$$

$$\boldsymbol{v}^{t+\Delta t} = \boldsymbol{v}^t + \boldsymbol{a}^t \Delta t \tag{3.33}$$

This explicit scheme is conditionally stable, which means that the time increment should be smaller than a certain value which depends on material density, stiffness and the minimum size of the elements. In other words the critical time step should statisfy the Courant, Friedrichs and Lewy (CFL) condition:

$$\Delta t_{crit} = \frac{l_e}{c_p} \tag{3.34}$$

where l_e = minimum lenght of the element mesh and

$$c_p = \sqrt{\frac{E_c}{\rho}} \tag{3.35}$$

is the velocity of the compression wave in the material. E_c is the constrained compression modulus and, for elastic material, it is a function on the poisson ration ν and the Young modulus E:

$$E_c = \frac{(1-\nu)}{(1+\nu)(1-2\nu)} E \tag{3.36}$$

Equation 3.34 insures the stability of the numerical scheme, however, in certain cases a smaller time step should be used to get an accurate solution.

The time step size can be controlled by mean of the Courant number C:

$$C = \frac{\Delta t}{\Delta t_{crit}} \tag{3.37}$$

In quasi static problem, where energy conservation is not very important, Courant number close to 1 can be used. For highly dynamic problems, where energy conservation is important $C \approx 0.5$ should be used. For example, in this thesis, the solution of the sliding block shown in section 6.4.2 required $C = 0.5$, while for the

slow-process of cone penetration $C = 0.98$ presented in chapter 9 is sufficient and a reduction of this factor does not improve significantly the results.

3.4 Solution procedure

In the current section the solution procedure used in the MPM is discussed in detail. The presentation follows (Al-Kafaji 2013). The attention is firstly focused on the initialization procedure, i.e. assignment of data to the material points (Sec. 3.4.1). Secondly the solution algorithm of each time step is explained (Sec. 3.4.2).

Each time increment consists of two main phase: the Lagrangian and the Convective phase. The Lagrangian phase is similar to the standard FEM: the governing equations are solved at the nodes of the mesh, which therefore deforms with the body. During the convective phase, strain, stresses and other state variables are updated at the MP location by mean of interpolation functions and the nodal values of the quantities computed in the previous phase.

3.4.1 Initialization of material points

As already mentioned, the MP carry all the information of the continuum. In this section, we discuss the initialization of MP within the background mesh. This includes association of mass, body forces, tractions and other properties of the continuum to MP. Elements filled with MP are called active elements and their nodes contribute to the solving system of equations; on the contrary the empty elements, i.e. those without any MP, are ignored thus reducing the computational cost.

Let us consider a single tetrahedral element to explain the full procedure of initialization of MP information. Each MP is initially positioned at a predefined local position inside the parent element, and hence the local position vector $\boldsymbol{\xi}_p$ of MP p is initialized. The global position vector $\boldsymbol{x}_p$ is then obtained as

$$\boldsymbol{x}_p(\boldsymbol{\xi}_p) \approx \sum_{i=1}^{n_{en}} N_i(\boldsymbol{\xi}_p^t)\boldsymbol{x}_i \tag{3.38}$$

in which n_{en} denotes the number of nodes per element, $N_i(\boldsymbol{\xi}_p)$ is the shape function of node i evaluated at the local position of MP p and $\boldsymbol{x_i}$ are the nodal coordinates.

Volumes associated with MP are calculated so that all the MP inside the element

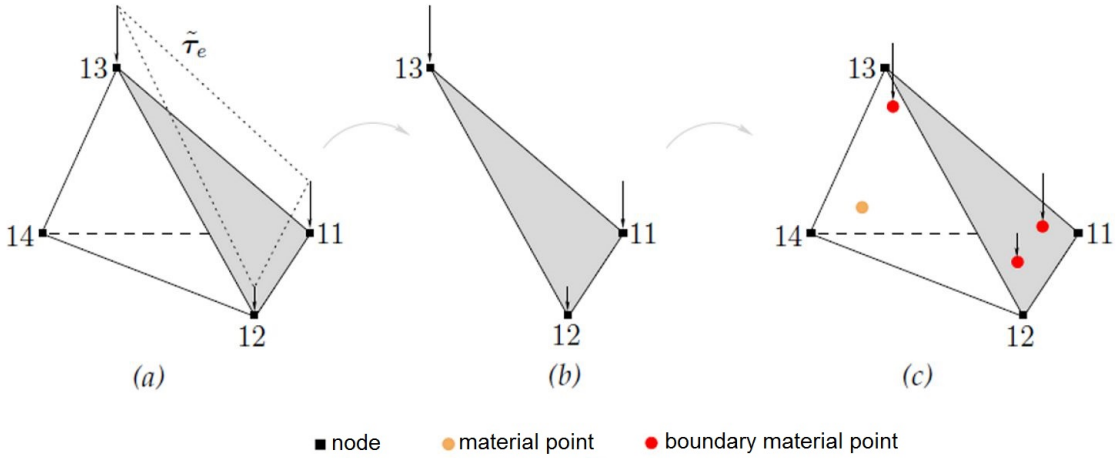

Figure 3.2: Intialization of surface traction. (a) terahedal element (b) triangular element (c) traction is mapped to the boundary MP (Al-Kafaji 2013).

have initially the same portion of the element volume, i.e.

$$\Omega_p = \frac{1}{n_{ep}} \int_{\Omega_e} d\Omega \approx \frac{1}{n_{ep}} \sum_{q=1}^{n_{eq}} w_q |\boldsymbol{J}(\boldsymbol{\xi}_q)| \tag{3.39}$$

where Ω_p is the volume associated with MP p, n_{ep} denotes the number of MP in the element, n_{eq} is the number of Gauss points in the element, w_q is the local integration weight associated with Gauss point q, and $\boldsymbol{J}$ is the Jacobian matrix. This implies that, at the beginning of the calculation, all the active elements are assumed to be fully filled by the continuum body. An element is said to be partially filled if the sum of the volumes of the contained MP is less than the element volume.

The mass m_p is then calculated as

$$m_p = \Omega_p \rho_p \tag{3.40}$$

with ρ being the mass density of the material to which the MP p belongs.

The gravity force $\boldsymbol{f}_p^{grav}$ is simply calculated using the mass of the MP and the vector of gravitational acceleration $\boldsymbol{g}$ as

$$\boldsymbol{f}_p^{grav} = m_p \boldsymbol{g} \tag{3.41}$$

The external forces applied at the traction boundary are mapped to the MP located next to the element border, also called boundary MP. These MP carry surface traction throughout the computations. Considering a tetrahedral element, the traction

vector $\boldsymbol{\tau}_e$ applied at the triangular surface is interpolated from the nodes of this surface to the boundary MP. Hence, the traction at boundary MP p is

$$\boldsymbol{\tau}_e(\boldsymbol{x}_p) \approx \sum_{i=1}^{n_{tri}} N_i(\boldsymbol{\xi}_q)\boldsymbol{\tau}_e(\boldsymbol{x}_i) \tag{3.42}$$

where N_i is the shape function of node i of the triangular surface element and $\boldsymbol{\xi}_q$ are the coordinates of the boundary MP p inside the parent triangular element. These coordinates simply represent the projection of the MP on the triangular surface element. The traction force vector $\boldsymbol{f}_p^{trac}$ is then

$$\boldsymbol{f}_p^{trac} = \boldsymbol{\tau}_e(\boldsymbol{x}_p)\frac{S_e}{n_{ebp}} = \frac{S_e}{n_{ebp}} \sum_{i=1}^{n_{tri}} N_i(\boldsymbol{\xi}_p)\boldsymbol{\tau}_e(\boldsymbol{x}_i) \tag{3.43}$$

in which n_{ebp} denotes the number of boundary MP located next to the loaded surface.

In the initialization of MP, initial conditions, material parameters and constitutive variables are assigned to them as well. Furthermore, book-keeping is initialized at this step, including information such as to which element each particle initially belongs and the initial number of particles per each active finite element.

3.4.2 Solution of the governing equations

In the present section the solution procedure for the MPM, known as modified Lagrangian algorithm, is presented.

Let us consider the state of a continuum at time t and describe the procedure of advancing the solution to time $t + \Delta t$. It consists of the following steps:

1. The momentum equation is initialized. This means that the lumped-mass matrix $\boldsymbol{M}^t$ is computed at the beginning of the time step, the traction force vector $\boldsymbol{F}^{trac,t}$ is calculated with:

$$\boldsymbol{F}^{trac,t} = \bar{\boldsymbol{F}}^{trac,t}T(t) \quad \text{in which} \quad \bar{\boldsymbol{F}}^{trac,t} \approx \sum_{p=1}^{n_{ebp}} m_p \boldsymbol{N}^T(\boldsymbol{\xi}_p^t)\boldsymbol{f}_p^{trac,t} \tag{3.44}$$

the gravity force $\boldsymbol{F}_{grav,t}$ and the internal force $\boldsymbol{F}_{int,t}$ are integrated as

$$\boldsymbol{F}^{grav,t} \approx \sum_{p=1}^{n_{ep}} \boldsymbol{N}^T(\boldsymbol{\xi}_p^t)\boldsymbol{f}_p^{grav,t} \tag{3.45}$$

$$\boldsymbol{F}^{int,t} \approx \sum_{p=1}^{n_{ep}} \boldsymbol{B}^T(\boldsymbol{\xi}_p^t)\boldsymbol{\sigma}_p^t\Omega_p^t \tag{3.46}$$

The discrete system of equations is complete:

$$\boldsymbol{M}^t\boldsymbol{a}^t = \boldsymbol{F}^{trac,t} + \boldsymbol{F}^{grav,t} - \boldsymbol{F}^{int,t} = \boldsymbol{F}^t \tag{3.47}$$

2. The system is solved for the nodal accelerations as

$$\boldsymbol{a}^t = \boldsymbol{M}^{t,-1}\boldsymbol{F}^t \tag{3.48}$$

3. In this step, the velocities of MP are updated using the nodal accelerations and the shape functions

$$\boldsymbol{v}_p^{t+\Delta t} = \boldsymbol{v}_p^t + \sum_{i=1}^{n_{en}} \Delta t N_i(\boldsymbol{\xi}_p^t)\boldsymbol{a}_i^t \tag{3.49}$$

4. The nodal velocities $\boldsymbol{v}^{t+\Delta t}$ are then calculated from the updated MP momentum solving the following equation

$$\boldsymbol{M}^t\boldsymbol{v}^{t+\Delta t} \approx \sum_{p=1}^{n_{ep}} m_p\boldsymbol{N}^T(\boldsymbol{\xi}_p^t)\boldsymbol{v}_p^t \tag{3.50}$$

5. Nodal velocities are integrated to get nodal incremental displacements

$$\Delta\boldsymbol{u}^{t+\Delta t} = \Delta t\boldsymbol{v}^{t+\Delta t} \tag{3.51}$$

6. Strains at MP are calculated as

$$\Delta\boldsymbol{\epsilon}_p^{t+\Delta t} = \boldsymbol{B}(\boldsymbol{\xi}_p^t)\Delta\boldsymbol{u}^{t+\Delta t} \tag{3.52}$$

and stresses are updated according to the constitutive relation

7. Volumes associated with MP are updated using the volumetric strain incre-

ment

$$\Omega_p^{t+\Delta t} = (1 + \Delta\epsilon_{vol,p}^{t+\Delta t}) \quad \text{with} \quad \Delta\epsilon_{vol} = \Delta\epsilon_{11} + \Delta\epsilon_{22} + \Delta\epsilon_{33} \tag{3.53}$$

Consequently the density is updated

$$\rho_p^{t+\Delta t} = \frac{\rho_p^t}{(1 + \Delta\epsilon_{vol,p}^{t+\Delta t})} \tag{3.54}$$

8. Displacements and positions of MP are updated according to

$$\boldsymbol{u}_p^{t+\Delta t} = \boldsymbol{u}_p^t + \sum_{i=1}^{n_{en}} \boldsymbol{N}(\boldsymbol{\xi}_p^t)\boldsymbol{u}_i^{t+\Delta t} \tag{3.55}$$

$$\boldsymbol{x}_p^{t+\Delta t} = \boldsymbol{x}_p^t + \sum_{i=1}^{n_{en}} \boldsymbol{N}(\boldsymbol{\xi}_p^t)\boldsymbol{u}_i^{t+\Delta t} \tag{3.56}$$

9. The mesh can be reset and the book-keeping is updated. At this step a new element is detected for those MP that crossed elements boundary. Consequently the new number of MP per each finite element is determined. The active and inactive elements are identified and the new local position of each particle inside the element are obtained.

The reader should have noted that the nodal velocity is not directly computed from the nodal acceleration, but from the MP momentum. This prevents the so-called small mass problem (Sulsky et al. 1995). When a MP enters a previously empty element and remains close to the boundary, the values of the associated shape functions relative to those element nodes which are far from the MP, i.e. $N_i(\boldsymbol{\xi}_p)$, approach zero. As a consequence, the nodal mass approaches zero, leading to a nearly singular, ill-conditioned mass matrix. The internal force involves the gradient of the shape function, which is constant inside the element, and hence the right-hand side term of Equation 3.47 does not approach zero. Unphisical nodal acceleration can therefore be obtained. The problem is solved on the level of velocity through steps 3 and 4 of the previous list.

3.5 Applicability of one-phase formulation in soil mechanics

Soil is, in general, a mixture of three phases: soild, fluid and gas. The fluid can be water, oil or other liquid substances; the gas can be air, hydrocarbon or other types of gas. Considering a soil sample of volume V, the volumes occupied by solid grains, fluid and gas as separate phases can be identified with V_s, V_f and V_g respectively. The volume collectively occupied by fluid and gas is also called void volume V_v since they occupies the pores between soil grains. In this thesis only the presence of water inside the pores is considered.

The void ratio e and the porosity n can be defined as:

$$e = \frac{V_v}{V_s} \qquad n = \frac{V_v}{V} \tag{3.57}$$

The degree of saturation represents the percentage of void volume occupied by the fluid and is expressed as

$$S_r = \frac{V_f}{V_v} \cdot 100\% \tag{3.58}$$

The soil is said to be dry if $S_r = 0\%$ and fully saturated if $S_r = 100\%$ otherwise it is partially saturated. In this thesis partially saturated conditions are not considered.

Considering the soild grain-water mixture different densities can be defined:

Dry density

$$\rho_d = (1 - n)\rho_s \tag{3.59}$$

where ρ_s represents the grain density of the solid phase and usually assumes values close to 2700 kg/m^3.

Saturated density

$$\rho_{sat} = \rho_d + n\rho_w = (1 - n)\rho_s + n\rho_w \tag{3.60}$$

where ρ_w is the water density.

Usually the soil density is comprise between these two, since some air is always included in the pores.

Similarly, the following unit weight can be defined:

Dry unit weight

$$\gamma_d = \rho_d g \tag{3.61}$$

Saturated unit weight

$$\gamma_{sat} = \rho_{sat} g \tag{3.62}$$

Submerged unit weight

$$\gamma' = \gamma_{sat} - \gamma_w \tag{3.63}$$

where g and γ_w are the gravity and the water unit weight respectively.

In saturated soil, depending on the soil permeability and the rate of load, drained, partially drained and undrained conditions can be encountered. In drained conditions a negligible excess pore pressure is generated and rapidly dissipates, therefore it can be neglected. In undrained conditions the rate of load is so fast that there is a significant generation of excess pore pressure, but negligible relative movement between solid and fluid phase, therefore pore pressure dissipation can be neglected. In partially drained conditions excess pore pressure generation and dissipation are not negligible, therefore a proper formulation, able to take into account the coupled behavior of solid and water should be used.

In numerical analyses dealing with drained conditions and undrained conditions the presence of the water can be considered in a simplified way. In the first case the presence of the water can be neglected and the soil can be regarded as dry. In the latter, because of the negligible relative movement between solid and water, the equilibrium of the soil-water mixture can be considered rather than the equilibrium of soil and water as separate phases. The stress state can be described in terms of total stresses or effective stresses. In the second case the excess pore pressures can be computed by means of the so-called Effective Stress Analysis, which is based on the assumption of strain compatibility between the soil skeleton and the enclosed pore water (Vermeer 1993); further detail are given in section 3.5.1.

Modelling of dry soil, saturated soil in drained and undrained conditions are the field of applicability of the one-phase formulation. For partially drained conditions a fully-coupled two-phase formulation is necessary. This is presented in chapter 4.

3.5.1 Effective stress analysis for elastic soil skeleton

In a saturated soil the total load is constantly divided between fluid a soil skeleton. According to the effective stress principle, the total stress σ_{ij} is decomposed into

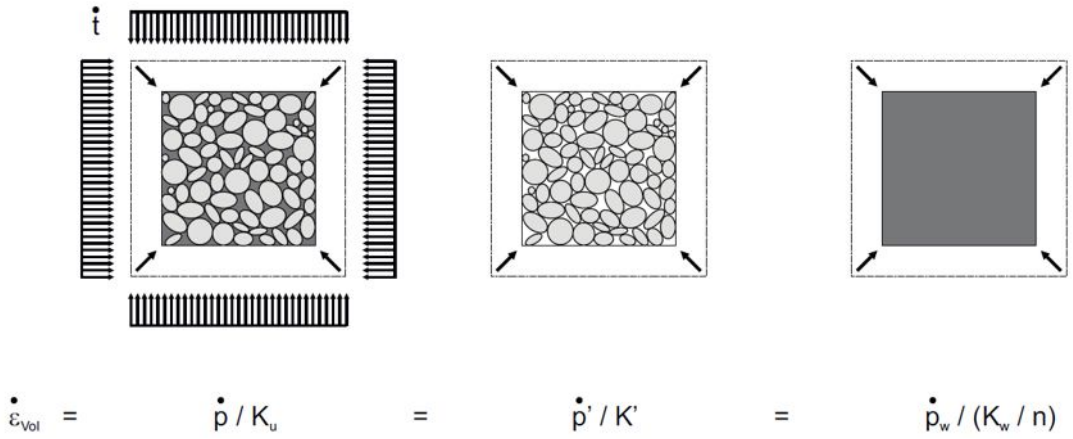

Figure 3.3: Rappresentation of strain compatibility

effective stress σ'_{ij} and pore pressure p_w:

$$\sigma_{ij} = \sigma'_{ij} + p_w \delta_{ij} \tag{3.64}$$

where δ_{ij} is the Kroneker delta.

A further distinction is made between the steady and the excess pore pressure. The first one is usually considered as an input, while the second one is generated by the loading mechanism. Since the time derivative of the steady pore pressure is null, only the variation in excess pore pressure will be considered.

Which fraction of an applied incremental load is carried by the soil skeleton and which fraction is carried by the pore water follows from the consideration of strain compatibility. The stiffnesses of the soil skeleton, the soil minerals and the pore water must be considered. This, of course, only holds for undrained conditions, when no dissipation of water with time is considered. The soil minerals can be considered as incompressible, since their bulk modulus is much higher than the one of soil skeleton (K') and water (K_w). Pore water is mostly assumed to be slightly more compressible than pure water because some air is always included even for a fully saturated soil.

Assuming undrained conditions and incompressible soil grains, strain compatibility requires that the change of volume of the soil-water mixture, due to total load, corresponds to the change of volume of the soil skeleton, due to effective pressure, and to the change of volume of the water-filled pores, due to pore water pressure. In other terms:

$$\dot{\epsilon}_{vol} = \frac{\dot{p}}{K_u} = \frac{\dot{p}_w}{K_w/n} = \frac{\dot{p}'}{K'} \tag{3.65}$$

where K_u is the so-called undrained bulk modulus and represent the stiffness of the soil mixture in undrained conditions. Eq. 3.65 is valid for an elastic soil skeleton; indeed in elastoplastic models the volumetric strain rate may also depend on deviatoric stresses and in viscoplastic models the time depencency of $\dot{\epsilon}_{vol}$ is included.

Considering the effective stress principle, Equation 3.65, leads to:

$$K_u = K' + \frac{K_w}{n} \tag{3.66}$$

The bulk modulus can be written as a function of the Poisson ratio ν and the shear modulus G (Eq. 3.67 and 3.68).

$$K' = \frac{2G(1+\nu')}{3(1-2\nu')} \tag{3.67}$$

$$K_u = \frac{2G(1+\nu_u)}{3(1-2\nu_u)} \tag{3.68}$$

ν_u indicates the Poisson's ration of the mixture in undrained conditions and is approximately 0.5, while the shear modulus G is the same for the mixture and the soil skeleton.

Inserting Equations 3.67 and 3.68 in Equation 3.66 and solving for the bulk modulus of water, it leads to:

$$\frac{K_w}{n} = \frac{3(\nu_u - \nu')}{(1-2\nu_u)(1+\nu')} K' \tag{3.69}$$

Upon sudden loading, a fully saturated soil shows no noteworthy change of volume and the applied load is found to be carried almost entirely by the pore water. On the other hand, assuming slight compressibility of the pore water is of advantage for numerical analyses. Indeed, a high stiffness of the pore water, resulting in a nearly incompressible material, causes numerical problems such as volumetric locking and a severe ill-conditioning of the stiffness matrix. In order to prevent numerical problems, the undrained Poisson ratio is generally set to a value between 0.485 and 0.495. In this thesis $\nu_u = 0.490$ is used for undrained calculations.

A useful parameter to represent the fraction of total load carried by the water is the Skempton's B-parameter. It is widely used in laboratory practice and can be written as:

$$B = \frac{\dot{p}_w}{\dot{p}} = \frac{K_w/n}{K_u} = \frac{1}{1 + \frac{K'}{K_w/n}} \tag{3.70}$$

For saturated soil it is close to 1.

4

Formulation of a two-phase MPM

In geotechnical engineering, problems characterized by the solid-fluid interaction are very common. As explained in section 3.5, sometimes the presence of the fluid can be treated in a simplified way; on the other hand, when the relative movement between solid skeleton and water is important, a fully coupled formulation is essential.

The current Chapter focuses on the MPM formulation to analyze coupled dynamic two-phase problems. In Section 4.1 the governing equations of the continuum problem are presented, to move on with the solution procedure within MPM in Section 4.2. Since the MPM implementation of the two-phase formulation consists in a natural extension of the one-phase formulation, many details are omitted; the reader can find further information in Al-Kafaji (2013). The validation and some applications of the two-phase formulation are in Chapter 7.

4.1 Governing equations

This section is devoted to the presentation of the governing equations that are required for the solution of coupled dynamic, two-phase problems. The first complete theoretical approach describing the coupling between solid and fluid phases was proposed by Biot (1941) for a linear elastic soil skeleton while considering fluid seepage based on Darcy's law, in quasi-static conditions. This work is based on the early work on porous media by von Terzaghi (1936). Biot's theory (BT) was further extended to anisotropic cases (Biot 1955). The dynamic extension of BT was published in two papers: (a) for low frequency range (Biot 1956c), and (b) for high frequency range (Biot 1956b). The theory was later extended to finite deformations in elasticity (Biot 1972). Zienkiewicz and co-workers (Zienkiewicz

et al. 1980; Zienkiewicz 1982; Zienkiewicz and Shiomi 1984; Zienkiewicz et al. 1990; Zienkiewicz et al. 1999) extended BT into nonlinear range, i.e. material and geometric non-linearities, under dynamic loads.

The equations that describe the two-phase physics are: conservation of mass, conservation of momentum, and the constitutive relation. In the exact solution, i.e. no simplifications are considered, the principal unknowns are the displacement of the soil ($\boldsymbol{u}$), the relative velocity between solid and fluid or the seepadge velocity ($\boldsymbol{w}_r$), and the fluid pressure. Due to its complexity this formulation is rarely used in FEM, however Zienkiewicz et al. (1980) observed that this formulation is necessary for extremely rapid motions.

In the so-called u-p-formulation the relative acceleration of the fluid is neglected. The primary variables are the solid displacement and the fluid pressure. Many of the currently available FEM implementations are based on this formulation due to its simplicity. This is suitable for low frequency and quasi static problems (Zienkiewicz et al. 1980).

The well-known consolidation equation neglects all acceleration terms and is therefore suitable only for this type of problems.

With the formulation used in this thesis, the equilibrium equations are solved for the accelerations of water phase and soil skeleton as the primary unknown variables. This two-phase approach is commonly called v-w-formulation (Verruijt 1996), where v and w denote the velocities of the solid and liquid phase respectively. This formulation proved to be able to capture the physical response of saturated soil under dynamic as well as static loading (van Esch et al. 2011a).

The detailed derivations of the governing equations is not discussed here. The reader can refer to the work by Zienkiewicz and co-workers (1984, 1990 and 1999) for further details on two-phase formulations and to Verruijt (1996) for more detail on the applications to dynamic loading. The main focus of the current Section is to clarify the assumptions which characterize the used formulation and define the terms of the governing equations.

4.1.1 Mass conservation

The conservation of mass of the solid phase is expressed as:

$$\frac{\partial}{\partial t}[(1-n)\rho_s] + \frac{\partial}{\partial x_j}[(1-n)\rho_s v_j] = 0 \tag{4.1}$$

in which v_j is the j-th component of the velocity vector of the solid phase.

On denoting the components of the vector of the (true) velocity of the water phase as w_j, the conservation of mass of this phase can be written as:

$$\frac{\partial}{\partial t}\left(n\rho_w\right) + \frac{\partial}{\partial x_j}\left(n\rho_w w_j\right) = 0 \tag{4.2}$$

When considering incompressible solid grains and disregarding the spatial variations in densities and porosity, one can reduce the expression for the conservation of mass of the solid and water phases to

$$-\frac{\partial n}{\partial t} + (1-n)\frac{\partial v_j}{\partial x_j} = 0 \tag{4.3}$$

and

$$n\frac{\partial \rho_w}{\partial t} + \rho_w \frac{dn}{dt} + n\rho_w \frac{\partial w_j}{\partial x_j} = 0 \tag{4.4}$$

respectively. Substituting Equation 4.3 into Equation 4.4 allows to eliminate the term $\frac{dn}{dt}$. Hence,

$$n\frac{\partial \rho_w}{\partial t} + \rho_w(1-n)\frac{\partial v_j}{\partial x_j} + n\rho_w \frac{\partial w_j}{\partial x_j} = 0 \tag{4.5}$$

The water is assumed to be linearly compressible via the relation

$$\frac{d\rho_w}{dp_w} = -\frac{\rho_w}{K_w} \tag{4.6}$$

Substituting Equation 4.6 into Equation 4.5 and rearranging terms yields:

$$\frac{\partial p_w}{\partial t} = \frac{K_w}{n}\left[(1-n)\frac{\partial v_j}{\partial x_j} + n\frac{\partial w_j}{\partial x_j}\right] \tag{4.7}$$

Equation 4.7 represents the conservation of mass of the saturated soil. It is also known as storage equation.

4.1.2 Conservation of momentum

The conservation of momentum of the solid phase can be expressed as

$$(1-n)\rho_s \frac{dv_j}{dt} - \frac{\partial \sigma'_{ij}}{\partial x_i} - (1-n)\frac{\partial p_w}{\partial x_j} - (1-n)\rho_s g_j - \frac{n^2 \rho_w g}{k}(w_j - v_j) = 0 \tag{4.8}$$

where k is the Darcy permeability. It can be expressed in terms of the intrinsic permeability $\tilde{k}$ and the dynamic viscosity of the water μ_d as:

$$k = \tilde{k}\frac{\rho_w g}{\mu_d} \tag{4.9}$$

The conservation of momentum of the liquid phase is written as:

$$n\rho_w \frac{dw_j}{dt} - n\frac{\partial p_w}{\partial x_j} - n\rho_w g_j + \frac{n^2 \rho_w g}{k}(w_j - v_j) = 0 \tag{4.10}$$

the therm $(w_j - v_j)$ represent the relative velocity of the water respect to the solid.

Adding the momentum of the solid phase (Eq. 4.8), to the momentum of the water phase (Eq. 4.10), the momentum conservation for the mixture can be written as:

$$(1-n)\rho_s \frac{dv_j}{dt} + n\rho_w \frac{dw_j}{dt} = \frac{\partial \sigma_{ij}}{\partial x_j} + \rho_{sat} g_j \tag{4.11}$$

Summarizing, the two-phase problem is described by two momentum equations, i.e. 4.10 for the liquid and 4.11 for the mixture, the storage equation (4.7), and the constitutive equation for the soil skeleton. These equations are derived neglecting the spatial variation of densities and porosity, assuming incompressible soil grains, and assuming the validity of the Darcy's law.

4.1.3 Boundary conditions

The v-w-formulation requires that the boundary of the domain is the union of the following components

$$\partial\Omega = \partial\Omega_u \cup \partial\Omega_\tau = \partial\Omega_w \cup \partial\Omega_p \tag{4.12}$$

where $\partial\Omega_w$ and $\partial\Omega_p$ are the prescribed velocity and prescribed pressure boundaries of the water phase, respectively, whereas $\partial\Omega_u$ is the prescribed displacement (velocity) boundary of the solid phase and $\partial\Omega_\tau$ is the prescribed total stress boundary.

The following conditions should also be satisfied at the boundary

$$\partial\Omega_u \cap \partial\Omega_\tau = \emptyset \quad \text{and} \quad \partial\Omega_w \cap \partial\Omega_p = \emptyset \tag{4.13}$$

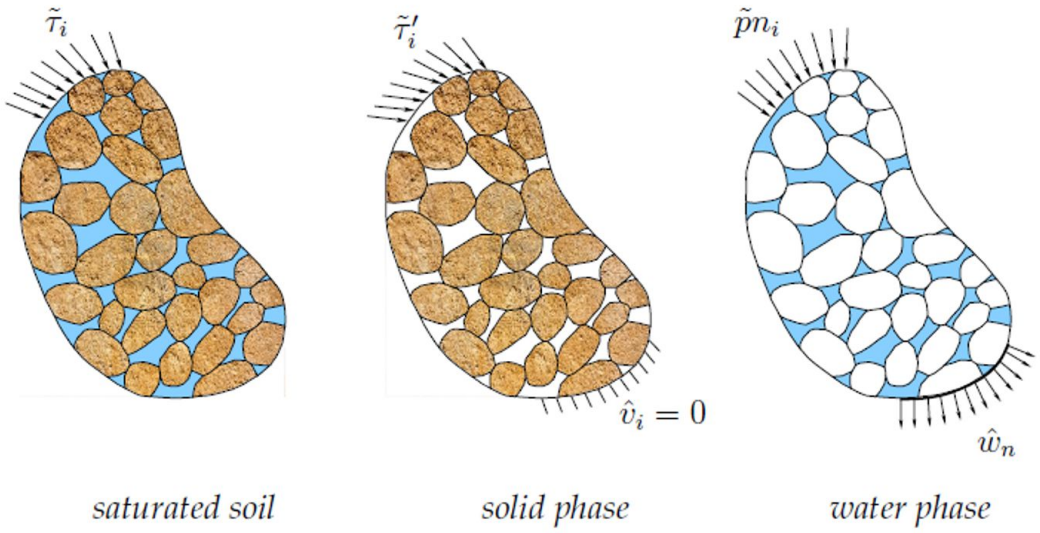

Figure 4.1: Displacement and traction boundary conditions for two phase problem (Al-Kafaji 2013).

4.1.4 Weak form of momentum equations

Before the discretization, the strong form of the governing equations has to be transformed in the weak form. This is achieved by multiplying Equations 4.10 and 4.11 by weighting function t_j and integrating over the current domain Ω:

$$\int_\Omega t_j \rho_w \frac{dw_j}{dt} d\Omega = \int_\Omega t_j \frac{\partial p_w}{\partial x_j} d\Omega + \int_\Omega t_j \rho_w g_j d\Omega - \int_\Omega t_j \frac{n \rho_w g}{k} (w_j - v_j) d\Omega \qquad (4.14)$$

$$\int_\Omega t_j (1-n) \rho_s \frac{dv_j}{dt} d\Omega = \int_\Omega t_j \frac{\partial \sigma_{ij}}{\partial x_j} d\Omega + \int_\Omega t_j \rho_{sat} g_j d\Omega - \int_\Omega t_j n \rho_w \frac{dw_j}{dt} d\Omega \qquad (4.15)$$

Applying the divergence theorem and the traction boundary conditions, the final weak forms are:

$$\int_\Omega t_j \rho_w \frac{dw_j}{dt} d\Omega = \int_{\partial\Omega_p} t_j p_{wj} dS - \int_\Omega \frac{\partial t_j}{\partial x_j} p_w d\Omega + \int_\Omega t_j \rho_w g_j d\Omega - \int_\Omega t_j \frac{n \rho_w g}{k} (w_j - v_j) d\Omega \qquad (4.16)$$

$$\int_\Omega t_j (1-n) \rho_s \frac{dv_j}{dt} d\Omega = + \int_{\partial\Omega_\tau} t_j \tau_j dS - \int_\Omega \frac{\partial t_j}{\partial x_j} \sigma_{ij} d\Omega + \int_\Omega t_j \rho_{sat} g_j d\Omega - \int_\Omega t_j n \rho_w \frac{dw_j}{dt} d\Omega \qquad (4.17)$$

The left-hand side terms in Equations 4.16 and 4.17 represent the inertia. In the right-hand side, the first terms represent the external force applied at the boundary, the second terms represent the internal load, the third terms represent the gravity. The last term in Equation 4.16 is the drag force. The last term in Equation 4.17 is the water inertia, where the porosity is taken into account.

4.2 Solution procedure

The presented solution procedure follows Al-Kafaji (2013), to which the reader is referred for further details. The space discretization of Equations 4.16 and 4.17 follows the same procedure presented in Section 3.2. The same shape functions are used to approximate the velocities of the water and solid phases as well as the weighting function.

The discrete system of equations can be written as:

$$\boldsymbol{M}_w^t \boldsymbol{a}_w^t = \boldsymbol{F}_w^{trac,t} + \boldsymbol{F}_w^{grav,t} - \boldsymbol{F}_w^{int,t} - \boldsymbol{F}^{drag,t} \tag{4.18}$$

$$\boldsymbol{M}_s^t \boldsymbol{a}_s^t = \boldsymbol{F}^{trac,t} + \boldsymbol{F}^{grav,t} - \boldsymbol{F}^{int,t} - \bar{\boldsymbol{M}}_w^t \boldsymbol{a}_w^t \tag{4.19}$$

where

$$\boldsymbol{M}_w^t = \int_\Omega \boldsymbol{N}^T \rho_w \boldsymbol{N} d\Omega \tag{4.20}$$

$$\boldsymbol{F}_w^{trac,t} = \int_{\partial\Omega_p} \boldsymbol{N}^T \boldsymbol{p} dS \tag{4.21}$$

$$\boldsymbol{F}_w^{grav,t} = \int_\Omega \boldsymbol{N}^T \rho_w \boldsymbol{g} d\Omega \tag{4.22}$$

$$\boldsymbol{F}_w^{int,t} = \int_\Omega \boldsymbol{B}^T \boldsymbol{\delta} p_w d\Omega \tag{4.23}$$

$$\boldsymbol{F}^{drag,t} = \int_\Omega \boldsymbol{N}^T \frac{n \rho_w g}{k} \boldsymbol{N} d\Omega (\boldsymbol{w} - \boldsymbol{v}) \tag{4.24}$$

in which $\boldsymbol{\delta} = \begin{bmatrix} 1 & 1 & 1 & 0 & 0 & 0 \end{bmatrix}$, and

$$\boldsymbol{M}_s^t = \int_\Omega \boldsymbol{N}^T (1-n)\rho_s \boldsymbol{N} d\Omega \tag{4.25}$$

$$\bar{\boldsymbol{M}}_w^t = \int_\Omega \boldsymbol{N}^T n\rho_w \boldsymbol{N} d\Omega \tag{4.26}$$

$$\boldsymbol{F}^{trac,t} = \int_{\partial\Omega_\tau} \boldsymbol{N}^T \boldsymbol{\tau} dS \tag{4.27}$$

$$\boldsymbol{F}^{grav,t} = \int_\Omega \boldsymbol{N}^T \rho_{sat} \boldsymbol{g} d\Omega \tag{4.28}$$

$$\boldsymbol{F}^{int,t} = \int_\Omega \boldsymbol{B}^T \boldsymbol{\sigma} d\Omega \tag{4.29}$$

Note that in Equations 4.18 and 4.19 the subscript w and s denote that the quantity is referred to the fluid and water phase respectively; no subscript indicates that the quantity belongs to the mixture.

The Euler-Cromer scheme is used to integrate the equations in time. From Equation 4.18 the fluid acceleration at time t is calculated and used to update the fluid velocity $\boldsymbol{w}^{t+\Delta t}$. The solid acceleration is calculated solving Equation 4.19 and used to update the solid velocity $\boldsymbol{v}^{t+\Delta t}$. Incremental strains are calculated at the MP from the updated velocities, after that the constitutive relations are used to calculate the stresses and pore water pressure.

In the implementation used for this thesis only one set of MP, representing the solid phase is considered. This means that the MP store all the informations regarding the soild and the liquid phase, and their positions are updated according to the solid displacement. The implementation of two layers of MP, one representing the solid phase and one representing the fluid phase is an issue of the on-going research and future development of MPM.

The initialization of MP explained in Section 3.4.1 is easily extended to the two-phase problem, then no more details are given in this Section.

The solution sequence of a single time step is described in the following:

1. The momentum equations for the fluid and the mixture are initialized by mapping the significative quantities from the MP to the mesh nodes. The procedure is similar to step 1 of the algorithm presented in Section 3.4.

2. Equation 4.18 is solved for $\boldsymbol{a}_w^t$

$$\boldsymbol{a}_w^t = \boldsymbol{M}_w^{t,-1} \left[\boldsymbol{F}_w^{trac,t} + \boldsymbol{F}_w^{grav,t} - \boldsymbol{F}_w^{int,t} - \boldsymbol{F}^{drag,t} \right] \tag{4.30}$$

3. The acceleration vector $\boldsymbol{a}_s^t$ is calculated from Equation 4.19 as:

$$\boldsymbol{a}_s^t = \boldsymbol{M}_s^{t,-1}\left[\boldsymbol{F}^{trac,t} + \boldsymbol{F}^{grav,t} - \boldsymbol{F}^{int,t} - \bar{\boldsymbol{M}}_w^t \boldsymbol{a}_w^t\right] \tag{4.31}$$

4. The velocities of the MP are updated using nodal accelerations and shape functions:

$$\boldsymbol{w}_p^{t+\Delta t} = \boldsymbol{w}_p^t + \sum_{i=1}^{n_{en}} \Delta t N_i(\boldsymbol{\xi}_p^t)\boldsymbol{a}_{w,i}^t \tag{4.32}$$

$$\boldsymbol{v}_p^{t+\Delta t} = \boldsymbol{v}_p^t + \sum_{i=1}^{n_{en}} \Delta t N_i(\boldsymbol{\xi}_p^t)\boldsymbol{a}_{s,i}^t \tag{4.33}$$

5. The nodal velocities $\boldsymbol{w}^{t+\Delta t}$ and $\boldsymbol{v}^{t+\Delta t}$ are then calculated from the updated MP momentum solving the following equation

$$\boldsymbol{M}_w^t \boldsymbol{w}^{t+\Delta t} \approx \sum_{p=1}^{n_{ep}} n_p^t m_{w,p} \boldsymbol{N}^T(\boldsymbol{\xi}_p^t)\boldsymbol{w}_p^{t+\Delta t} \tag{4.34}$$

$$\boldsymbol{M}_s^t \boldsymbol{v}^{t+\Delta t} \approx \sum_{p=1}^{n_{ep}} (1-n_p^t) m_{s,p} \boldsymbol{N}^T(\boldsymbol{\xi}_p^t)\boldsymbol{v}_p^{t+\Delta t} \tag{4.35}$$

6. Nodal velocities are integrated to get nodal incremental displacements

$$\Delta\boldsymbol{u}^{t+\Delta t} = \Delta t \boldsymbol{v}^{t+\Delta t} \tag{4.36}$$

7. Strains at MP are calculated as

$$\Delta\boldsymbol{\epsilon}_w^{t+\Delta t} = \boldsymbol{B}(\boldsymbol{\xi}_p^t)\boldsymbol{w}^{t+\Delta t}\Delta t \tag{4.37}$$

$$\Delta\boldsymbol{\epsilon}_s^{t+\Delta t} = \boldsymbol{B}(\boldsymbol{\xi}_p^t)\boldsymbol{v}^{t+\Delta t}\Delta t \tag{4.38}$$

and stresses are updated according to the constitutive relation

8. Water pressure at MP p is updated as:

$$p_{w,p}^{t+\Delta t} \approx p_{w,p}^t + \frac{K_{w,p}}{n_p^t}\boldsymbol{\delta}^T[(1-n_p^t)\Delta\boldsymbol{\epsilon}_{vol,s} + n_p^t\Delta\boldsymbol{\epsilon}_{vol,w}] \tag{4.39}$$

where $\boldsymbol{\delta} = \begin{bmatrix} 1 & 1 & 1 & 0 & 0 & 0 \end{bmatrix}$, $\Delta\boldsymbol{\epsilon}_{vol,s}$ and $\Delta\boldsymbol{\epsilon}_{vol,w}$ are the volumetric strain, i.e. $\Delta\epsilon_{vol} = \Delta\epsilon_{11} + \Delta\epsilon_{22} + \Delta\epsilon_{33}$, at the MP for the solid and liquid phase respectively.

9. The total stress is calculated as:

$$\boldsymbol{\sigma}_p^{t+\Delta t} = \boldsymbol{\sigma}_p'^{t+\Delta t} + \boldsymbol{\delta} p_{w,p}^{t+\Delta t} \tag{4.40}$$

10. Volumes associated with MP are updated using the volumetric strain increment

$$\Omega_p^{t+\Delta t} = (1 + \Delta \epsilon_{vol,p}^{t+\Delta t}) \tag{4.41}$$

11. The positions of MP are updated using the displacements of the solid phase

12. The book-keeping is updated using the new position of particles

The reader should observe that, similarly to the one-phase solution procedure, MP velocity are calculated from nodal accelerations and nodal velocities are computed from the nodal momentum. This is called modified Lagrangian algorithm and allows to overcome the small mass problem.

5

Constitutive modeling

The analysis of any problem requires noncontroversial statements of equilibrium and kinematics or compatibility (the definition of strain) as shown in the previous chapters; the link between these is provided by the relationship between stress change and strain change: the constitutive response.

Geotechnical journals and conferences abound with constitutive models. However, the scope of the current chapter is to provide only a brief introduction on the most popular constitutive equations used in geoengineering. Attention will be focused on those models used in this thesis. The convention commonly adopted in geomechanics, i.e. compression is positive, is adopted in this chapter.

The choice of the constitutive model to be used for analysis is in the hands of the modeler. As suggested by Wood (2003), the modeler should develop some awareness of the particular features of soil history and soil response that are likely to be important in a particular application and ensure that the adopted constitutive model is indeed able to reproduce these features. As in all modeling, adequate complexity should be sought.

5.1 Elastic models

A truly elastic model or hyper-elastic, is defined as a model that does not generate or dissipate energy in closed load loops. Despite soil exhibits inelastic behavior during loading, geotechnical engineer have made a good use of the theory of elasticity for several decades. Elastic descriptions of soil behavior are useful for the wide range of quick analytical solutions to which they give access. If we need some idea about the stress distribution around a footing, wall or pile then at least a first estimate

can be obtained using an elastic analysis.

The simplest model is the isotropic linear elastic, also called Hooke's law, in which the stress-strain relationship can be fully written using two constants. In matrix notation it can be written as:

$$\boldsymbol{d\sigma} = \boldsymbol{D}\boldsymbol{d\epsilon} \tag{5.1}$$

in which

$$\boldsymbol{D} = \frac{E}{(1-2\nu)(1+\nu)} \begin{bmatrix} 1-\nu & \nu & \nu & 0 & 0 & 0 \\ \nu & 1-\nu & \nu & 0 & 0 & 0 \\ \nu & \nu & 1-\nu & 0 & 0 & 0 \\ 0 & 0 & 0 & \frac{1}{2}-\nu & 0 & 0 \\ 0 & 0 & 0 & 0 & \frac{1}{2}-\nu & 0 \\ 0 & 0 & 0 & 0 & 0 & \frac{1}{2}-\nu \end{bmatrix} \tag{5.2}$$

where E is the Young modulus and ν is the Poisson ratio.

The Linear Elastic model is usually inappropriate to model the highly non-linear behaviour of soil, but it is of interest to simulate the behaviour of structures, such as thick concrete walls or piles, for which strength properties are usually very high compared with those of soil.

5.2 Elastoplastic models

Plasticity is associated with the development of irreversible strains. Elastoplastic models assume that, after a certain stress threshold, irreversible and time-independent deformations occur. If no stress increment is observed during plastic deformations, the material is called perfectly plastic. On the contrary hardening plasticity corresponds to an increase or decrease of the stress level with plastic deformations. The model consist of: an elastic stress-strain relation, a yield criterion, a plastic flow rule and and hardening law. This features are discussed further in this section.

The elastic law. The elastic stress-strain relation is the first ingredient of any elastoplastic model; it can be linear or non-linear, isotropic or anysotropic as convenient.

The yield criterion. In the classical plasticity theory there is a region of the stress space which can be reached elastically, without incurring any irrecoverable de-

formations. It is delimited by the yielding function F, which depends on the stress state $\boldsymbol{\sigma}$ and some hardening parameters. The conditions $F < 0$ represents the elastic domain. Plastic deformations occur in yielding conditions, i.e. $F = 0$. $F > 0$ is an unphysical condition (Fig. 5.1).

The flow rule. In yielding conditions the plastic strains are given by the flow rule as:

$$\boldsymbol{d\epsilon}^p = d\Lambda \frac{dG}{d\sigma} \tag{5.3}$$

where the scalar $d\mu$ is called plastic multiplier, and G is the plastic potential. If $F = G$, the flow rule is called associative, if not it is called non-associative. The plastic multiplier may be determined by introducing the conditions:

$$F \leq 0 \tag{5.4a}$$

$$d\Lambda \geq 0 \tag{5.4b}$$

$$F d\Lambda = 0 \tag{5.4c}$$

which help distinguishing between plastic and elastic loading and unloading. $F = 0$ and $d\Lambda > 0$ indicates plastic conditions, $F < 0$ with $d\Lambda = 0$ represents elastic conditions, $F = d\Lambda = 0$ is called neutral loading. These conditions have to be fulfilled at all times, which implies that during plastic flow, the increase of stresses should relate to the increase of the hardening parameters such that the stresses remain at the yield surface. In other words $F + dF = 0$, and with $F = 0$ this implies that $dF = 0$ during plastic flow. This is called the consistency condition.

The hardening law. The yield surface is generally not fixed in the stress space, rather it expands (hardening) or contract (softening). The change of the yield surface under plastic conditions is defined by the hardening law.

Using the incremental theory of elasto-plasticity, it is assumed that the strain increment is a composition of the elastic and the plastic strain increments. Furthermore, the stress increment is only related to the change in elastic strain, so

$$\boldsymbol{d\epsilon} = \boldsymbol{d\epsilon}^e + \boldsymbol{d\epsilon}^p \tag{5.5}$$

$$\boldsymbol{d\sigma} = \boldsymbol{D} d\boldsymbol{\epsilon}^e \tag{5.6}$$

where $\boldsymbol{d\epsilon}$, $\boldsymbol{d\epsilon}^e$, $\boldsymbol{d\epsilon}^p$ denote the total, elastic and plastic strain increments respectively, $\boldsymbol{d\sigma}$ the stress increment, and $\boldsymbol{D}$ the elastic stiffness matrix.

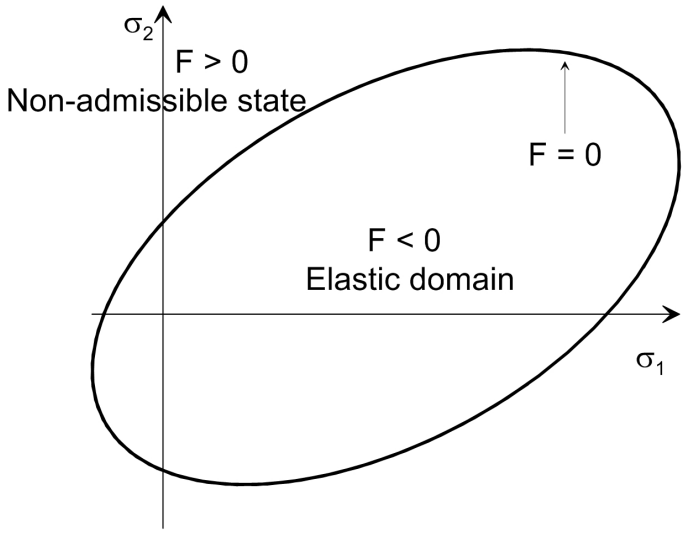

Figure 5.1: Yielding function

A large number of elastoplastic models has been proposed to describe the behavior of geomaterials; no attemps is made here to cover all these models; this section focuses only on a few of them that are used in this thesis. For further details the reader can refer to Yu (2007), Davis and Selvadurai (2002) and Wood (2003).

5.2.1 The Tresca failure criteria

For cohesive soils the most used elastoplastic models are those developed by Tresca and von Mises initially for metals. After a series of tests on metal, Tresca (1884) concluded that yielding occurs when the shear stress reaches a certain limit value (τ_{max}):

$$F_1 = 1/2|\sigma_2 - \sigma_3| - \tau_{max} \quad (5.7a)$$

$$F_2 = 1/2|\sigma_1 - \sigma_3| - \tau_{max} \quad (5.7b)$$

$$F_3 = 1/2|\sigma_1 - \sigma_2| - \tau_{max} \quad (5.7c)$$

For cohesive soil in undrained conditions $\tau_{max} = s_u$, where s_u is the undrained shear strength. Equations 5.7 represent an exhagonal prism in the stress space (Fig. 5.2).

Soil exhibits different s_u for triaxial extension, triaxial compression and simple shear. However, the model does not incorporate the dependency of soil strength on the stress path. For numerous geotechnical problems a unique loading type cannot be specified, therefore a proper average value of the shear strength must be used.

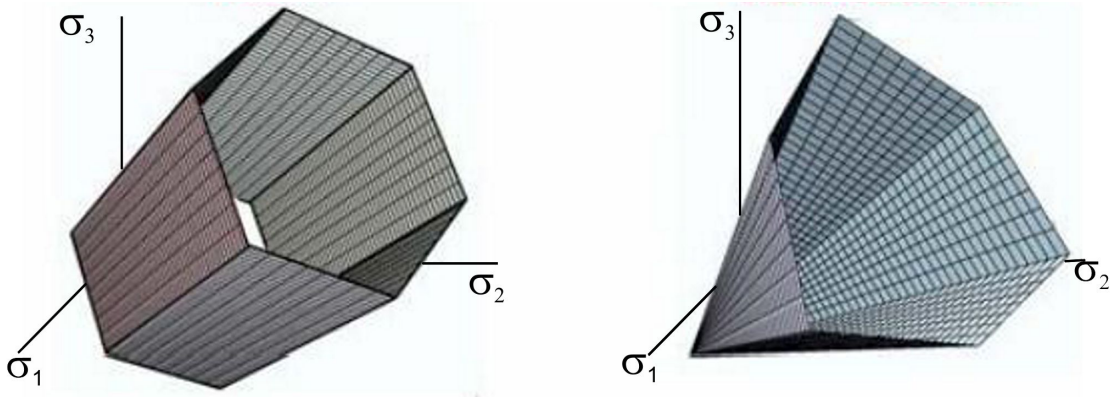

Figure 5.2: Tresca (left) and Mohr-Coulomb (right) failure surfaces (compression is positive).

An associative flow rule characterize the model, i.e. the plastic potential coincide with the yielding function. The model is elastic-perfectly plastic, i.e. the yielding function does not change during plastic deformations, therefore no hardening law needs to be specified. The isotropic linear elastic law is used within this constitutive model.

5.2.2 The Mohr-Coulomb failure criteria

Coulomb developed his failure criteria observing that the soil derives its strength from cohesion (c) and friction (ϕ):

$$\tau_{max} = c + \tan(\phi)\sigma \tag{5.8}$$

The Mohr-Coulomb yield condition is an extension of Coulomb's friction law to general states of stress. The full Mohr-Coulomb yield condition consists of six yield functions when formulated in terms of principal stresses:

$$F_1 = 1/2|\sigma_2 - \sigma_3| + 1/2(\sigma_2 + \sigma_3)\sin(\phi) - c\cos(\phi) \tag{5.9a}$$
$$F_2 = 1/2|\sigma_1 - \sigma_3| + 1/2(\sigma_1 + \sigma_3)\sin(\phi) - c\cos(\phi) \tag{5.9b}$$
$$F_3 = 1/2|\sigma_1 - \sigma_2| + 1/2(\sigma_1 + \sigma_2)\sin(\phi) - c\cos(\phi) \tag{5.9c}$$

The conditions $F_i = 0$ represent a hexagonal cone in principal stress space (Fig. 5.2). It should be noted that the Tresca failure criteria (5.7) can be regarded as a particular case of Equations 5.9 in which $\phi = 0$ and $c = s_u$. No hardening rule is included in the original model, therefore the yielding function is fixed in the stress space.

The plastic potential function contains the parameter ψ called dilatancy angle. The functions are defined as:

$$G_1 = 1/2|\sigma_2 - \sigma_3| + 1/2(\sigma_2 + \sigma_3)\sin(\psi) \quad (5.10a)$$

$$G_2 = 1/2|\sigma_1 - \sigma_3| + 1/2(\sigma_1 + \sigma_3)\sin(\psi) \quad (5.10b)$$

$$G_3 = 1/2|\sigma_1 - \sigma_2| + 1/2(\sigma_1 + \sigma_2)\sin(\psi) \quad (5.10c)$$

Apart from heavily overconsolidated layers, clay soils tend to show little dilatancy ($\psi \approx 0$). The dilatancy of sand depends on both the density and the friction angle. For further information about the link between friction angle and dilatancy, see Bolton (1986).

The elastic-perfectly plastic Mohr-Coulomb model is widely used for geotechnical analysis. It provides a very crude match to actual shearing behavior of soils. This model should be adopted in combination with effective stress analysis; an effective friction angle ϕ' and cohesion c' should be used. The choice of the strength parameters must be done with care; taking into account the characteristics of loading and deformations of the problem is essential. Indeed, soil strength often exhibits a pick, associated with a volumetric extension, followed by a strength reduction which leads to the critical state, at which no volumetric strain is observed, and finally a residual state is reached (Fig. 5.3).

Several extensions of the model have been proposed in the literature to incorporate specific soil behavior such as non-linear dilatancy, strain softening, density dependent strength ect.; this often requires a modification of the yielding function and the introduction of an hardening law. A very brief but effective overview can be found in Wood (2003).

5.2.3 The Modified Cam Clay model

Historically it is probably reasonable to consider the Cam Clay as the first hardening plastic model that has become generally adopted for soils. It has formed a basis for much subsequent development of soil models. Originally developed in the early 1960s, the models of the Cam Clay form have been widely and successfully used for analysis of problems involving the loading of soft clays.

The Cam Clay models are based on the critical state concept, which states that the soil and other granular materials, if continuously distorted until they flow as a

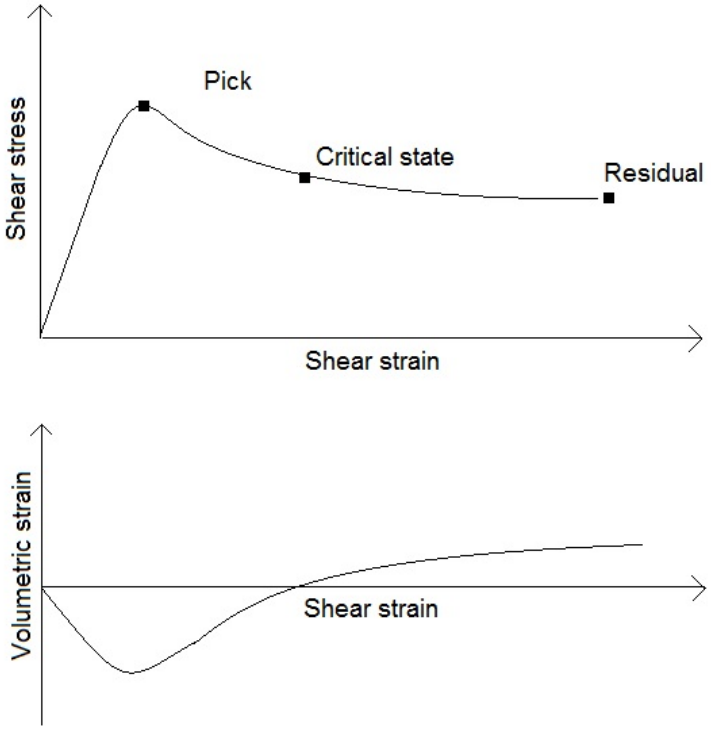

Figure 5.3: Simplified rappresentation of shear test results (compression is positive).

frictional fluid, will come into a well defined critical state. In other words, at the critical state, soil behaves as a frictional fluid and yields at constant strains and stresses, i.e. the plastic volumetric strain increment is zero (Schofield and Wroth 1968).

The Modified Cam Clay Model (MCC) model consists of two state variables: the specific volume, υ, and the preconsolidation stress, p_c. The specific volume can be determined from the void ratio: $\upsilon = 1+e$. These two variables govern the hardening or softening of the soil, and whether the soil tends to dilate or contract.

The stresses are represented by the volumetric mean effective stress p' and the deviatoric stress q, which are defined as follows:

$$p = \frac{\sigma'_1 + \sigma'_2 + \sigma'_3}{3} \tag{5.11}$$

$$q = \frac{1}{\sqrt{2}}\sqrt{(\sigma'_1 - \sigma'_3)^2 + (\sigma'_1 - \sigma'_2)^2 + (\sigma'_2 - \sigma'_3)^2} \tag{5.12}$$

The volumetric strain and the deviatoric strain are defined as:

$$\epsilon_p = \epsilon_1 + \epsilon_2 + \epsilon_3 \tag{5.13}$$

$$\epsilon_q = \frac{\sqrt{2}}{3}\sqrt{(\epsilon_1 - \epsilon_3)^2 + (\epsilon_1 - \epsilon_2)^2 + (\epsilon_2 - \epsilon_3)^2} \tag{5.14}$$

The model assumes that when a soft soil sample is slowly compressed under isotropic stress and perfectly drained conditions, the relationship between specific volume and mean effective stress is logaritmic. The first time the soil is loaded with a load greater than the previous experienced loading, p_c, the behaviour follows the isotropic or virgin compression line (NCL). If the soil afterwards is unloaded, it will follow an unloading-reloading line (URL). All deformations along the URL are reversible, i.e. elastic deformations.

The equations of the compression lines can be written as

$$\upsilon = N - \lambda \ln(p') \tag{5.15}$$

$$\upsilon = \upsilon_s - \kappa \ln(p') \tag{5.16}$$

where υ_s and N represents the specific volume at unit stress, and λ and κ the slopes of the NCL and the URL respectively. The NCL is uniquely defined for a certain soil, while multiple URL exist depending on the state parameters. An increase in p_c corresponds to a shift from one URL to another.

Sustained shearing of a soil sample eventually leads to a state in which further shearing can occur without any changes in stress or volume. This state is characterized by the Critical State Line (CSL) which is unique for a given soil, regardless of the stress path used to bring the sample from any initial condition to the critical state. The CSL is determined by two equations:

$$\upsilon = \Gamma - \lambda \ln(p') \tag{5.17a}$$

$$q = Mp' \tag{5.17b}$$

where Γ is a basic soil parameter representing the specific volume at unit stress, and M determines the soil strength. The latter can be related to the soil's critical friction angle ϕ'; for triaxial compression it is estimated as:

$$M = \frac{6\sin(\phi')}{3 - \sin(\phi')} \tag{5.18}$$

A detailed description of the main features of the model is provided in the following:

Elastic properties. A change in p' and q is related to the elastic strain components by:

$$\begin{bmatrix} d\epsilon_p^e \\ d\epsilon_p^e \end{bmatrix} = \begin{bmatrix} 1/K' & 0 \\ 0 & 1/3G \end{bmatrix} \begin{bmatrix} dp' \\ dq \end{bmatrix} \tag{5.19}$$

where K' and G are the effective bulk molulus and the shear modulus of the soil, which can be defined as:

$$K' = \frac{\upsilon p'}{\kappa} \tag{5.20a}$$

$$G = \frac{3K(1-2\nu)}{(2+2\nu)} = \frac{3\upsilon p'(1-2\nu)}{\kappa(2+2\nu)} \tag{5.20b}$$

It is worth noting that the moduli are nonlinear as they are function of both the stress state and the specific volume.

The yield surface. The original Cam clay model proposed a logarithmic yield surface, but this poses some difficulties in constitutive soil modelling as the function is not differentiable at all points. The yield surface of the MCC, however, is an ellipse in the p-q-space, with a center in $(p_c/2, 0)$, shown in Figure 5.4 for $q > 0$. The equation for the elliptic yield surface is

$$F = q^2 - M^2 p'(p_c - p') = 0 \tag{5.21}$$

The hardening function. The hardening function defines how the yield surface expands (hardening) or contracts (softening). For MCC we experience softening behaviour for largely over-consolidated soils, and hardening otherwise. Cam clay is a volumetric hardening model in which it is assumed that the size of the yield locus depends only on the plastic volumetric strain. The change in the hardening parameter p_c is derived from the relation between the plastic volumetric strain $d\epsilon_p^p$ and the plastic change in specific volume $d\upsilon_p$, written as

$$d\epsilon_p^p = -\frac{d\upsilon_p}{\upsilon} = \frac{\lambda - \kappa}{\upsilon} \frac{dp_c}{p_c} \tag{5.22}$$

Note the negative sign of $d\upsilon_p$ which stems from the sign convention normally used in geotechnical engineering, with compression being positive.

Integrating over a finite interval and solving for Δp_c, the hardening function

is written as

$$\Delta p_c = p_c \exp[\zeta \Delta \epsilon_p^p] \tag{5.23}$$

where $\zeta = \upsilon/(\lambda - \kappa)$.

The flow rule. In MCC, the flow rule is associative, i.e $G = F$. For the stress and strain invariants, the flow rule is written as

$$\begin{bmatrix} d\epsilon_p^e \\ d\epsilon_q^e \end{bmatrix} = d\Lambda \begin{bmatrix} \frac{dF}{dp'} \\ \frac{dF}{dq} \end{bmatrix} = d\Lambda \begin{bmatrix} M^2(2p' - p_c) \\ 2q \end{bmatrix} \tag{5.24}$$

where $d\Lambda$ is the plastic multiplier which can be found by applying the consistency condition $dF = 0$, giving

$$d\Lambda = \frac{\begin{bmatrix} \frac{dF}{dp'} & \frac{dF}{dq} \end{bmatrix} \boldsymbol{D} \begin{bmatrix} d\epsilon_p \\ d\epsilon_q \end{bmatrix}}{\begin{bmatrix} \frac{dF}{dp'} & \frac{dF}{dq} \end{bmatrix} \boldsymbol{D} \begin{bmatrix} \frac{dF}{dp'} & \frac{dF}{dq} \end{bmatrix} - A} \tag{5.25}$$

where A is the plastic resistance modulus defined as

$$A = \frac{\partial F}{\partial p_c} \frac{\partial p_c}{\partial \epsilon_p^p} \frac{\partial \epsilon_p^p}{d\Lambda} = M^2 p' \zeta p_c M^2 (2p' - p_c) \tag{5.26}$$

In summary the Cam clay model has five material properties. There are two elastic properties κ and G (or ν), two plastic properties M and λ and a reference for volume, in order to calculate the volumetric strains, which can be the initial void ratio e_0. Figure 5.4 shows the CLS, NCL and URL in the $e - \ln(p')$ plane and the yelding surface and CSL in the $p - q$ plane. On the right plot, a typical stress path during undrained triaxial compression of a normal consolidated clay is shown.

The MCC model incorporates many fundamental characteristic of soil behavior such as non linear compressibility, hardening behavior, occurrence of shear and volumetric deformations during yielding and fluid-like plastic flow at large deformations. The real behavior of natural soils is more complicated because factors such as anisotropy and strain-rate effects play an important role. Indeed, during deposition, clay is generally compacted vertically under its self-weight, which leads to the arrangement of clay particles in layers rather than a random configuration. Any subsequent loading, which induces plastic straining, will cause changes of the internal structure of the clay and, therefore, the initial anisotropy is modified (stress-induced anisotropy). Moreover, straining can progressively destroy boning between particles (destructuration) (Burland 1990). In case of cyclic loading things becomes even more

complicated because aspects such as densification and pressure generation must be correctly captured.

In the 80s many extensions of the Cam Clay model have been proposed; a brief review of the most important modifications can be found in Gens and Potts (1988). Examples of these modifications includes research on the following topics:

- yield surface for heavily overconsolidated clays (e.g. Zienkiewicz and Naylor 1973, Atkinson and Bransby 1978)
- anisotropic yield surfaces for one-dimensionally consolidated soils (e.g. Ohta and Wroth 1976, Whittle 1993)
- inclusion of plastic deformation within the main yield surface for soils subjected to cyclic loading (e.g. Dafalias and Herrmann 1980, Carter et al. 1982)
- 3D critical state formulation (e.g. Roscoe and Burland 1968, Zienkiewicz and Pande 1977)
- modelling of rate-dependent behaviour of clays (e.g. Borjia and Kavazanjian 1985, Kutter and Sathialingam 1992)

In addition to this several more advanced constitutive models, which eventually deviates from the critical state theory have been proposed (e.g. Pastor et al. 1990, Modaressi and Laloui 1997, Masin 2005); however the discussion of this subject exceeds the purpose of the current chapter.

The MCC model has been used in the literature mainly to model soft clay and silt. It seems not appropriate for stiff clay and sands. Determining its input parameters is relatively easy, while difficulties often arise with more sophisticated models which may require considerable non-standard testing.

The numerical implementation of the MCC model, recently introduced in the MPM code in the frame of this thesis, uses an explicit integration scheme known as Dorman-Prince method. This method is considered one of the most accurate; moreover a substepping algorithm and a correction method has been included by Aas Nost (2011) in the implementation adopted in this study.

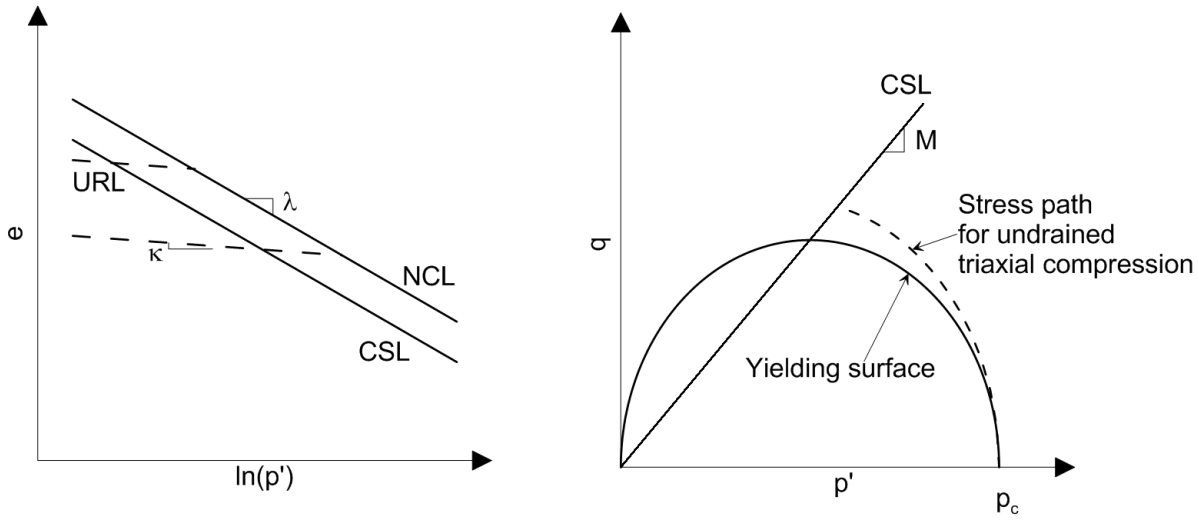

Figure 5.4: NCL, CSL and URL in the $e - \ln(p')$ plane (left) and CSL, yield surface and an example of stress path for triaxial compression (right).

6

Other numerical aspects

The current chapter collects some special techniques adopted in the used MPM implementation to deal with particular problems:

Enhanced volumetric strain Since low-order finite elements are used within the MPM, problems of volumetric locking rise when incompressible materials are considered. Section 6.1 presents a possible solution to this shortcoming.

Dissipation of dynamic waves Numerical simulations with dynamic code may need the introduction of special procedures to dissipate dynamic waves unphysically generated, for example, by reflection at boundaries. Absorbing boundary and local damping can be introduced to achieve this scope as shown in section 6.2.

Mass scaling Since in explicit code the time step size can be very small and simulating long-time processes may be computationally expensive, a procedure called mass scaling, can be used to improve computational efficiency in quasi-static problems; it is presented in section 6.3.

Contact between bodies Contact problems are very common in engineering. The problem is discussed in section 6.4.1, where the implemented contact algorithm is presented and validated.

The moving mesh procedure Because of MP moving through the mesh, the application of non-zero traction or kinematics can rise some difficulties. A possible solution is presented in section 6.5.

Attention will be paid to both one and two-phase formulations.

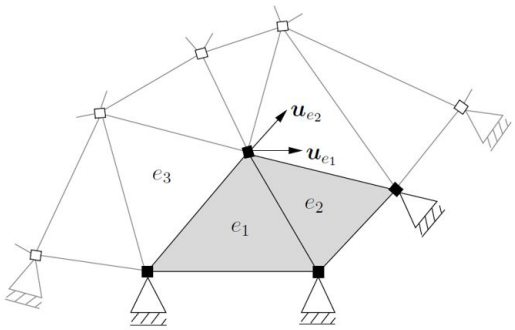

Figure 6.1: Illustration of locking with 3-noded triangular elements (Al-Kafaji 2013).

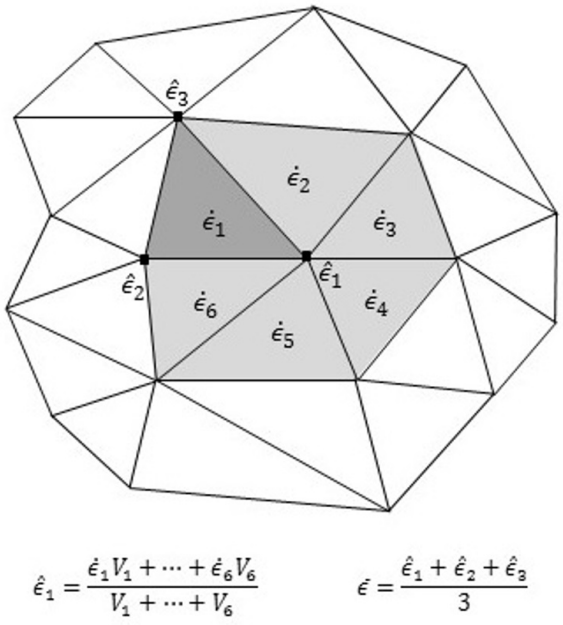

Figure 6.2: Nodal Mixed Discretization technique.

6.1 Mitigation of volumetric locking

The MPM suffers from the same numerical problems that are encountered when using low-order elements in FEM for incompressible materials. For such a material, the bulk modulus is very large and small errors in strain will yield large errors in stress. Furthermore, when dealing with low-order elements, the mesh may lock when constraints from neighboring elements are imposed.

For a simple demonstration of the locking phenomenon, a two-dimensional domain discretized with 3-noded triangular elements is shown in Figure 6.1. Elements e_1 and e_2 share the same free node. Since the material is incompressible, the area of the element cannot change, therefore only displacements parallel to the triangle base

are allowed, i.e. u_{e1} and u_{e2} respectively. Since the two directions are not parallel, this node locks. As the material is incompressible, constrains of this node also leads to the locking of the free node attached to element e_3. Hence, such locking usually propagates throughout the entire mesh yielding unrealistic stiff response.

Volumetric locking can be reduced by means of a Nodal Mixed Discretization technique as proposed by Detournay and Dzik (2006). This technique has been successfully introduced by Stolle et al. (2010) to the 3D dynamic MPM code with explicit time integration using the same 4-noded tetrahedral elements.

With the Nodal Mixed Discretization technique the number of degrees of freedom per element is increased by incorporating information of surrounding elements. The deviatoric strain components $\dot{\epsilon}_d$ remain unchanged while the volumetric strain component is modified through an averaging procedure. The algorithm forms an intermediate step between the element-wise determination of strain rates from the kinematic relation and the computation of stresses.

Let $\hat{\epsilon}_i$ denote nodal volumetric strain rates obtained by weighted averaging of the volumetric strain rates $\dot{\epsilon}_l$ of all elements connected to a node i:

$$\hat{\epsilon}_i = \frac{\sum \dot{\epsilon}_l \Omega_l}{\sum \Omega_l} \tag{6.1}$$

where Ω_l denotes the volume of element l.

Averaged volumetric strain rates $\bar{\epsilon}$ are then computed for each element by averaging the nodal volumetric strain rates $\hat{\epsilon}_i$ of all nodes connected to an element

$$\bar{\epsilon} = \frac{\sum \hat{\epsilon}_i}{n_n} \tag{6.2}$$

where n_n denotes the number of nodes per element (4 in case of the low-order tetrahedral elements). From the averaged element volumetric strain rates the updated strain rates $\tilde{\dot{\epsilon}}_{ij}$ are computed by means of

$$\tilde{\dot{\epsilon}}_{ij} = \dot{\epsilon}_d + \frac{1}{3}\delta_{ij}\bar{\epsilon} \tag{6.3}$$

where δ_{ij} is the Kronecker delta.

On the basis of the modified strain rates, stresses are computed using the constitutive relation. No average procedure is applied on the stress rates.

In two-phase analyses the procedure is applied to the volumetric strain of water and

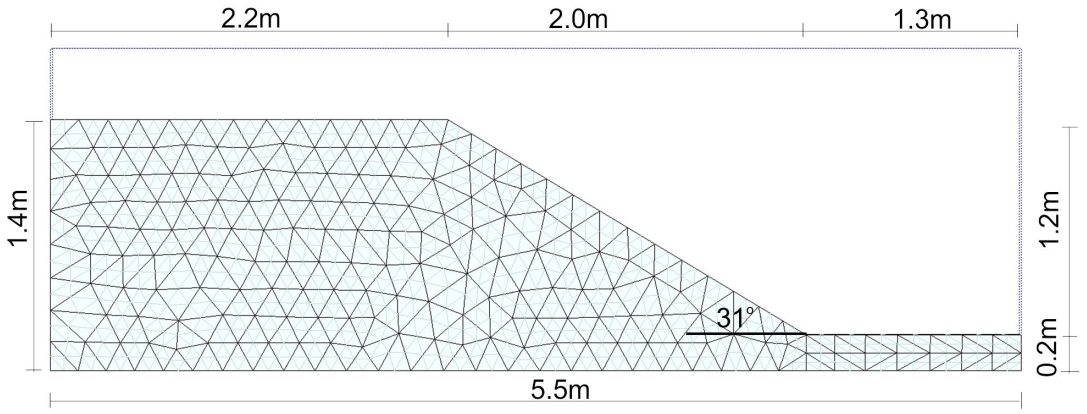

Figure 6.3: Geometry and disctretization.

Parameter	Symbol	Value
Dry unit weight of the sand $[kN/m^3]$	γ_{sat}	20
Water bulk modulus [kPa]	K_w	45310
Effective Young modulus [kPa]	E'	5000
Effective Poisson ratio [-]	ν'	0.2
Cohesion [kPa]	c'	0
Friction angle [deg]	ϕ'	32
Dilatancy angle [deg]	ψ'	0
Porosity [-]	n	0.45

Table 6.1: Material parameters for the slope stability benchmark problem.

solid phase separately. Hence, the pore pressure rates is calculated as:

$$\dot{p}_w = \frac{K_w}{n}[(1-n)\bar{\epsilon}_{vol,s} + n\bar{\epsilon}_{vol,w}] \tag{6.4}$$

where $\bar{\epsilon}_{vol,s}$ and $\bar{\epsilon}_{vol,w}$ are the enhanced volumetric strains for the solid and water phase respectively. All the results showed in this thesis make use of this technique.

As example of locking effect, let consider the slope in Figure 6.3. The slope is submerged; neglecting pore pressure dissipation, the problem can be simulated with the one-phase effective stress analysis, i.e. undrained conditions are hypotized. The elastoplastic constitutive model with Mohr-Coulomb failure criteria is used for the soil and input parameter are summarized in Table 6.1.

Stresses are initialized via gravity loading, i.e. the gravity is applied and the static equilibrium is reached in several time steps. After that the friction angle is decreased to 28°. Being the slope angle 31° the soil body is no longer in static equilibrium and the failure is triggered.

Figure 6.4 shows the displacements at the MP when the slope reaches its final configuration. The effect of applying the enhanced volumetric strain and refining the mesh is considered. If no correction for the volumetric strain is applied, only small displacements are predicted because of locking effects, the slope does not fail (Fig. 6.4a). This problem can be solved by introducing the enhanced volumetric strain as presented in the current section (Fig. 6.4b). However the procedure works better with a fine mesh; indeed comparing Figures 6.4b and 6.4c it can be observed that displacements are smaller if a coarse mesh is used, meaning that some locking is still present.

This simple example demonstrates that the described procedure is able to overcome locking effects when dealing with incompressible materials and a fine mesh should be used to improve results.

6.2 Dissipation of dynamic waves

In numerical simulations of dynamic problems sometimes wave propagation can produce unsatisfactory results and even numerical problems. The use of finite boundaries leads to reflection of waves upon reaching the boundaries of the mesh. In geomechanics, rigid boundary is mostly numerical artifact and reflecting waves are not physical. They affect the solution considerably; therefore, the attenuation of waves reflection is necessary in problems where there are artificial boundaries. This problem might be overcome by choosing the finite boundaries of the mesh far enough so that no reflection occurs. This is however not always a practical solution as it makes the mesh unnecessarily large leading to a substantial increase in the computational effort. The use of absorbing boundaries, as discussed in section 6.2.1, can overcome these problems.

On the top of this, any complex real system naturally dissipate a certain amount of energy for internal friction of the material or slippage at the internal surfaces. In numerical simulations this features must be considered. A possibility consist in the use of the local damping. It is commonly applied in quasi-static problems, but can sometimes be used in slow-process problems. Local damping is discussed in section 6.2.2.

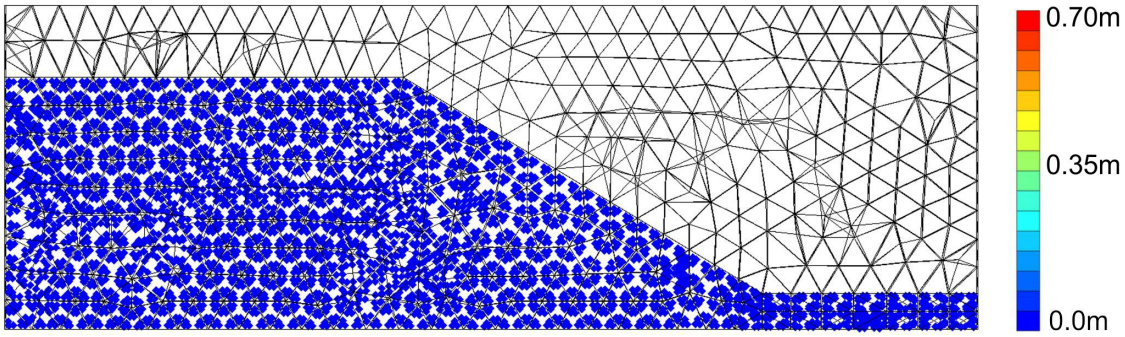

(a) No enhanced volumetric strain.

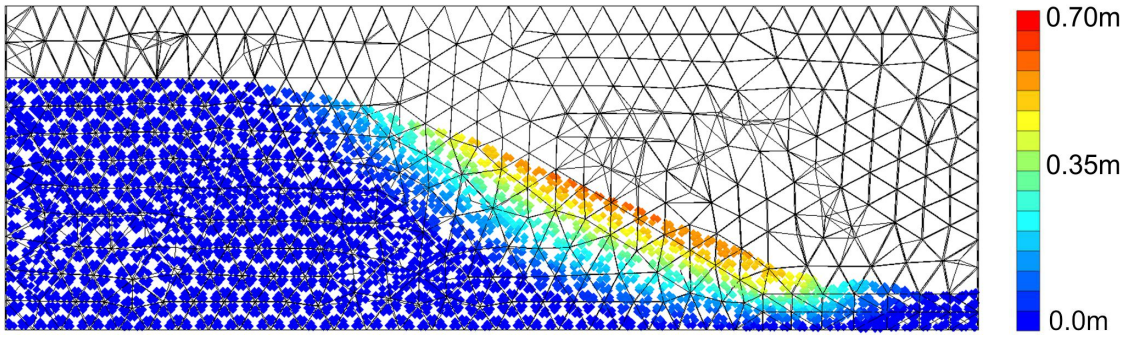

(b) Enhanced volumetric strain.

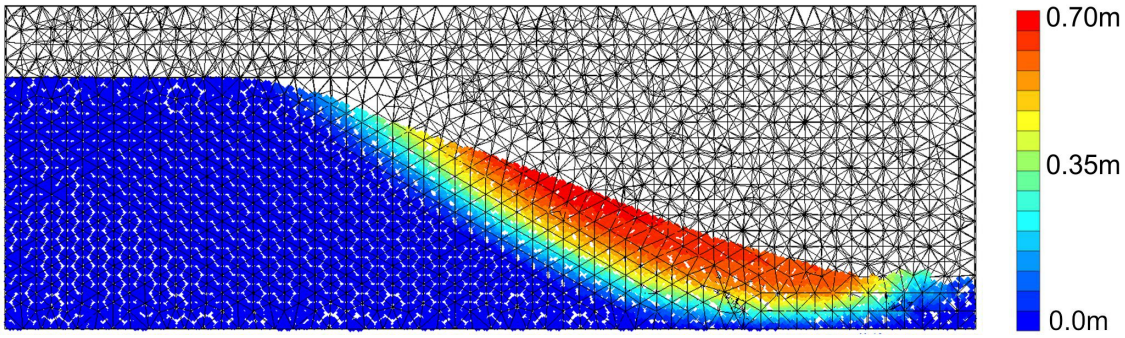

(c) Enhanced volumetric strain with mesh refinement.

Figure 6.4: Effect of enhanced volumetric strain

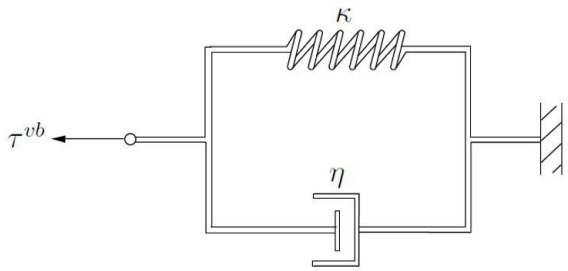

Figure 6.5: The Kelvin-Voigt element

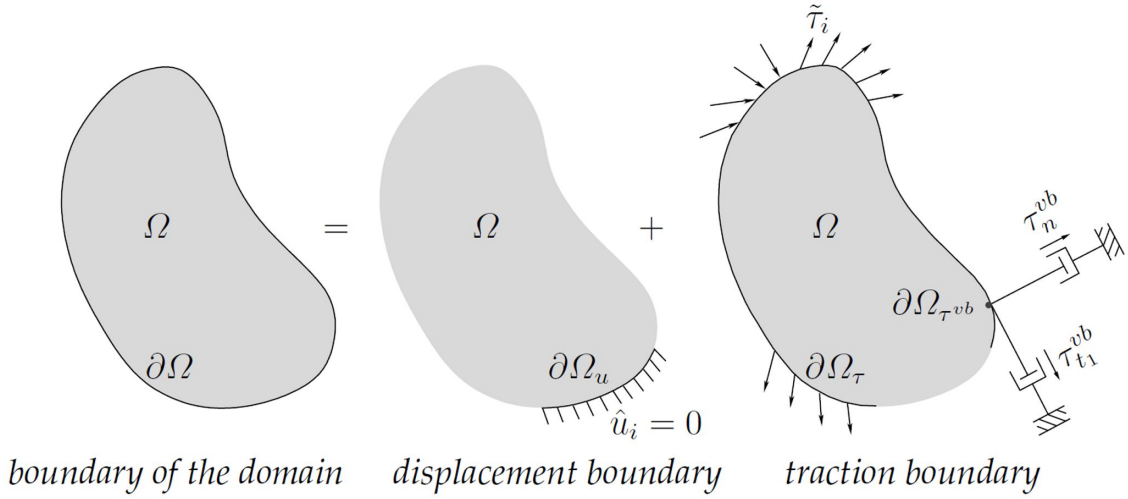

Figure 6.6: The boundary conditions including absorbing boundaries (Al-Kafaji 2013).

6.2.1 Absorbing boundaries

The use of finite boundaries produces wave reflections that does not characterize the naturally unbounded domain, therefore unphysical results may be obtained. A solution of this problem is the use of the absorbing boundaries.

The absorbing boundary used in this thesis can be visualized with the so-called Kelvin-Voigt element. It consist in a viscous part (dashpot) and an elastic part (spring), working in parallel (Fig. 6.5). The method of the boundary dashpots was originally presented by Lysmer and Kuhlemeyer (1969), and implemented with some modification in the MPM by Al-Kafaji (2013).

When the absorbing boundary is introduced, the boundary conditions becomes:

$$\partial\Omega_u \cup \partial\Omega_\tau \cup \partial\Omega_{\tau^{ab}} \tag{6.5}$$

and

$$\partial\Omega_i \cap \partial\Omega_j = \emptyset \quad i,j = u,\tau,\tau^{ab} \tag{6.6}$$

being $\partial\Omega_{\tau^{ab}}$ the boundary where the Kelvin-Voigt element is applied (Fig. 6.6).

The traction vector corresponding to the absorbing boundary has, in general, three components, i.e.

$$\boldsymbol{\tau}^{ab} = \begin{bmatrix} \tau_n^{ab} & \tau_{t_1}^{ab} & \tau_{t_2}^{ab} \end{bmatrix}$$

in which the first is the component normal to the boundary and the other two are the tangential components.

The response of the Kelvin-Voigt element is described by the following equations:

$$\tau_n^{ab} = -a\rho c_p v_n - k_p u_n \tag{6.7a}$$
$$\tau_{t_1}^{ab} = -b\rho c_s v_{t_1} - k_s u_{t_1} \tag{6.7b}$$
$$\tau_{t_2}^{ab} = -b\rho c_s v_{t_2} - k_s u_{t_2} \tag{6.7c}$$

where a and b are dimensionless parameters, v_n, v_{t_1} and v_{t_2} are the velocities, u_n, u_{t_1} and u_{t_2} are the displacements, ρ is the mass density, c_p and c_s are the speeds of the compression and shear waves respectively, k_p and k_s represent the stiffness per unit area associated to the elastic component.

The wave speeds are functions of the constrained and shear elastic moduli and the mass density as follows:

$$c_p = \sqrt{\frac{E_c}{\rho}} \tag{6.8}$$

$$c_s = \sqrt{\frac{G}{\rho}} \tag{6.9}$$

Equations 6.7a-6.7c can be expressed in a compact form as:

$$\tau_i^{ab} = -\eta_{ij} v_j - k_i u_i \tag{6.10}$$

The first addend in the right-hand-side of Equation 6.10 represents the traction given by the dashpot, which is proportional to the velocity. The second addend represents the traction given by the spring, which is proportional to the displacement.

The virtual work equation (3.12) is rewritten introducing the traction corresponding

to the absorbing boundary:

$$\int_\Omega t_i \rho \frac{dv_i}{dt} d\Omega = \int_{\partial\Omega_\tau} t_i \tau_i dS + \int_{\partial\Omega_\tau^{ab}} t_i \tau_i^{ab} dS + \int_\Omega t_i \rho g_i d\Omega - \int_\Omega \frac{\partial t_i}{\partial x_i} \sigma_{ij} d\Omega \qquad (6.11)$$

introducing Equation 6.10 it yelds to:

$$\int_\Omega t_i \rho \frac{dv_i}{dt} d\Omega = \int_{\partial\Omega_\tau} t_i \tau_i dS - \int_{\partial\Omega_\tau^{ab}} t_i \eta_{ij} v_j dS - \int_{\partial\Omega_\tau^{ab}} t_i k_i u_i dS + \int_\Omega t_i \rho g_i d\Omega - \int_\Omega \frac{\partial t_i}{\partial x_i} \sigma_{ij} d\Omega \qquad (6.12)$$

The matrix form of the discretized equation of motion, including the force at the absorbing boundary, is:

$$\boldsymbol{M a} = \boldsymbol{F}^{trac} - \boldsymbol{F}^{ab} + \boldsymbol{F}^{grav} - \boldsymbol{F}^{int} \qquad (6.13)$$

in which

$$\boldsymbol{F}^{ab} = \boldsymbol{C v} + \boldsymbol{K u} \qquad (6.14)$$

where $\boldsymbol{C}$ is the matrix containing the dashpot coefficients η_{ij} and is therefore called dashpot matrix, and $\boldsymbol{K}$ is the matrix containing the spring coefficients k_i and is called spring matrix.

In this thesis the dashpot coefficients a and b are assumed equal to one. Lysmer and Kuhlemeyer (1969) showed that this choice gives the maximum absorption for both compression and shear wave for a wide range of the incidence angles.

The coefficients k_p and k_s can be expressed as function of the elastic moduli and a so-called virtual thikness δ:

$$k_p = \frac{E_c}{\delta} \qquad (6.15)$$

$$k_s = \frac{G}{\delta} \qquad (6.16)$$

The virtual thickness δ can be interpreted as the thickness of a virtual layer which extends outside the boundary. Note that for $\delta \to 0$ the absorbing boundary reduces to a rigid bounday; for $\delta \to \infty$ it reduces to a dashpot boundary. Spatially unbounded domain can therefore be represented with a finite mesh by the use of the absorbing boundary defined in this section.

For the two-phase formulation, two-sets of Kelvin-Voigt elements need to be defined.

For the solid part, the traction at the absorbing boundary represents the traction applied on the soil skeleton and is therefore proportional to the solid velocity $\boldsymbol{v}_s$ and displacement $\boldsymbol{u}_s$. Moreover the dry density ρ_{dry} and the effective constrained modulus E'_c should be used to estimate dashpot and spring coefficients in Equation 6.10.

The response of the Kelvin-Voigt element for the water phase has only the normal component and is given by:

$$p_w^{ab} = -a\rho_w c_w w_n - k_w u_{w,n} \tag{6.17}$$

where w_n and $u_{w,n}$ are the normal component of water velocity and displacement respectively. The speed of the compression wave in the water is

$$c_w = \sqrt{\frac{K_w}{\rho_w}} \tag{6.18}$$

Taking into account the absorbing boundary term, the momentum equation of the fluid becomes:

$$\boldsymbol{M}_w \boldsymbol{a}_w = \boldsymbol{F}_w^{trac} - \boldsymbol{F}_w^{ab} + \boldsymbol{F}_w^{grav} - \boldsymbol{F}_w^{int} - \boldsymbol{F}^{drag} \tag{6.19}$$

where

$$\boldsymbol{F}_w^{ab} = \boldsymbol{C}_w \boldsymbol{w} + \boldsymbol{K}_w \boldsymbol{u}_w \tag{6.20}$$

the momentum equation for the mixture, considering the boundary force, is:

$$\boldsymbol{M}_s \boldsymbol{a}_s = \boldsymbol{F}^{trac} - \boldsymbol{F}^{ab} + \boldsymbol{F}^{grav} - \boldsymbol{F}^{int} - \bar{\boldsymbol{M}}_w \boldsymbol{a}_w \tag{6.21}$$

Where the absorbing boundary force applied on the mixture is:

$$\boldsymbol{F}^{ab} = \boldsymbol{F}_w^{ab} + \boldsymbol{F}_s^{ab} = \boldsymbol{C}_w \boldsymbol{w} + \boldsymbol{K}_w \boldsymbol{u}_w + \boldsymbol{C}_s \boldsymbol{v} + \boldsymbol{K}_s \boldsymbol{u}_s \tag{6.22}$$

$\boldsymbol{C}_w$ and $\boldsymbol{K}_w$ are the dashpot matrix and the spring matrix for the water phase respectively.

Since MP move through the mesh, the scheme must be implemented in an incremental form so that displacement and velocity increments of a material point are only accounted for when it enters the considered element. Hence,

$$\boldsymbol{F}^{ab,t} = \boldsymbol{F}^{ab,t-\Delta t} + \Delta \boldsymbol{F}^{vb,t} \tag{6.23}$$

where

$$\Delta \boldsymbol{F}^{vb,t} = \boldsymbol{C}^t \Delta \boldsymbol{v} + \boldsymbol{K}^t \Delta \boldsymbol{u} \tag{6.24}$$

This, of course, is valid for both one-phase and two-phase formulation.

Examples of the application of the viscous boundary can be found in sections 7.1 and 7.2. Appendix B provides some additional basic information on the oscillatory system and damped vibrations.

6.2.2 Local damping

Natural dynamic systems contain some degree of damping of the vibration energy within the system; otherwise, the system would oscillate indefinitely when subjected to driving forces. Damping is due, in part, to energy loss as a result of internal friction in the intact material and slippage along interfaces, if these are present.

For a dynamic analysis, the damping in the numerical simulation should reproduce in magnitude and form the energy losses in the natural system when subjected to a dynamic loading. In soil and rock, natural damping is mainly hysteretic, i.e. independent of frequency, see Gemant and Jackson (1937) and Wegel and Walther (1935). This type of damping is difficult to reproduce numerically. However, if a constitutive model is found that contains an adequate representation of the hysteresis that occurs in a real material, then no additional damping would be necessary (Cundall 2001).

Rayleigh damping is commonly used to provide damping that is approximately frequency-independent over a restricted range of frequencies. However, this kind of damping introduces body forces that retard the steady state collapse and might influence the mode of failure (Hart et al. 1988). Cundall (1987) describes a local non-viscous damping to overcome the difficulty associated with the viscous damping.

An alternative to Rayleigh damping is the so-called local damping. The local damping force is proportional to the out of balance force $f = f^{ext} - f^{int}$ and acts opposite to the direction of the velocity. For any degree-of-freedom in the considered system, the local damping can be described as follows

$$ma = f + f^{damp} \tag{6.25}$$

where

$$f^{damp} = -\alpha |f| \frac{v}{|v|} \tag{6.26}$$

is the damping force at the considered degree of freedom. The dimensionless parameter α is called local damping factor.

In the two-phase formulation the fluid and the solid phase are damped separately. At any degree of freedom the momentum equation for the water assumes the form:

$$m_w a_w = f_w^{trac} + f_w^{grav} - f_w^{int} - f_w^{drag} + f_w^{damp} \tag{6.27}$$

if $f_w = f_w^{trac} + f_w^{grav} - f_w^{int}$ is the unbalanced force for the water, the damping force for the water can be written as:

$$f_w^{damp} = -\alpha_w |f_w| \frac{w}{|w|} \tag{6.28}$$

The momentum equation for the mixture is:

$$m_s a_s = -\bar{m}_w a_w + f^{trac} + f^{grav} - f^{int} + f^{damp} \tag{6.29}$$

where

$$f^{damp} = f_s^{damp} + f_w^{damp} \tag{6.30}$$

The out of balance force for the solid phase is $f = f^{trac} + f^{grav} - f^{int}$, hence the damping force for the solid can be written as:

$$f_s^{damp} = -\alpha_s |f - f_w| \frac{v}{|v|} \tag{6.31}$$

In this thesis the local damping factor for the fluid (α_w) and the solid (α_s) phase always assume the same value.

Local damping was originally designed for static simulations. However, it has some characteristics that make it attractive for dynamic simulations if proper values of the damping coefficient are used. In quasi-static problems high value of α, i.e. 0.7-0.8, can be used to accelerate convergence. In slow-process problems a small value of α, i.e. 0.05-0.15, can simulate natural energy dissipation of the material, if it is not taken into account by the constitutive model. Local damping should not be used or used only with high care in highly dynamic problem, where wave propagation is of great importance.

An example of application of local damping for two-phase problem can be found in section 7.2.

6.3 Mass scaling

The simulation of quasi-static or slow-process problems with a dynamic explicit code can require high computational effort because the time step size is bounded by the condition 3.34. However, if the inertia effect is negligible, then the time step size can be artificially increased by scaling the density. Introducing the mass scaling factor β, the critical time step size increases by a factor $\sqrt{\beta}$. Indeed:

$$\Delta t^{\beta}_{crit} = \frac{l_e}{\sqrt{\frac{E_c}{\beta\rho}}} = \sqrt{\beta}\Delta t^{1}_{crit} \tag{6.32}$$

where Δt^{1}_{crit} is the critical time step for $\beta = 1$, i.e. no mass scaling is applied.

Note that in problems involving consolidation, the process is governed by the consolidation coefficient c_v, which is a function of the permeability k, the unit weight of the water γ_w and the soil compressiblity m_v. The use of mass scaling should not affect the consolidation coefficient c_v otherwise the consolidation time changes too. In other terms the unit weight γ_w must be constant and an eventual reduction of the gravity is necessary

$$c_v = \frac{k}{\gamma_w m_v} = \frac{k}{(\beta\rho_w)(g/\beta)m_v} \tag{6.33}$$

Mass scaling is a very useful technique to improve computational efficiency of dynamic codes in simulating quasi-static ans slow-process motion. However, sensitivity analysis are necessary to calibrate the mass scaling factor in slow process problems, indeed extremely high values of β can significantly affect the result. In this thesis the mass scaling procedure is used to improve computational efficiency when MPM is applied to the simulation of cone penetration as shown in section 9.4.1.1 where the effect of the mass scaling factor is also discussed.

6.4 The contact between bodies

Problems of soil-structure interaction are common in geotechnical engineering. MPM is naturally capable of handling non-slip contact between different bodies, indeed interpenetration cannot occur because the bodies' velocities belong to the same vector field. However, when continuum bodies come into contact, in most cases frictional sliding occurs at the contact surface. To simulate such a sliding interaction a specific

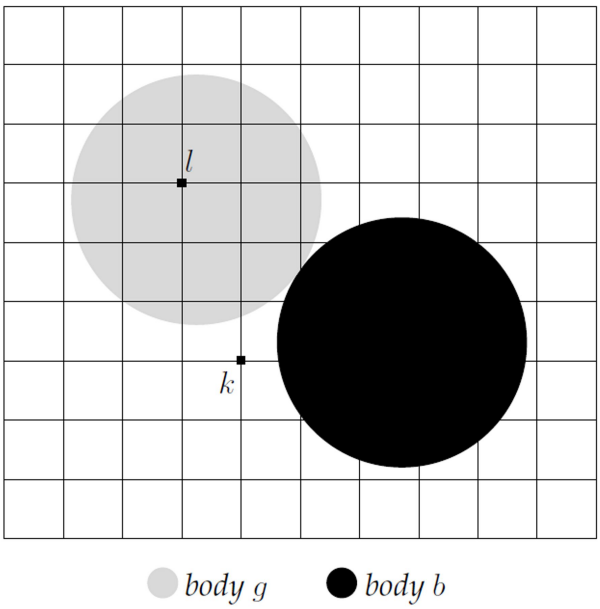

Figure 6.7: Example of two bodies in contact (Al-Kafaji 2013).

contact algorithm that allows relative motion at the interface between contacting bodies is required.

In this section the contact algorithm proposed by Bardenhagen et al. (2001) is presented as well as its extension to the adhesive contact. The advantage of this algorithm is that it detects the contact surface automatically and does not require any special interface element. It proved to be efficient in modeling interaction between solid bodies as well as shearing in granular materials.

The extension to adhesive contact follows Al-Kafaji (2013) and has been implemented in the used MPM code in the frame of this thesis. The adhesive type of contact is well suited to simulate soil-structure interaction in case of cohesive soil under undrained conditions. Indeed, in this case the tangential force cannot exceed the undrained shear strength.

6.4.1 Formulation

The contact algorithm used in this thesis can be considered as a predictor-corrector scheme, in which the velocity is predicted from the solution of each body separately and then corrected using the velocity of the coupled bodies following the contact law.

Consider body g (gray in Fig. 6.7) and body b (black in Fig. 6.7), which are in contact at time t. The procedure starts with the initialization of the equation of

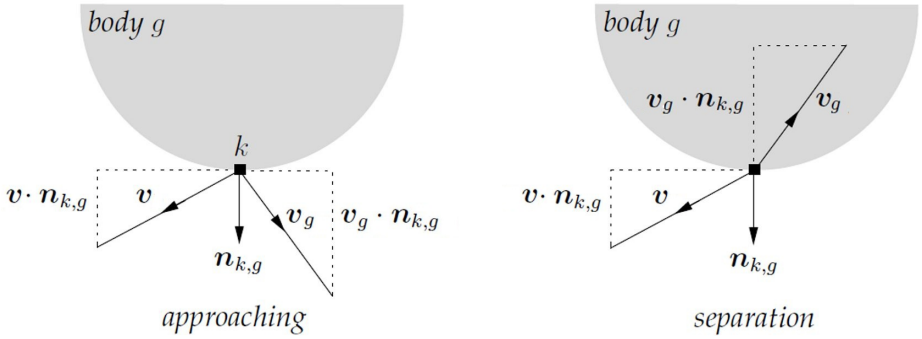

Figure 6.8: Cases of approaching bodies (left) and separating bodies (right) (Al-Kafaji 2013).

motion (Eq. 3.47) for each body separately, as well as for the combined system.

The nodal accelerations for each body and the combined system are calculated solving the momentum equations and then used to predict the nodal velocities at time $t + \Delta t$ as follows:

$$\boldsymbol{v}_g^{t+\Delta t} = \boldsymbol{v}_g^t + \Delta t \boldsymbol{a}_g^t \tag{6.34}$$

$$\boldsymbol{v}_b^{t+\Delta t} = \boldsymbol{v}_b^t + \Delta t \boldsymbol{a}_b^t \tag{6.35}$$

$$\boldsymbol{v}^{t+\Delta t} = \boldsymbol{v}^t + \Delta t \boldsymbol{a}^t \tag{6.36}$$

Contact nodes are detected by comparing the velocity of a single body ($\boldsymbol{v}_g^{t+\Delta t}, \boldsymbol{v}_b^{t+\Delta t}$) to that of the combined bodies ($\boldsymbol{v}^{t+\Delta t}$). If the velocities differ than the node is identified as a contact node. For example, considering nodes l and k of body g, it is clear that at node l the velocity of body g is equal to the one of the combined system, therefore it is not a contact node and no correction is required. On the contrary, at node k, which is shared between two bodies, the combined velocity differs from the single body velocity; consequently this node is defined as a contact node and correction is required.

When a node is detected as a contact node, the algorithm proceeds with checking if the bodies are approaching or separating. This is done by comparing the normal component of the single body velocity with the normal component of the combined bodies velocity. Hence, the following two cases are possible:

$$(\boldsymbol{v}_g^{t+\Delta t} - \boldsymbol{v}^{t+\Delta t}) \cdot \boldsymbol{n}_k^t > 0 \quad \Rightarrow \quad \text{approaching}$$
$$(\boldsymbol{v}_g^{t+\Delta t} - \boldsymbol{v}^{t+\Delta t}) \cdot \boldsymbol{n}_k^t < 0 \quad \Rightarrow \quad \text{separating}$$

where $\boldsymbol{n}_k^t$ is the unit outward normal to body g at node k. The algorithm allows

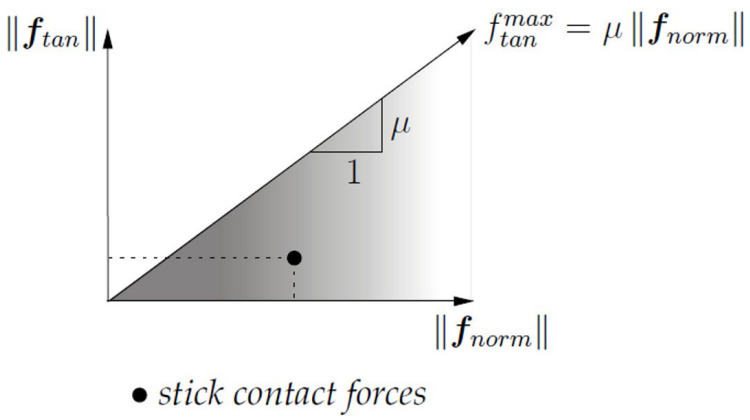

Figure 6.9: Contact forces for the stick case (Al-Kafaji 2013).

for free separation, i.e. no correction is required in this case and each body moves with the single body velocity $\boldsymbol{v}_{g(b)}^{t+\Delta t}$. If the bodies are approaching, than we need to check whether sliding occurs.

The predicted relative normal and tangential velocities at an approaching contact node can be respectively written as:

$$\boldsymbol{v}_{norm}^{t+\Delta t} = \left[\left(\boldsymbol{v}_{g}^{t+\Delta t} - \boldsymbol{v}^{t+\Delta t}\right) \cdot \boldsymbol{n}_{k}^{t}\right] \boldsymbol{n}_{k}^{t} \tag{6.37}$$

$$\boldsymbol{v}_{tan}^{t+\Delta t} = \boldsymbol{n}_{k}^{t} \times \left[\left(\boldsymbol{v}_{g}^{t+\Delta t} - \boldsymbol{v}^{t+\Delta t}\right) \times \boldsymbol{n}_{k}^{t}\right] \tag{6.38}$$

These components can be used to predict the contact forces at the node as:

$$\boldsymbol{f}_{norm}^{t+\Delta t} = \frac{m_{k,g}^{t}}{\Delta t} \boldsymbol{v}_{norm}^{t+\Delta t} \tag{6.39}$$

$$\boldsymbol{f}_{tan}^{t+\Delta t} = \frac{m_{k,g}^{t}}{\Delta t} \boldsymbol{v}_{tan}^{t+\Delta t} \tag{6.40}$$

where $m_{k,g}^{t}$ is the nodal mass integrated from MP of body g.

The maximum tangential force is:

$$f_{tan}^{max,t+\Delta t} = f_{adh}^{t+\Delta t} + \mu |\boldsymbol{f}_{tan}^{t+\Delta t}| \tag{6.41}$$

where $f_{adh}^{t+\Delta t}$ is the adhesive force at the contact and μ is the friction coefficient.

Depending on the magnitude of the predicted contact forces we can distinguish

between stick and slip contact:

$$\begin{aligned} \text{If} \quad |\boldsymbol{f}_{tan}^{t+\Delta t}| < f_{tan}^{max,t+\Delta t} \quad &\Rightarrow \quad \text{stick contact} \\ \text{If} \quad |\boldsymbol{f}_{tan}^{t+\Delta t}| > f_{tan}^{max,t+\Delta t} \quad &\Rightarrow \quad \text{slip contact} \end{aligned}$$

In the first case, i.e. the bodies stick to each others, no correction is required and the velocity corresponds to $\boldsymbol{v}^{t+\Delta t}$. In the second case, i.e. the bodies are sliding one respect to the other, the velocity needs to be corrected in such a way that no interpenetration is allowed and the magnitude of the tangential force respect Equation 6.41.

The predicted single body velocity $\boldsymbol{v}_g^{t+\Delta t}$ is corrected to a new velocity $\tilde{\boldsymbol{v}}_{k,g}^{t+\Delta t}$ such that the normal component coincide with the normal component of the combined bodies velocity, i.e.,

$$\tilde{\boldsymbol{v}}_g^{t+\Delta t} \cdot \boldsymbol{n}_k^t = \boldsymbol{v}^{t+\Delta t} \cdot \boldsymbol{n}_k^t \tag{6.42}$$

which can also be written as

$$\tilde{\boldsymbol{v}}_g^{t+\Delta t} = \boldsymbol{v}_g^{t+\Delta t} + \boldsymbol{c}_{norm}^{t+\Delta t} \tag{6.43}$$

where

$$\boldsymbol{c}_{norm}^{t+\Delta t} = -\big[\big(\boldsymbol{v}_g^{t+\Delta t} - \boldsymbol{v}^{t+\Delta t}\big) \cdot \boldsymbol{n}_k^t\big]\boldsymbol{n}_k^t \tag{6.44}$$

is the correction of the normal component of the predicted velocity.

This correction is equivalent to apply the following normal contact force:

$$\tilde{\boldsymbol{f}}_{norm}^{t+\Delta t} = \frac{m_{k,g}^t}{\Delta t}\boldsymbol{c}_{norm}^{t+\Delta t} \tag{6.45}$$

When sliding occurs, the maximum tangential contact force assumes the expression:

$$\tilde{\boldsymbol{f}}_{tan}^{t+\Delta t} = f_{tan}^{max,t+\Delta t}\boldsymbol{t} \tag{6.46}$$

with $\boldsymbol{t}$ being a unit vector indicating the direction of the tangent.

Substituting Equation 6.41 into Equation 6.46 we get:

$$\tilde{\boldsymbol{f}}_{tan}^{t+\Delta t} = \big(f_{adh}^{t+\Delta t} + \mu|\boldsymbol{f}_{norm}^{t+\Delta t}|\big)\boldsymbol{t} \tag{6.47}$$

The total contact force is:

$$\tilde{\boldsymbol{f}}_{cont}^{t+\Delta t} = \tilde{\boldsymbol{f}}_{tan}^{t+\Delta t} + \tilde{\boldsymbol{f}}_{norm}^{t+\Delta t} \tag{6.48}$$

which is used to correct the velocity as:

$$\tilde{\boldsymbol{v}}_g^{t+\Delta t} = \boldsymbol{v}_g^{t+\Delta t} + \frac{\tilde{\boldsymbol{f}}_{cont}^{t+\Delta t}}{m_{k,g}^t}\Delta t \tag{6.49}$$

It can also be written as:

$$\tilde{\boldsymbol{v}}_g^{t+\Delta t} = \boldsymbol{v}_g^{t+\Delta t} + \boldsymbol{c}_{norm}^{t+\Delta t} + \boldsymbol{c}_{tan}^{t+\Delta t} \tag{6.50}$$

where the correction for the tangential component assumes the form:

$$\boldsymbol{c}_{tan}^{t+\Delta t} = \frac{\Delta t}{m_{k,g}^t}\big(f_{adh}^{t+\Delta t} + \mu|\boldsymbol{f}_{norm}^{t+\Delta t}|\big)\boldsymbol{t} \tag{6.51}$$

The force introduced by the adhesion a can be expressed as;

$$f_{adh}^{t+\Delta t} = aA_k^t \tag{6.52}$$

where A_k^t is the contact area associated with the node k. It is integrated from the contact elements that share node k.

Substituting equations 6.52 and 6.45 in 6.51, the corrected velocity can be written as:

$$\begin{aligned}\tilde{\boldsymbol{v}}_g^{t+\Delta t} = \boldsymbol{v}_g^{t+\Delta t} &- \big[\big(\boldsymbol{v}_g^{t+\Delta t} - \boldsymbol{v}^{t+\Delta t}\big)\cdot\boldsymbol{n}_k^t\big]\boldsymbol{n}_k^t \\ &- \left\{\big[\big(\boldsymbol{v}_g^{t+\Delta t} - \boldsymbol{v}^{t+\Delta t}\big)\cdot\boldsymbol{n}_k^t\big]\mu + \frac{aA_k^t\Delta t}{m_{k,g}^t}\right\}\boldsymbol{t}\end{aligned} \tag{6.53}$$

Figure 6.10 illustrates with a flow chart the main steps of the implemented contact algorithm.

Having calculated the velocity of the contact node k at time $t + \Delta t$, the corrected acceleration vector at the node must be recalculated as:

$$\tilde{\boldsymbol{a}}_g^t = \frac{\tilde{\boldsymbol{v}}_g^{t+\Delta t} - \boldsymbol{v}_g^t}{\Delta t} \tag{6.54}$$

This corrected acceleration is used to update the MP velocity according to the algo-

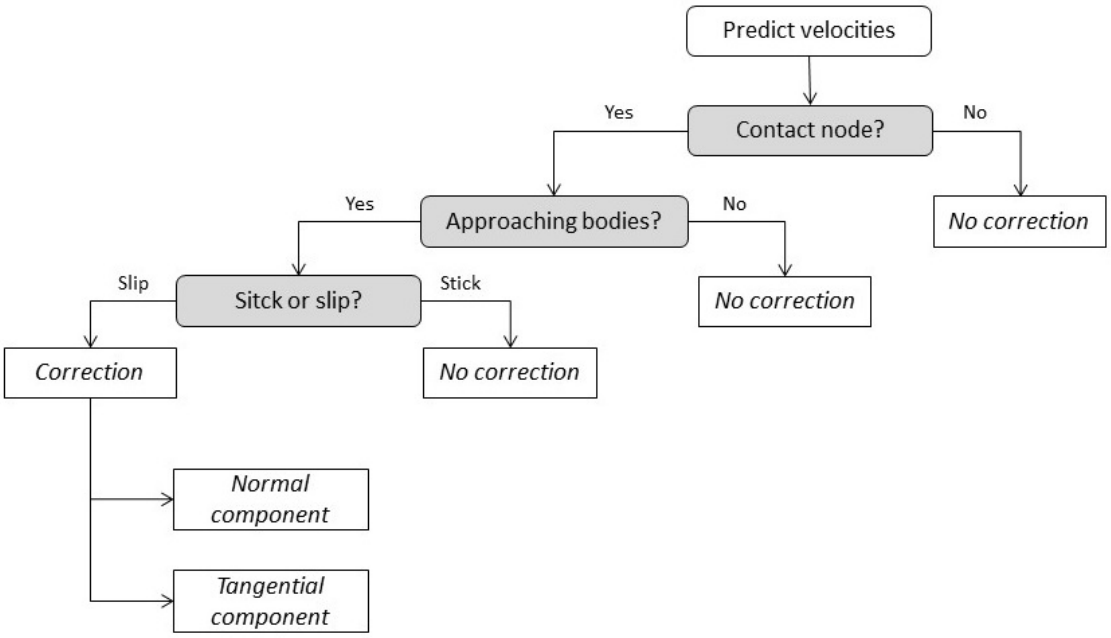

Figure 6.10: Flow chart illustrating the contact algorithm.

rithm presented in section 3.4.2. It should be remarked that the contact algorithm is applied between the Lagrangian phase and the convective phase. Indeed the nodal velocities are first predicted in the Lagrangian phase, then the corrected nodal velocities and accelerations are computed by the contact algorithm and these new values of nodal accelerations are used to compute the velocities at the MP in the convective phase. The same procedure explained here for body g must be applied to body b.

6.4.2 Validation

The implemented contact algorithm is validated with a benchmark problem consisting in two blocks sliding on the top of each other. The mesh counts of 5265 elements, 3225 of which are initially filled with 4 particles each (Fig. 6.11). The dimensions of the blocks and their material parameters are summarized in Table 6.2.

The upper block, also called block 1, is pushed by an horizontal force $\boldsymbol{T}$ linearly increasing with time. The contact is characterized by a friction coefficient $\mu = 0.25$ and an adhesion $a = 5kPa$. The maximum contact force can be calculated as:

$$\boldsymbol{F}_{tan,max} = \mu \boldsymbol{F}_{g,1} + aA = 0.25 \cdot 40 + 5 \cdot 2 = 20kN \tag{6.55}$$

where $\boldsymbol{F}_{g,1}$ is the weight of the upper block and A is the contact area.

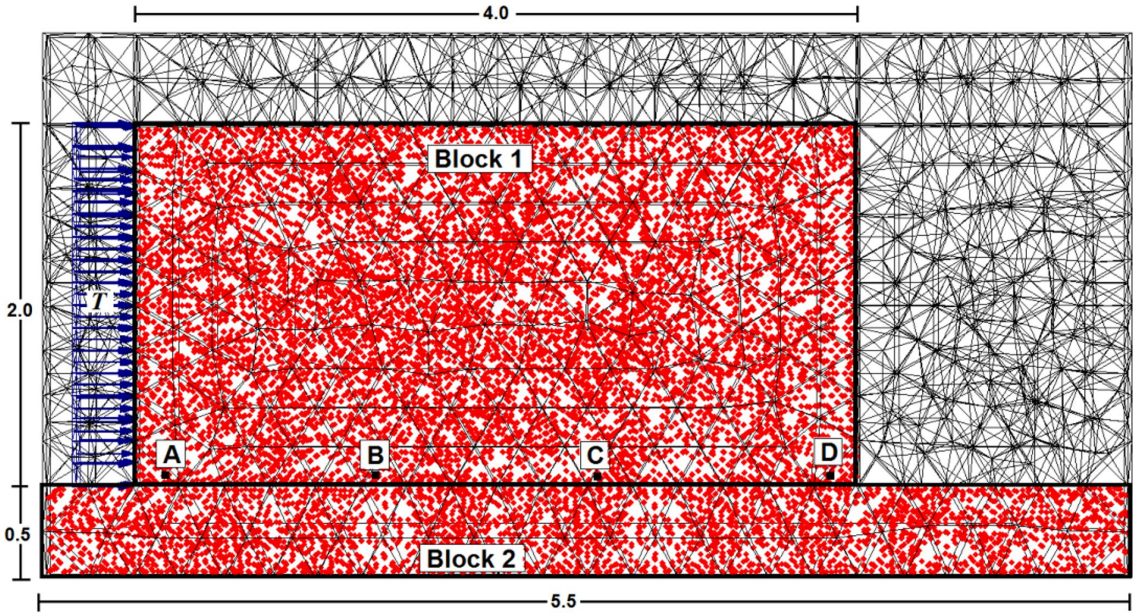

Figure 6.11: Geometry and discretization.

		Upper block	Lower block
Young modulus [kPa]	E	15000	75000
Poisson ratio [-]	ν	0	0
Density $[kg/m^3]$	ρ	1000	5000
High [m]	h	2	0.5
Lenght [m]	l	4	5.5
Width [m]	d	0.5	0.5

Table 6.2: Geometry and material parameters for the sliding-block benchmark

The two blocks stick to each other while $\boldsymbol{T} < \boldsymbol{F}^{cont}_{tan,max}$; as soon as $\boldsymbol{T} > \boldsymbol{F}^{cont}_{tan,max}$ the upper block starts sliding. In order to avoid dynamic effects the rate of loading should be reasonably small, for example $1kN/s$, and the courant number is set to 0.5, i.e. the time step size is 50% of the critical.

Figure 6.12 plots the contact force components as function of the applied external force. The tangential contact force $\boldsymbol{F}^{cont}_{tan}$ increases linearly in time up to its maximum value and then remains constant. The normal contact force $\boldsymbol{F}^{cont}_{norm}$ is equal to the weight of block 1. Oscillations are present and increase when the block starts sliding. They can be reduced by refining the mesh, decreasing the rate of load, or the time step size.

The kinetic energy of the system and the displacements of four MP are plotted in Figure 6.13. As expected the kinetic energy is close to zero while $\boldsymbol{T} < \boldsymbol{F}_{tan,max}$; beyond this value it increases suddenly, meaning that the block is sliding. The

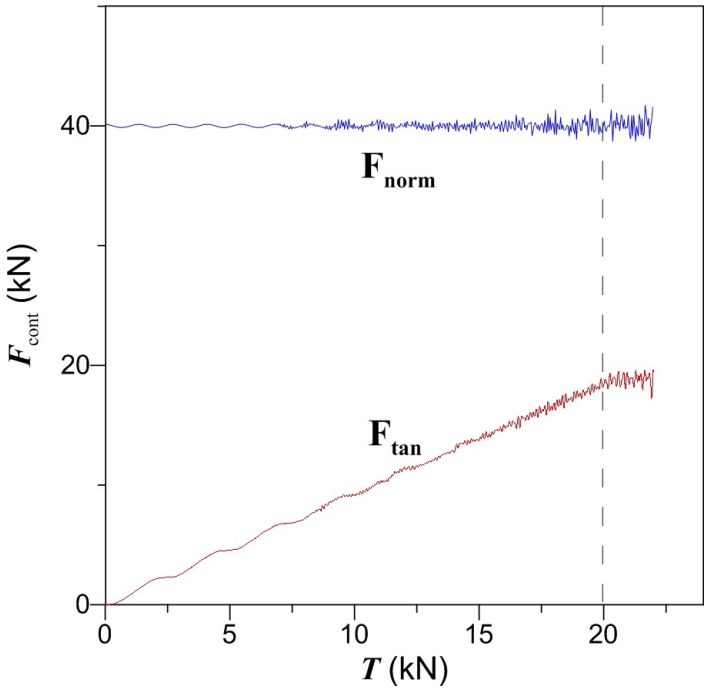

Figure 6.12: Contact forces on block 1.

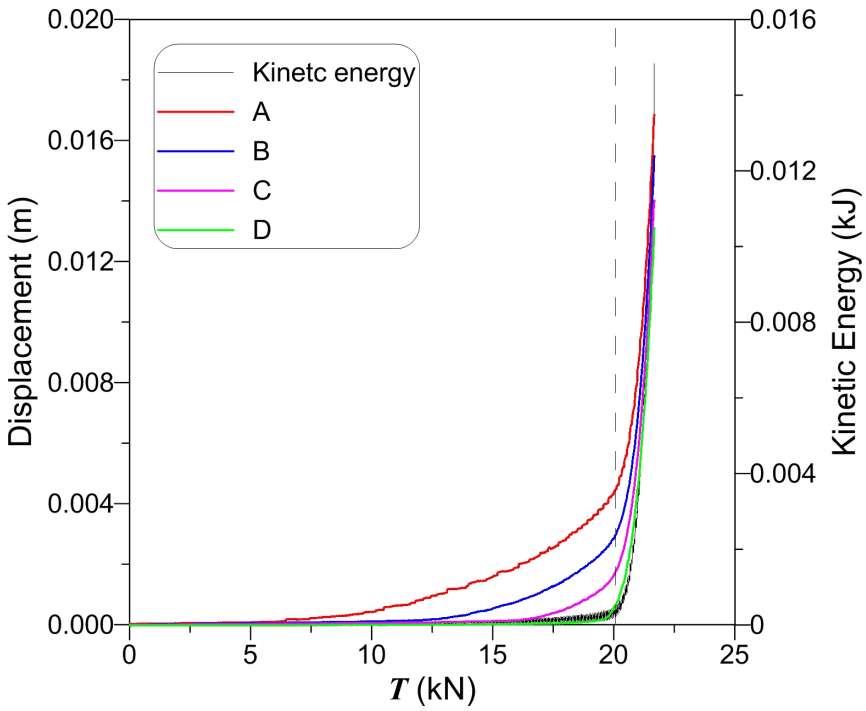

Figure 6.13: Kinetic energy of the system and displacement of representative MP.

displacements at the MP are not zero for $\boldsymbol{T} < 20kPa$ because of the deformability of the block. However it is evident that they increase rapidly as soon as the applied force exceeds the maximum contact force. MP labeled A, which is on the back of block 1, shows higher displacements than MP labeled D, which is at the front of the same block. This means that there is a progressive failure: the movement starts from the back and propagates to the front. When the maximum value of the contact force is reached along the entire surface the whole block slides.

The results shown for this benchmark problem with adhesive and frictional contact are in agreement with theoretical expectations which proves the validity of the implemented contact algorithm.

6.5 The moving mesh procedure

With MP moving through the mesh, the application of non-zero traction and kinematic boundary conditions is not straightforward. The problem can be solved by using the moving mesh procedure, in which it is always ensured that the computational mesh aligns with the surface where tractions (kinematics) are prescribed (Beuth 2012).

To illustrate this procedure, let us consider a rigid block being displaced by the action of surface tractions, see Figure 6.14. A moving mesh zone is attached to the the rigid block and moves with the same displacement. Thereby, the traction is kept at the same boundary nodes and never mapped between particles and nodes. A consequence of using this procedure is that the mesh in front of the block (right) gets compressed and that behind the block (left) gets stretched with time by the same displacement of the rigid block.

For extremely large deformations the mesh can get distorted; however, since with the MPM the mesh could be arbitrarily modified after each time step, the domain can be remeshed. The moving mesh zone could be made fine and the moving mesh procedure ensures that it will always remain around the block. On the contrary, with standard MPM, the block would move through a fixed mesh, requiring mesh refinement over the entire region where it is expected to move through.

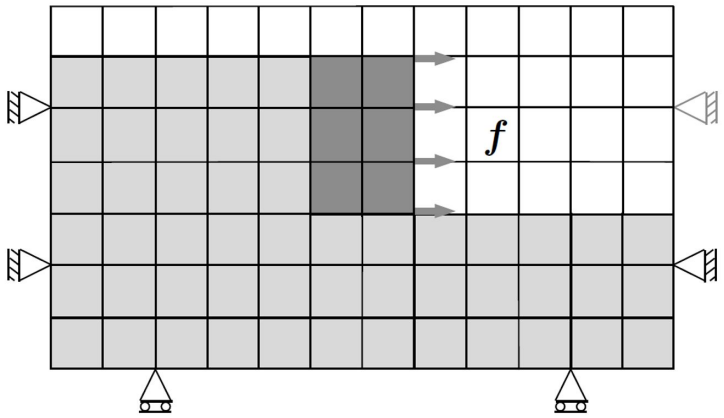

(a)

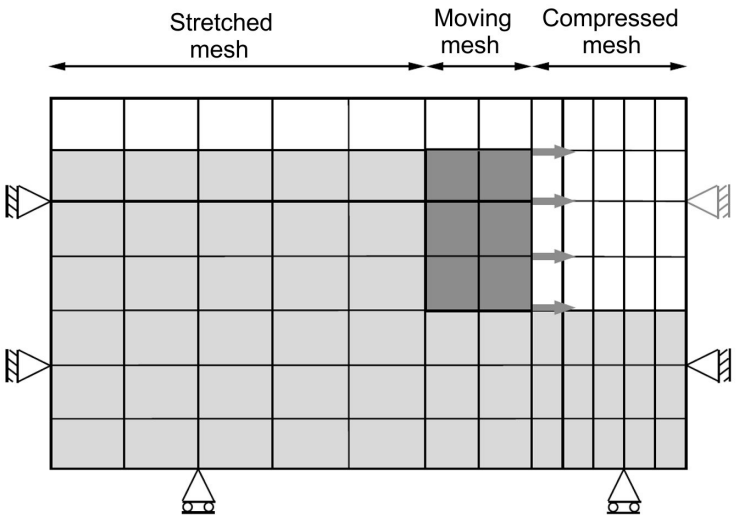

(b)

Figure 6.14: Illustration of the moving mesh procedure. (a) initial configuration, (b) deformed configuration (Beuth 2012)

7

Validation of the two-phase MPM

The current chapter is devoted to the validation of the two-phase MPM by the simulation of benchmark problems, for which analytical reference solutions are available. A simple dynamic problem such as the wave propagation in a porous material is considered in Section 7.1. The use of absorbing boundary is studied analyzing the effect of the virtual thickness. Since the problem is characterized by undrained conditions, results obtained with the one-phase and the two-phase formulations are compared.

Pore pressure dissipation is considered in Section 7.2, with the one-dimensional consolidation problem. Results obtained with MPM are compared to Terzaghi's analytical solution for small strain problem (Sec. 7.2.1). The introduction of absorbing boundary and local damping is also investigated; moreover the application of the mass scaling procedure to improve computational efficiency is discussed. One-dimensional consolidation for large deformation is considered in Section 7.2.2.

The chapter ends with concluding remarks on the applicability of the used two-phase MPM implementation.

7.1 One-dimensional wave propagation

The v-w formulation, i.e. soil velocity-water velocity are the primary variables, is preferred over the v-p formulation because the latter cannot accurately capture the two-phase dynamic behavior (van Esch et al. 2011a). The capability of the implemented formulation to capture the undrained wave propagation is shown in this section.

Parameter	Symbol	Value
Effective Young modulus [kPa]	E'	$5 \cdot 10^6$
Effective Poisson ratio [-]	ν'	0
Water bulk modulus [kPa]	K_w	$2 \cdot 10^6$
Porosity [-]	n	0.4
Dry density $[kg/m^3]$	ρ_{dry}	1600
Water density $[kg/m^3]$	ρ_w	1000
Permeability $[m/s]$	k	$1.0 \cdot 10^{-5}$

Table 7.1: Material parameters for the one-dimensional wave propagation problem.

A 2.5m-long column, discretized with 1000 rows of 6 tetrahedral elements, is instantly loaded by $\sigma_y = 1kPa$. Each element contains 1 MP. Roller boundaries are prescribed at the lateral surfaces, the bottom is impermeable and fully fixed. Note that to capture the dynamic behavior of the system a very fine mesh is required. The material parameters are listed in Table 7.1 The propagation of the undrained wave is studied following the pore pressure of a MP located at 0.675m from the top surface.

The wave speed can be calculated with:

$$c_{p,u} = \sqrt{\frac{E_{c,u}}{\rho_{sat}}} \tag{7.1}$$

where $E_{c,u} = E'(1-\nu')/[(1+\nu')(1-2\nu')] + K_w/n$ is the undrained confined compression modulus and ρ_{sat} is calculated with Equation 3.60. For the considered problem $c_{p,u} = 2236m/s$.

The wave travels through the soil and is expected to reach the considered MP at $t = 3.02 \cdot 10^{-4}s$. At the bottom it is reflected and starts traveling upward doubling the pore pressure of the MP at $t = 1.93 \cdot 10^{-3}s$; at the top it is reflected again. The expected normalized pore pressure p_w/σ_y is a function of the undrained confined compression modulus and the water bulk modulus:

$$\frac{p_w}{\sigma_y} = \frac{K_w/n}{E_{c,u}} = 0.5 \tag{7.2}$$

As can be seen from Figure 7.1 the numerical solution agrees well with the theoretical one. There are some oscillations typical of the numerical solutions in which the load is applied instantaneously.

The same problem is studied with the introduction of the viscous boundary at the

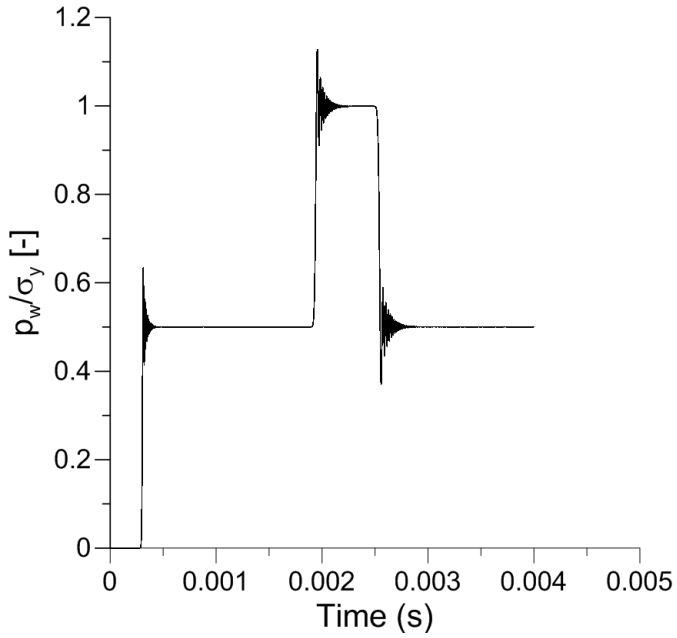

Figure 7.1: Normalized pore pressure hystory for a MP at 0.675m from the top surface. Two-phase analysis with rigid bottom boundary.

bottom. The same virtual thickness δ is applied for solid and liquid phase when the v-w-formulation is used. As expected, increasing δ/h, where h is the length of the column, the reflection decreases (Figg. 7.2 and 7.3).

Since in the considered problem the pore pressure dissipation is negligible, it can be also studied with the one-phase formulation (Chap. 3). The obtained results are nearly coincident, thus confirming that the approaches are interchangeable. The tow-phase solution shows slightly lower oscillations; this is due to the drag force, i.e. the last term in equation 4.18, that has a stabilizing effect, damping out the oscillations. The one-phase effective stress analysis is simpler and computationally less expensive than the two-phase approach.

7.2 One-dimensional consolidation

The current section deals with pore pressure dissipation; as already mentioned in Chapter 4, a fully coupled two-phase formulation is necessary in this case. The one-dimensional consolidation problem is considered. Firstly, the case of small deformations is studied and the numerical solution is compared to the Terzaghi's analytical solution. Secondly, large deformations are taken into account. The effect of using absorbing boundaries and local damping is investigated in this section too.

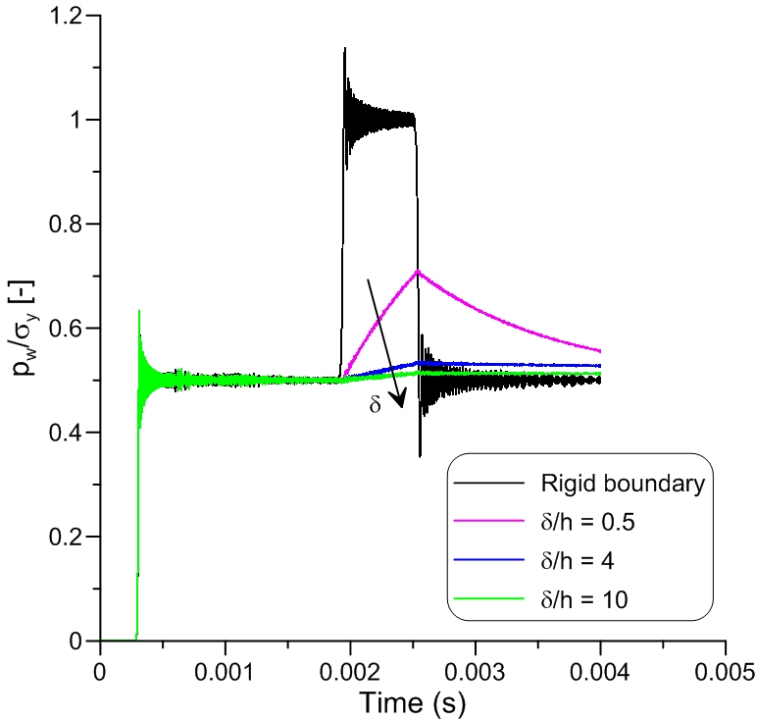

Figure 7.2: Normalized pore pressure hystory for a MP at 0.675m from the top surface. Introduction of absorbing boundary in one-phase formulation.

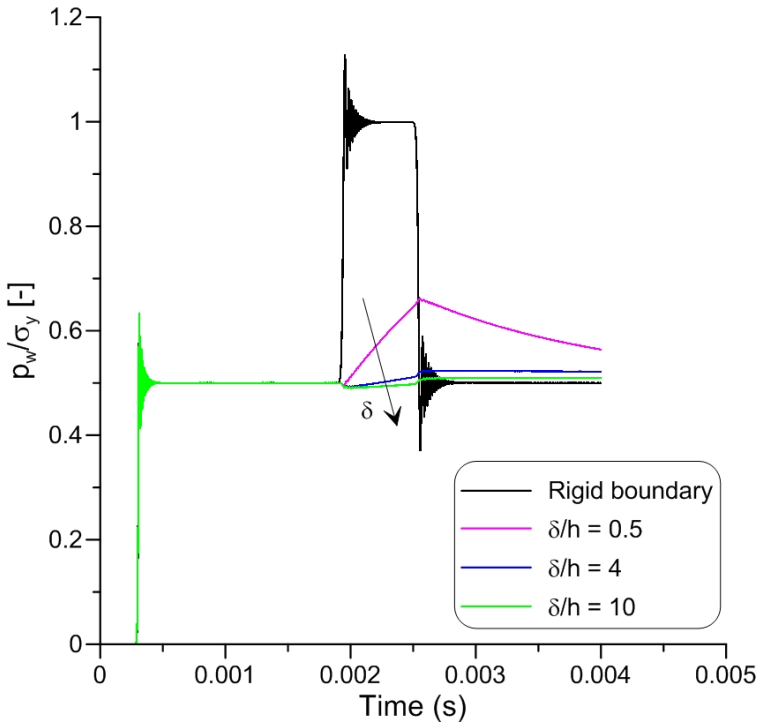

Figure 7.3: Normalized pore pressure history for a MP at 0.675m from the top surface. Introduction of absorbing boundary in two-phase formulation.

Parameter	Symbol	Value
Effective Young modulus [kPa]	E'	10000
Effective Poisson ratio [-]	ν'	0
Water bulk modulus [kPa]	K_w	75000
Porosity [-]	n	0.3
Water density $[kg/m^3]$	ρ_w	1000
Permeability $[m/s]$	k	$1.0 \cdot 10^{-3}$

Table 7.2: Material parameters for the one-dimensional consolidation problem. Small-strain case.

7.2.1 Small deformations

A 1m-soil column, discretized with 40 rows of 6 tetrahedral elements containing 4 MP each, is considered. A linear elastic material model is used, whose parameters are listed in Table 7.2. These parameters correspond to and undrained Poisson's ratio $\nu_u = 0.490$, which is considered a reasonable approximation of the material incompressibility in undrained conditions. Higer values of ν_u, i.e. higher K_w, increase the oscillations of the solution. Roller boundaries are prescribed at the lateral surfaces, the bottom is fully fixed. The head of the column is permeable and the bottom is impermeable, therefore the water can flow out of the column from the top surface and the drainage length h is 1m.

A total stress of 10kPa is applied at the first time step and kept constant during the analysis. The excess pore pressure is initialized at $p_{w0} = 10kPa$, therefore the load is initially fully carried by the water and the system is in equilibrium. While water flows out of the column, the pore pressure diminishes and the effective stress increases, according to the well-known Terzaghi's one-dimensional consolidation theory.

The process is governed by the consolidation coefficient, defined here as:

$$c_v = \frac{k}{\rho_w g\left(1/E'_c\right)} \tag{7.3}$$

The non-dimensional time factor can be defined as:

$$T = \frac{c_v t}{h^2} \tag{7.4}$$

Figure 7.4 plots the normalized pore pressure p_w/p_{w0} against the normalized depth y/h as function of the non-dimensional time. There is good agreement between the

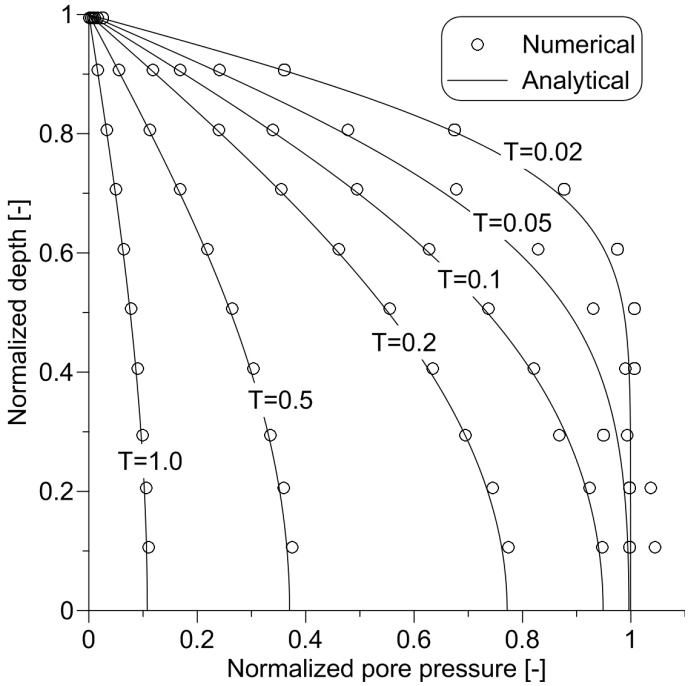

Figure 7.4: Normalized pore pressure along depth, comparison between numerical and analytical solution.

numerical and the analytical solution.

Oscillations appears for small values of T, which are due to reflections of dynamic waves. As discussed in Section 6.2 this noise can be reduced by introducing absorbing boundary or local damping.

The introduction of the absorbing boundary can effectively reduce wave reflections for small time factors, but introduces an error for long term consolidation (Fig. 7.5). Large values of δ improve results at the beginning of the process, but give unacceptable overestimation of the pore pressure for long-term. On the other hand small values of δ do not damp dynamic waves. A compromise between acceptable oscillation at the beginning of the process and deviation from analytical solution at long-time process should be found. A constant value of $\delta = 0.1h$ is considered acceptable, but changing the virtual thickness throughout the calculation is also possible.

The local damping is a valid alternative to the absorbing boundary. In this thesis the damping factor for the liquid phase coincides with the damping factor for the solid phase. The damping factor artificially simulates the natural energy dissipation which characterizes the real material (Cundall 2001); this dissipation is probably lower for the water than for the soil skeleton, but this is not considered in the present study even though should be investigated in the future.

Dynamic waves are effectively damped, but overestimation of pore pressure at long term is observed (Fig. 7.6) which increases with the damping factor α. Although there is the possibility to change the damping factor throughout the calculation, constant value of $\alpha = 0.05$ is suggested for this problem.

Both absorbing boundary and local damping can be used to reduce oscillations due to dynamic effects. The introduction of the viscous boundary can require a reduction of the time step size to achieve convergence, while this is not necessary in case of local damping. For example the presented results are obtained using a time step size of 50% of the critical, in case of absorbing boundary and 98% of the critical in case of local damping.

Consolidation of real soil deposits can take days, months or years and the numerical simulation of such processes with explicit dynamic codes becomes totally inefficient. Being a quasi-static process, the mass scaling procedure (Sec. 6.3) can be adopted. The use of mass scaling accentuate the dynamic effects and therefore increases the noise at small time, but this problem disappears at long time.

The material considered in this section is characterized by a very high consolidation coefficient ($c_v = 1m^2/s$); the pore pressure dissipates almost completely in 1s. In this specific case, the use of mass scaling is not necessary; on the contrary it generates unacceptable oscillations in the first phase of the consolidation process (Fig. 7.7). If a lower permeability is considered, i.e. $k = 10^{-5}m/s$, the consolidation time is longer ($T = 1$ correspond to $t = 100s$); however, by the use of the mass scaling procedure, i.e. introducing a mass scaling factor $\beta = 100$, the computational time does not increase dramatically, because the critical time step is larger, and nice results are obtained throughout the simulation (Fig. 7.8).

7.2.2 Large deformations

This section shows the possibility to simulate consolidation for large deformations. The same geometry and discretization considered in the previous section is used, but a much softer material; see material parameters in Table 7.3. A load of $\sigma_y = 50kPa$ is applied at the top surface at the beginning of the calculation and kept constant. The pore pressure is initialized at $50kPa$, which means that the load is initially fully carried by the water.

As in the previous case, while the pore pressure decreases the effective stress increases, but now this generates considerable vertical deformations and the decrease

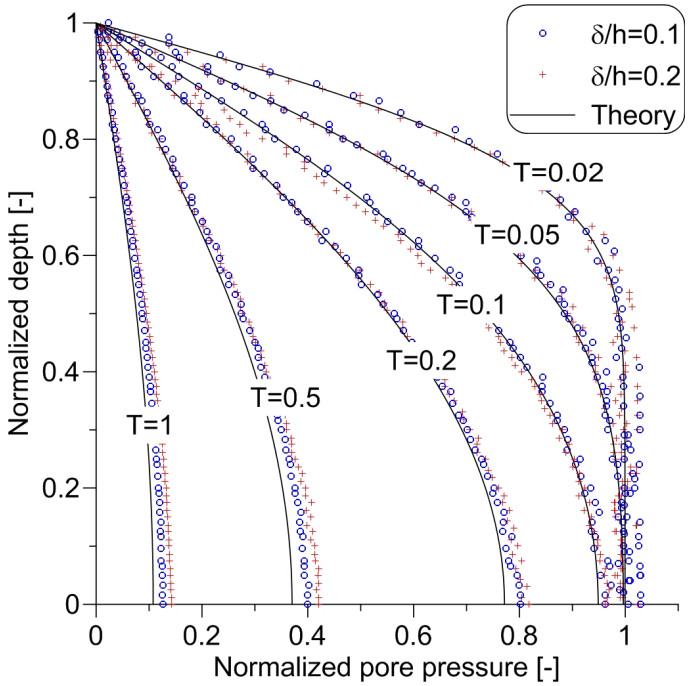

Figure 7.5: Normalized pore pressure along depth, effect of the introduction of absorbing boundary and comparison with analytical solution

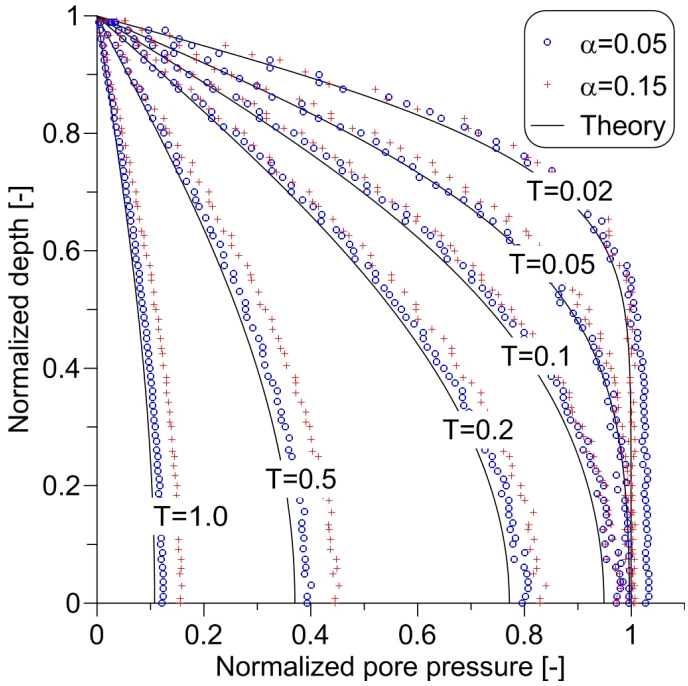

Figure 7.6: Normalized pore pressure along depth, effect of the introduction of local damping and comparison with analytical solution

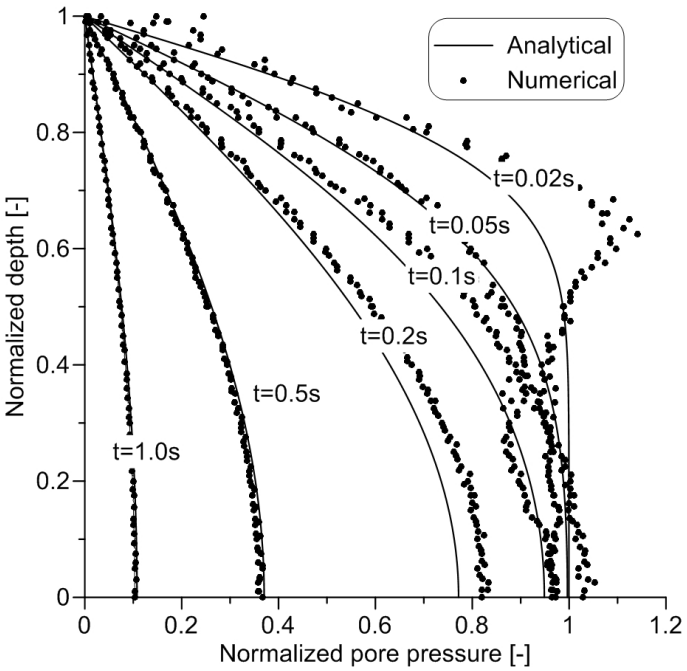

Figure 7.7: Normalized pore pressure along depth, effect of the use of a mass scaling factor $\beta = 10$ in a material with a high consolidation coefficient ($c_v = 1m^2/s$)

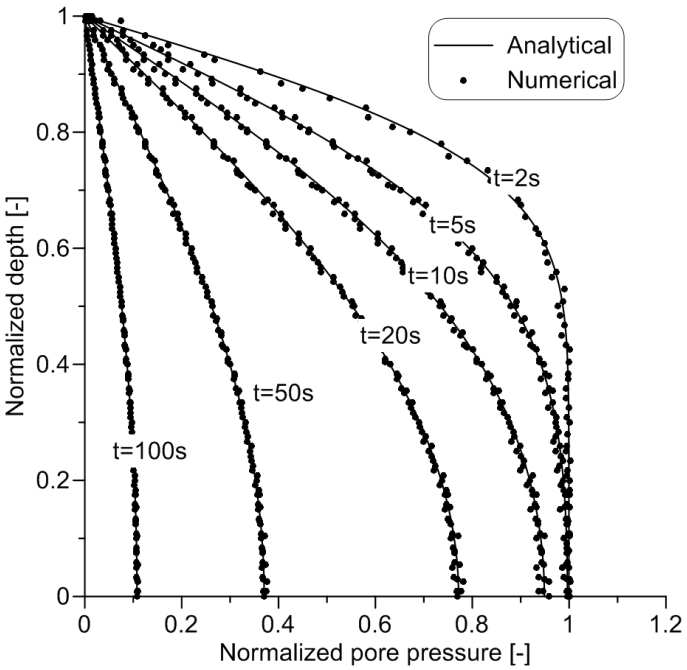

Figure 7.8: Normalized pore pressure along depth, effect of the use of a mass scaling factor $\beta = 100$ in a material with a consolidation coefficient $c_v = 0.01m^2/s$

Parameter	Symbol	Value
Effective Young modulus [kPa]	E'	100
Effective Poisson ratio [-]	ν'	0
Water bulk modulus [kPa]	K_w	750
Porosity [-]	n	0.3
Water density $[kg/m^3]$	ρ_w	1000
Permeability $[m/s]$	k	$1.0 \cdot 10^{-2}$

Table 7.3: Material parameters for the one-dimensional consolidation problem. Large-strain case.

of the column-length is not negligible, therefore the small-strain Terzaghi's theory is no longer valid.

This material is characterized by a consolidation coefficient $c_v = 0.1m^2/s$; a time factor T_L defined by Equation 7.4 in which h is the initial length of the column can be considered. Figure 7.9 shows the normalized pore pressure at specific material points, choosen along the column, against their y coordinate, the value zero corresponds to the bottom of the mesh. Since the drainage-lenght decreases significantly with the time, the pore pressure dissipation is faster compared with the small strain case (Fig. 7.4).

As usual in MPM, large deformations are simulated with material points moving through the mesh. Figure 7.10 shows the change in column-length along time.

7.2.3 The time step citerium

The implemented numerical scheme for the two-phase formulation is conditionally stable and the critical time step size is defined by Equation 3.34. The reference velocity is the speed of the undrained wave, which can be determined as:

$$c_p = \sqrt{\frac{E_{c,u}}{\rho_{sat}}} \tag{7.5}$$

where $E_{c,u}$ is the undrained constrained modulus.

However, this condition does not guarantee the stability of the scheme, which appears to be also dependent on the permeability of the material. Indeed, considering the simple one-dimensional consolidation problem presented in Section 7.2.1, if the permeability is decreased to $10^{-5}m/s$ the solution diverges using a Courant number of 0.98, but converges if it is reduced to 0.1. With such a low permeability

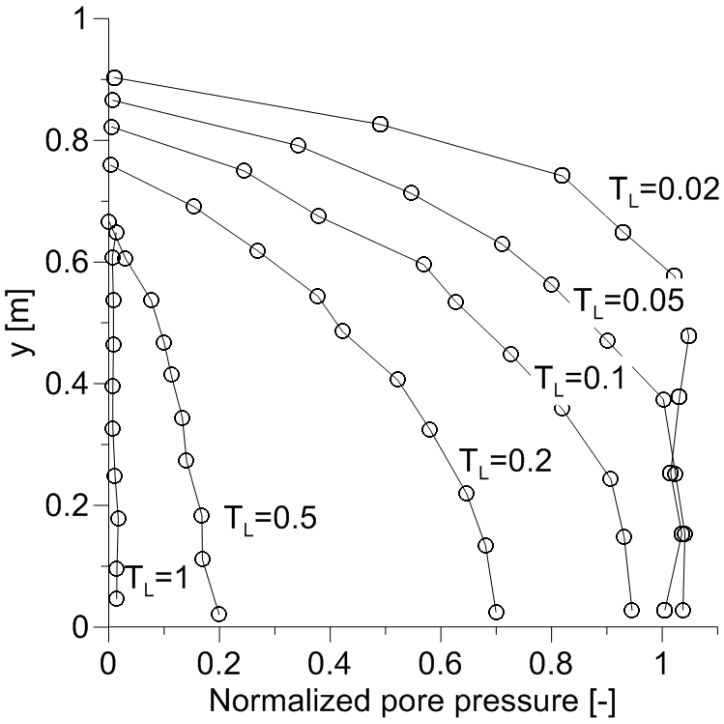

Figure 7.9: Normalized pore pressure with depth.

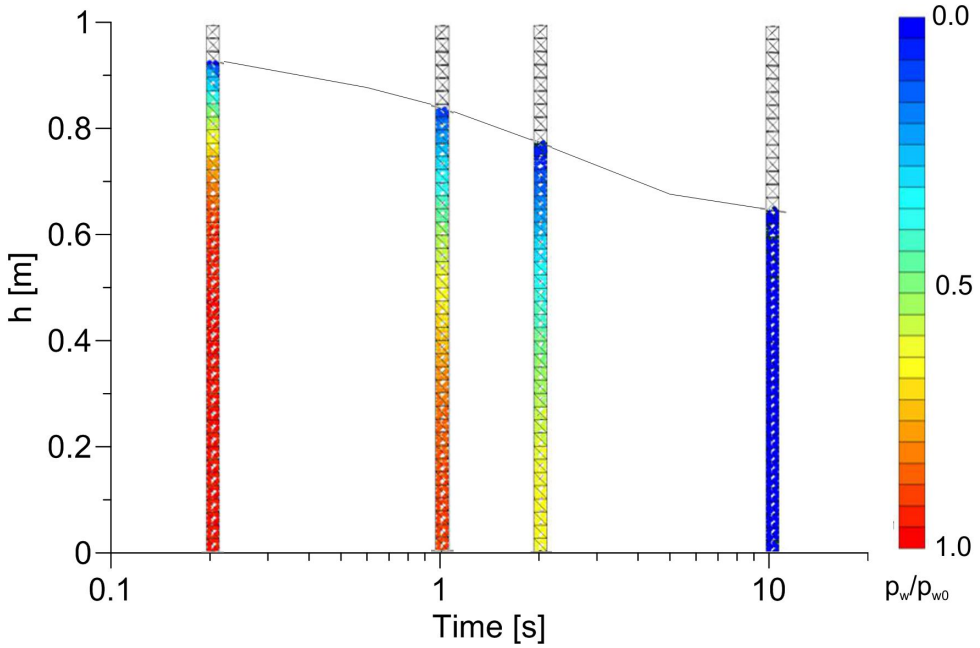

Figure 7.10: Height of the column along time; colors indicates the normalized pore pressure.

the scheme is stable with $C = 0.98$ if a mass scaling factor $\beta = 100$ is used or the Young modulus is increased by a factor 100. This suggests that permeability, density and elastic modulus influence the critical time step size. The study of the stability criterion for the implemented formulation is object of the on-going research.

7.3 Concluding remarks

This chapter shows the validation of the current two-phase MPM implementation for the simulation of dynamic and quasi-static problems in case of both small and large deformations involving two-phase materials.

The two-phase dynamic MPM can correctly capture the propagation of the undrained wave along a column of saturated porous media (Sec. 7.1). The arrival time of the wave agrees with the analytical solution and no energy dissipation is observed.

The MPM can accurately capture how the pore pressure distribution changes with time in the one-dimensional consolidation problem (Sec. 7.2); indeed, the numerical result for small strain is in excellent agreement with the analytical solution by Terzaghi. At large strain, the pore pressure dissipation is faster because the drainage length decreases with time. With the MPM, the effect of significant soil deformations on the pore pressure dissipation can easily be taken into account.

In Sections 7.1 and 7.2 it is proved that absorbing boundary can be used to damp dynamic waves. The rate of damping increases with the virtual thickness δ. The physical meaning of this parameter is explained in Section 6.2.1; sensitivity analysis are necessary to choose the most suitable value for the specific problem under-consideration.

As shown in Section 7.2.1, the local damping can be a valid alternative to solve problems related to dynamic effects. The local damping factor α must be small in slow-process problems since it affects the pore pressure at long term (see Fig. 7.6). In this thesis the same virtual thickness and the same damping factor are applied for the fluid and the solid phase, however different values can be used and the effect of this choice will be investigated in the future.

The mass scaling procedure can be used to improve the computational efficiency of quasi-static and slow-process problems. It increases the noise due to the propagation and reflection of dynamic waves; this problem is more severe at short time, but disappears at long term.

The used two-phase MPM implementation is capable to simulate geomechanical problems involving pore pressure dissipation with small and large deformations.

8

Simulation of the collapse of a submerged slope

The stability of submerged slopes is an important issue in many countries. In the Netherlands the problem has a great impact in the south-western province of Zeeland, characterized by numerous islands. The shoreline has been severely damaged erosion and submarine landslides compromising the safety of the area. The phenomenon needs to be deeply investigated in order to enforce the design of mitigation techniques.

In order to study the stability of loose sand slopes, small scale laboratory tests were performed at Deltares (Delft, the Netherlands). To gain a deeper understanding of the problem, the experiments were enhanced by an advanced numerical study. Indeed, laboratory tests are affected by scale effects, which may leave some doubts on the extension of the small-scale observations to the real case. Numerical simulations can be easily done on the full-scale geometry. Moreover, parametric studies can easily be performaed to detect the most significant parameters affecting the occurance and evolution of the landslides.

Slope stability problems have been intensively studied for decades, both experimentally and numerically to understand the mechanics and to predict the failure. Most of the numerical analyses focus on the identification of the limit condition of static equilibrium of the slope. The finite element methods (FEM) are popular in this field because they can represent accurately the geometry of the slope and allow for incorporation of advanced constitutive models. The shape of the sliding surface can be well captured with FEM, but the dynamic evolution of the landslide and its run-out cannot be reproduced.

Large soil deformations, occurring after the trigger, can be simulated with advanced methods, which may be grouped in three broad classes:

- discontinuous, particle methods
- depth integrated methods
- a combination of finite element methods and Lagrangian integration points

Discontinuous methods, such as DEM (see Section 2.2), are based on a microscopic description of the granular material, which is often difficult to relate to macroscopic constitutive properties. In addition to this, taking into account the interaction with fluids is not simple. Depth integrated models describes the soil as a viscous fluid and are therefore suitable mainly to analyze certain mudslides, avalanches and submarine landslides, in which the soil acts more like a fluid than a solid during part of the slide. There are several variants for the Lagrangian (or particle, or material points) integration methods: SPH, PFEM, FEMLIP, MPM (see Section 2.3.2 for an overview). These methods reproduce the original source of instability using appropriate soil constitutive models and are capable of following the transition from static to dynamic conditions.

The MPM recently demonstrated to be able to describe slope failure in dry conditions (Andersen and Andersen 2010b) as well as in saturated conditions (Alonso and Zabala 2011, Bandara 2013, Alonso et al. 2014). This chapter presents a further application of the two-phase MPM to the collapse of a submerged sand slope. The two-phase MPM can simulate the movements of water inside the saturated soil and take into account the interaction between pore fluid and solid skeleton. The interaction with free water is neglected.

The capability of the implemented two-phase MPM formulation to capture the experimental results is tested. This is an important step before the analysis of the more complex full-scale problem. A full-scale experiment and the relative numerical analyses are being performed at Deltares at the time this chapter is written and could not be included here.

The main features of the physical model which have been considered for the set-up of the MPM simulations are summarized in Section 8.1. Section 8.2 briefly presents the set-up of the numerical model. Results are discussed in Section 8.3.

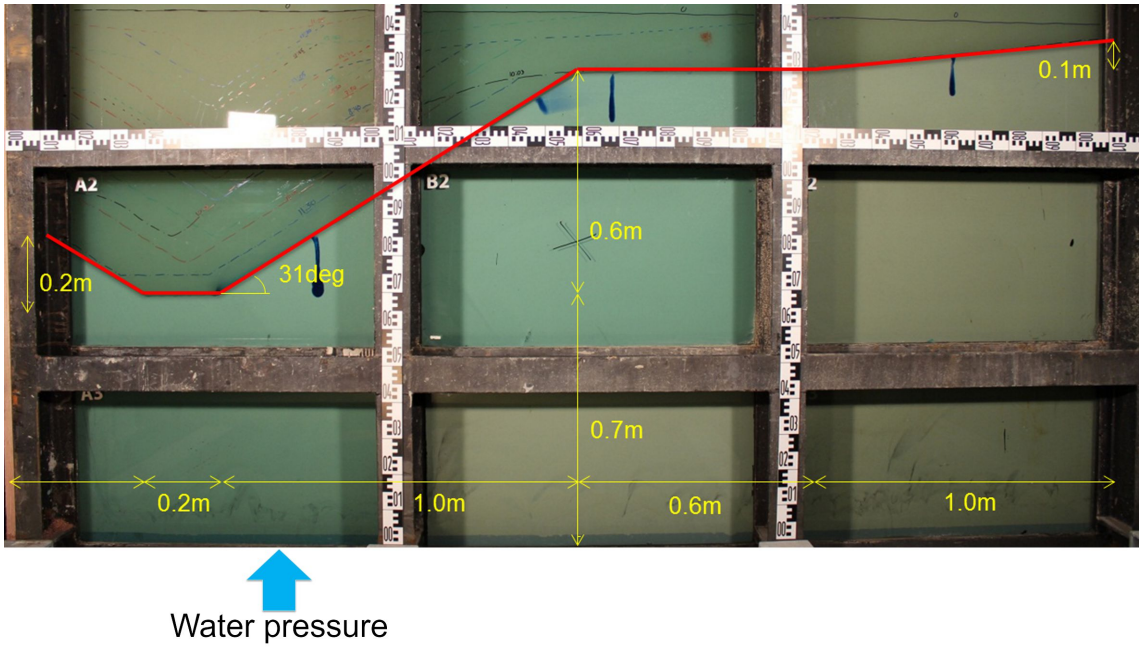

Figure 8.1: Initial configuration of the slope in the experiment. The blue arrow indicates the location where the water pressure is injected to trigger the failure.

8.1 Physical model

The slope is completely submerged in a test flume which is 5.4m long, 2.5m high and 0.5m wide. The slope is build by a nozzle slowly sucking the sand, which flows under a natural slope of the embankment to the nozzle. The geometry just before triggering the failure is shown in Figure 8.1. At that moment the slope has an inclination of 31° and a height of 0.60 m.

In the experiment, the failure is triggered by injection of water under the toe of the slope. The first macro-scale movement is observed in a superficial layer of about one decimeter sliding downward. This lasted for a few seconds (5 to 10 seconds). The movement continued slowly in a thinner layer. The whole failure process lasted about a minute.

8.2 Geometry, discretization and material parameters of the numerical model

The configuration immediately before triggering the failure is considered at the beginning of the simulation (Fig. 8.1). The discretized domain is shown in Figure 8.2.

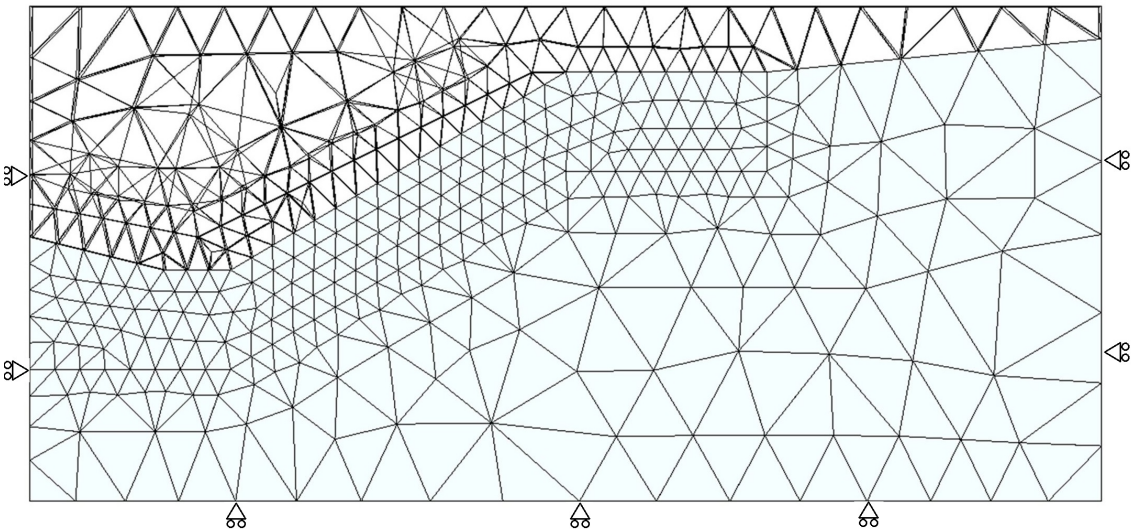

Figure 8.2: Discretization of the problem.

The mesh consists of 2202 tetrahedral elements; 6252 MP are placed inside the 1567 initially active elements. The part of the mesh in which significant deformations are expected is refined to increase the accuracy of the results. Mesh coarseness significantly influences the results, especially when low order elements are used, because of locking problems. Volumetric locking is mitigated by using the procedure explained in Section 6.1. The final discretization has been chosen after a mesh refinement analysis as a compromise between accuracy and computational efficiency.

At the left and right boundary the displacements are constrained in horizontal direction, while at the bottom no displacements are allowed. All boundaries are impermeable for water, except during triggering of the failure at the location where the water pressure is applied.

The failure is triggered by applying an excess pore pressure at the bottom of the domain. The pore pressure is increased linearly from 0 to $p_{max} = 10kPa$ in $t_{loading} = 5.0s$. For $t > t_{loading}$ the pore pressure is reduced to zero again.

To describe the constitutive behaviour of loose sand, the elasoplastic model with Mohr-Coulomb failure criteria is used, and input parameters are shown in Table 8.1. They are derived from experimental data. A local damping factor of 0.05 is used for the calculation.

Parameter	Symbol	Value
Saturated unit weight of the sand $[kN/m^3]$	γ_{sat}	18.7
Effective Young modulus $[kPa]$	E'	5000
Effective Poisson ratio [-]	ν'	0.2
Water bulk modulus $[kPa]$	K_w	45310
Cohesion $[kPa]$	c'	0
Friction angle $[deg']$	ϕ	32
Dilatancy angle $[deg]$	ψ	0
Porosity [-]	n	0.45
Permeability $[m/s]$	k	$1.0 \cdot 10^{-4}$

Table 8.1: Material parameters for the slope liquefaction problem

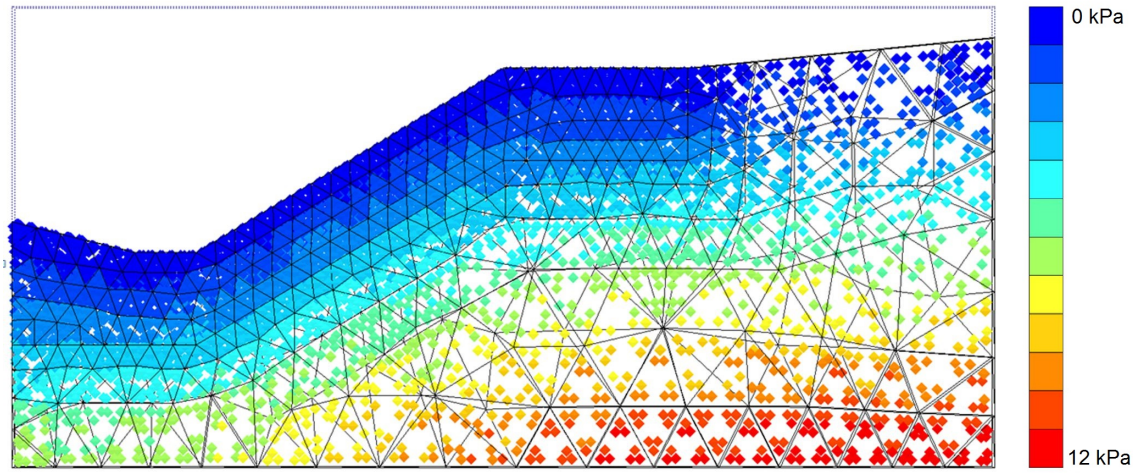

Figure 8.3: Initial vertical effective stresses at the material points.

8.3 Results

The initial stress distribution is generated by a gravity loading phase, i.e. the gravity force is applied at the first time step and the static equilibrium condition is approached. A quasi-static convergence criterion is applied, which implies that the slope is assumed to be in static equilibrium when the normalized kinetic energy $E_{kinetic}/(F_{ext} - F_{int})$ and the normalized unbalance force $(F_{ext} - F_{int})/F_{ext}$ are below the limit value of 0.1%. The pore pressure distribution is initially assumed hydrostatic.

It can be seen in Figure 8.3 that the effective stresses after the initialisation phase are, as expected, linearly increasing with depth reaching a maximum value of $\sigma'_{y,max} = (\gamma_{sat} - \gamma_w)h_{max} = 12.1kPa$.

After the initialization phase, failure is triggered as described in the previous section by applying an excess pore pressure at the bottom of the mesh. The pressure front propagates upwards with a speed that is a function of the consolidation coefficient. The development of excess pore pressure distribution with time is shown in Figures 8.4 and 8.5.

While the excess pore pressure increases, the effective stress decreases causing the instability of the slope. The first clearly visible displacements appear at the crest of the slope at 3.75s after the application of the excess pore pressure. The final equilibrium state is reached after approximately 8.5s. The failure surface is shallow with a depth of about 0.15m, in agreement with the experimental observation.

The final equilibrium state is compared with the experimental results in Figures 8.6 and 8.7, where the initial and final shape of the slope observed in the laboratory are marked with the red and blue line respectvely. It can be concluded that the numerical simulation is in very good agreement with the experiment.

Sensitivity analyses have been performed to study the effect of the Young modulus (E') of the sand, the bulk modulus of the water (K_w) and the dilatancy angle (ψ). Alternative triggering mechanisms have been considered, too.

Permeability Compared to the reference calculation, in which $k = 10^{-4}m/s$, a much higher permeability of $10^{-2}m/s$ has been considered. This value is closer to the typical permeability of gravel than of sand. Although it is not representative of the field conditions, it shows the effect of the Darcy's permeability on the dynamic of the collapse. An increase of the permeability results in a faster propagation of the excess pore pressure initially applied at the bottom. The collapse starts much earlier than in the reference case and the slides is faster. The excess pore pressures are, on average, slightly lower, because the dissipation is facilitated.

Young modulus of the sand Compared to the reference calculation, in which $E' = 5000kPa$, a lower Young modulus of $1000kPa$ has been considered. Such a value is typical of very loose sands at low stress levels. Indeed, a rough estimate of the elastic modulus for loose sand can be achieved by

$$E_{50} \approx E_{50}^{ref}(\sigma'_x/100)^{0.5}$$

where σ'_x is the horizontal effective stress in kPa and $E_{50}^{ref} \approx 15MPa$ (Schanz and Vermeer 1998). Assuming $\sigma'_x = 0.7kPa$, because of shallow failure, a value

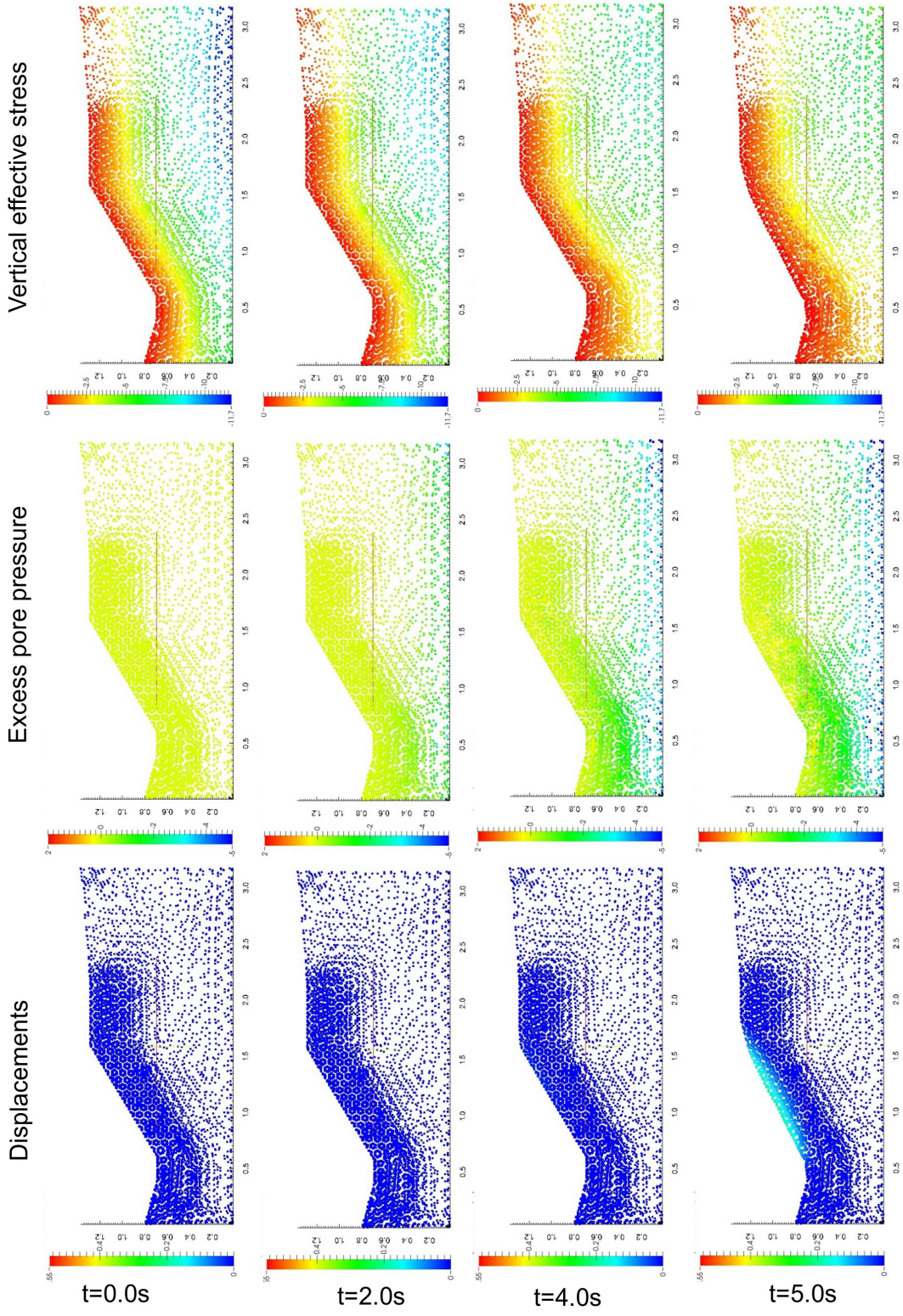

Figure 8.4: Total displacements, excess pore pressure and vertical effective stress distributions with time. $t = 0$ corresponds to the moment at which the applied pore pressure starts to increase.

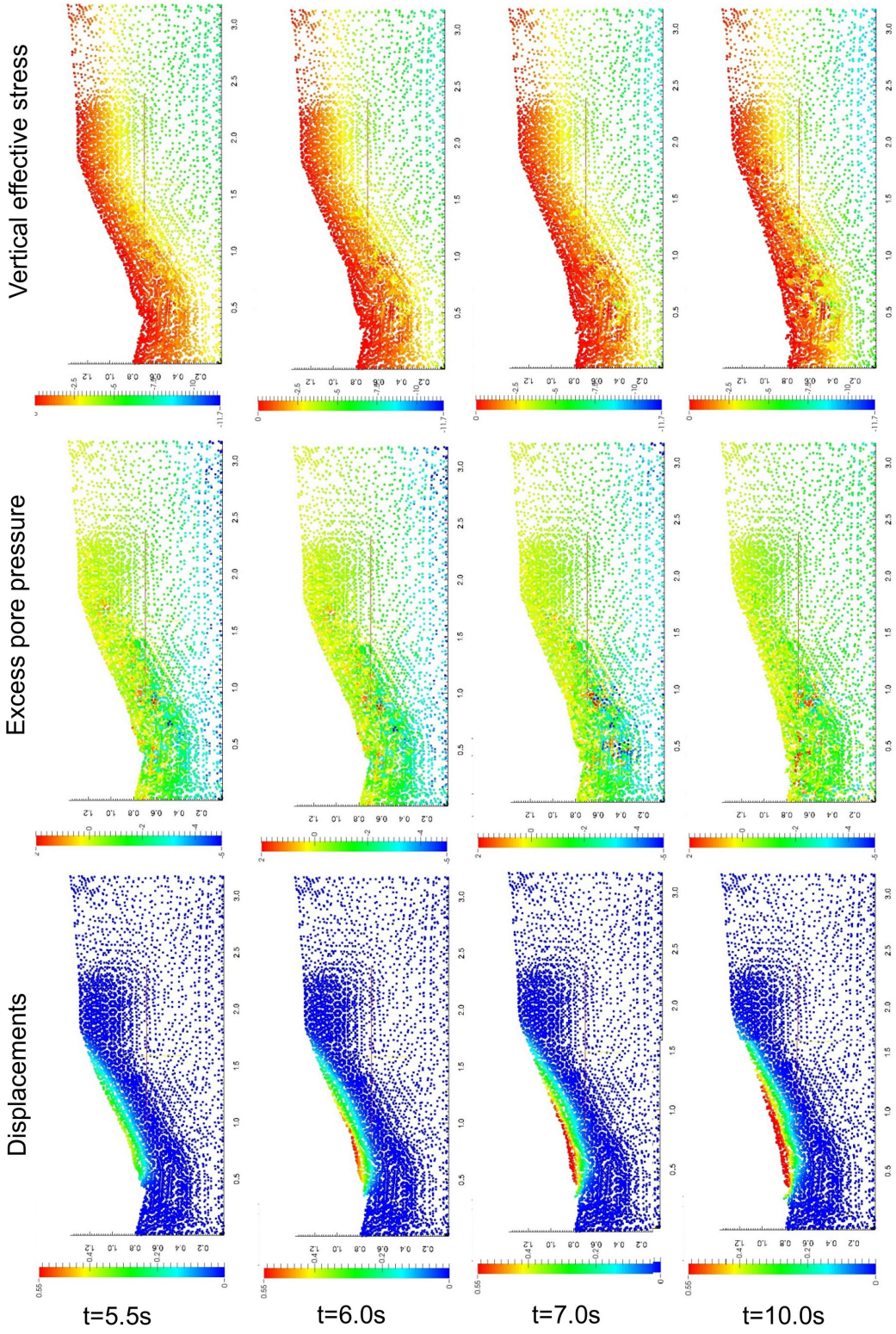

Figure 8.5: Total displacements, excess pore pressure and vertical effective stress distributions with time. $t = 0$ corresponds to the moment at which the applied pore pressure starts to increase.

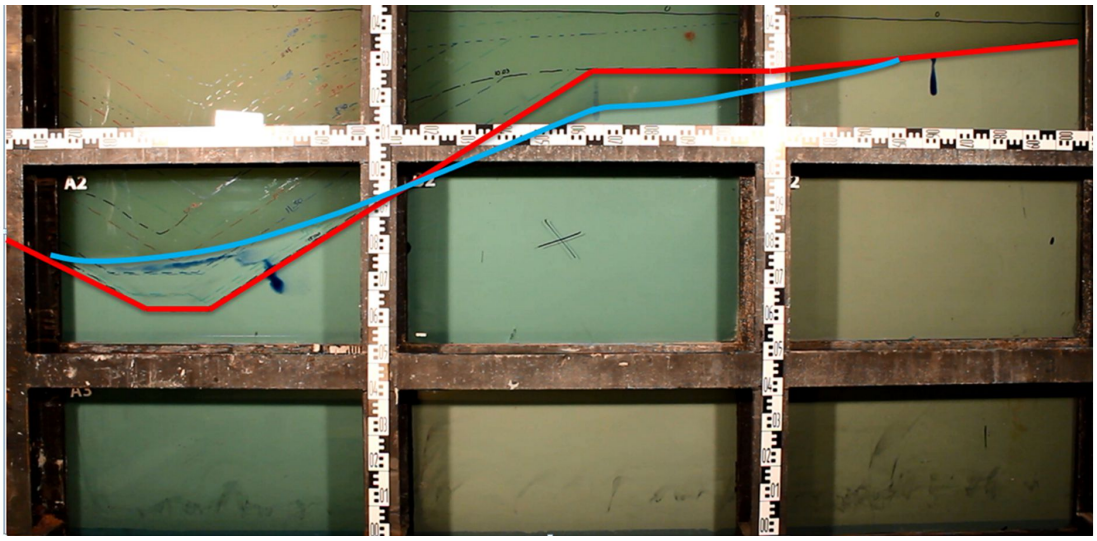

Figure 8.6: Final configuration of the slope in the experiment marked by the blue line. The red line traces the initial configuration.

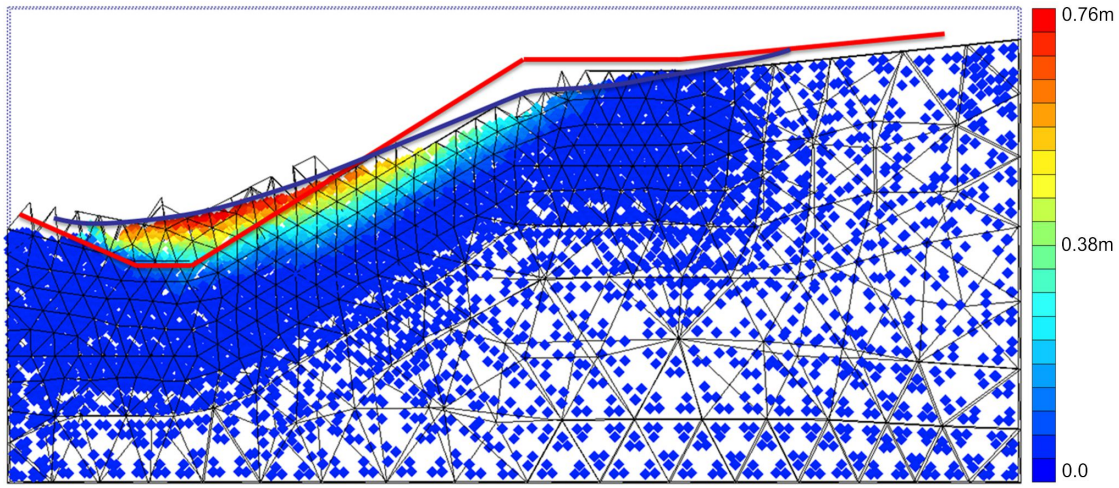

Figure 8.7: Final configuration of the slope in the numerical simulation. The red line and the blue line trace respectively the initial and the final experimental configurations. Color scale indicates the displacements.

of about $1MPa$ is obtained. The soil movement proceeds slower, and the final equilibrium state is reached later, i.e. after about 20s. The final displacements are smaller because more energy is dissipated in internal work.

Bulk modulus of the water Compared to the reference calculation, in which $K_w = 45310kPa$ a lower bulk modulus of the water of $3100kPa$ is considered in order to take into account the eventual inclusion of air, and therefore higher compressibility of the water. To illustrate the effect of the bulk modulus of the water, consider a soil in fully undrained conditions which behaves usually incompressible. This means that the undrained Poisson ratio is approximately 0.5. The applied reduction of bulk modulus of the water would correspond to an undrained Poisson ratio of the saturated sand of 0.40 and can be calculated with Equation 3.69. This illustrates that a certain compressibility of the material even in undrained conditions is taken into account. Note that the calculations are performed with the two-phase formulation, which means that pore pressures dissipation is taken into account and the behaviour of the soil is not undrained. For the calculations with reduced bulk modulus of the water the excess pore pressures and the displacements are slightly lower.

Dilatancy In the reference calculation a dilatancy angle of zero is used. The introduction of a negative dilatancy angle ($\psi = -1°$) leads to a catastrophic failure of the slope. Indeed, in this case the excess pore pressure increases monotonically with deformation as shown in Figure 8.8. This does not represent the real behaviour of sand, which shows, instead, volumetric deformation and excess pore pressure development only for small deformations. At high level of strains, i.e. critical conditions, the dilatancy angle is zero. For the considered slope failure problem, where large deformations are taken into account, $\psi = 0°$ should be applied when the soil behaviour is modelled using the Mohr-Coulomb constitutive model.

Local damping A local damping factor of 0.05 has been used for the reference calculation. This simulates the natural energy dissipation of the material due to internal friction. Higher values has been considered, i.e. 0.10 and 0.15, resulting in smaller displacements.

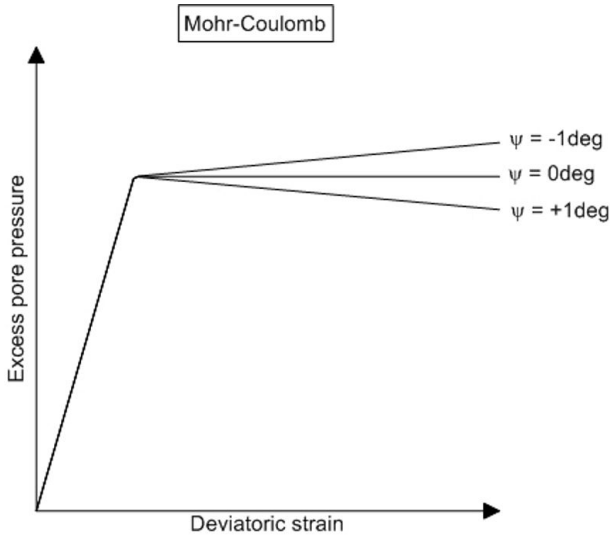

Figure 8.8: Illustration of development of excess pore pressures for different dilatancy angles.

8.4 Conclusions and future developments

The failure of a submerged slope triggered by a sudden increase of water pressure at the bottom can be successfully simulated using the two-phase MPM implementation. The numerical results of the deformed slope in the final equilibrium state are in good agreement with experimental data (Fig. 8.7).

The behavior of sand is complex; the elasto-plastic model with Mohr-Coulomb failure criteria is a very simplified way of describing its behavior. Deeper understanding of the failure process could be achieved with more sophisticated material models. For example the Mohr-Coulomb with strain softening model (Abbo and Sloan 1995) proved to be able to capture the progressive failure of the slope (Alonso and Zabala 2011; Yerro et al. 2014).

It is of great interest to investigate the behavior of true scale slopes, as found in the region of Zeeland, whose height ranges between 10 and 50 m. It is expected that the large-scale slopes would behave differently than slopes in model scale. Numerical simulations can indicate safe inclination angle in the natural conditions. Revetments of various types have been used to prevent erosion and improve the stability of the slope. The effect of a stone revetment will be considered in the future also in the numerical simulations.

The interaction with free water is neglected in this study; however, future developments of the MPM will be able to include this effect. The implementation of

multi-layer formulations, i.e. solid and fluid are simulated with two separates sets of MP, allows to simulate free water, saturated soil as well as soil-water suspensions; see Bandara (2013), Wieckowski (2013) and Vermeer et al. (2013). These advanced MPM formulations can simulate erosion-sedimentation processes and therefore close the gap between geomechanical models and hydromechanical models.

9

Simulation of Cone Penetration Testing

As shown in Chapter 7 the MPM can be successfully used to simulate large displacement problems, taking into account the generation and dissipation of pore pressure. The method has been also used to reproduce soil penetration problems such as pile and spudcan installation (Nuygen et al. 2014).

In this chapter the MPM is applied to simulate the cone penetration test (CPT) accounting for different drainage conditions. The study of CPT in partially drained conditions is particularly interesting; indeed partial drainage can characterize cone penetration in silty soils and arises difficulties in interpreting the measurements (Schneider et al. 2008b). So far, this problem has been mainly took on experimentally. Indeed, its numerical simulation is extremely complex as large deformations, soil-cone contact and soil-water coupled mechanical behavior need to be considered.

A description of the cone penetration test and how it is used in geo-engineering is given in Section 9.1. A brief literature review is found in Section 9.2. The main features of the numerical model are explained in Section 9.3. Section 9.4 presents results of MPM simulations in undrained conditions using the Tresca material model, while in Section 9.5 the effect of partial drainage is considered. The chapter ends with concluding remarks and future developments of the research (Sec. 9.6).

9.1 Introduction

The Cone Penetration Test (CPT) is a widely used in situ soil testing technique. It was invented in the Netherlands in 1932 by P. Barentsen, an engineer at Rijkswaterstraat (department of public works); in order to get a quick and economic impression of the structure of the underground. Many technological developments,

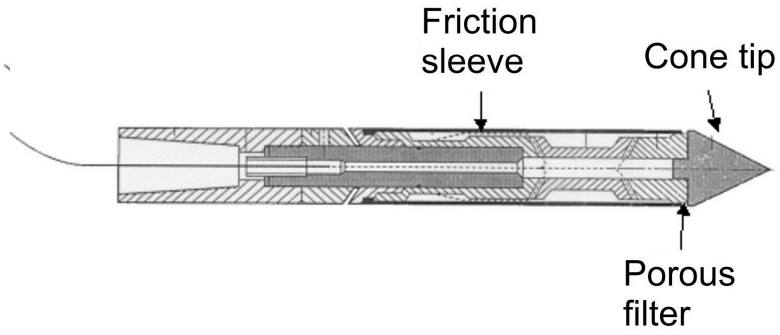

Figure 9.1: Standard cone penetrometer.

as well as extensive scientific and theoretical studies on data interpretation, have been done since then.

CPT consists in a conical tip placed at the end of a series of rods, pushed into the ground at a constant rate. According to the ISSMFE IRTP standard, the rate of penetration should be $20mm/s \pm 5mm/s$. The combined resistance to penetration of the cone and outer surface of a sleeve is measured, as well as the single sleeve resistance. In the CPTU equipment the pore pressure is measured too. Extra sensors are available in the market to measure additional soil properties such as the shear wave velocity and the dielectrical conductivity.

The reference test equipment consists of a 60° cone, with $10cm^2$ base area and $150cm^2$ friction sleeve located above the cone. The total force acting on the cone Q_c, divided by the projected area A_c produces the cone resistance q_c. The total force acting on the friction sleeve F_s, divided by the surface area of the friction sleeve A_s produces the sleeve friction f_s. Depending on the specific device, the pore pressure can be measured at the tip of the cone, at the cone face or, more often, behind the cone; the latter is referred to as the u_2 position. Figure 9.1 schematically represents the device.

The CPT has three main applications in the site investigation process:

1. determine sub-surface stratigraphy and identify the present materials,
2. estimate geotechnical parameters,
3. provide results for direct geotechnical design.

The determination of soil stratigraphy and the identification of soil type have typically been accomplished using charts that link cone parameters to soil type. Early

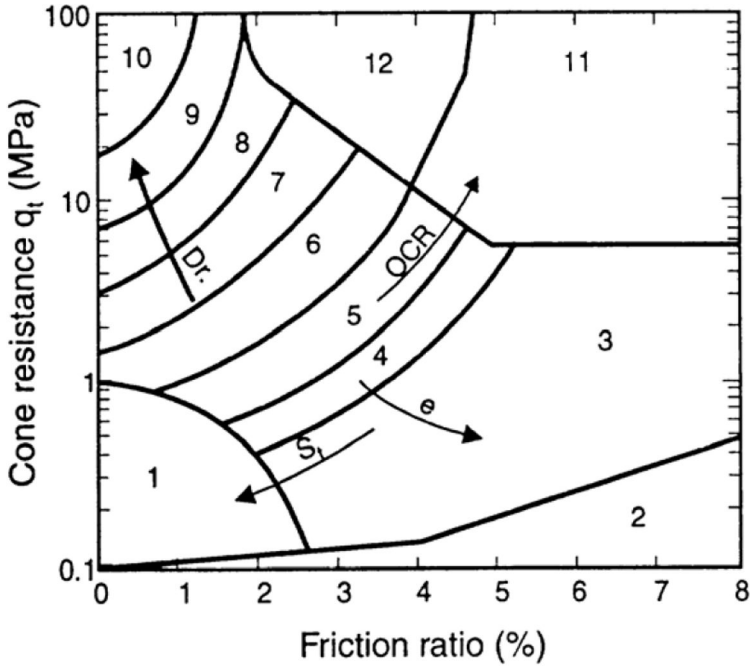

Zone	Soil Behavior Type
1	Sensitive fine grained
2	Organic material
3	Clay
4	Silty clay to clay
5	Clayey silt to silty clay
6	Sandy silt to clayey silt
7	Silty sand to sandy silt
8	Sand to silty sand
9	Sand
10	Gravelly sand to sand
11	Very stiff fine grained
12	Sand to clayey sand

Figure 9.2: Soil behavior chart by Robertson et al. (1986) based on cone resistance and friction ratio

charts using q_c and friction ratio $R_f = (f_s/q_c)100\%$ were proposed by Schmertmann (1978) and Douglas and Olsen (1981), but the chart proposed by Robertson et al. (1986) has become more popular. Robertson (1990) proposed to identify the soil behavior type by mean of chart based on normalized cone parameters such as

$$Q_{t1} = \frac{q_t - \sigma_{v0}}{\sigma'_{v0}} \tag{9.1}$$

$$F_r = \frac{f_s}{q_t - \sigma_{v0}} \tag{9.2}$$

$$B_q = \frac{\Delta u}{q_t - \sigma_{v0}} \tag{9.3}$$

where q_t is a corrected cone resistance (Campanella et al. 1982), Δu is the excess pore pressure, σ_{v0} and σ'_{v0} are the in situ total vertical stress and the in situ effective vertical stress respectively. The use of charts based on normalized parameters usually gives more reliable estimations of the soil type. Since 1990 several charts has been suggested (see e.g. Jefferies and Davies 1991, Robertson and Wride 1998, Jefferies and Been 2006). The original Robertson et al. (1986) chart, based on q_c and R_f, is shown in Figure 9.2.

Following Lunne and Powell (1997), the interpretation process of geotechnical parameters can be divided into three categories:

1. fine grained soil, in which the penetrations occurs in undrained conditions,
2. coarse grained soil, in which the penetration occurs in drained conditions,
3. other or intermediate materials, which are characterized by a very complex penetration process.

This chapter deals with cone penetration in clay, however the full range of drainage conditions is considered by varing the penetration rate. This allows to compare the numerical result with similar published data and validate the method.

This study focuses on the estimation of the tip resistance q_c; issues regarding the sleeve friction are not considered. However this can be done in future developments of the research.

CPT allows to estimate soil parameters that can be used as input for geotechnical analyses; however, the in situ test results can be directly used for engineering problems such as pile design, bearing capacity, settlement estimation ect. This particular application of CPT is not considered in this study, which, on the other hand, can give interesting insight on the link between soil properties and CPT measurements.

9.2 Literature review

Being CPT a widely used technique, the literature on the topic is very extended. This section summarizes the most interesting studies regarding undrained cone penetration in clay (Sec. 9.2.1) and the effect of drainage conditions (Sec. 9.2.2).

9.2.1 Undrained penetration

In saturated clays and other fine-grained soils, the test is carried out at a penetration rate that does not permit drainage, therefore the cone resistance may be interpreted as a measure of the undrained shear strength of the soil. Conventionally, the shear strength is derived by dividing the net cone resistance by a cone factor N_c:

$$N_c = \frac{q_c - \sigma_{v0}}{s_u} \tag{9.4}$$

where σ_{v0} is the in situ total vertical stress (Lunne and Powell 1997). It would be helpful to have a reliable estimation of this cone factor. Real soils render this task difficult because of complex rheological characteristics, where a shear strength is a function of the rate of strain, the particular induced stress path and other factors such as the physical structure of the deposit.

Theoretical and empirical solutions have been proposed to estimate N_c. The theoretical solutions can be grouped in the following classes:

Classical bearing capacity theory: the solution is obtained considering the incipient failure of a rigid, plastic material and are highly dependent on the assumed shape of the plastic zone, see e.g. Meyerhof (1951) and Janbu and Senneset (1974)

Cavity expansion theory: it is assumed that the penetration of the cone into the soil is equivalent to the expansion of a cilindrical or spherical cavity in an infinite elastoplastic medium, see e.g. Ladanyi (1963) and Vesic (1972)

Strain path theory: the soil is treated as a viscous fluid, and a flow field is established from a potential function, strain rates are computed from differentiation of the velocity field and stress by means of constitutive equations, see e.g. Levadoux and Baligh (1980) and Baligh (1985)

Numerical approaches: methods capable to handle large deformation are neces-

sary, e.g. ALE (van den Berg 1994, Lu et al. 2004), CEL (Qiu 2014), MPM (Beuth 2012). An alternative approach for large deformation analysis is the Eulerian FE formulation; extra terms are included in the governing equations to account for the rotation of the material and convection of the stress field, which can lead to mathematical difficulties when complex constitutive models are adopted (van den Berg et al. 1996).

Since cone penetration is a complex phenomenon, all the theoretical solutions make several simplifying assumptions regarding soil behavior, failure mechanism and boundary conditions. Theoretical solutions have limitations in modeling the real soil behavior. Hence, empirical correlations are sometimes preferred.

The soil undrained shear strength can be estimated from different empirical correlations using alternatively the total cone resistance, the effective cone resistance or the excess pore pressure. Over the years, a large number of studies have been performed, many of them resulting in cone factor in the range 6-20, more commonly in the range 9-17, with the shear strength measured in triaxial compression generally used to normalize the cone resistance (Lunne and Powell 1997).

9.2.1.1 Theoretical estimations of the cone factor

A number of different theoretical solutions have been presented in the litterature, see Yu and Mitchell (1998) for a short overview. All solutions have shown that, even for a simple Tresca soil model, the theoretical cone factor is influenced by:

1. The rigidity index $I_r = G/s_u$ where G is the shear modulus of the soil
2. The in situ stress ratio $\Delta = (\sigma_{v0} - \sigma_{h0})/(2s_u)$ where σ_{v0} and σ_{h0} are the in situ vertical and horizontal stresses
3. The roughness of the cone $\alpha_c = a/s_u$ where a is shear stress at the contact surface.

The use of **cavity expansion theory** allows to obtain relatively simple analytical solution. A review of cavity expansion theory and its application is provided in Yu, Herrmann, and Boulanger (2000). With this method the prediction of the cone resistance requires two steps: first the limit pressure for cavity expansion in soil must be determined, second the limit pressure must be related to the cone resistance.

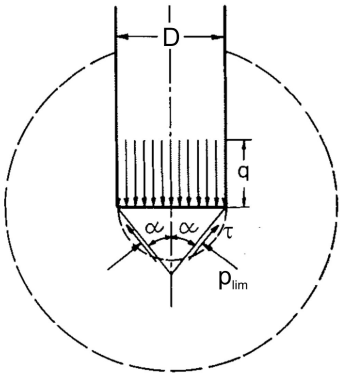

Figure 9.3: Scheme to transform cavity expansion limit pressure to cone resistance.

The relationship between spherical cavity expansion limit pressure and cone resistance is generally based on the approach shown in Figure 9.3 (Ladanyi and Johnston 1974). The cone tip is replaced by an hemispherical surface on which the cavity expansion limit pressure p_{lim} is assumed to act. An additional shear stress $\tau = \alpha_c s_u$ acts on the surface of the cone. For a 60° cone the tip resistance is expressed as:

$$q_c = p_{lim} + \sqrt{3}\alpha_c s_u \tag{9.5}$$

Using Tresca failure criteria, the limit pressure is expressed as (Vesic 1972):

$$p_{lim} = \frac{4}{3} s_u (1 + \ln(I_r)) + p_0 \tag{9.6}$$

where p_0 is the initial mean stress which can be estimated as $p_0 = (\sigma_{v0} + 2\sigma_{h0})/3$. Introducing Equations 9.5 and 9.6 into 9.4 the conventional cone factor assumes the expression:

$$N_c = 1.33 + 1.33 \ln(I_r) + \sqrt{3}\alpha_c - 0.33\Delta \tag{9.7}$$

Teh and Houlsby (1991) discussed several methods to estimate the cone factor using the **strain path method** with small-displacement finite-element analysis used to establish the final equilibrium stress field. Using the von Mises failure criteria they suggest the following equation:

$$N_c = 1.25 + 1.84 \ln(I_r) + 2\alpha_c - 2\Delta \tag{9.8}$$

Lu et al. (2004) applied the Remeshing and Interpolation Technique combined with Small Strain (**RITSS**) proposed by Hu and Randolph (1998) with nodal force interface elements and the Tresca failure criteria. The proposed equation for the

Method	Reference	I_r	α_c	Δ	N_c
ALE	van den Berg (1994)	100.7	0	0	10.9
		100.7	0.5	0	12.2
		100.7	1.0	0	12.9
MPM	Beuth (2012)	101	0	0	10.9
		101	0.5	0	11.8
		101	1.0	0	13.4
CEL	Qiu (2014)	100	0	0	10.8

Table 9.1: Estimated cone factors with several numerical methods

cone factor is:

$$N_c = 3.4 + 1.6\ln(I_r) + 1.3\alpha_c - 1.9\Delta \tag{9.9}$$

van den Berg (1994) adopted the **ALE** method with 4-noded interface elements at the soil-cone contact. He carried out undrained total stress anayses with Tresca material model. He considered the effects of the soil stiffness, the roughness of the cone and the initial stress state.

Beuth (2012) used the implicit **quasi-static MPM** formulation with 3-noded triangular interface elements to perform undrained total and effective stress analysis of cone penetration. His results are in good agreement with those of van den Berg (1994) and Lu et al. (2004). This study represent an important reference for this thesis in which the dynamic MPM formulation with explicit time integration scheme and Bardenhagen's contact algorithm is applied in the same field.

The **CEL method** demonstrates to be able to simulate geotechnical problems involving large deformations (Qiu et al. 2011). It has been applied for cone penetration in clay by Qiu (2014). Table 9.1 summarizes the estimated cone factors for $I_r \approx 100$ obtained by the ALE, the CLE methods and the quasi-static MPM.

9.2.2 Effect of drainage conditions

During cone penetration at the standard rate, drained and undrained conditions prevail for clean sand and pure clay, respectively. For soils consisting of mixtures of silt, sand, and clay, cone penetration may take place under partially drained conditions depending on the ratios of these three broad particle size groups. However, the fact that the penetration rate affects the value of cone penetration resistance for these soils was not taken into account at the time the standards were prepared for

the CPT. This means that the use of correlations developed for sand, in which tests would be drained, or clay in which tests would be undrained, will not work for soils in which the penetration at the standard rate takes place under partially drained conditions.

If the penetration rate is relatively low compared to the pressure dissipation rate, the soil ahead of the advancing cone consolidates during penetration, thereby developing larger shear strength and stiffness than it would have under undrained conditions. The closer the conditions are to fully drained during penetration, the higher the value of q_c.

Another physical process that play a role for soils with large clay content for penetration under undrained conditions, is the effect of the rate of loading on shear strength (viscosity effect). The higher the penetration rate is, the larger the undrained shear strength is, and the larger the tip resistance is. These two physical processes, i.e. drainage and loading rate effects, have opposite effects on q_c (Kim et al. 2008).

A normalized penetration rate has been introduced by Finnie and Randolph (1994):

$$V = \frac{vD}{c_v} \tag{9.10}$$

where v = penetration rate, D = penetrometer diameter and c_v = consolidation coefficient. It has been proved that it is able to characterize the degree of partial consolidation during penetration. However, for very high penetration rate, if strain-rate effect are significant, q_c increases with v and it is shown to be a function of v/D (Chung et al. 2006, Lehane et al. 2009). In this chapter attention is focused on the effect of the drainage conditions; since strain rate effects are neglected, V is an appropriate parameter to normalize the results.

The research on the effect of penetration rate on the tip resistance comprises numerous experimental data obtained with laboratory tests, such as centrifuge and calibration chamber tests, and in situ tests (House et al. 2001, Randolph and Hope 2004, Schneider et al. 2007, Kim et al. 2008, Lehane et al. 2009, Jaeger et al. 2010, Oliveira et al. 2011). Centrifuge tests are mainly performed on kaolin clay (House et al. 2001, Randolph and Hope 2004, Schneider et al. 2007), however different type of soil such as natural clay (Chung et al. 2006), mixture of sand and kaolin (Kim et al. 2008, Jaeger et al. 2010), sand and bentonite (Schneider et al. 2007) and silt (Oliveira et al. 2011) have been considered. Most of the tests have been performed on normally consolidated soil; the effect of overconsolidation has been investigated by Schneider et al. (2007) and Lehane et al. (2009). Different shape of

the penetrometer has been used, such as T-bar, ball, plate and cone.

Experimental evidence shows that a typical backbone curve can be drown in the $q_c - \log(V)$ plane. The cone resistance is constant for high values of V, i.e. undrained conditions, as well as low values of V, i.e. drained conditions. The range of partially drained conditions highly depends on the penetrometer and soil characteristic. According to the literature, the transition to fully drained conditions lies between 0.01 and 4; the transition to fully undrained conditions lies in the range 10-100. Differences can also be attributed to the method used to estimate c_v by the different authors. Since the water flow is mainly horizontal, the c_h is adopted in a few publications; this choice seems reasonable, but sometimes difficult to put in practice especially in laboratory tests.

The tip resistance q is usually normalized by a reference penetration resistance q_{ref}; q/q_{ref} is called normalized resistance or resistance ratio. Data can be interpolated by a function of the form:

$$\frac{q}{q_{ref}} = a + \frac{b}{1 + cV^m} \tag{9.11}$$

where a, b, c and m are constants that need to be calibrated. Usually q_{ref} is the value corresponding to the fully undrained penetration. In many publications the results are presented referring to the net tip resistance $q_{net} = q_c - \sigma_{v0}$, however also the total tip resistance can be adopted. In this thesis normalized results are presented in terms of net tip resistance and undrained net tip resistance, i.e. $q = q_{net}$ and $q_{ref} = (q_{net})_{undrained}$.

The values assumed by the constants in Equation 9.11 depend on the penetrometer shape and the type of soil. They seem to vary in a relatively narrow range for the test performed on kaolin, while results differ for other types of soil. The sum $a + b$ assumes the meaning of the resistance ratio between drained and undrained conditions $q_{drained}/q_{ref}$. As can be deduced from Figure 9.4, the parameter c modifies the inflection point of the curve, while m influences the curvature.

An alternative expression for the backbone curve has been proposed by Oliveira et al. (2011), in which a physical meaning can be given to the constants. However, Equation 9.11 is preferred because it is more popular in the literature.

Only a few authors addressed the problem with numerical techniques (Silva et al. 2006, Yi et al. 2012). In his PhD thesis, Silva (2005) studied the effect of penetration rate and OCR on the tip resistance and pore pressure dissipation using a coupled cavity expansion-finite element method. In this method, only radial soil deformations and water flow are considered, i.e. the bidimensional penetration process

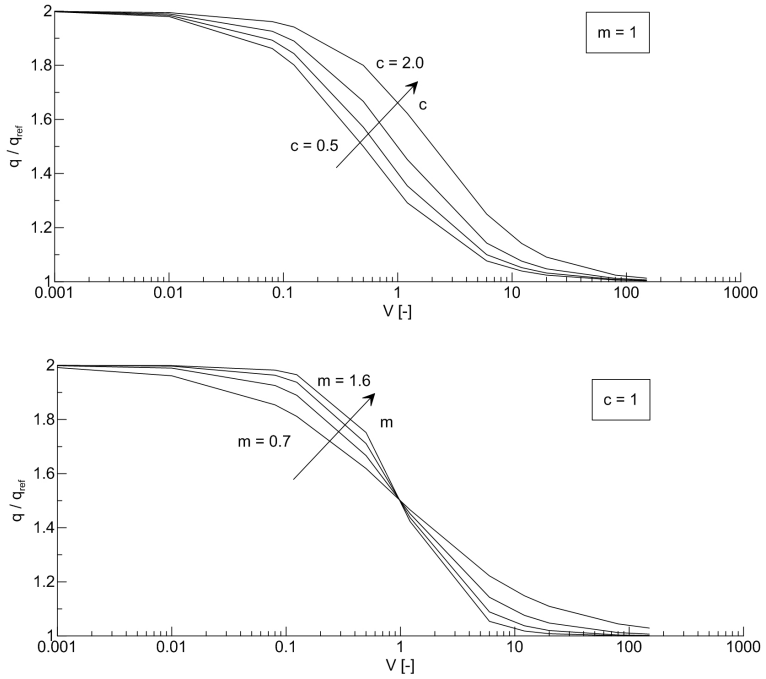

Figure 9.4: Effect of parameters c and m on the curves given by Eq. 9.11 ($a = b = 1$).

is simulated in a simplified way neglecting axial soil deformation.

The soil is modeled with the Modified Cam Clay model and the tip resistance is calculated with

$$q_c = \sigma_r + \frac{\mu}{\tan\alpha}\sigma'_r \tag{9.12}$$

where σ_r and σ'_r are the total and effective radial stress from the cavity expansion solution, respectively; μ = interface friction, and α = angle of the cone tip. The friction coefficient at cone surface is assumed equal to the tangent of the soil friction angle, i.e. $\mu = \tan(\phi)$.

Silva (2005) normalized the results using the horizontal consolidation coefficient, estimated with:

$$c_h = \frac{k(1+e)\sigma'_r}{\lambda\gamma_w} \tag{9.13}$$

where k is the Darcy's permeability, λ is the virgin compression index, e and σ'_r are the void ratio and the horizontal effective stress of the soil adjacent to the cone immediately after cavity expansion. The author pointed out that the experimental c_v values are comparable to the computed c_h (Eq. 9.13) under undrained conditions. However, the values of c_h increase in magnitude as consolidation during penetration is allowed due to greater change in values of σ'_r at low speeds. This affects the shape of the backbone curve.

He considered OCR values ranging from 1 to 32 showing that, for a given undrained

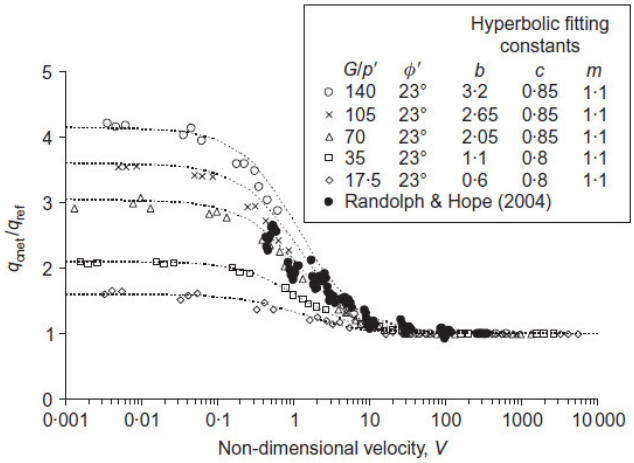

Figure 9.5: Resistance ratio against normalized penetration velocity for various modulus ratio G/p' according to Yi et al. (2012)

shear strenght, OCR influences the generation of excess pore pressure in undrained conditions; higher pressures are observed with lower OCR. However, the normalized pore pressure $\Delta u_{max}/\Delta u_{ref}$ (Δu_{max} = maximum excess pore pressure, Δu_{ref} = excess pore pressure for undrained conditions) is not influenced by the OCR and only a slight effect on the resistance ratio is observed.

Yi et al. (2012) used the updated Lagrangian FEM with logarithmic strain to study the effect of partial consolidation during cone penetration on the tip resistance and excess pore pressure. The influence of soil strength and stiffness on the backbone curve is investigated. The soil behavior is characterized by the Drucker-Prager model; further analyses included the effect of volumetric yielding by using the modified Drucker-Prager cap model. The soil-cone contact is assumed to be smooth since numerical difficulties were encountered introducing friction at the interface. This method suffers of problem of mesh distortion in the cone vicinity, which are controlled by modifying the mesh density and the element aspect ratio through a trial-and-error process.

This publication shows how the net cone resistance increases with the modulus ratio (G/p', p' = mean effective stress) and the friction angle in the whole range of drainage conditions. On the other hand, the resistance ratio q_{net}/q_{ref} increases only with the modulus ratio and is relatively insensitive to the friction angle (Fig. 9.5). Considering the volumetric yielding, the resistance ratio reduces as λ/κ increases; for λ/κ between 3 and 5, as common in clay, the reduction is between 5% and 15%.

DeJong and Randolph (2012) analyzed the effect of drainage conditions considering published experimental data and numerical parametric studies. This study

addressed the determination of soil behavior type by mean of the charts proposed by Robertson (1990) and Schneider et al. (2008a). These charts, widely used in engineering practice, were developed for standard rate of penetration. DeJong and Randolph (2012) showed that they should not be used for $v \neq 2cm/s$ since the effect of drainage conditions shifts the data in a different chart area, corresponding to an inappropriate soil type.

From this literature review it can be concluded that the cone penetration in partially drained conditions is a complex process which has been mainly studied experimentally. Numerical simulations with cavity expansion theory (Silva et al. 2006) and FEM (Yi et al. 2012) give an interesting contribution in the comprehension of the main features of the phenomenon, even though they have some limitations and drawbacks as previously discussed.

The lack of advanced numerical simulations of cone penetration in partially drained conditions, together with the importance of a better understanding of the phenomenon for the engineering practice, form the motivation of the present study, in which the two-phase MPM with contact algorithm is applied to the study of CPT in different drainage conditions.

9.3 How to simulate CPT?

This section discusses the most important features that a numerical model should have to simulate the cone penetration and how they are considered in this study. As already pointed out in Chapter 2, a model is an appropriate simplification of reality, which means that only the essential features of the real process must be included.

During cone penetration, the soil initially located underneath the tip is pushed aside; this obviously generates large deformations. The numerical model has to take this into account. As already shown in previous chapters of this thesis, the MPM is well suited to simulate large deformations, therefore the study of the cone penetration process represents an interesting application of the method.

The attention of this study is focused on the cone tip resistance which is calculated with:

$$q_c = \frac{\sum_{i=1}^{n_c} F_{i,y}}{A} \tag{9.14}$$

where the numerator is the sum of the vertical reaction forces $F_{i,y}$ at the n_c nodes belonging to the cone tip and A is the area of the cone slice which is considered

in the model. Considering a soil element connected to the cone, the reaction force consists in:

$$\boldsymbol{F} = \int_V \boldsymbol{B}^T \boldsymbol{\sigma} dV \tag{9.15}$$

where V is the element volume and $\boldsymbol{\sigma}$ is the total stress.

One of the most difficult issue is the proper simulation of the saturated soil behavior. On one hand the soil-water interaction must be included. On the other hand, the constitutive model must be capable to describe the response of the soil under loading conditions in a good enough way for the considered problem.

As already discussed in Section 3.5 in undrained and drained conditions the soil-water interaction can be handled in a simplified way by using the one-phase approach (Chap. 3). In partially drained conditions a fully coupled two-phase approach must be applied (Chap. 4).

Constitutive modeling of the real soil behavior is challenging because several factors such as non-linear compressibility, stress-path dependency of shear strength, anisotropy, internal structure, viscosity and so on should be considered. In engineering practice very simple models, such as Tresca and Mohr-Coulomb, are often applied. They can give only a crude representation of the soil mechanical response, but they are easy to use and can give a first idea of the main features of the problem. Very advanced constitutive models are able to capture several characteristics of soil behavior, but a certain level of complexity is added to the numerical model and the input parameters may be not easy to calibrate. The choice of the constitutive model should guarantee a realistic simulation of the considered problem with an acceptable level of complexity.

The purpose of this chapter is to simulate cone penetration in clay, therefore the material model must be selected between those which demonstrated to be suitable for this type of soil. The undrained behavior of clay is very often modeled with the elastic perfectly plastic model with Tresca failure criteria (Sec. 5.2.1). This very simple model does not consider the stress path dependency of the shear strength, neither the non-linear elastic response of the material, but has been successfully used to simulate CPT in undrained conditions, see e.g. van den Berg (1994), Lu et al. (2004) and Beuth et al. (2008).

The Modified Cam Clay model (Schofield and Wroth 1968) has been widely used to model soft clay both in drained and undrained conditions. It can take into account the non-linear soil compressibility, the occurance of shear and volumetric deformations during yielding and the stress-path dependency of the shear strength.

This model is easy to use as the calibration of its material parameters with standard laboratory tests is quite simple. Silva et al. (2006) used this material model to simulate cone penetration considering the effect of partial drainage with the cavity expansion method. In this study MCC is used to simulate CPT in the whole range of drainage conditions. Anisotropy, strain-rate effects and other properties of the real soil behavior can be considered with more advanced constitutive models, but this exceed the purpose of this thesis.

As commonly founded in many geotechnical problems, CPT involves soil-structure interaction. The problem can be solved in different ways; here the contact formulation presented in Section 6.4 is used. This algorithm was originally developed for the frictional contact in the MPM by Bardenhagen et al. (2001) and has been extended to the adhesive contact in the frame of this thesis, following the procedure suggested by Al-Kafaji (2013).

The adhesive contact, i.e. the maximum tangential force is independent of the normal contact force, is well suited to simulate the soil-structure interaction in case of cohesive materials in undrained condition. In this case, indeed, the maximum tangential force at the interface is bounded by the soil undrained shear strength. This type of contact is applied in Section 9.4 to reproduce the roughness of the cone when the constitutive behavior is described by Tresca material model. The frictional contact, i.e. the maximum tangential contact force is proportional to the normal force, is used when the soil is modeled with the modified Cam Clay model.

In addition to this, the geometry and the discretization of the numerical model must be defined, together with the calibration of some purely numerical parameters such as the Courant number C (Eq. 3.37) and the local damping factor α (Sec. 6.2.2). To improve computational efficiency the mass scaling procedure (Sec. 6.3) can be used and the mass scaling factor β must be calibrated. Preliminary calculations are needed to define these features of the numerical model.

9.4 Undrained analyses with Tresca material model

9.4.1 Preliminary analyses

Preliminary calculations are performed in order to investigate the effect of the mass scaling factor, the damping factor, the Courant number, and the optimal dimensions of the discretized domain. A detailed description of the performed test calculations is provided in this section supporting the choices adopted for the final analyses.

9.4.1.1 Shallow penetration

In order to define the effect of the Courant number, the damping factor and the mass scaling factor, a shallow penetration of 2 cone diameters is simulated.

The standard CPT device possesses a discontinuous edge at the base of the cone. At this location, boundary conditions are not uniquely defined. In order to circumvent numerical problems, the cone is slightly rounded (Beuth 2012). Apart from this modification, the dimensions of the penetrometer correspond to those of a standard penetrometer: the apex angle is 60° and the diameter (D) is $3.56cm$, which results in an horizontal base area of $10cm^2$. Taking advantage of the symmetry of the problem, only a sector of 20° is considered. The soil domain has a height of $0.22m$ and a width of $0.14m$, corresponding to 6.2 and 4 cone diameter respectively. The mesh counts 5324 tetrahedral elements and 40606 MP. 20 MP are placed inside each element in the vicinity of the cone, while only 10 or 4 MP fill the elements far away from the cone.

Displacements are constrained in normal direction at the lateral surfaces, while the bottom of the mesh is fully fixed. The application of a roller boundary condition at the tip of the cone, together with the use of the contact algorithm, leads do numerical difficulties. Allowing the cone apex to be free, results improve considerably; this has been already observed by Al-Kafaji (2013) during MPM simulation of pile driving.

The moving mesh concept (Sec. 6.5) is applied. The computational domain is divided into a moving mesh and a compressing mesh zone as illustrated in Figure 9.7. The moving mesh is attached to the cone, i.e., this zone moves with the same displacement of the cone. The elements of this zone keep the same shape throughout the computations; on the contrary the elements of the compressing mesh zone are compressed during the computation.

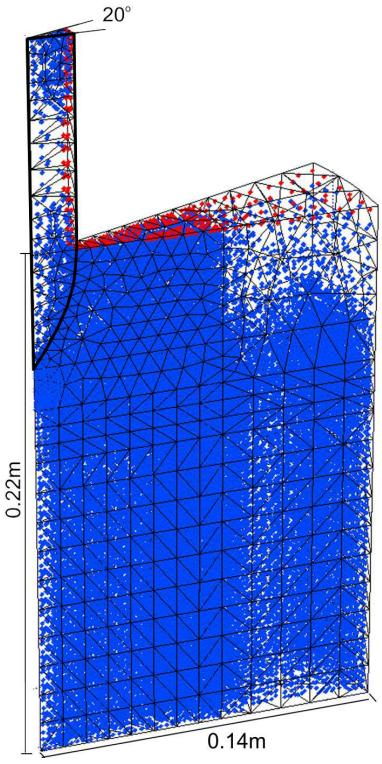

Figure 9.6: Geometry and discretization for the shallow penetration.

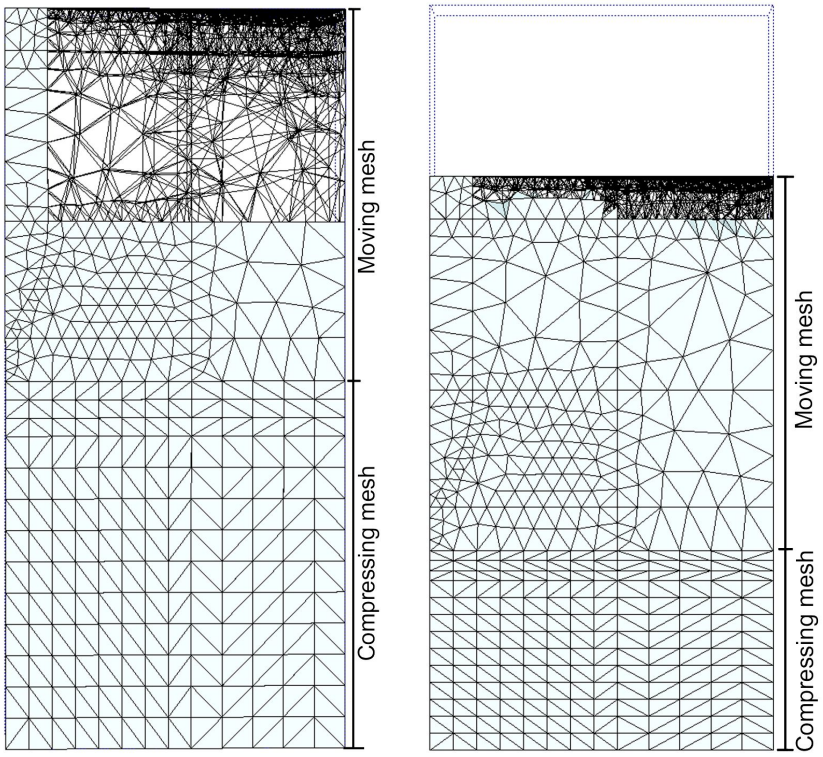

(a) (b)

Figure 9.7: Illustration of the moving mesh procedure applied to the cone penetration problem. (a) initial configuration, (b) deformed configuration

Thanks of this procedure, the fine mesh is always kept around the cone and the occurrence of elements having cone and soil particles is avoided. Moreover, the need of identifying the new soil-structure interface during the computation is eliminated as the interface nodes coincide with the geometry of the cone throughout the computation. As a consequence, the unit normal vectors, which are required in the contact algorithm, do not change and hence the inaccuracy of recomputing them is eliminated (Al-Kafaji 2013).

Because of the downwards movement of the moving mesh zone, a region with initially empty elements is required above the soil surface to accommodate the material during computations. The elements of the compressed zone must have a reasonable aspect ratio (vertical to radial dimensions) in the initial configuration to avoid excessive mesh distortion after considerable penetration.

In this preliminary study the penetration of the cone in soft clay under undrained conditions is simulated. The soil is considered as a weightless material, modeled with the elastic perfectly plastic model with Tresca failure criteria. The Young's modulus is $E_u = 6000kPa$, the Poisson ratio is $\nu_u = 0.49$ and the undrained shear strength is $s_u = 20kPa$.

The cone penetrates at a rate of $2cm/s$, this means that it's a slow process; indeed it has been well simulated by quasi-static numerical formualtions (Beuth 2012). In simulations of slow processes, mass scaling can be used to improve efficiency. The original soil density is $\rho_{sat} = 1700g/cm^3$, but can be increased by the factor β, speeding up the calculation by a factor $\sqrt{\beta}$. Figure 9.8 shows the tip stress over the normalized cone displacement for several values of the mass scaling factor. Extremely high values of β generate high oscillations, especially at the beginning of the calculation, when dynamic effects are more relevant, together with an overestimation of q_c. A mass scaling factor equal to 400 is considered reasonable for this problem.

Natural materials normally dissipate a certain amount of energy, however the constitutive model often does not take this into account. The introduction of the local damping allows to dissipate dynamic waves that generate noise in the numerical solution (Sec. 6.2.2); on the other hand the damping factor α should not be too large in order to avoid overestimation of the tip stress (Fig. 9.9). A value of $\alpha = 0.15$ is considered optimal for the considered problem.

In CPT simulation, energy conservation is not an issue, therefore a Courant number C close to 1 can be used. As shown in Figure 9.10 a reduction of C does not improve

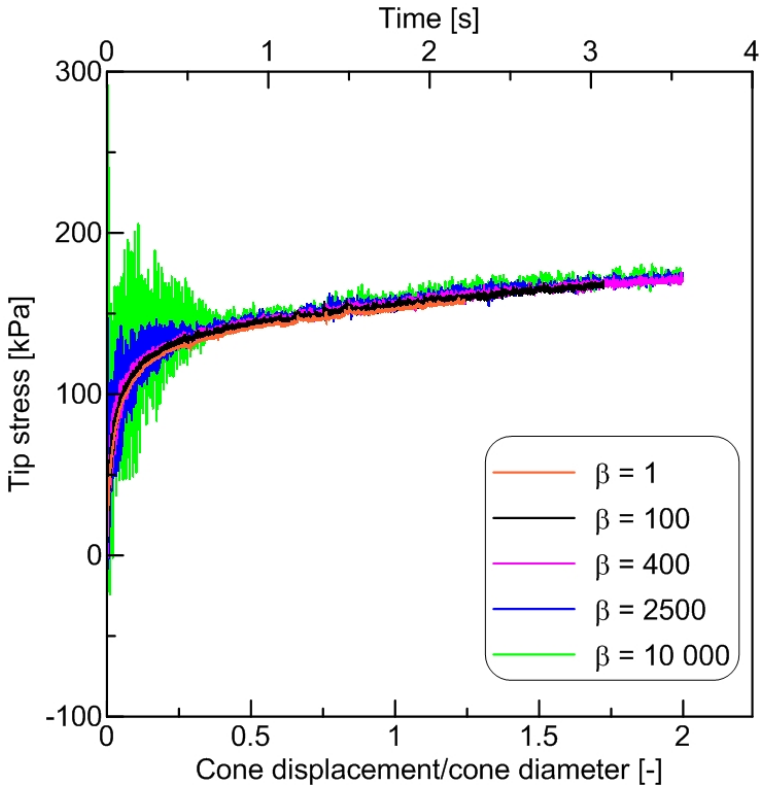

Figure 9.8: Effect of mass scaling.

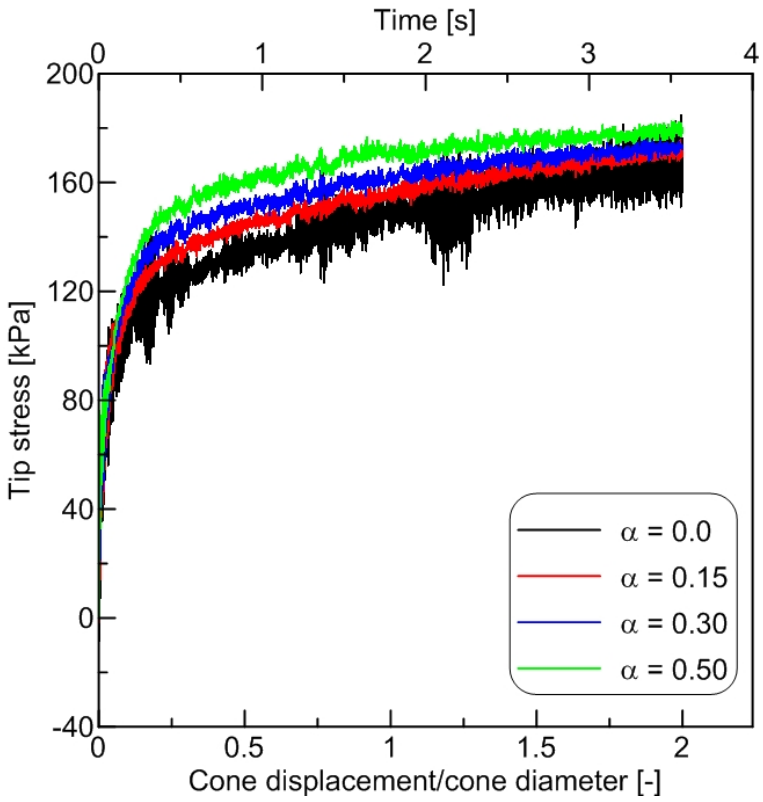

Figure 9.9: Effect of local damping factor.

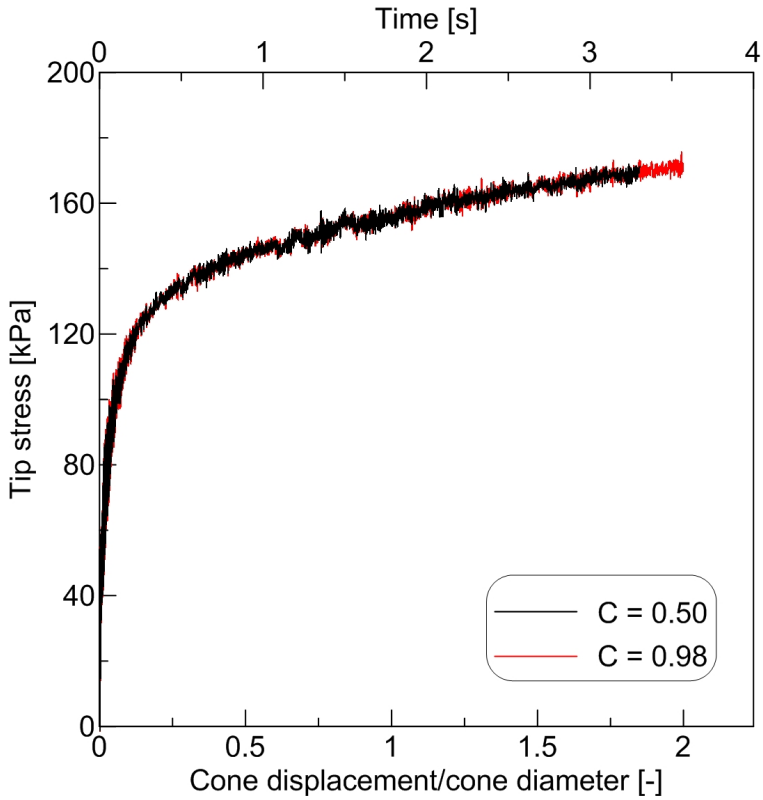

Figure 9.10: Effect of the Courant number.

significantly the result.

A large number of MP in the vicinity of the cone permits to have nice results without increasing dramatically the computational cost. Oscillations can be further reduced by refining the mesh; this results in high computational effort and is not considered necessary for the scope of this study. In general the accurancy and the computational cost increase more with the mesh refinement than with the number of MP.

9.4.1.2 Deep penetration

In the current section the definition of the optimal geometry to simulate a deep penetration of the cone is discussed. Beuth (2012) observed that the steady state solution is approximately reached after 6D penetration, therefore the domain should be big enough to accommodate approximately a penetration of 10D without observing any boundary effect.

From numerical analyses the radius of the plastic zone is shown to depend on the soil rigidity index I_r, the initial stress state Δ and secondly by the roughness of the cone

α_c (Lu et al. 2004). From cylindrical cavity expansion theory the plastic zone has a radius of about $0.75\sqrt{I_r}D$ which, for the current problem ($I_r = 101$), corresponds to $7.5D$. Lu et al. (2004) observed that the plastic zone extends approximately $5D$ from the symmetry axis in horizontal direction, and $6D$ from the barycenter of the cone in vertical direction. Larger domain radius has been used by Beuth (2012) ($14D$) and van den Berg (1994) ($20 - 25D$).

Very wide domains simulate better the free field conditions, but they increase the computational cost, therefore they are inapplicable to a series of parametric calculations. Here the geometry is chosen in such a way that no significant effect on the tip resistance is observed increasing the domain size.

The considered mesh extends $14D$ below the tip at the beginning of the computation. Three different domain radius (R) have been considered: $4D$, $6D$ and $8D$. Figure 9.11 shows the tip stress curve for these values of R in case of $\Delta = 0$ and $\alpha_c = 0$. A mesh radius of $4D$ results to be too small, indeed a different value of tip resistance is observed if a larger domain is considered. Minor effect is observed increasing the domain radius from $6D$ to $8D$. Similar calculations have been performed including the roughness of the cone finding the same conclusions.

Figure 9.12 shows the deviatoric stress q at the end of the simulation. It can be observed that in case of $R = 6D$ the plastic region hits the boundary, however this seems to have a negligible effect on the total tip resistance.

Results are also affected by the mesh refinement. The use of a very fine mesh around the cone reduces the oscillations of the tip stress, especially with increasing cone roughness, but this increases the computational time too. The discretization has been chosen as a compromise between accuracy and computational cost.

9.4.2 Results

This section presents the results of cone penetration in undrained conditions, in which the soil is modeled with the elastoplastic model with Tresca failure criteria. As already mentioned in Section 9.4.1, only 20° of the axisymmetric problem are simulated and the moving mesh approach is applied. The geometry and discretization of the problem has been determined through preliminary calculations (Sec. 9.4.1.2). The domain extends $0.214m$ in horizontal direction and the bottom boundary initially lays at $0.500m$ below the cone tip. The mesh counts 13221 tetrahedral elements and 105634 MP (Fig. 9.13). Roller boundary conditions are applied

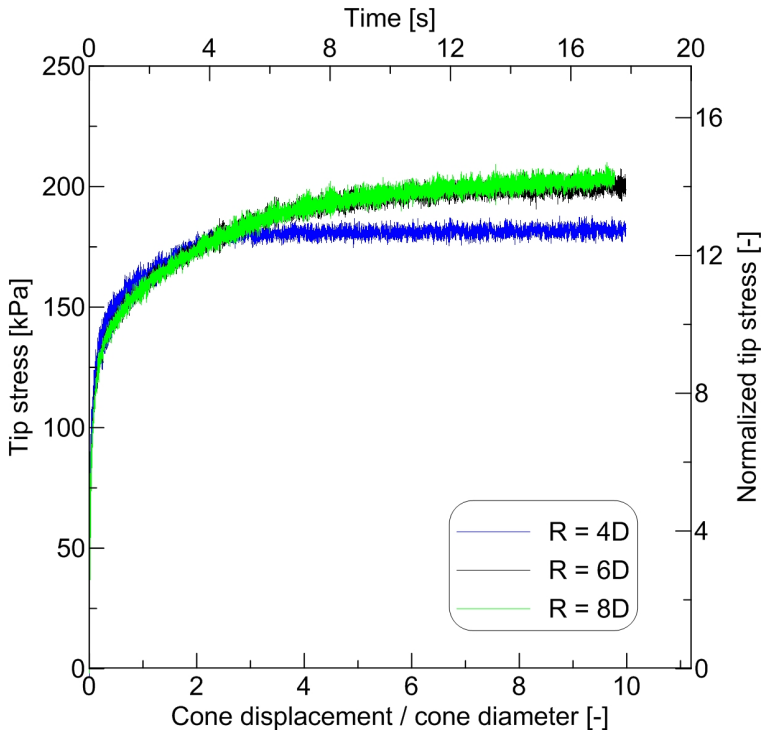

Figure 9.11: Effect of the domain radius for undrained penetration with $I_r = 101$, $\Delta = 0$ and $\alpha_c = 0$.

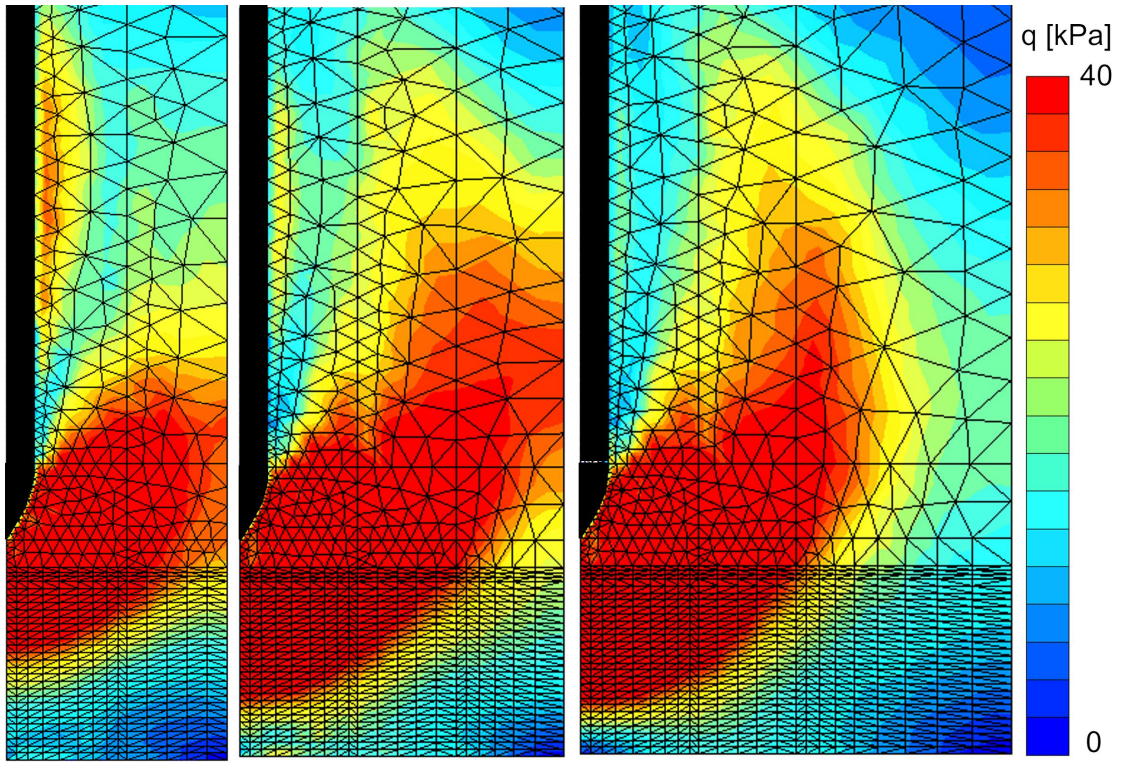

(a) R = 4D (b) R = 6D (c) R = 8D

Figure 9.12: Deviatoric stress q after 10D penetration for different size of the mesh.

Material property	Symbol	Value
Young's modulus [kPa]	E'	5033
Effective poisson ratio [-]	ν'	0.25
Porosity [-]	n	0.3
Bulk modulus of water [kPa]	K_w	28987
Undrained shear stregth [kPa]	s_u	20

(a) Effective stress analysis

Material property	Symbol	Value
Young's modulus [kPa]	E_u	6000
Undrained poisson ratio [-]	ν_u	0.49
Undrained shear stregth [kPa]	s_u	20

(b) TotalStress analysis

Table 9.2: Material properties used in CPT analyses with Tresca material model

at the boundaries; but the cone tip is free to avoid numerical problems.

The soil is simulated as a weightless material and the vertical and horizontal stresses are initially null; indeed the gradient of the vertical effective stress is negligible compared to the stress level developed during the penetration.

The one-phase MPM formulation is used for this set of calculations. The simulations can be performed with the total stress analyses or with the effective stress analyses; the latter allows the estimation of the pore pressure, however they give identical results in term of total tip resistance. The material properties are summarized in Table 9.2; the problem is characterized by a rigidity index of 101.

To reduce the dynamic effects a local damping factor of 0.15 is used. The mass scaling procedure is adopted with $\beta = 400$ in order to increase computational efficiency.

The roughness of the cone is taken into account assigning a non-zero value of the adhesion a at the contact surface. Figure 9.14 shows the tip stress as function of the normalized penetration for different cone roughness. It can be noted that the steady state solution, which corresponds to the tip resistance q_c, is reached after about $7D$ of penetration independently of α_c. The tip resistance increases with the cone roughness.

The cone factor varies between 10.2, for smooth cone, and 15.8, for very rough cone. According to Potyondy (1961), the cone roughness α_c for steel is comprises between 0.25 and 0.5. The MPM results are in agreement with the measurements obtained with calibration chamber tests by Kurup et al. (1994), who found a cone factor

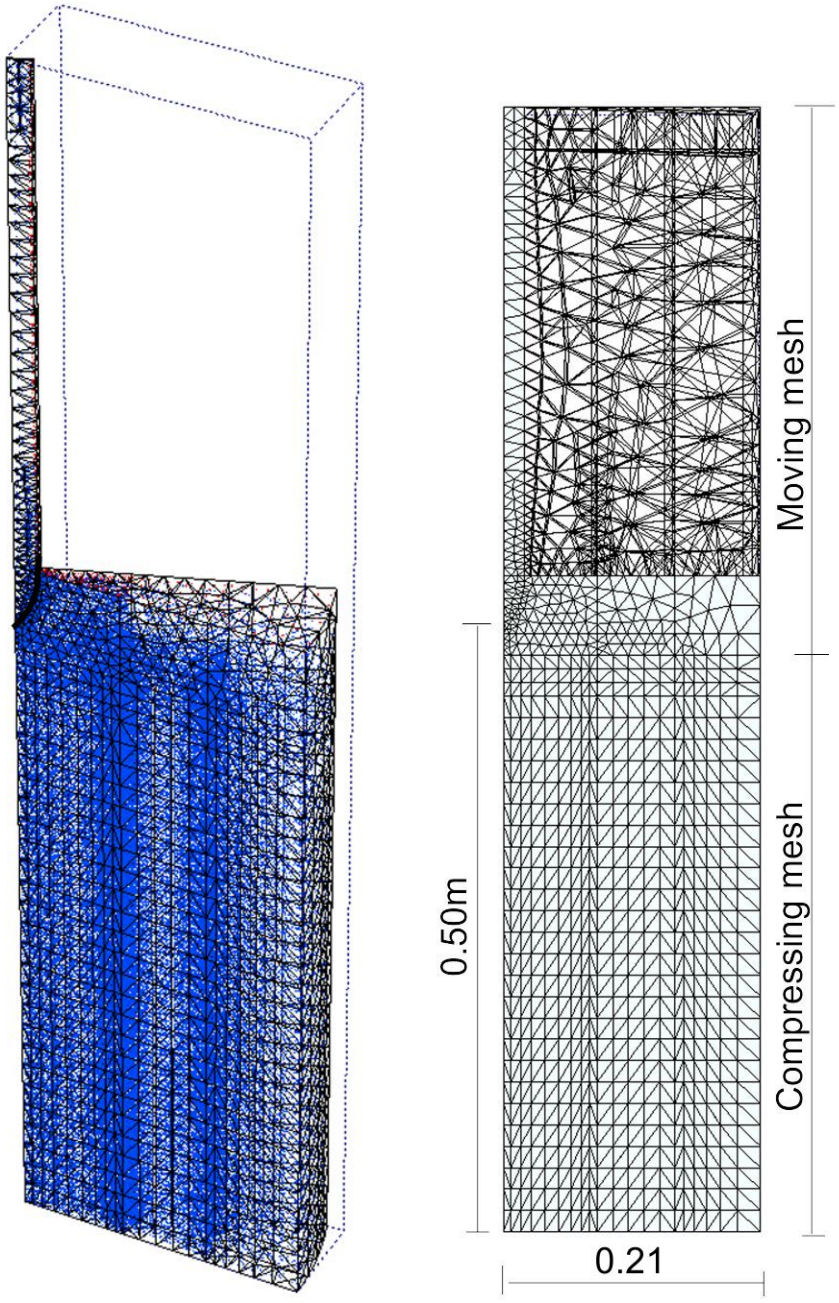

(a) MP discretization (b) Connectivity plot

Figure 9.13: Geometry and discretization for CPT simulation in undrained conditions with Tresca model.

$N_c = 13$ for a rigidity index $I_r = 100$.

Figure 9.15 compares the cone factors N_c obtained in this study with the estimates relative to different analytical methods for three values of α_c. The estimated cone factor for smooth cone is in very good agreement with previous studies, but an overestimation of N_c is observed for increasing cone roughness. Moreover, in contrast with theoretical expectations N_c appears to be a non linear function of α_c. This may be possibly caused by the contact formulation. Indeed, Ma et al. (2014) observed that the Bardenhagen's algorithm generates oscillations and an overestimation of the contact forces especially when bodies with very different compressibility are involved. Future developments of the research will investigate this problem.

Figure 9.16 plots the principal stress direction for smooth and rough contact; as expected they are parallel to the cone surface in case of $\alpha_c = 0$ and rotated by 45° in case of $\alpha_c = 1$.

During cone penetration the soil below the cone is compacted vertically and laterally (Fig. 9.17). When a body penetrates into a low permeability clay, there is minimal migration of pore water within the surrounding soil mass and, hence, the volume displaced during penetration must be accommodated by undrained shear deformations. It is well established that the pile penetration causes heave at the ground surface (e.g. Hagerty and Peck 1971). Heave is indeed observed during cone penetration as shown in Figure 9.17b.

Performing undrained effective stress analyses the pore pressure and the effective stresses can be computed separately. Since the bulk modulus of the water is much higher than the bulk modulus of the soil skeleton, the pore pressure p_w is much higher than the mean effective stress p'. This can be visualized comparing Figure 9.18 and Figure 9.19 which show p_w and p' for the smooth and rough contact. As expected stresses are higher in case of rough contact.

As observed by Beuth (2012), the use of lower values of K_w, i.e. lower undrained Poisson's ratios, leads to slightly lower cone resistances. On the contrary, a higher bulk modulus increases the oscillations and may give numerical problems. The input parameters of this study correspond to $\nu_u = 0.490$, which is considered a reasonable approximation of the clay's incompressibility in undrained conditions.

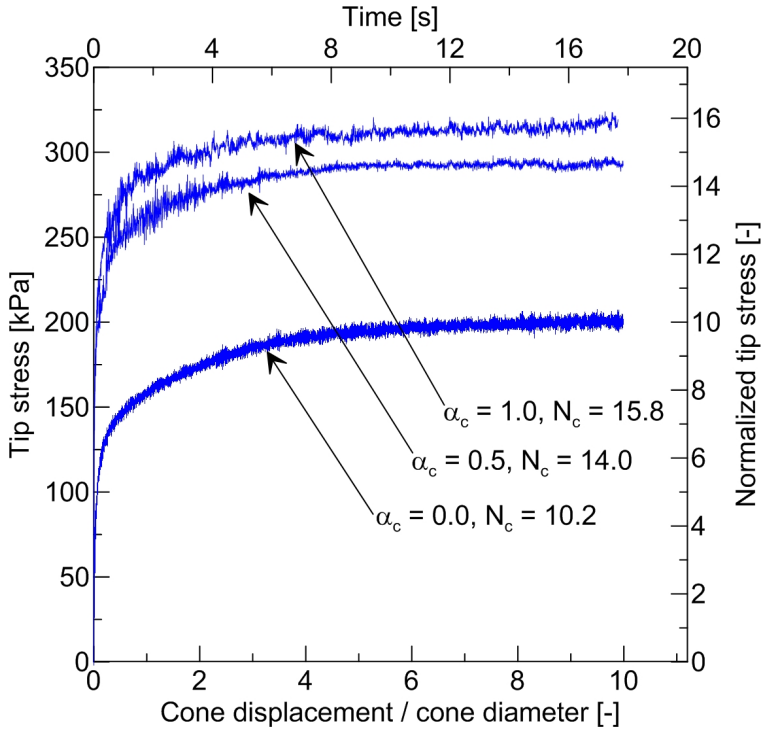

Figure 9.14: Effect of cone roughness for undrained penetration with $I_r = 101$, $\Delta = 0$.

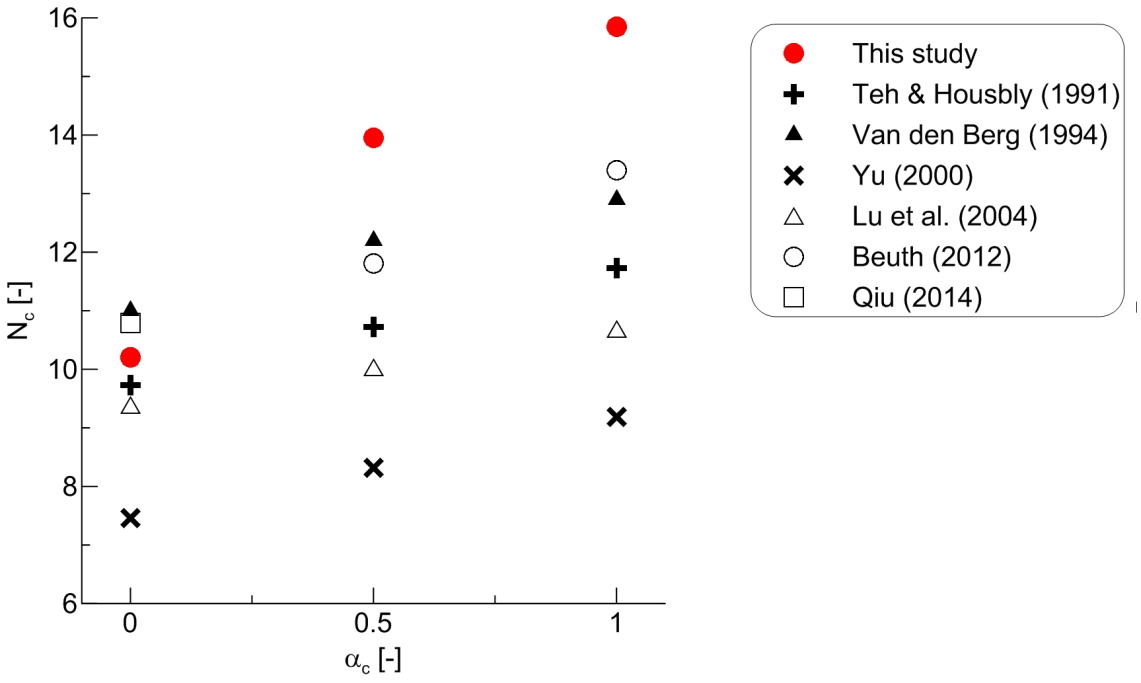

Figure 9.15: Estimated cone factor as function of cone roughness; comparison with literature results.

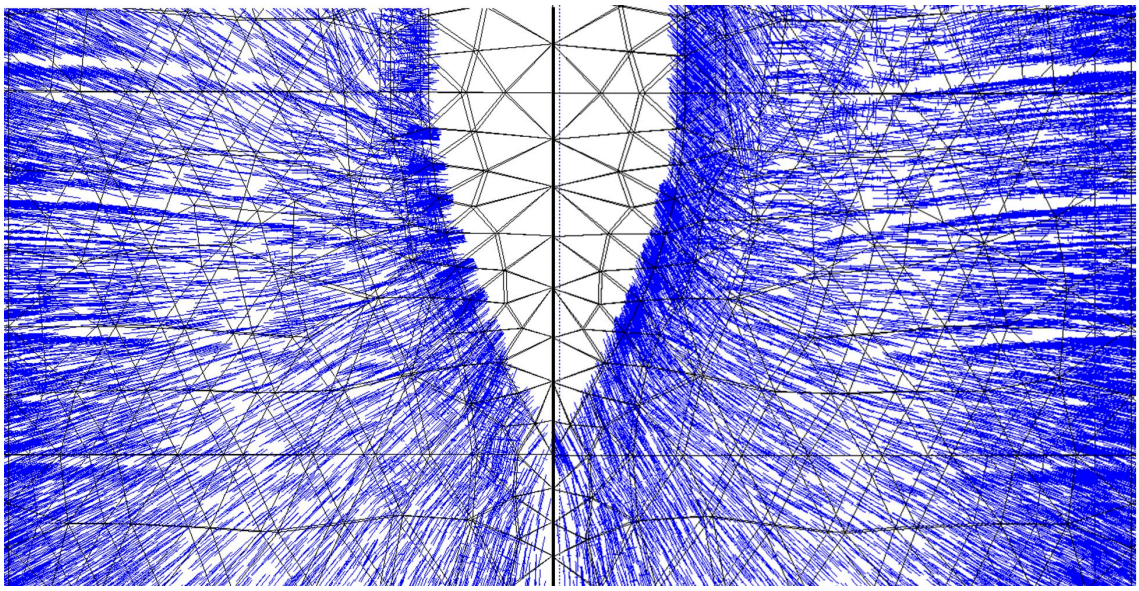

Figure 9.16: Principal stress direction around the cone in case of $\alpha_c = 0$ (left) and $\alpha_c = 1$ (right).

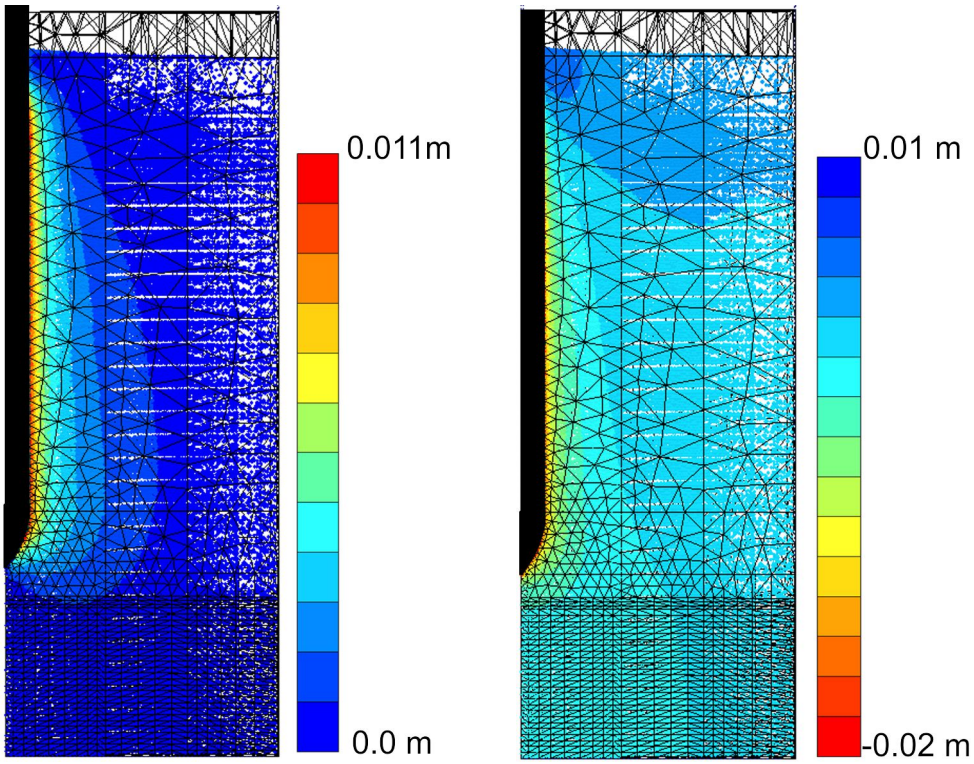

(a) u_x (b) u_y

Figure 9.17: Horizontal and vertical displacments for $\alpha_c = 0$.

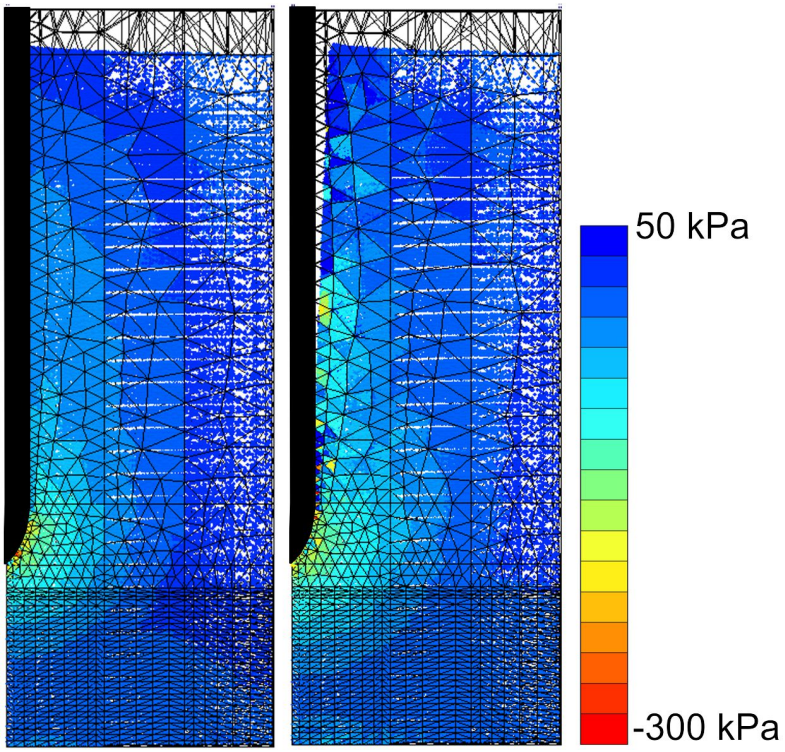

Figure 9.18: Excess pore pressure in case of $\alpha_c = 0$ (left) and $\alpha_c = 1$ (right).

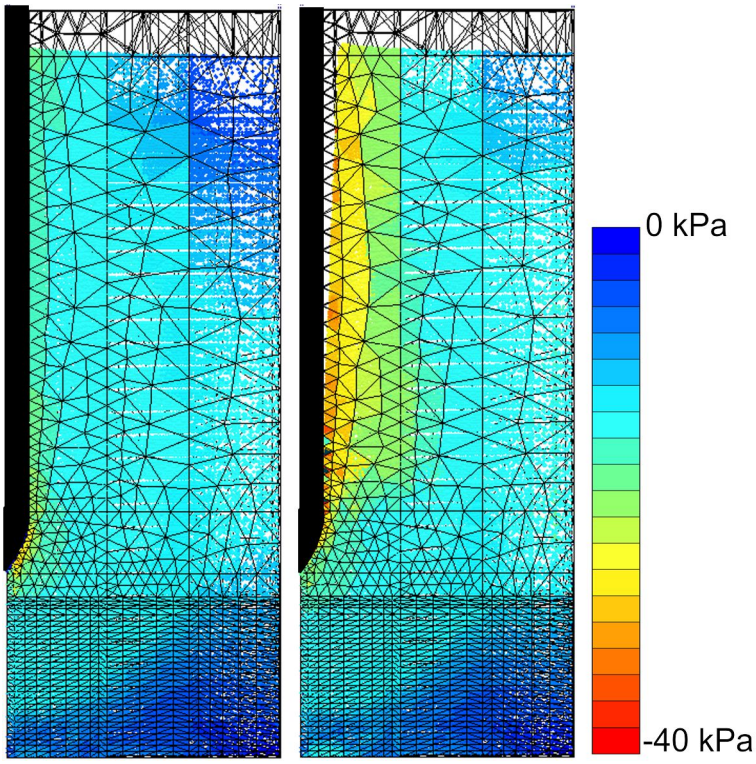

Figure 9.19: Mean effective stress case of $\alpha_c = 0$ (left) and $\alpha_c = 1$ (right).

9.5 Consideration of partially drained conditions with Modified Cam Clay Model

In this section the two-phase MPM with contact algorithm is applied to the study of the effect of the drainage conditions on the cone resistance. As mentioned in Section 9.2.2, advanced numerical simulations of CPT in partially drained conditions are rare in the literature, because of the high level of complexity of the problem. Previous numerical study focused on undrained conditions, see e.g. Qiu (2014), Beuth and Vermeer (2013), Lu et al. (2004), or drained conditions, see e.g. Kouretzis et al. (2014), Huang et al. (2004), Salgado (1997). Pore pressure dissipation during penetration was simulated with the cavity expansion theory by Silva et al. (2006) and the finite element method by Yi et al. (2012). The first considered only radial soil deformations and water flow, thus neglecting the bidimensional characteristics of the problem. The latter suffered of problems of mesh distortion and instability in case of frictional contact, thus neglecting the cone roughness.

The bidimensional large deformations induced in the soil by the advancing cone, as well as the bidimensional water flow, can be captured by the two-phase MPM. Moreover, the soil-cone contact and the non-linear behavior of soil are taken into account. To the author knowledge, this is a novelty in computational geomechanics.

Simple constitutive models such as Tresca and von Mises are acceptable to simulate the undrained behavior of clay. The Tresca model has been successfully used to simulate undrained cone penetration, see e.g. van den Berg (1994), Lu et al. (2004) and Beuth et al. (2008), but a more appropriate constitute model is required for partially drained and drained conditions.

A large number of constitutive models exists for different soils. To capture as many aspects of soil behaviour as possible, some of these are very sophisticated and involve a lot of parameters, which are often difficult to estimate. The Morh-Coulomb and the Drucker-Prager models are the most common in dry simulations of CPT; see e.g. Yu and Houlsby 1991, Salgado 1997, Susila and Hryciw 2003 and Huang et al. 2004. The latter has been also used for undrained and partially drained conditions by Yi et al. (2012). However, the undrained shear strength obtained with these models may be significantly overestimated for normally consolidated soils (Puzrin et al. 2010).

In this study, the soil behavior is simulated with the Modified Cam Clay model (MCC) (Schofield and Wroth 1968), which incorporates several of the most impor-

Material property	Symbol	Value
Virgin compression index [-]	λ	0.205
Recompression index [-]	κ	0.044
Effective poisson ratio [-]	ν'	0.25
Slope of CSL in p-q plane [-]	M	0.92
Initial void ratio [-]	e_0	1.41

Table 9.3: Material properties used in CPT analyses with MCC material model

tant non-linearity of real soil behaviour; moreover its input parameters are relatively easy to calibrate. The main features of the model are summarized in Section 5.2.3.

It is an elastoplastic-hardening model based on the critical state concept, i.e. it is assumed that the soil at large deformations reaches a well defined critical state condition and behaves as a frictional fluid. The critical state line (CSL) is unique for a given soil, regardless of the stress path used to bring the sample from any initial condition to the critical state and is identified by the Equations 5.17. The second of Equations 5.17 implies that the failure conditions is a generalization of the Drucker-Parger yielding condition and can be considered as an approximation of a Mohr-Coulomb surface with a particular critical state friction angle.

The model assumes logarithmic soil compressibility; the unloading-reloading lines in the $v - \ln(p')$ plane are characterized by the recompression index κ, while the normal compression line is characterized by λ.

The input parameters used for this study are listed in Table 9.3. This set of parameters is typical of Kaolin clay; such a material has been often used for laboratory tests, therefore allowing the comparison between the numerical and the experimental results. The bulk modulus of the water K_w is calculated by mean of Equation 3.69 assuming an undrained poisson ratio $\nu_u = 0.49$ and estimating the effective bulk modulus with Equation 5.20a.

Although the complete range of drainage conditions can be simulated with the two-phase formulation, drained and undrained conditions are simulated in a simplified way using the one-phase formulation. The two-phase formulation is, indeed, computationally more expensive than the one-phase, moreover a very small time step size is required with low values of the permeability in order to achieve the stability of the numerical scheme (Sec. 7.2.3).

The dependence upon the drainage conditions is taken into account through the

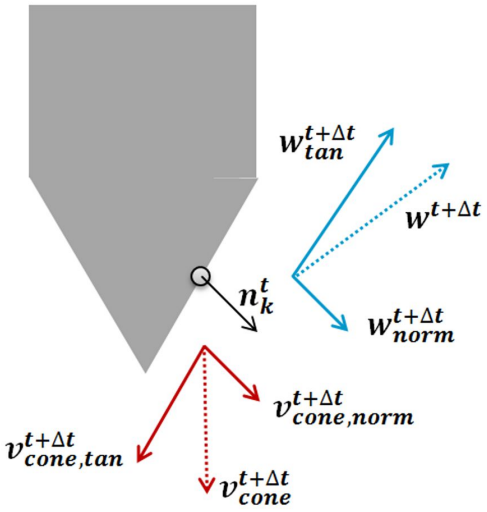

Figure 9.20: Schematic reppresentation of the correction for the water velocity at the contact.

normalized penetration rate V (Eq. 9.10), in which c_v can be estimated by:

$$c_v = \frac{k(1+e_0)\sigma'_{v0}}{\lambda\gamma_w} \tag{9.16}$$

where k is the Darcy's permeability and σ'_{v0} is the initial vertical effective stress (Schneider et al. 2007).

In the literature the variation of V is usually achieved by varying the penetration velocity v, on the contrary in this thesis it is obtained by changing the permeability k, while keeping $v = 0.02m/s$. This approach seems closer to what happens in the field, where D and v are standardized. Moreover, since a dynamic code is used, modifying the penetration velocity requires new calibration of the Courant number, the mass scaling factor and the damping factor.

In the two-phase calculations, additional care is required to solve the soil-cone contact. Immediately after solving the momentum equation for the fluid (Eq. 4.18), the water velocities and accelerations must be corrected to take into account the presence of the impermeable cone surface. The contact algorithm for the fluid phase is similar to the one presented in Section 6.4, but no correction for the tangential component is required because the water-cone contact is assumed to be smooth.

The normal component of the fluid velocity $\boldsymbol{w}_{norm}$ must be equal to the normal component of the cone velocity $\boldsymbol{v}_{cone,norm}$, therefore preventing inflow of water into the cone (Fig. 9.20). The corrected velocity for the water at the generic node k

assumes the expression:

$$\tilde{\boldsymbol{w}}^{t+\Delta t} = \boldsymbol{w}^{t+\Delta t} - \left[\left(\boldsymbol{w}^{t+\Delta t} - \boldsymbol{v}_{cone}^{t+\Delta t}\right) \cdot \boldsymbol{n}_k^t\right] \boldsymbol{n}_k^t \tag{9.17}$$

where $\boldsymbol{w}^{t+\Delta t}$ is the predicted water velocity and $\boldsymbol{n}_k^t$ is the normal unit vector. Having calculated the velocity of the contact node k at time $t+\Delta t$, the corrected acceleration vector at the node must be recalculated as:

$$\tilde{\boldsymbol{a}}_w^t = \frac{\tilde{\boldsymbol{w}}^{t+\Delta t} - \boldsymbol{w}^t}{\Delta t} \tag{9.18}$$

The corrected water acceleration is used in the momentum equation for the mixture (Eq. 4.19), which is solved to obtain the acceleration of the solid phase.

The velocity of the solid is predicted and then corrected according to the algorithm presented in Section 6.4. No modifications are required at this step in case of the two-phase formulation.

Section 9.5.1 discusses the results of preliminary analyses through which the set-up of the numerical model has been optimized. Section 9.5.2 presents the results of MPM simulations of CPT allowing for consolidation effects during cone penetration. Numerical results are compared with experimental data from the literature, thus confirming the validity of the model.

9.5.1 Preliminary analyses

The problem is simulated as discussed in Section 9.4.1: only 20° of the cone are simulated, the moving mesh approach is applied, roller boundary conditions for the soil skeleton are assigned at the lateral boundaries and the bottom is fully fixed. The radial boundaries of the 20° slice are impermeable since they corresponds to symmetry axes of the problem. The bottom and the lateral boundary are permeable according to the choice of Yi et al. (2012). However, if the domain is wide enough this does not have any significative influence on the results, as observed during preliminary calculations.

A load of $50kPa$ is activated at the top surface of the soil, thus simulating an initial position of the cone at 5m depth. Indeed, assuming a submerged weight of $10kN/m^3$, the 5m-soil column can be reproduced by such a vertical load. A further penetration of the cone for $10D$ is simulated.

The gradient of initial vertical effective stress is negligible compared to the stress

level encountered during the penetration. Therefore the material weight is neglected and the initial stresses are constant with depth. The stresses are initialized by K_0 procedure and the clay is considered normally consolidated.

The bottom boundary is located $14D$ below the cone tip; this dimension affects the results only for very deep penetration, and is therefore considered suitable for the considered level of penetration. The results are more sensitive to the mesh radius R; its effect has been investigated in one-phase calculations as function of the cone roughness.

Four values of the mesh radius have been considered: 4D, 6D, 8D and 10D. The refinement of the mesh around and below the cone is identical in the four cases. Figure 9.21 shows how the tip stress increases as the cone penetrates into the soil in case of undrained conditions (Fig. 9.21a) and drained conditions (Fig. 9.21b). If the domain size is too small the steady state conditions are not reached or the obtained tip resistance differs form the one obtained with a wider domain.

The preliminary analyses show that to simulate drained conditions wider domains are necessary compared to the case of undrained conditions; the introduction of the cone roughness increases the required domain radius. This means that the volume of soil significantly affected by the cone penetration depends on the drainage conditions. Considerations of computational efficiency and accurancy lead to the conclusion that a radius of $6D$ is sufficient for the undrained case, while $8D$ is necessary for the drained case. The latter proved to be suitable for the analyses in partially drained conditions too.

Unacceptable oscillations of the tip stress in undrained conditions appears when values of the friction coefficient greater or equal to 0.2 are used (Fig. 9.22). A reduction of the Courant number does not improve the results, not even the increase of the discretized domain size, but better results are obtained with a very fine mesh around the cone (Fig. 9.23). Since this increases the computational cost, such a fine mesh is used only for high friction coefficients in one-phase undrained calculations and two-phase calculations with low permeablity.

In this set of calculations $C = 0.98$ and $\beta = 400$ revealed to be appropriate in undrained, drained and partially drained conditions. The damping factor of 0.15 is suitable for the one-phase analyses, but a smaller value is used for the two-phase simulations.

As shown in Figure 9.24, high damping ($\alpha = 0.15$) produces and overestimation of the pore pressure (Fig. 9.24b) and therefore of the cone resistance (Fig. 9.24a); on the

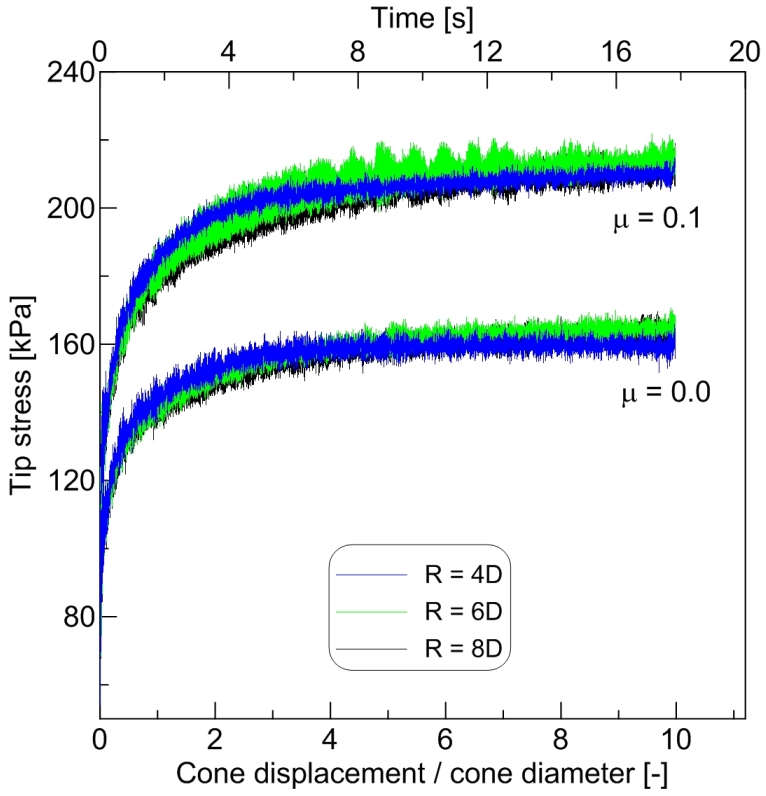

(a) Undrained conditions

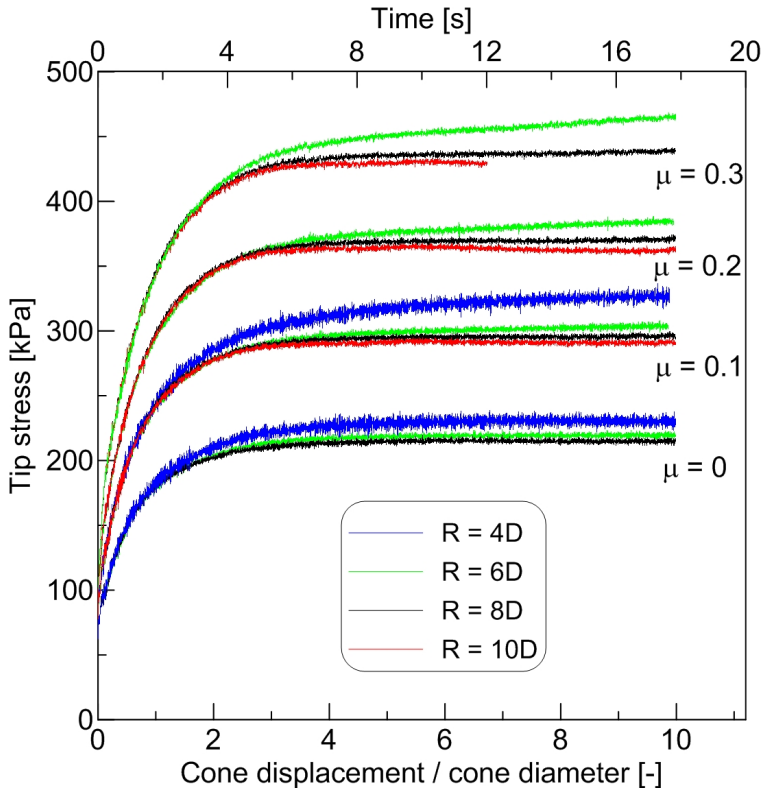

(b) Drained conditions

Figure 9.21: Effect of the mesh radius on the tip stress for different values of the friction coefficient in one-phase analyses.

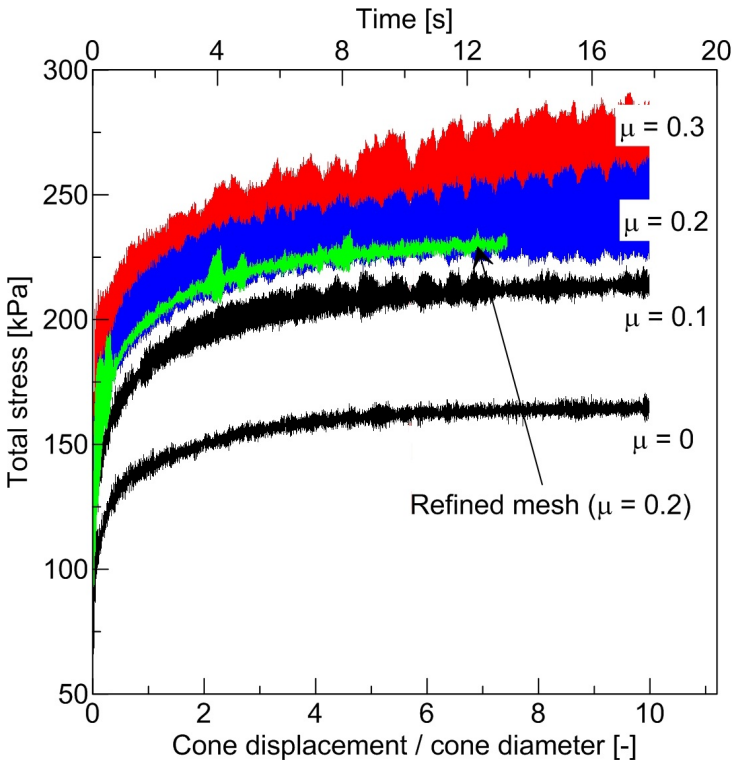

Figure 9.22: Oscillations of the tip stress for $\mu = 0.2$ (blue line) and 0.3 (red line); improvement of the result with finer mesh (green line)

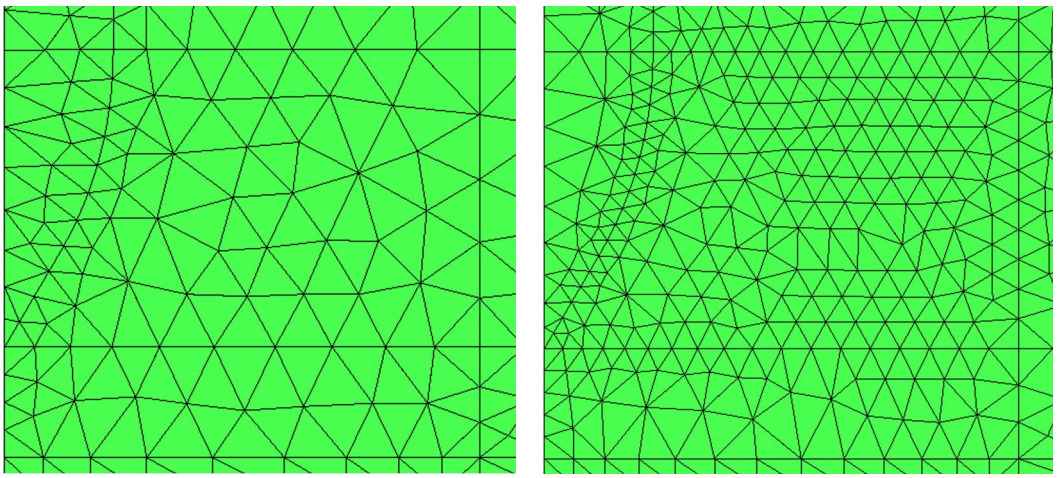

Figure 9.23: Refinement of the mesh around the cone for analyses with rough cone. The standard is on the left and refined mesh is shown on the right.

contrary, it does not affect the effective stress (Fig. 9.24c). This effect is more severe for low permeabilities, i.e. high normalized velocities. It can be explained observing that the local damping artificially reproduces the natural energy dissipation of a material (Cundall 2001). The dissipation is lower for the fluid than for the soil skeleton; however, the same value of the damping factor α is applied on both phases. This leads to an overestimation of the pore pressure, which is more severe when the importance of this contribute is more significant, i.e. for low permeability.

If no damping is used, severe oscillations of the tip stress are observed and difficulties in running the calculations till the steady state are encountered in some cases; for these reasons $\alpha = 0.05$ is considered a good compromise and an overestimation smaller than 5% is assumed to affect the tip resistance q_c.

9.5.2 Results

In this section the results of MPM simulations of CPT accounting for different drainage conditions are presented. The effect on the tip resistance of the pore pressure dissipation during cone penetration is investigated considering also the relative importance of the effective stress and the pore pressure. The effect of the initial horizontal stress and the cone roughness on the tip resistance is studied too. Numerical results are compared with theoretical and experimental data available in the literature.

The problem is simulated as presented in the previous section. The geometry and discretization adopted for the undrained penetration coincide with Figure 9.13; for partially drained and drained conditions the mesh is wider ($0.29m$) and counts 13221 elements and 105634 material points (Fig. 9.25). The material parameters are shown in Table 9.3; the soil is assumed normally consolidated and the initial vertical effective stress is $50kPa$.

Figure 9.26 shows the tip stress over the normalized penetration in case of smooth contact for several values of the normalized velocity V. The tip stress increases with the cone displacement up to a steady state condition which corresponds to the tip resistance q_c. This steady state condition is reached after a penetration of approximately 5D in drained conditions and 7D or 8D in partially drained and undrained conditions.

As expected, the tip resistance increases with the decrease of V, i.e. moving from undrained to drained conditions. In case of $V = 1.2$ the tip resistance is only 4%

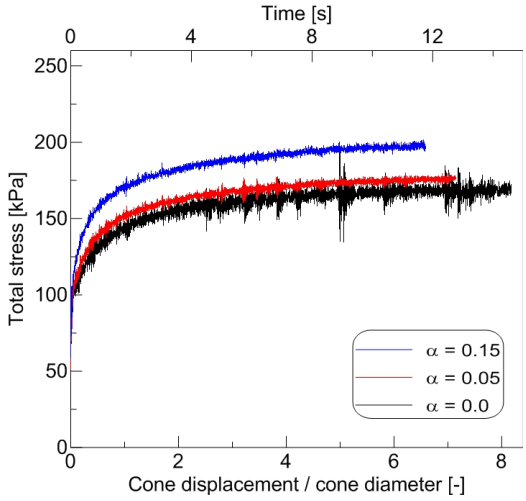

(a) Total tip stress

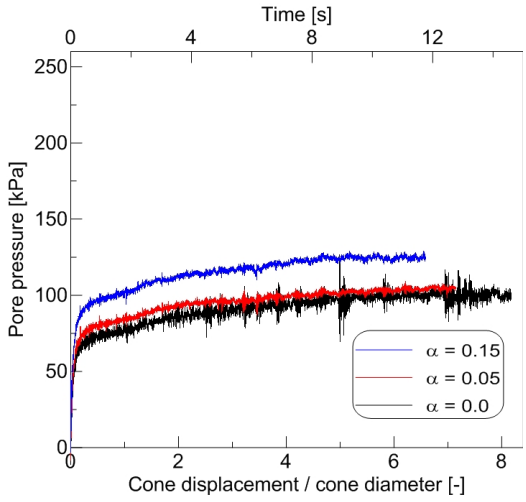

(b) Pore pressure

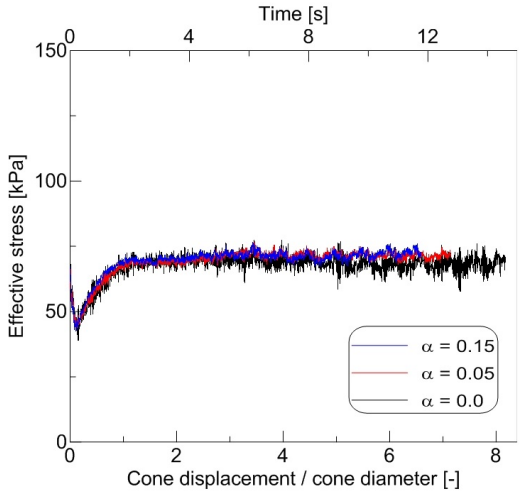

(c) Effective tip stress

Figure 9.24: Effect of the damping factor on the vertical component of the stresses acting on the cone ($V = 12$, $\mu = 0$).

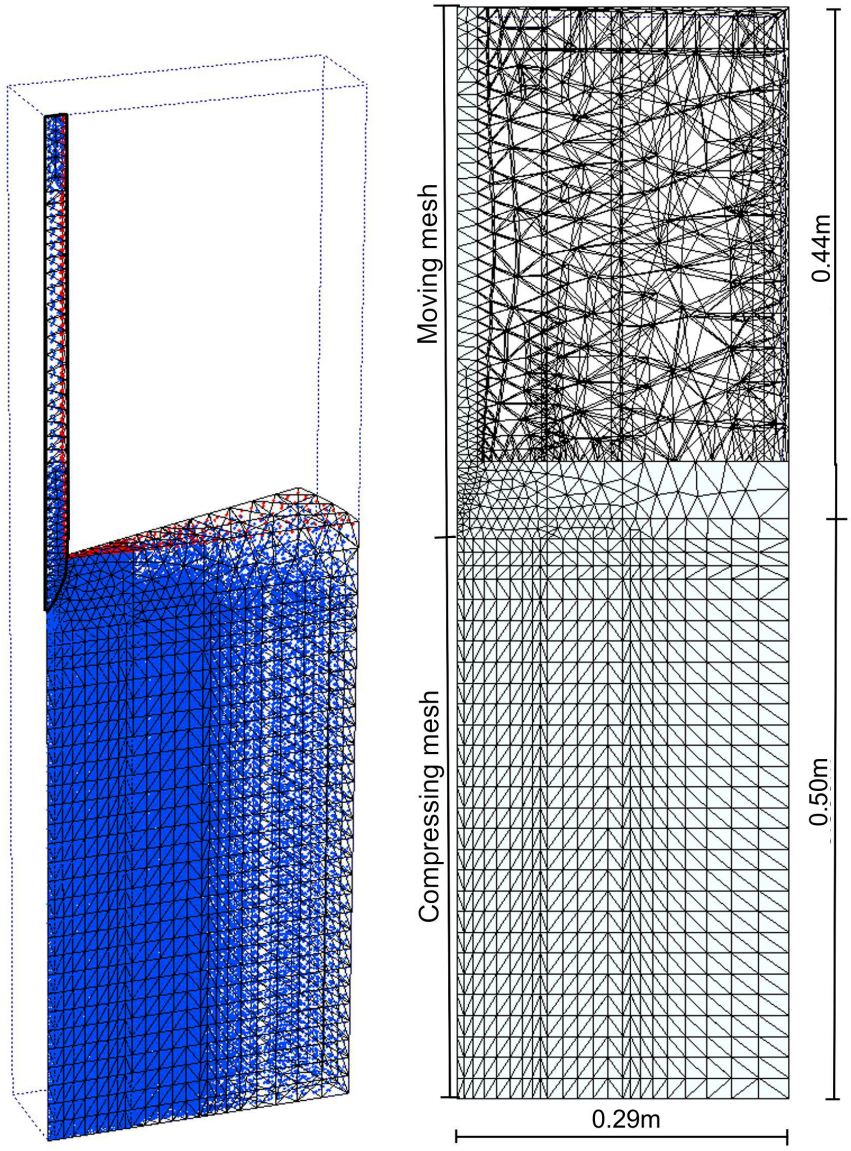

(a) MP discretization (b) Connectivity plot

Figure 9.25: Geometry and discretization for CPT simulation in partially drained and drained conditions with MCC model.

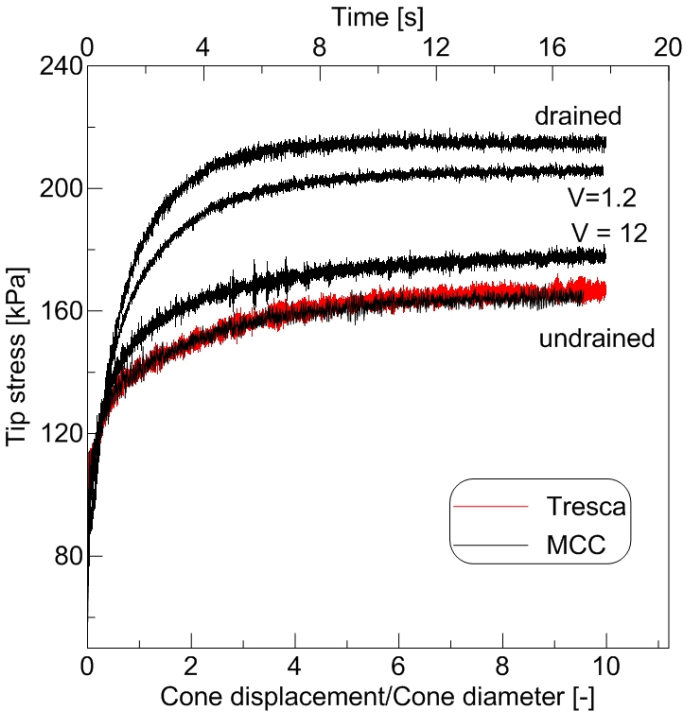

Figure 9.26: Tip stress for different drainage conditions in case of smooth contact.

lower than the drained value, and in case of $V = 12$ the tip resistance is only 4% higher than the undrained value. This means that, for this problem, the range of normalized velocity in which partially drained conditions occur is relatively narrow.

As shown in Section 9.4 the undrained behavior of clay can be well simulated even with Tresca material model. For this analyses the shear modulus is estimated as a function of the recompression index κ, the initial void ratio e_0, the effective Poisson ratio ν' and the initial effective mean stress p'_0:

$$G = \frac{3(1-2\nu')}{2(1+\nu')}\frac{1+e_0}{\kappa}p'_0 \tag{9.19}$$

The undrained shear strength adopted for the Tresca model coincides with the s_u obtained, for the considered MCC parameters, in triaxial compression. This entails the assumption that the triaxial compression dominates the stress state around the penetrating cone. The s_u value obtained from K_0-consolidated triaxial undrained compression test, with confining pressure equal to the initial horizontal stress is used (12kPa).

The tip stress curve obtained with this simple model has been included in Figure 9.26 and agrees with the one obtained with the MCC model. The cone factor calculated for undrained conditions with the MCC model is $N_c = 9.6$, with the Tresca model

is $N_c = 9.7$ and the one calculated with Equation 9.9, where $I_r = 108$, $\Delta = 0.7$ and $\alpha = 0$ is 9.55. There is excellent agreement between MPM simulations and reference literature results.

The accumulated shear strains after 10D penetration for the undrained and drained conditions are shown in Figure 9.27. In case of smooth contact, extreme shear deformations, i.e. accumulated deviatoric strain (Eq. 5.14) $\epsilon_q > 10\%$, extend about 2D in radial direction and 0.5D below the cone for undrained conditions and 1.5D in radial direction and 0.3D below the cone for drained conditions. The dimensions of this area of extreme deformations slightly increase with the rough contact.

Figure 9.28 shows the excess pore pressure for two values of the normalized penetration rate V. Approximately undrained behavior is observed for $V = 12$ at which the pore pressure is about $150kPa$. On the contrary, for $V = 1.2$ the behavior is nearly drained and the pressure is about $30kPa$. This agrees with considerations on the tip resistance.

The effective stress path of a point next to the cone surface is plotted in Figure 9.29 as function of the normalized velocity. The initial condition is identical for the considered cases, the mean effective stress is $p'_0 = 40kPa$ and the deviatoric stress is $q_0 = 15.5kPa$. This stress state lies on the yielding surface (Eq. 5.21) because the soil is assumed normally consolidated; the initial preconsolidation pressure p_{c0} is $47kPa$.

As the cone penetrates, the soil yields and the stress path moves toward the CSL. The undrained path is typical for normally consolidated clays. The stress path for a normalized penetration rate $V = 12$ approaches the undrained behavior, while the one for $V = 1.2$ approaches the drained stress path. The final mean effective stress and deviatoric stress increase reducing the normalized penetration rate, i.e. moving from undrained to drained conditions, as result of the pore pressure dissipation during cone penetration.

The tip resistance can be written as $q_c = q_{c,eff} + q_{c,water}$ where $q_{c,eff}$ is the contribute of the soil effective stress and $q_{c,water}$ is the contribute of the pore pressure. Figure 9.30 shows how the contribute of the pore pressure increases with the normalized velocity while the one of the effective stress decreases.

In drained conditions $q_{c,water} = 0$ and therefore $q_c = q_{c,eff}$ because there is no excess pore pressure generation. In undrained conditions there is a significant generation of pore pressure with no dissipation which leads to $q_{c,water} \approx 75\% q_c$ and $q_{c,eff}$ is even lower than the initial vertical effective stress. In case of partially drained conditions,

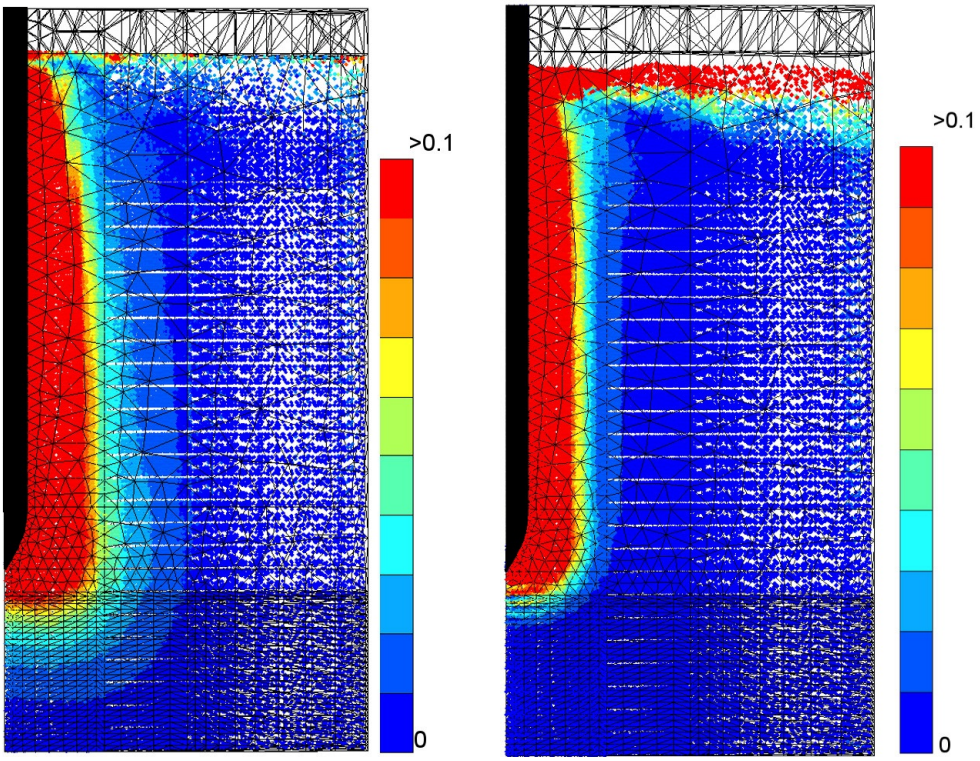

(a) Undrained conditions, $\mu = 0$ (b) Drained conditions, $\mu = 0$

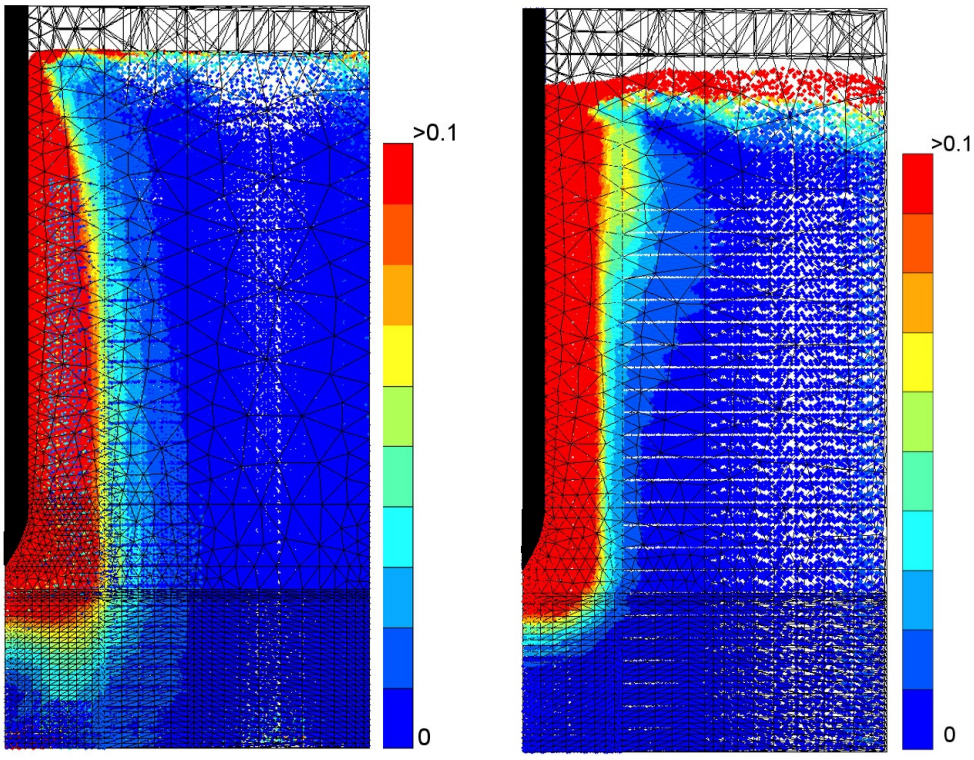

(c) Undrained conditions, $\mu = 0.4$ (d) Drained conditions, $\mu = 0.4$

Figure 9.27: Accumulated deviatoric strain for one-phase simulations using MCC model.

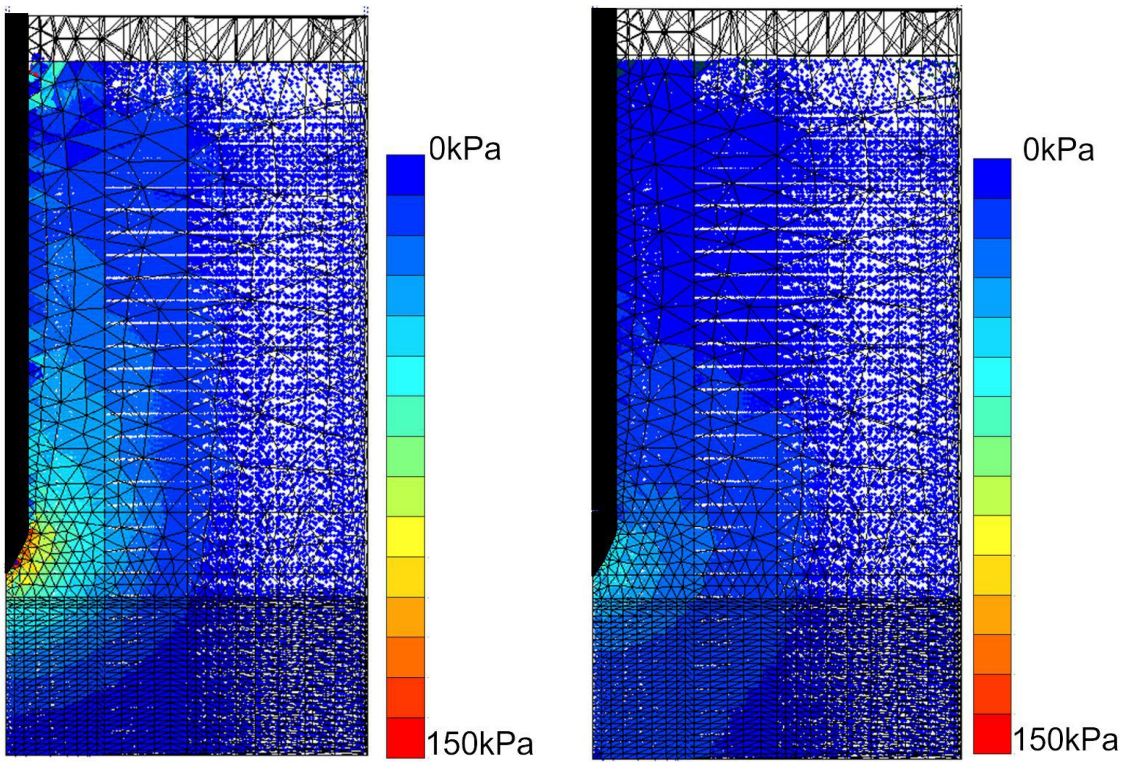

(a) Normalized penetration rate $V = 12$ (b) Normalized penetration rate $V = 1.2$

Figure 9.28: Excess pore pressure for two-phase simulations using the MCC model.

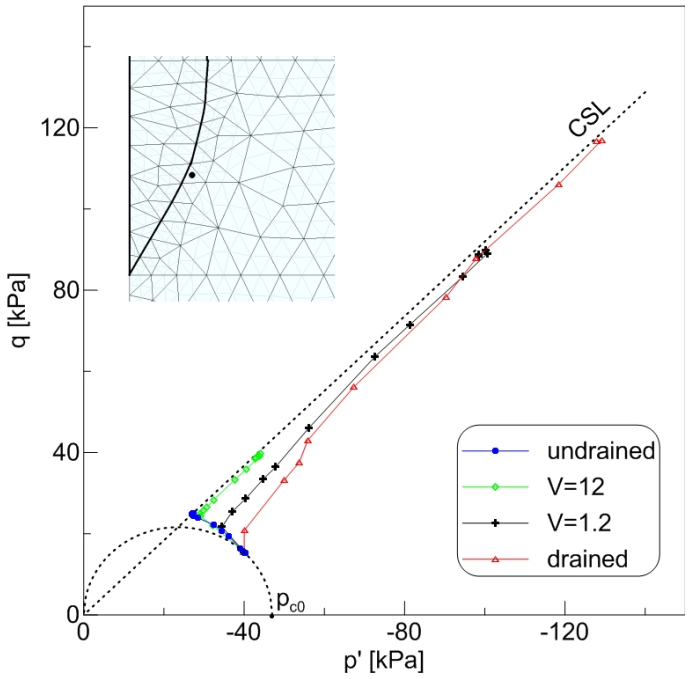

Figure 9.29: Effective stress path of an element close to the cone surface for different normalized velocities V in case of smooth contact.

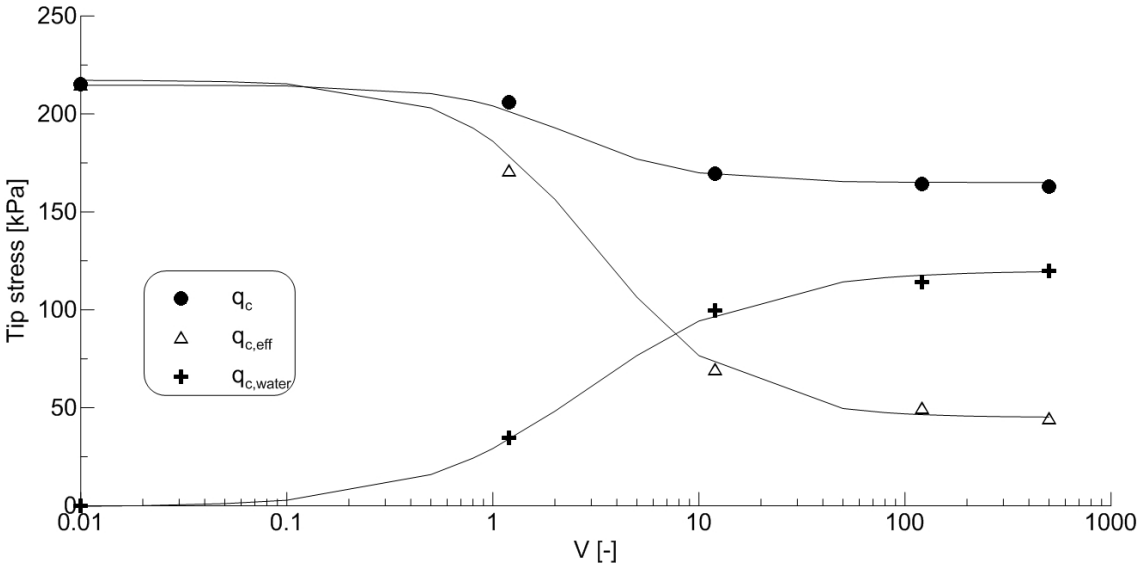

Figure 9.30: Effect of the normalized velocity V on the contributes of effective stress $q_{c,eff}$ and pore pressure $q_{c,water}$ on the tip resistance.

the contribution of the pore pressure is approximately 60% of the total tip resistance for $V = 12$, and 17% for $V = 1.2$. This agrees with the considerations on the stress path.

The effect of the initial stress state is investigated changing the initial horizontal stress σ'_{x0}, i.e. the problem is characterized by different values of K_0, p'_0 and q'_0, but the same initial vertical effective stress σ'_{v0} and the same initial void ratio. In reality, these parameters are correlated. Moreover, the initial stress state is a function of the overconsolidation ratio OCR; usually it is estimated as a function of OCR and the critical state friction angle ϕ by (Mayne and Kulhawy 1982):

$$K_0 = \frac{\sigma'_{h0}}{\sigma'_{v0}} = (1 - \sin(\phi))OCR^{\sin(\phi)} \tag{9.20}$$

but in this study the soil is assumed normally consolidated, i.e. $OCR = 1$. Further developments will consider the effect of overconsolidation.

Figure 9.31 shows that the initial stress state influences the tip resistance q_c; the lowest resistances are observed for $K_0 = 0.69$. The resistance ratio q/q_{ref}, i.e. the ratio between the net tip resistance and the undrained net tip resistance, is not significantly influenced by the initial horizontal stress (Fig. 9.32).

In engineering practice the measure of the pore pressure is commonly used to identify the soil type. The pore pressure factor B_q, defined by Equation 9.3, is often employed in normalized charts to identify the soil behavior type (Robertson 1990). This factor

represents a measure of the relative importance of the pore pressure on the net tip resistance. In the numerical analyses the pore pressure factor is estimated as

$$B_q = \frac{q_{c,water}}{q_{c,net}} \tag{9.21}$$

where $q_{c,water}$ represents an average of the pore pressures around the cone. On the contrary, in practice the pore pressure is measured behind the cone. The pore pressure factor is not significantly influenced by the horizontal stress state (Fig. 9.33).

The cone roughness is simulated assigning a friction coefficient μ which varies between 0, i.e. smooth contact, and 0.42, i.e. rough contact ($\tan\phi = 0.42$). The friction coefficient depends on the relative dimension of the surface roughness and the size of the soil particles. Reasonable values of μ for low plasticity clay in contact with steel lie between 0.2 and 0.35 (Lemos and Vaughan 2000). Potyondy (1961) suggested an interface friction angle equal to one half the critical soil friction angle, which corresponds to a friction coefficient of 0.21 in this case.

Figure 9.34 shows how the introduction of the cone roughness increases the tip resistance in one-phase undarined and drained analses. In undrained conditions, the cone factor N_c (Eq. 9.4) ranges from 9.6 to 16; this is in agreement with what was observed in Section 9.4.2 for a similar rigidity index.

A different definition of the cone factor is commonly adopted in drained conditions (Lunne and Powell 1997):

$$N_q = \frac{q_c}{\sigma'_{v0}} \tag{9.22}$$

It increases linearly with the friction coefficient from a value of 4.3 to 10.2. These values are extremely low, compared to the usual values assumed for sand, which varies from 20 to 100 (Lunne and Powell 1997). This can be attributed to the low modulus ratio G/p' and friction angle used in this study, where a soft clay is modeled. The MPM results are in agreement with the study of Yi et al. (2012) where $N_q \approx 5$ is found for smooth contact with a similar friction angle and modulus ratio.

The cone roughness increases the tip resistance in the entire range of drainage conditions. In drained conditions the increase is linear, while in partially drained and undrained conditions it is less than linear and seems to stabilize for $\mu > 0.3$ (Fig. 9.35). This non-linear trend is in contrast with other numerical studies in total stress where the Tresca material model and the adhesive contact are used (see e.g.

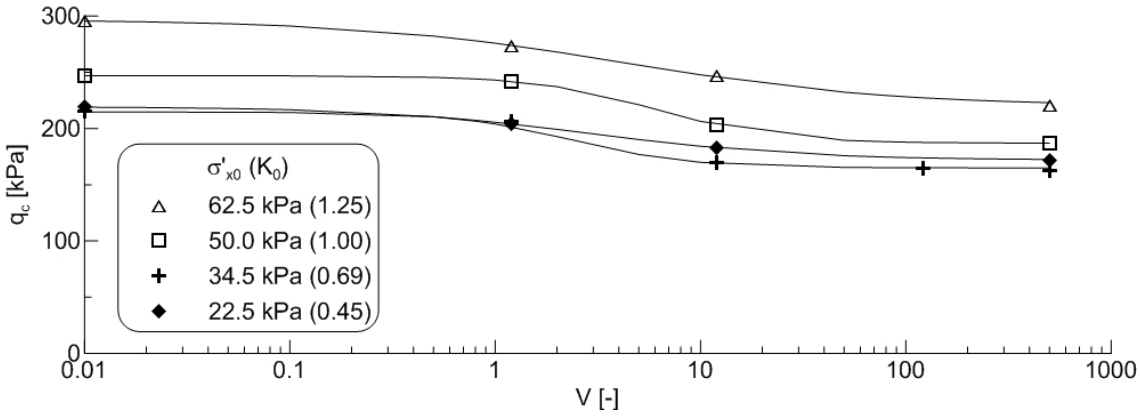

Figure 9.31: Effect of the initial stress state and the normalized velocity V on the tip resistance q_c.

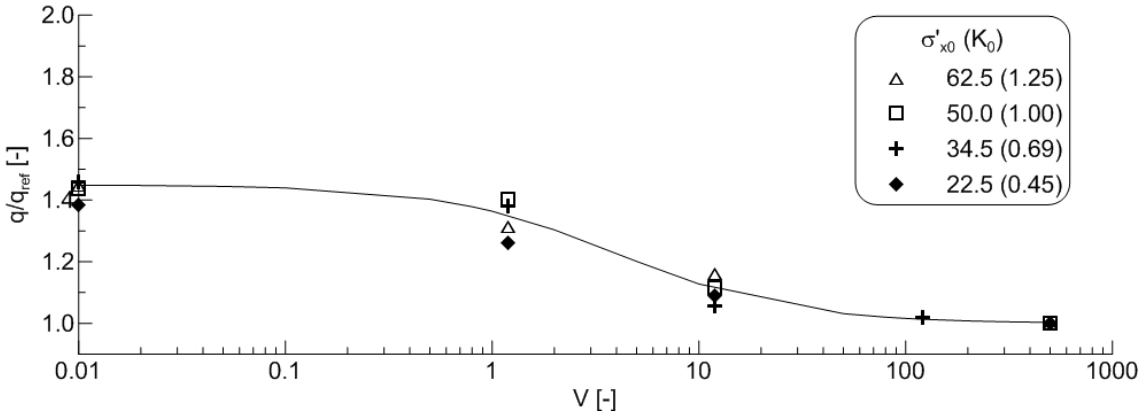

Figure 9.32: Effect of the initial stress state and the normalized velocity V on the resistance ratio q/q_{ref}.

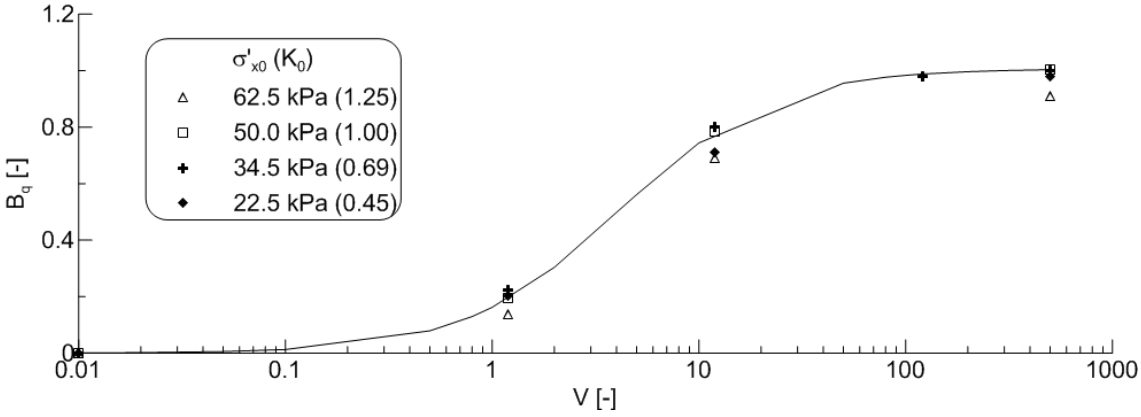

Figure 9.33: Effect of the initial stress state and the normalized velocity V on the pore pressure factor B_q.

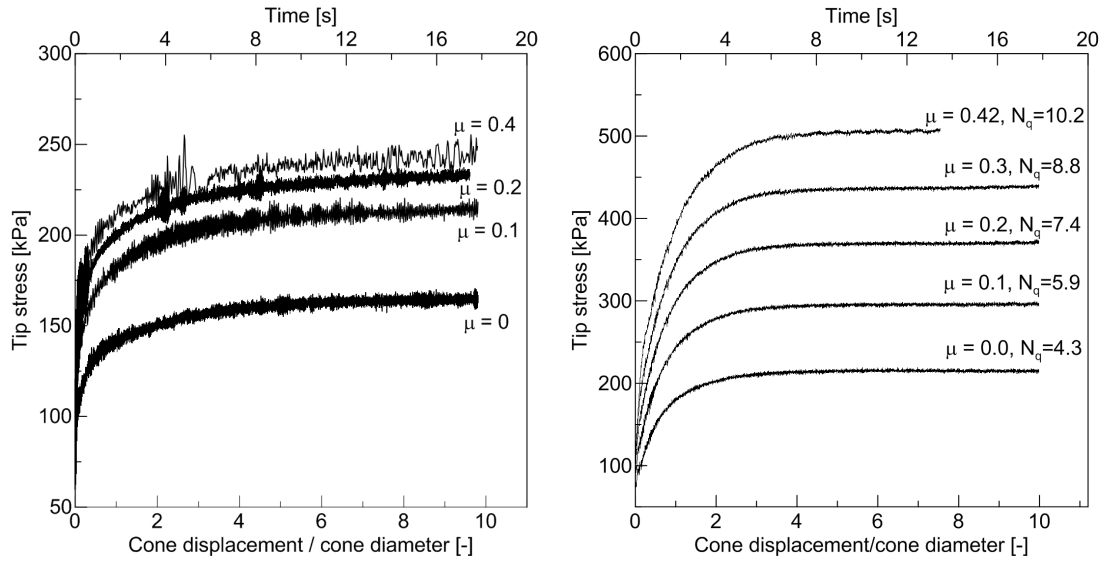

(a) Undrained conditions (b) Drained conditions

Figure 9.34: Tip stress for different values of the friction coefficient μ in one-phase analyses.

Lu et al. 2004 and Beuth and Vermeer 2013). The penetration process is a complex phenomenon to simulate numerically, further investigations are required to explain this result.

Figure 9.36 shows the resistance ratio as a function of the normalized velocity V for different values of the friction coefficient μ. The maximum resistance ratio increases with the cone roughness from a value of 1.4 for $\mu = 0$ to a value of 2.4 for $\mu = 0.42$.

The numerical data can be fitted by the backbones curves represented by Equation 9.11; the coefficients corresponding to the best fit are included in Figure 9.36. The coefficient b increases with μ because the maximum resistance ratio is proportional to the friction coefficient. This also affect the rage of partially drained conditions, which is narrower for smooth cone (V comprises between 0.3 and 50) than for very rough cone (V comprises between 0.1 and 200).

Figure 9.37 shows that the pore pressure factor is a function of the normalized velocity and the cone roughness. Lower values of the friction coefficient generate higher pore pressure factors. This means that the relative importance of the pore pressure on the tip resistance decreases with the cone roughness.

The results obtained with the MPM are compared with centrifuge model CPT results by Randolph and Hope (2004) (black dot in Fig. 9.36 and in Fig. 9.37) and numerical result obtained with the cavity expansion theory by Silva (2005) (dashed line in

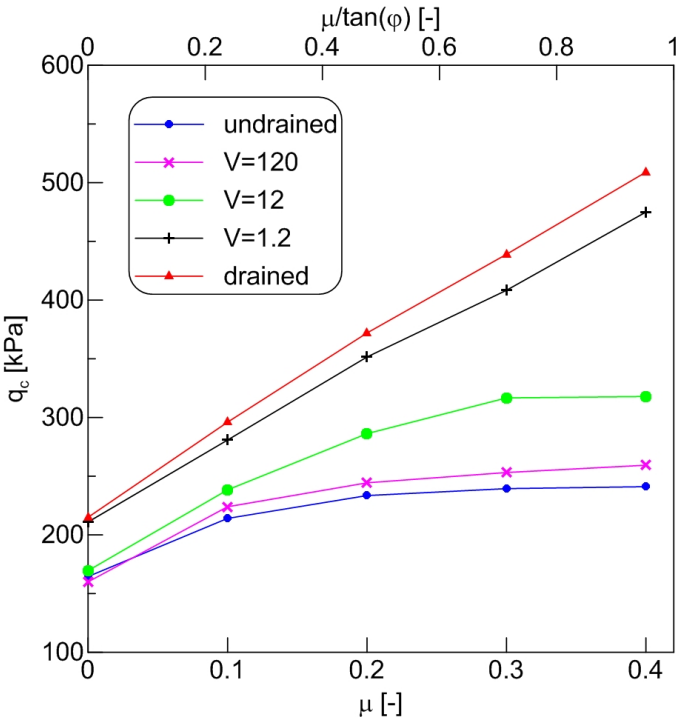

Figure 9.35: Effect of the friction coefficient μ on the tip resistance q_c.

Fig. 9.36).

The backbone curves obtained with the MPM are in good agreement with the experimental results. Differences can be attributed to the fact that the real tested material may be characterized by slightly different material parameters form the one assumed in the numerical model; in particular a higher modulus ratio which seems to be comprises between 35 and 75 (Yi et al. 2012). Moreover, the experimental consolidation coefficient, used to calculate the normalized velocity, may differs from the numerical estimate. There is a slight overestimation of the pore pressure parameter, especially for undrained conditions, which can attributed to the use of the MCC model.

The experimental data seems to be well fitted by MPM simulations obtained with friction coefficient comprises between 0.3 and 0.4. The friction coefficient assumed by Silva (2005) is equal to the tangent of the soil friction angle. However, for $\mu = \tan(\phi) = 0.42$ the MPM gives higher values of the resistance ratio; this can be explained by the fact that the cavity expansion theory considers only radial soil deformations, while the MPM simulates the threedimensional process of cone penetration.

Schneider et al. (2007) published experimental data obtained with centrifuge tests on kaolin. The material properties of this soil are summarized in Table 9.4. In

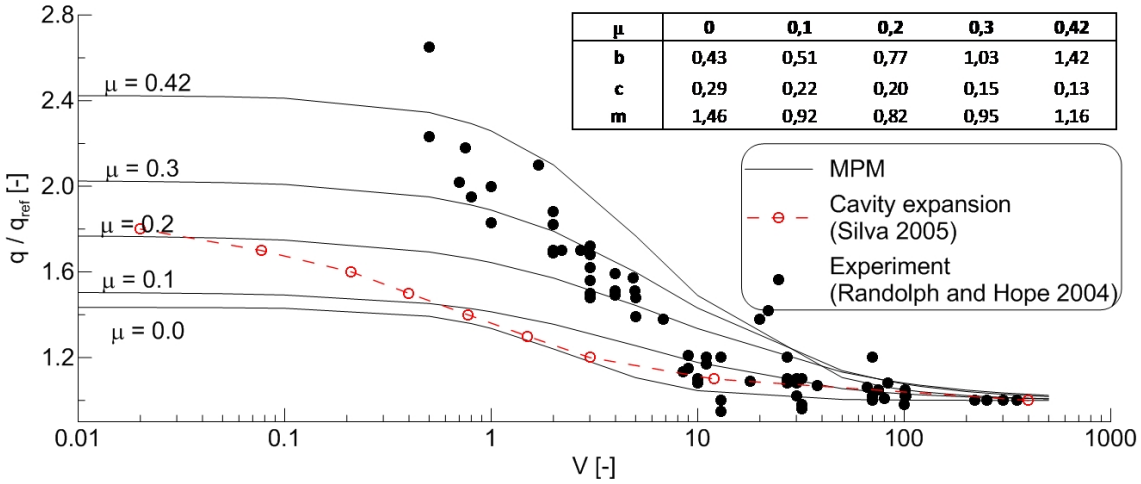

μ	0	0,1	0,2	0,3	0,42
b	0,43	0,51	0,77	1,03	1,42
c	0,29	0,22	0,20	0,15	0,13
m	1,46	0,92	0,82	0,95	1,16

Figure 9.36: Effect of the normalized velocity V on the resistance ratio q/q_{ref} for several values of the friction coefficient μ.

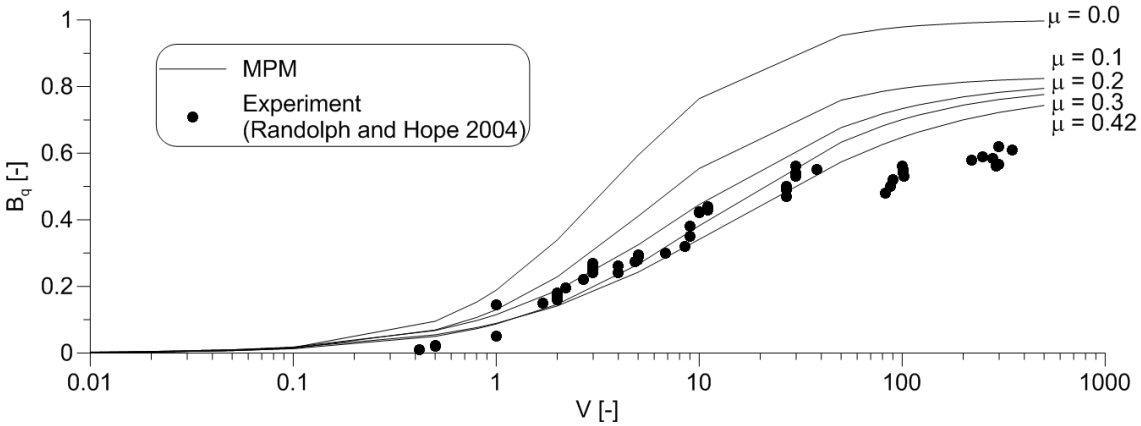

Figure 9.37: Effect of the normalized velocity V on the pore pressure factor B_q for several values of the friction coefficient μ.

Material property	Symbol	Value
Virgin compression index [-]	λ	0.26
Recompression index [-]	κ	0.06
Effective poisson ratio [-]	ν'	0.25
Slope of CSL in p-q plane [-]	M	0.92
Initial void ratio [-]	e_0	1.6

Table 9.4: Material properties of the kaolin used by Schneider et al. (2007)

the experiment, the initial vertical effective stress varies from $80kPa$ to $100kPa$ and a penetrometer with a diameter of $10mm$ is used. The effect of the drainage conditions is studied by varying the penetration rate from $0.003mm/s$ to $3mm/s$ and the consolidation coefficient is estimated from the soil parameters by Equation 9.16.

Assuming that the cone diameter does not significantly influence the tip resistance, the same geometry and discretization used in the previous problem is adopted (Fig. 9.25). The initial vertical and horizontal effective stress are $90kPa$ and $54kPa$ respectively. A friction coefficient of 0.28 is assumed reasonable for this problem; this value corresponds to an interface friction angle equal to $2/3\phi$ (ϕ = critical soil friction angle). The normalized velocity is again varied by changing the soil permeability.

Figure 9.38 shows how the net tip resistance varies with the normalized velocity. The experimental data are relative to the initial vertical effective stresses between $80kPa$ and $100kPa$, while the MPM results are obtained for $\sigma'_{v0} = 90kPa$. The tip resistance in drained conditions is very well captured, while there is a slight overestimation of $q_{c,net}$ for undrained conditions.

Figure 9.39 represents the resistance ratio as a function of the normalized velocity. It can be observed that the initial vertical effective stress does not significantly influence the resistance ratio. The maximum q/q_{ref} is slightly underestimated and this is due to the overestimation of the undrained tip resistance.

Numerical results in terms of B_q are in good agreement with the experimental measurements (Fig. 9.40). The overestimation of B_q, which is observed for high normalized velocities, can again be attributed to the soil constitutive model. This suggests that a further improvement of the results can be achieved by improving the simulation in undrained conditions, for example with the use of a more advanced constitutive model. The MPM estimation of cone resistance, resistance ratio and pore pressure factor are in very good agreement with the experimental data.

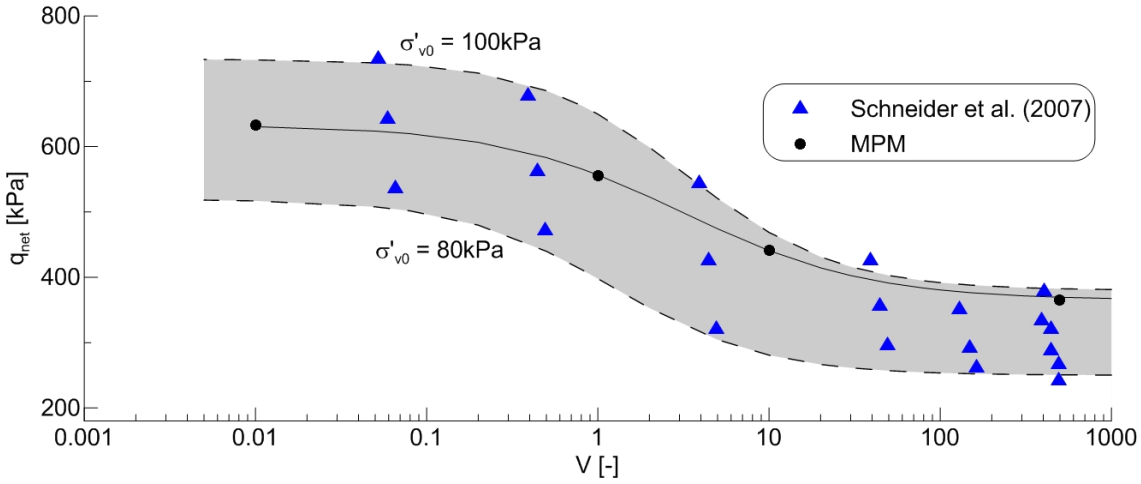

Figure 9.38: Effect of the normalized velocity V on the net cone resistance q_{net}. Comparison between MPM result and experimental data by Schneider et al. (2007).

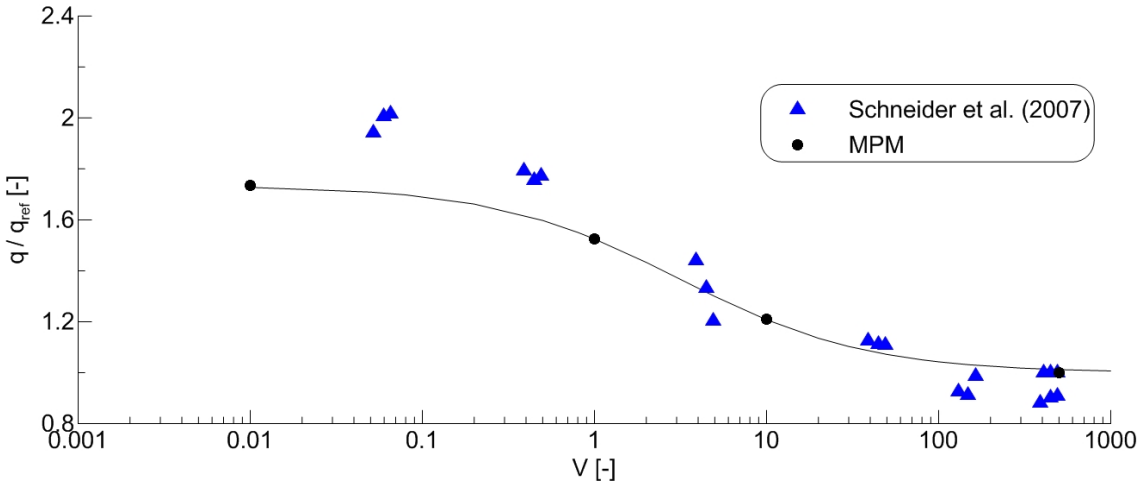

Figure 9.39: Effect of the normalized velocity V on the resistance ratio q/q_{ref}. Comparison between MPM result and experimental data by Schneider et al. (2007).

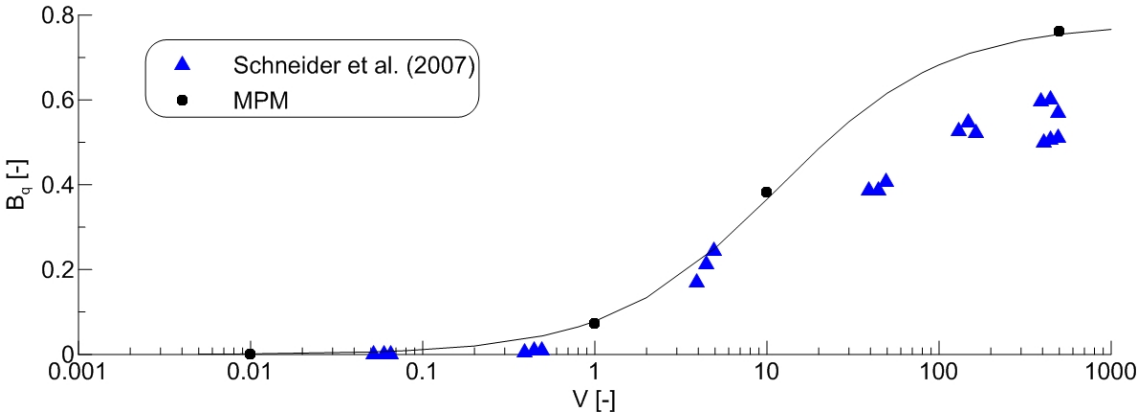

Figure 9.40: Effect of the normalized velocity V on the pore pressure factor B_q. Comparison between MPM result and experimental data by Schneider et al. (2007).

9.6 Conclusions and future developments

In this chapter the MPM has been applied to the simulation of cone penetration in clay, considering the effect of the drainage conditions, the initial stress state and the cone roughness on the tip resistance and the pore pressure factor.

Numerical studies of CPT in partially drained conditions are rare because of the high complexity of the penetration process. Indeed, large deformations, soil-cone contact, soil-water interaction and non-linear soil constitutive behavior have to be taken into account.

To the author's knowledge, there are only a couple of papers on numerical simulation of CPT including pore pressure dissipation during penetration: Silva et al. (2006), who used the cylindrical cavity expansion theory coupled with FEM, and Yi et al. (2012), who used the FEM with logarithmic strain. Despite the these studies give an important contribution to the understanding of the penetration process, they have some limitations and drawbacks which are discussed in Section 9.2.2.

The present study adds several novelties to the numerical simulations of soil penetration problems. Indeed, here the bidimensional large deformations of soil and the bidimensional water flow, induced by the advancing cone, are taken into account. The effect of cone roughness is investigated and the mechanical response of soil is simulated with the MCC constitutive model that can capture many non linearities of the real soil behavior.

The first part of this chapter considers CPT in undrained conditions (Sec. 9.4). Since the pore pressure dissipation is negligible, the one-phase MPM is used to simulate the penetration process. The undrained behavior of clay is simulated with the elatoplastic model with Tresca failure criteria.

The cone factor is a function of the rigidity index, the initial stress state and the cone roughness. In this study ($I_r = 100$ and $\Delta = 0$), cone factors of 10.2, 14.0 and 15.8 are found for cone roughness α_c equal to 0, 0.5 and 1 respectively. MPM results are in excellent agreement with experimental data by Kurup et al. (1994), in which a cone factor of 13 is found. Good agreement is also found with other analytical studies for the smooth contact, but a slight overestimation of the cone factor is observed for rough cone. This may be related to the use of the contact algorithm proposed by Bardenhagen et al. (2001), as recent studies seems to suggest. Ma et al. (2014) observed an overestimation of the contact forces when bodies with very different stiffness are in contact. A more detailed investigation of this problem

should be considered in a future development of the research.

The second part of the chapter introduce the effect of pore pressure dissipation during cone penetration (Sec. 9.5). A more realistic constitutive model is necessary to achieve this purpose. The modified Cam Clay model can reproduce several of the most important characteristic of soft soil behavior and its input parameters are easy to calibrate. For undrained conditions the tip stress corresponds to the one obtained with the Tresca material model assuming the undrained shear strength for triaxial compression.

The tip resistance increases moving from undrained to drained conditions because, decreasing the penetration rate V, the pressure dissipates and the soil consolidates therefore developing higher shear strength and stiffness.

The initial stress state influence the tip resistance, but it has a negligible effect on the resistance ratio (q/q_{ref}) and the pore pressure factor B_q. In this study the different initial stress states have been simulated by assigning different initial horizontal stresses while keeping the other parameters constant. In future studies, a more realistic simulation of different initial conditions, in the same soil, will consider the relation between K_0, overconsolidation ratio OCR and initial void ratio.

The present study shows that the resistance ratio depends on the friction coefficient. Indeed, for the considered case, its maximum varies between 1.4 for smooth contact and 2.4 for rough contact.

The cone roughness affects the pore pressure factor too: increasing the friction coefficient decreases B_q. This means that the relative importance of the pore pressure on the tip resistance decreases with the cone roughness. It also influences the range of partially drained conditions, which is found to be wider for rough cone. A proper simulation of the soil-cone contact is important for a realistic simulation of the penetration process.

The MPM simulations with the MCC constitutive model capture very well the experimental results on kaolin published by Randolph and Hope (2004) and Schneider et al. (2007) confirming the validity of the method.

The kaolin has a relatively low plasticity index as commonly found also for silt, which is the soil type where penetration at standard rate can be characterized by partially drained conditions. The results of this study can be considered a reasonable representation of real field situations in which partially drained conditions occur.

For isotropically normal consolidated states, the mechanical behavior can be reason-

ably well captured by the MCC model. However, natural clays are anisotropically consolidated, which has a significant influence on the undrained strength and thus on the undrained tip resistance (Beuth 2012). In addition to this, strain-rate effects dominates the behavior at high penetration rates (Randolph 2004). The influence of soil anisotropy and viscoplasticity will be considered in the future by implementing more advanced constitutive models in the MPM. Different types of soil will be considered too.

The study can be extended to the pore pressure dissipation subsequent the cone penetration. This is of particular interest in practice, because the dissipation test is widely used to estimate the soil's consolidation coefficient and permeability. Data interpretation is based on analytical studies which neglect the installation effects and assume undrained conditions of penetration, see e.g. Baligh and Levadoux (1986), Teh and Houlsby (1991), Robertson et al. (1992). With the MPM the effects of cone installation as well as the occurrence of partial pore pressure dissipation during penetration can be considered. A practical method to estimate the consolidation coefficient even in case of partially drained cone penetration can be suggested. This is of practical interests as it allows to extend the dissipation test to silty soil.

10

General conclusions and final remarks

This thesis addresses the problem of simulating large deformations in geomechanics accounting for the soil-water interaction. Taking into account large displacements of soil is necessary in several geotechnical cases. The Material Point Method (MPM) is a promising tool in this field. This work focuses on its developments and applications. The aim of this chapter is to summarize the study, draw some conclusions and define further developments of the research.

The numerical modeling process has been introduced in Chapter 2, including an overview of the most common numerical methods. Numerical methods improved considerably in the last decades, increasing the number of problems which can be studied. Numerical simulations are often cheaper and more feasible than field and laboratory tests. A large number of variables can be controlled and parametric studies are possible, thus allowing a deeper understanding of the physical phenomena. The field of computational mechanics is in constant expansion and offers wide possibilities of research and applications in geoengineering.

The most important developments of the Material Point Method, starting from its infancy at Los Alamos, where it was originally developed, is discussed in Section 2.5. From this literature review, it can be concluded that the MPM is a powerful numerical technique, providing possibilities of modeling large deformations, multiphase materials and interaction between solid bodies. It has been successfully applied to solve a wide range of problems in different engineering fields and the number of applications can be further extended.

Chapters 3 and 4 present in detail the MPM formulation and the solution procedure for the one-phase and two-phase material respectively. The applicability of these formulations in geomechanics has been discussed. The one-phase formulation is

suitable for soil in drained and undrained conditions, i.e. when the generation or the dissipation of pore pressures are negligible, while the two-phase formulation should be used when both the generation and dissipation of pore pressures are relevant, e.g. in the case of cone penetration in partially drained condition (Sec 9.5).

The two-phase formulation is validated for small and large deformations in Chapter 7. In the future, the two-phase MPM will be compared with other solutions at large strain, e.g. Borja et al. (1998), Xie and Leo (2004), Nazem and Sheng (2008), eventually discussing the source of differences. The possibility to couple large deformations and soil-water interaction is extremely interesting in geomechanics. It allows the study of complex problems in which the generation and dissipation of pore pressure is a key point such as landslides, debris flows and mud flows.

This study considers only water-saturated soil. Partially saturated soil can be described by a three-phase formulation, i.e. the governing equations for the gas phase are included. The implementation of the three-phase MPM is in progress (Yerro 2014) and will be considered in the future to study problems involving partially saturated soil such as the stability of slopes, embankments and dams under transient hydraulic conditions.

In this thesis one set of material points, moving with the solid velocity, is used even when the presence of the water is considered. This one-layer formulation is acceptable to simulate the saturated soil behavior, but the interaction with free water cannot be included.

Problems of seepage and erosion-sedimentation, in which part of the domain is occupied by pure water, part by dry or saturated soil and part by suspensions of soil particles in water, need to be simulated by two sets of material points. Implementation and developments of this two-layer formulation is the subject of the on-going work of MPM research groups (Vermeer et al. 2013, Rohe and Vermeer 2014, Martinelli and Rohe 2014).

The possibility of simulating the solid-suspension-fluid transition is extremely important to study several problems of engineering interest such as injection of fluids in the ground (jet-grouting), sedimentation of mine waste, stability of submerged slopes subjected to erosion processes and installation of footings on the seabed. Geotechnical models consider the saturated soil behavior, while hydromechanical models consider the fluid and fluidized mixture behavior, but the transition between these phases and their interaction are hardly considered. Future developments of the MPM can fill the gap between geomechanical and hydromechanical models. The

author thinks that this aspect is one of the most interesting to follow in the future.

In addition to the interaction with fluids, one of the main issue of geotechnical engineering is the constitutive modeling of soil. Despite its importance, this theme is not the main concern of the present study and has been shortly treated in Chapter 5. Simple models such as Tresca, Mohr-Coulomb and Modified Cam Clay have been applied in this study. Tresca and Mohr-Coulomb models provide a crude representation of soil behavior. However, this is sometimes sufficient in the engineering practice and they can be used to catch the main features of the considered problem. The Modified Cam Clay model is more advanced and can better reproduce the non-linear soil behavior. To the author's knowledge, this thesis is the first application of this constitutive model in the study of large deformation problems with a dynamic MPM code. Simple models may not be able to represent accurately the real soil behavior, but they are easy to use. Sophisticated models are more realistic, but they add significative complexity to the simulation and the estimation of input parameters may be demanding. Implementations and applications of more advanced constitutive models will be considered in the future.

Many geotechnical problems involve soil-structure interaction; in the MPM there are several algorithms able to solve contact problems, one of the most popular was introduced by Bardenhagen et al. (2001). This algorithm was originally developed for the frictional contact. In cohesive soils under undrained conditions, the maximum tangential force is independent on the normal contact force and it is often referred to the undrained shear strength of the soil. In order to simulate this type of contact, the original algorithm has been enhanced including the adhesive component of the contact force. This algorithm is presented and validated in Section 6.4 and has been applied to simulate the contact between cone and undrained clay in Section 9.4.

The use of high friction coefficients with this algorithm requires a fine mesh to keep an acceptable accuracy. An overestimation of the contact forces when bodies with very different stiffness are in contact is reported by Ma et al. (2014) and it is also observed in this thesis with the simulation of CPT in undrained conditions (Sec. 9.4). A detailed study of the performances of the implemented algorithm for geomechanical problems is suggested.

The simulation of real problems is difficult because reality is complex and simplifications are necessary. These simplifications, together with the particular features of the numerical method, sometimes lead to numerical difficulties. Some of these problems are discussed in Chapter 6, e.g. volumetric locking for incompressible materials when low order elements are used and noise due to dynamic waves.

The use of absorbing boundary and local damping can reduce the noise due to unphysical dynamic effects. The first virtually simulates the presence of a layer of material beyond the boundary. The latter represents the natural energy dissipation of the material. The effects of the virtual thickness and the damping factor are discussed showing that proper values of these parameters can improve the numerical results.

On of the most interesting application of the MPM is the study of landslides. This theme is considered in Chapter 8, in which a laboratory test of slope failure is simulated. The Mohr-Coulomb model is used to describe the constitutive behavior and the two-phase formulation is adopted to take into account the interaction with the water. The method can capture the initialization of the failure, the propagation of the slide and its final configuration with good agreement with experimental results. More often the trigger is analyzed with geotechnical FE models, while the propagation is studied with hydrological models. The possibility of simulating the slope collapse from the trigger to the deposition with the same methods is of great interest in geotechnics. Only a few methods, such as DEM and SPH, can satisfy this need, however they suffer of some disadvantages such as computational effort and numerical instability. This ability of the MPM will be improved and further exploited in the future.

The cone penetration problem is studied in Chapter 9. From a detailed literature review it can be concluded that, despite the CPT has been intensively studied, numerical simulations of cone penetration, considering the effect of the drainage conditions, are rare because of the high complexity of the phenomenon. Indeed, to the author's knowledge, Silva et al. (2006) and Yi et al. (2012) are the only contributions. The implemented MPM can simulate large deformations and generation/dissipation of pore pressure during cone penetration. The soil-cone contact is simulated realistically and the cone roughness can be taken into account. In addition to this, the mechanical behavior of clay is simulated with the MCC model, which is able to capture most of the non linearities of the soil response.

The two-phase MPM can capture the effect of pore pressure dissipation during cone penetration, showing higher tip resistances in drained and partially drained conditions than in undrained conditions. The tip resistance and the resistance ratio are a function of the cone roughness too. Numerical results of this study agree with experimental evidence therefore confirming the capability of the model to simulate CPT.

This study confirms that the MPM is a very powerful numerical method. It can

be applied to a wide set of physical problems in geotechnical engineering; indeed, multiphase material, contact between bodies and complex constitutive models can be considered. Large deformation problems are its preferential field of applicability, therefore it can be widely used to study geotechnical problems such as landslides, embankment and dam failure, pile installations etc. The field of applicability can be further extended by future developments of the method. It is on the interest of the author to be involved in this research activity.

A

Basics of continuum mechanics

A basic knowledge in continuum mechanics is fundamental to understand the numerical models based on the continuum approach, such as the FEM and the MPM. This Appendix summarizes the main issue of continuum mechanics in order to give to the reader the basic knowledge to understand the mathematical formulation adopted in this thesis. The exposition follows Belytschko et al. (2013), where the reader can also find further details.

Continuum mechanics is concerned with models of solids and fluids in which the properties and response can be characterized by smooth functions of spatial variables, with at most a limited number of discontinuities. It ignores inhomogeneities such as molecular, grain or crystal structures. The objective of continuum mechanics is to provide a description to model the macroscopic behavior of fluids, solids and structures.

A.1 Motion and deformation

Consider a body in an initial state at a time t=0 as shown in Figure A.1; the domain of the body in the initial state is denoted by Ω_0 and called the initial configuration. In describing the motion of the body and deformation, we also need a configuration to which various equations are referred; this is called the reference configuration. Unless we specify otherwise, the initial configuration is used as the reference configuration. However, other configurations can also be used as the reference configuration. The significance of the reference configuration lies in the fact that motion is defined with respect to this configuration.

In this Chapter, the undeformed configuration is considered to be the initial con-

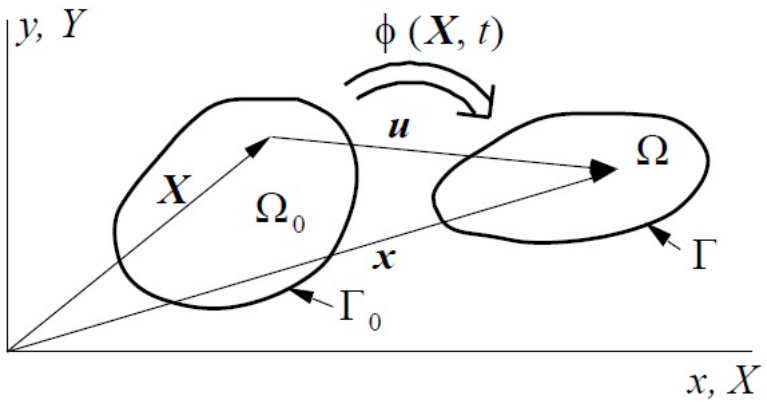

Figure A.1: Initial and deformed configuration

figuration unless we specifically say otherwise, so it is tacitly assumed that in most cases the initial, reference, and undeformed configurations are identical.

The current configuration of the body is denoted by Ω; this will often also be called the deformed configuration. The domain currently occupied by the body will also be denoted by Ω. The boundary of the domain is denoted by $\partial\Omega$.

The motion of the body is described by

$$\boldsymbol{x} = \phi(\boldsymbol{X}, t) \quad \text{or} \quad x_i = \phi_i(\boldsymbol{X}, t) \tag{A.1}$$

where $\boldsymbol{x} = x_i \boldsymbol{e}_i$ is the position at time t of the material point $\boldsymbol{X}$. The coordinates $\boldsymbol{x}$ give the spatial position of a point, and are called spatial, or Eulerian coordinates. The function $\phi(\boldsymbol{X}, t)$ maps the reference configuration into the current configuration at time t, and is often called a mapping or map.

The deformation gradient can now be defined as:

$$\boldsymbol{F} = \frac{\partial \boldsymbol{x}}{\partial \boldsymbol{X}} \tag{A.2}$$

When the reference configuration is identical to the initial configuration, as assumed in this Chapter, the position vector $\boldsymbol{x}$ of any point at time $t = 0$ coincides with the material coordinates, so

$$\boldsymbol{X} = \boldsymbol{x}(\boldsymbol{X}, 0) \equiv \phi(\boldsymbol{X}, 0) \quad \text{or} \quad X_i = x_i(\boldsymbol{X}, 0) = \phi(\boldsymbol{X}, 0) \tag{A.3}$$

A.2 Eulerian and Lagrangian descriptions

Two approaches are used to describe the deformation and response of a continuum. In the first approach, the independent variables are the material coordinates $\boldsymbol{X}$ and the time t; this description is called a material description or Lagrangian description. In the second approach, the independent variables are the spatial coordinates $\boldsymbol{x}$ and the time t. This is called a spatial or Eulerian description.

In fluid mechanics, it is often impossible and unnecessary to describe the motion with respect to a reference configuration. For example, if we consider the flow around an airfoil, a reference configuration is usually not needed for the behavior of the fluid, which is independent of its history. On the other hand, in solids, the stresses generally depend on the history of deformation and an undeformed configuration must be specified to define the strain. Because of the historydependence of most solids, Lagrangian descriptions are prevalent in solid mechanics.

A.3 Displacement, velocity and acceleration

The displacement is given by the difference between the current position and the original position (see Fig. A.1), so

$$\boldsymbol{u}(\boldsymbol{X},t) = \phi(\boldsymbol{X},t) - \phi(\boldsymbol{X},0) = \phi(\boldsymbol{X},t) - \boldsymbol{X} \quad \text{or} \quad u_i = \phi_i(X_j,t) - X_i \tag{A.4}$$

where $\boldsymbol{u}(\boldsymbol{X},t) = u_i \boldsymbol{e}_i$. The displacement is often written as

$$\boldsymbol{u} = \boldsymbol{x} - \boldsymbol{X} \quad \text{or} \quad u_i = x_i - X_i \tag{A.5}$$

The velocity $\boldsymbol{v}(\boldsymbol{X},t)$ is the rate of change of the position vector $\boldsymbol{x}$, i.e. the time derivative with $\boldsymbol{X}$ held constant. Time derivatives with $\boldsymbol{X}$ held constant are called material time derivatives; or sometimes material derivatives. Material time derivatives are also called total derivatives. The velocity can be written in the various forms shown below

$$\boldsymbol{v}(\boldsymbol{X},t) = \dot{\boldsymbol{x}} = \frac{\partial \phi(\boldsymbol{X},t)}{\partial t} = \frac{\partial u(\boldsymbol{X},t)}{\partial t} = \dot{\boldsymbol{u}} \tag{A.6}$$

The superposed dot denotes a material time derivative.

The acceleration $\boldsymbol{a}(\boldsymbol{X}, t)$ is the rate of change of velocity of a material point, or in other words the material time derivative of the velocity, and can be written in the forms

$$\boldsymbol{a}(\boldsymbol{X}, t) = \dot{\boldsymbol{v}} = \frac{\partial \boldsymbol{v}(\boldsymbol{X}, t)}{\partial t} = \frac{\partial^2 u(\boldsymbol{X}, t)}{\partial t^2} \tag{A.7}$$

The above expression is called the material form of the acceleration. When the velocity is expressed in terms of the spatial coordinates and the time, i.e. in an Eulerian description as in $\boldsymbol{v}(\boldsymbol{x}, t)$, the material time derivative is obtained as follows:

$$\dot{v}_i(\boldsymbol{x}, t) = \frac{\partial v_i(\boldsymbol{x}, t)}{\partial t} + \frac{\partial v_i(\boldsymbol{x}, t)}{\partial x_j} \frac{\partial \phi_j(\boldsymbol{X}, t)}{\partial t} = \frac{\partial v_i}{\partial t} + \frac{\partial v_i}{\partial x_j} v_j \tag{A.8}$$

The second addend is the convective term; $\frac{\partial v_i}{\partial t}$ is called the spatial time derivative.

A.4 Strain measures

In contrast to linear elasticity, many different measures of strain and strain rate are used in nonlinear continuum mechanics. Only two of these measures are considered here:

1. the Green (Green-Lagrange) strain $\boldsymbol{E}$

2. the rate-of-deformation tensor $\boldsymbol{D}$, also known as the velocity strain or rate-of-strain.

In the following, these measures are defined and some key properties are given. Many other measures of strain and strain rate appear in the continuum mechanics literature; however, the above are the most widely used in finite element methods.

The Green strain tensor $\boldsymbol{E}$ is defined by

$$ds^2 - dS^2 = 2d\boldsymbol{X} \times \boldsymbol{E} \times d\boldsymbol{X} \quad \text{or} \quad dx_i dx_i - dX_i dX_i = 2dX_i E_{ij} dX_j \tag{A.9}$$

so it gives the change in the square of the length of the material vector $d\boldsymbol{X}$. The vector $d\boldsymbol{X}$ pertains to the undeformed configuration. Therefore, the Green strain measures the difference of the square of the length of an infinitesimal segment in the current (deformed) configuration and the reference (undeformed) configuration.

The Green strain tensor can be written in terms of deformation gradient $\boldsymbol{F}$ as:

$$\boldsymbol{E} = \frac{1}{2}(\boldsymbol{F}^T \cdot \boldsymbol{F} - \boldsymbol{I}) \tag{A.10}$$

The second measure of strain to be considered here is the rate-of-deformation $\boldsymbol{D}$. It is also called the velocity strain and the stretching tensor. In contrast to the Green strain tensor, it is a rate measure of strain.

In order to develop an expression for the rate-of-deformation, we first define the velocity gradient $\boldsymbol{L}$ by

$$\boldsymbol{L} = \frac{\partial \boldsymbol{v}}{\partial \boldsymbol{x}} = (\nabla \boldsymbol{v})^T \quad \text{or} \quad L_{ij} = \frac{\partial v_i}{\partial x_j} \tag{A.11}$$

$$d\boldsymbol{v} = \boldsymbol{L} \times d\boldsymbol{x} \quad \text{or} \quad dv_i = L_{ij} dx_j \tag{A.12}$$

In the above, the symbol ∇ preceding the function denotes the spatial gradient of the function, i.e., the derivatives are taken with respect to the spatial coordinates. The velocity gradient tensor can be decomposed into symmetric and skew symmetric parts by

$$\boldsymbol{L} = \frac{1}{2}(\boldsymbol{L} + \boldsymbol{L}^T) + \frac{1}{2}(\boldsymbol{L} - \boldsymbol{L}^T) \tag{A.13}$$

This is a standard decomposition of a second order tensor or square matrix: any second order tensor can be expressed as the sum of its symmetric and skew symmetric parts in the above manner.

The rate-of-deformation $\boldsymbol{D}$ is defined as the symmetric part of $\boldsymbol{L}$, i.e. the first term on the right hand side of A.13 and the spin $\boldsymbol{W}$ is the skew symmetric part of $\boldsymbol{L}$, i.e. the second term on the right hand side of A.13. Using these definitions, we can write

$$\boldsymbol{L} = \boldsymbol{D} + \boldsymbol{W} \tag{A.14}$$

$$\boldsymbol{D} = \frac{1}{2}(\boldsymbol{L} + \boldsymbol{L}^T) \tag{A.15}$$

$$\boldsymbol{W} = \frac{1}{2}(\boldsymbol{L} - \boldsymbol{L}^T) \tag{A.16}$$

It can be demonstrated that the rate-of-deformation is a measure of the rate of change of the square of the length of infinitesimal material line segments. The definition is

$$\frac{\partial}{\partial t}(ds^2) = \frac{\partial}{\partial t}(d\boldsymbol{x} \cdot d\boldsymbol{x}) = 2d\boldsymbol{x} \cdot \boldsymbol{D} \cdot d\boldsymbol{x} \quad \forall d\boldsymbol{x} \tag{A.17}$$

The rate-of-deformation can be related to the rate of the Green strain tensor.

$$\boldsymbol{D} = \boldsymbol{F}^{-T} \cdot \dot{\boldsymbol{E}} \cdot \boldsymbol{F}^{-1} \tag{A.18}$$

where $\boldsymbol{F}$ is the deformation gradient.

A.5 Stress measures

In nonlinear problems, various stress measures can be defined. Here the Cauchy stress tensor will be considered. The expression for the traction $\boldsymbol{t}$ in terms of the Cauchy stress σ is called Cauchys law or sometimes the Cauchy hypothesis.

$$\boldsymbol{t}(\boldsymbol{n}) = \boldsymbol{\sigma} \cdot \boldsymbol{n} \tag{A.19}$$

where

$$\boldsymbol{t}(\boldsymbol{n}) = \lim_{\Delta A \to 0} \frac{\Delta \boldsymbol{T}}{\Delta A} \tag{A.20}$$

It involves the normal $\boldsymbol{n}$ to the current surface of area A and the force $\boldsymbol{T}$ on the current surface. For this reason, the Cauchy stress is often called the physical stress or true stress.

Many constitutive equations are designed in the form of a relation between a stress-rate and a strain-rate (or the rate of deformation tensor). The mechanical response of a material should not depend on the frame of reference. In other words, material constitutive equations should be frame indifferent (objective). In continuum mechanics, objective stress rates are time derivatives of stress that do not depend on the frame of reference. There are numerous objective stress rates in continuum mechanics, this study adopt the Jaumann stress rate:

$$\boldsymbol{\sigma}^{J} = \dot{\boldsymbol{\sigma}} - \boldsymbol{W} \cdot \boldsymbol{\sigma} + \boldsymbol{\sigma} \cdot \boldsymbol{W}^{T} \tag{A.21}$$

Equation A.21 shows that the material derivative of the Cauchy stress is the sum of the rate of change due to the material response (term on the left hand side) and the change of stress due to rotation (last two terms on the right hand side).

B

Damped vibrations

This appendix provide and introduction on the behavior of single degree of freedom oscillatory system in order to help the reader to understand Section 6.2. Verruijt (1996) is followed as reference.

Consider the system of a single mass, supported by a spring and a dashpot, in which the damping is of a viscous character. According to Newton's second law the equation of motion of the mass is

$$m\frac{d^2u}{dt^2} = P(t) \tag{B.1}$$

where $P(t)$ is the total force acting upon the mass m, and u is the displacement of the mass.

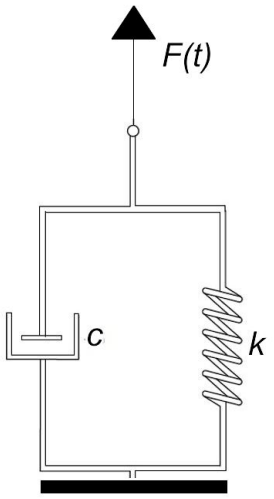

Figure B.1: Single degree of freedom system supported by a spring and a Dashpot

Assume that the total force P consists of an external force $F(t)$, and the reaction of a spring and a dashpot. In its simplest form a spring leads to a force linearly proportional to the displacement u, and a dashpot leads to a response linearly proportional to the velocity du/dt. If the spring constant is k and the viscosity of the dashpot is c, the total force acting upon the mass is

$$P(t) = F(t) - ku - c\frac{du}{dt} \tag{B.2}$$

Thus the equation of motion for the system is

$$m\frac{d^2u}{dt^2} + c\frac{du}{dt} + ku = F(t) \tag{B.3}$$

Consider a perturbation of the system and no external force; in this case the oscillations of the system are called free vibrations.

Let introduce:

$$\omega_0 = \sqrt{\frac{k}{m}} \tag{B.4}$$

$$2\zeta = \frac{c}{m\omega_0} = \frac{c}{\sqrt{km}} \tag{B.5}$$

where ω_0 is the natural frequency of the undamped system and ζ represents a measure of the damping in the system.

Equation B.3 can be written as:

$$\frac{d^2u}{dt^2} + 2\zeta\omega_0\frac{du}{dt} + \omega_0^2 u = 0 \tag{B.6}$$

This is an ordinary differential equation, with constant coefficients.

The solution must have the form:

$$u = A\exp(\alpha t) \tag{B.7}$$

where A is a constant related to the initial conditions and α is one of the root of the equation:

$$\alpha^2 + 2\zeta\omega_0\alpha + \omega_0^2 = 0 \tag{B.8}$$

Equation B.8 can have real or complex root depending on the sign of its discriminant, which is:

$$\frac{\Delta}{4} = \omega_0^2(\zeta^2 - 1) \tag{B.9}$$

Thus, the character of the response of the system depends on the value of the damping ratio ζ. The three possible cases, i.e. $\Delta < 0$, $\Delta = 0$ and $\Delta > 0$, are considered in the following:

Small damping When $\zeta < 1$ the roots of the characteristic equation (B.8) are both complex:

$$\alpha_{1,2} = -\zeta\omega_0 \pm i\omega_0\sqrt{\zeta^2 - 1} \tag{B.10}$$

where $i = \sqrt{-1}$ and the solution can be written as:

$$u = A\exp(i\omega_1 t)\exp(-\zeta\omega_0 t) + B\exp(-i\omega_1 t)\exp(-\zeta\omega_0 t) \tag{B.11}$$

or alternatively as:

$$u = (C\cos\omega_1 t + D\sin\omega_1 t)\exp(-\zeta\omega_0 t) \tag{B.12}$$

where $\omega_1 = \omega_0\sqrt{1-\zeta^2}$ represents the frequency of the vibrations. The coefficients A, B, C, D depends on the initial conditions. In this case the system is said to be underdamped and it does oscillate, but the amplitude of oscillations reduces in time (Fig. B.2a).

Critical damping When $\zeta = 1$ the characteristic equation has two coincident real roots and the damping is said to be critical. The solution is:

$$u = (A + Bt)\exp(-\omega_0 t) \tag{B.13}$$

in which the constants A and B depends on the initial conditions. The system does not oscillate.

Large damping When $\zeta > 1$ the characteristic equation has two real root and the solution assumes the form:

$$u = A\exp(-\alpha_1 t) + B\exp(-\alpha_2 t) \tag{B.14}$$

where

$$\alpha_1 = \omega_0(-\zeta + \sqrt{\zeta^2 - 1}) \tag{B.15}$$
$$\alpha_2 = \omega_0(-\zeta - \sqrt{\zeta^2 - 1}) \tag{B.16}$$

In this case the system is overdamped and does not oscillate, but monotonously tends towards the equilibrium state (Fig. B.2b).

The behavior of the damper The damper has been so far characterized by the viscosity of the dashpot c. Alternatively this element can be characterized by a response time of the spring-dashpot combination. The response of a system consisting of a spring and a dashpot, connected in parallel, to a unit step load of magnitude F_0 is

$$u = \frac{F_0}{k}[1 - \exp(-t/t_r)] \tag{B.17}$$

where t_r is the response time of the system, defined by

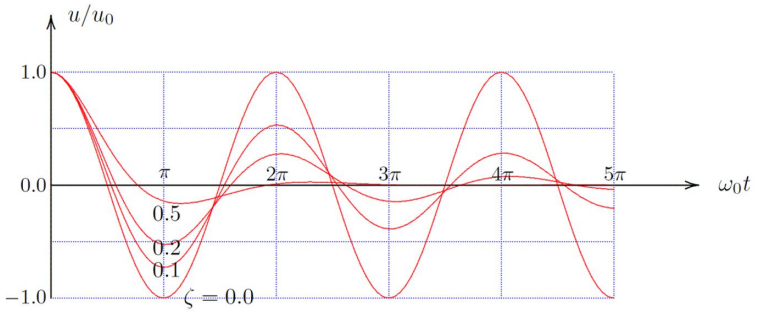

(a) Free vibrations of an underdamped system.

(b) Free vibrations of an overerdamped system.

Figure B.2: Free vibrations

$$t_r = c/k \tag{B.18}$$

This quantity expresses the time scale of the response of the system. After a time $t \approx 4t_r$ the system has reached its final equilibrium state, in which the spring dominates the response.

This feature should be considered when the spring-dashpot element is subjected to constant load. In other terms, when a Kelvin-Voigt element is applied at the boundary of the mesh and is constantly loaded, the boundary will experience an increase of displacement in time whose equilibrium value depends on the spring stiffness.

Bibliography

Aad, G., E. Abat, J. Abdallah, A. Abdelalim, A. Abdesselam, O. Abdinov, B. Abi, M. Abolins, H. Abramowicz, E. Acerbi, et al. (2008). The atlas experiment at the cern large hadron collider. *Journal of Instrumentation 3*(08), S08003.

Aas Nost, H. (2011). *Undrained soft soil modelling with the Material Point Method*. Master thesis, Norwegian University of science and technology.

Abbo, A. J. and S. W. Sloan (1995). A smooth hyperbolic approximation to the mohr-coulomb yield criterion. *Computers & Structures 54*(3), 427–441.

Abe, K., K. Soga, and S. Bandara (2013). Material Point Method for Coupled Hydromechanical Problems. *Journal of Geotechnical and Geoenvironmental Engineering 140*, 1–16.

Al-Kafaji, I. K. J. (2013). *Formulation of a Dynamic Material Point Method (MPM) for Geomechanical Problems*. Ph. d. thesis, University of Struttgart, Germay.

Alder, B. J. and T. Wainwright (1959). Studies in molecular dynamics. i. general method. *The Journal of Chemical Physics 31*(2), 459–466.

Allahdadi, F. A., T. C. Carney, J. R. Hipp, L. D. Libersky, and A. G. Petschek (1993). High strain lagrangian hydrodynamics: a three dimensional sph code for dynamic material response. Technical report, DTIC Document.

Alonso, E., N. Pinyol, and A. Yerro (2014). Mathematical Modelling of Slopes. In *Procedia Earth and Planetary Science*, Volume 9, pp. 64–73. Elsevier B.V.

Alonso, E. and F. Zabala (2011, September). Progressive failure of Aznalcóllar dam using the material point method. *Géotechnique 61*(9), 795–808.

Andersen, S. (2009a). *Material-point analysis of large-strain problems: Modelling of landslides*. Ph. D. thesis, Aalborg University, Faculty of Engineering and Science, Research Group for Computational Mechanics.

Andersen, S. (2009b). *Material-point analysis of large-strain problems: Modelling of landslides*. Ph. D. thesis, AAlborg University.

Andersen, S. and L. Andersen (2010a, April). Analysis of spatial interpolation in the material-point method. *Computers & Structures 88*(7-8), 506–518.

Andersen, S. and L. Andersen (2010b, April). Modelling of landslides with the material-point method. *Computational Geosciences 14*(1), 137–147.

Andreykiv, A., F. Keulen, D. J. Rixen, and E. Valstar (2012). A level-set-based large sliding contact algorithm for easy analysis of implant positioning. *International Journal for Numerical Methods in Engineering 89*(10), 1317–1336.

Atkinson, J. H. and P. L. Bransby (1978). *The mechanics of soil*. McGraw-Hill London.

Atluri, S., J. Cho, and H.-G. Kim (1999). Analysis of thin beams, using the meshless local petrov–galerkin method, with generalized moving least squares interpolations. *Computational Mechanics 24*(5), 334–347.

Atluri, S. and T. Zhu (1998). A new meshless local petrov-galerkin (mlpg) approach in computational mechanics. *Computational mechanics 22*(2), 117–127.

Augarde, C. and C. Heaney (2009). The use of meshless methods in geotechnics. In *Proceedings of the 1st International Symposium on Computational Geomechanics (COMGEO I)*, Number Comgeo I, Juan-les-Pins, France, pp. 311–320.

Baligh, M. and J. Levadoux (1986). Consolidation after undrained piezocone penetration. II: interpretation. *Journal of geotechnical engineering 112*(7), 727–745.

Baligh, M. M. (1985). Strain path method. *Journal of Geotechnical Engineering 111*(9), 1108–1136.

Bandara, S. and K. Soga (2015, January). Coupling of soil deformation and pore fluid flow using material point method. *Computers and Geotechnics 63*, 199–214.

Bandara, S. S. (2013). *Material Point Method to simulate Large Deformation Problems in Fluid-saturated Granular Medium*. Ph. D. thesis, Cambridge, UK.

Baran, S. (1968). *Monopoly Capital. An Essay on the American Economic and Social Order*.

Bardenhagen, S. (2002, July). Energy Conservation Error in the Material Point Method for Solid Mechanics. *Journal of Computational Physics 180*(1), 383–403.

Bardenhagen, S., J. Brackbill, and D. Sulsky (2000a, September). Numerical study of stress distribution in sheared granular material in two dimensions. *Physical review. E 62*(3), 3882–90.

Bardenhagen, S., J. Brackbill, and D. Sulsky (2000b). Shear deformation in granular material. In *11th International Detonation Symposium, Snowmass, CO*, pp. 547–555.

Bardenhagen, S., J. Brackbill, and D. Sulsky (2000c, July). The material-point method for granular materials. *Computer Methods in Applied Mechanics and Engineering 187*(3-4), 529–541.

Bardenhagen, S., J. Guilkey, K. Roessig, J. Brackbill, W. Witzel, and J. Foster (2001). An improved contact algorithm for the material point method and application to stress propagation in granular material. *Computer Modeling in Engineering and Sciences 2*, 509–522.

Bardenhagen, S. and E. Kober (2004). The generalized interpolation material point method. *Computer Modeling in Engineering and Sciences 5*(6), 477–495.

Bardet, J. (1992). A viscoelastic model for the dynamic behavior of saturated poroelastic soils. *Journal of applied mechanics 59*(March).

Batchelor, G. K. (2000). *An introduction to fluid dynamics*. Cambridge university press.

Bathe, K.-J. (2006). *Finite element procedures*. Klaus-Jurgen Bathe.

Belytschko, T. and Y. Krongauz (1998). Efg approximation with discontinuous derivatives. *International Journal for Numerical Methods in Engineering 41*(7), 1215–1233.

Belytschko, T., W. K. Liu, B. Moran, and K. Elkhodary (2013). *Nonlinear finite elements for continua and structures* (Second ed.). John Wiley & Sons.

Belytschko, T., Y. Y. Lu, and L. Gu (1994). Element-free galerkin methods. *International journal for numerical methods in engineering 37*(2), 229–256.

Beuth, L. (2011). Solution of quasi-static large-strain problems by the material point method. *Internationsl Journal for Numerical and Analytical Methods in Geomechanics 35*(13), 1451–1465.

Beuth, L. (2012). *Formulation and Application of a Quasi-Static Material Point Method*. Ph. d. thesis, University of Struttgart.

Beuth, L., T. Benz, and P. A. Vermeer (2008). Large deformation analysis using a quasi-static material poin method. *Journal of Theoretical and Applied Mechanics 38*(1-2), 45–60.

Beuth, L., T.Benz, P. A. Vermeer, C. J. Coetzee, P. Bonnier, P. van den Berg, and T. Benz (2007). Formulation and validation of a quasi-static material point method. In *Proceedings of the 10th international symposium on numerical methods in Geomechanics (NUMOG)*, Rhodes, Greece, pp. 189–195.

Beuth, L. and P. A. Vermeer (2013). Large deformation analysis of cone penetration testing in undrained clay.

Biot, M. (1956a). Theory of propagation of elastic waves in a fluidsaturated porous solid. I. Lowfrequency range. *The Journal of the Acoustical Society of America 28*(2).

Biot, M. (1956b). Theory of propagation of elastic waves in a fuid-saturatedporous solid. ii. higher frequency range. *The Journal of the Acoustical Society of America 28*, 179–191.

Biot, M. (1972). Theory of finite deformations of porous solids. *Indiana University Mathematics Journal 21*(7), 597–620.

Biot, M. a. (1941). General Theory of Three-Dimensional Consolidation. *Journal of Applied Physics 12*(2), 155.

Biot, M. a. (1955). Theory of Elasticity and Consolidation for a Porous Anisotropic Solid. *Journal of Applied Physics 26*(2), 182.

Biot, M. A. (1956c). Theory of propagation of elastic waves in a fluid-saturated porous solid. i. low frequency range. *The Journal of the Acoustical Society of America 28*(2), 168–178.

Bolton, M. (1986). The strength and dilatancy of sands. *Geotechnique 36*(1), 65–78.

Borja, R., C. Tamagnini, and E. Alarcón (1998). Elastoplastic consolidation at finite strain part 2: finite element implementation and numerical examples. *Computer Methods in Applied Mechanics and Engineering 5*, 103–122.

Borja, R. I., C. Tamagnini, and A. Amorosi (1997). Coupling plasticity and energy-conserving elasticity models for clays. *Journal of geotechnical and geoenvironmental engineering 123*(10), 948–957.

Borjia, R. and E. Kavazanjian (1985). A viscoplasticity model for the stress-strain-time behaviour of wet clays. *Geotechnique 35*, 283–298.

Brackbill, J. and H. Ruppel (1986). Flip: A method for adaptively zoned, particle-in-cell calculations of fluid flows in two dimensions. *Journal of Computational Physics 65*(2), 314–343.

Brackbill, J. U., D. B. Kothe, and H. M. Ruppel (1988). Flip: A low-dissipation, particle-in-cell method for fluid flow. *Computer Physics Communications 48*(1), 25–38.

Bui, H. H., K. Sako, and R. Fukagawa (2007). Numerical simulation of soil–water interaction using smoothed particle hydrodynamics (sph) method. *Journal of Terramechanics 44*(5), 339–346.

Bui, H. H., K. Sako, R. Fukagawa, and J. Wells (2008). Sph-based numerical simulations for large deformation of geomaterial considering soil-structure interaction. In *The 12th International Conference of International Association for Computer Methods and Advances in Geomechanics (IACMAG)*, Volume 1, pp. 570–578. Citeseer.

Burland, J. (1990). 30th rankine lecture: On the compressibility and shear strength of natural clays. *Gotechnique 40*(3), 327–378.

Campanella, R., D. Gillespie, and P. Robertson (1982). Pore pressures during cone penetration testing. In A. Verruijt, F. Beringen, and de Leeuw E.H. (Eds.), *Proceedings of the 2nd European Symposium on Penetration Testing*, pp. 507–512. Balkema, Rotterdam.

Carter, J., J. Booker, and C. Wroth (1982). *Soil mechanics - Transient and cyclic loads*, Chapter A critical state model for ciclic loading, pp. 219–252. Wiley.

Chen, J.-S., C. M. O. L. Roque, C. Pan, and S. T. Button (1998, August). Analysis of metal forming process based on meshless method. *Journal of Materials Processing Technology 80-81*, 642–646.

Chung, S., M. F. Randolph, and J. A. Schneider (2006). Effect of penetration rate on penetrometer resistance in clay. *Journal of Geotechnical and Geoenvironmental Engineering* (September), 1188–1196.

Coetzee, C., A. Basson, and P. Vermeer (2007, April). Discrete and continuum modelling of excavator bucket filling. *Journal of Terramechanics 44*(2), 177–186.

Coetzee, C. J. (2003). *The Modelling of Granular Flow Using the Particle-in-Cell Method*. Phd thesis, Stellenbosch.

Coetzee, C. J. (2005). The material point method. Technical Report November, University of Stellenbosh, Stellenbosh, South Africa.

Coetzee, C. J., P. A. Vermeer, and A. H. Basson (2005, August). The modelling of anchors using the material point method. *International Journal for Numerical and Analytical Methods in Geomechanics 29*(9), 879–895.

Courant, R. et al. (1943). Variational methods for the solution of problems of equilibrium and vibrations. *Bull. Amer. Math. Soc 49*(1), 1–23.

Cummins, S. and J. Brackbill (2002, August). An Implicit Particle-in-Cell Method for Granular Materials. *Journal of Computational Physics 180*(2), 506–548.

Cundall, P. (1987). Distinct element models of rock and soil structure. *Analytical and computational methods in engineering rock mechanics 4*, 129–163.

Cundall, P. (2001). *FLAC Manual: A Computer Program for Fast Lagrangian Analysis of Continua*.

Cundall, P. A. and O. D. Strack (1979). A discrete numerical model for granular assemblies. *Geotechnique 29*(1), 47–65.

Cuomo, S., N. Prime, a. Iannone, F. Dufour, L. Cascini, and F. Darve (2012, August). Large deformation FEMLIP drained analysis of a vertical cut. *Acta Geotechnica*.

Dafalias, Y. F. and L. R. Herrmann (1980). *Soil mechanics - Transient and cyclic loads*, Chapter Bouclays surface formulation of soil plasticity, pp. 253–282. Wiley.

Davis, R. O. and A. P. Selvadurai (2002). *Plasticity and geomechanics*. Cambridge University Press.

De Borst, R., M. Crisfield, J. Remmers, and C. Verhoosel (2012). Non-linear finite element analysis of solids and structures. *John Wiley & Sons*.

De Borst, R. and P. Vermeer (1984). Possibilites and limitations of finite elements for limit analysis. *Geotechnique 34*(2), 199–210.

DeJong, J. and M. Randolph (2012). Influence of Partial Consolidation during Cone Penetration on Estimated Soil Behavior Type and Pore Pressure Dissipation Measurements. *Journal of Geotechnical and geoenvironmental Engineering* (July), 777–788.

Detournay, C. and E. Dzik (2006). Nodal mixed discretization for tetrahedral elements. In *4th international FLAC symposium, numerical modeling in geomechanics. Minnesota Itasca Consulting Group, Inc. Paper*, Number 07-02.

Donea, J. and A. Huerta (2004). Arbitrary LagrangianEulerian methods. *Encyclopedia of Computational Mechanics* (1969), 1–38.

Douglas, B. and R. Olsen (1981). Soil classification using electric cone penetrometer. In A. Geotechnical Engineering Division (Ed.), *In Proceedings of Symposium on Cone Penetration Testing and Experience*, St. Louis, Missouri, pp. 209–227.

Elkadi, A. and P. Nguyen (2013). Mpm validation with centrifuge tests: pilot case pile installation. Technical Report 1206750-G05-HYE-GG01-Jvm, Deltares, Delft, The Netherlands.

Ferronato, M., A. Mazzia, G. Pini, and G. Gambolati (2007). A meshless method for axisymmetric poroelastic simulations: numerical study. *Int. J. Numer. Methods Eng.* (70), 13461365.

Finnie, I. and M. Randolph (1994). Punch-through and liquefaction induced failure of shallow foundations on calcareous sediments. In *Proc. 7th Int. Conf. on Behaviour of Offshore Structures, Boston*, pp. 217–230.

Gadala, M. and J. Wang (1998). ALE formulation and its application in solid mechanics. *Computer Methods in Applied Mechanics and engineering 167*(98), 33–55.

Gemant, A. and W. Jackson (1937). Xciii. the measurement of internal friction in some solid dielectric materials. *The London, Edinburgh, and Dublin Philosophical Magazine and Journal of Science 23*(157), 960–983.

Gens, A. and D. Potts (1988). Critical state models in computational geomechanics. *Engineering Computations 5*(3), 178–197.

Gingold, R. A. and J. J. Monaghan (1977). Smoothed particle hydrodynamics: theory and application to non-spherical stars. *Monthly notices of the royal astronomical society 181*(3), 375–389.

Godoy, L. and P. Dardati (2001). Validación de modelos en mecánica computacional.

Griffiths, D. (1982). Elasto-plastic analyses of deep foundations in cohesive soil. *International Journal for Numerical and Analytical Methods in Geomechanics 6*(2), 211–218.

Guilkey, J. and J. Weiss (2001). An implicit time integration strategy for use with the material point method. In *Proceedings from the First MIT Conference on Computational Fluid and Solid Mechanics*. Citeseer.

Guilkey, J. E., J. B. Hoying, and J. A. Weiss (2006). Computational modeling of multicellular constructs with the material point method. *Journal of biomechanics 39*(11), 2074–2086.

Guilkey, J. E. and J. a. Weiss (2003, July). Implicit time integration for the material point method: Quantitative and algorithmic comparisons with the finite element method. *International Journal for Numerical Methods in Engineering 57*(9), 1323–1338.

Gutfraind, R. and S. B. Savage (1998). Flow of fractured ice through wedge-shaped channels: smoothed particle hydrodynamics and discrete-element simulations. *Mechanics of materials 29*(1), 1–17.

Hagerty, D. J. and R. B. Peck (1971). Heave and lateral movements due to pile driving. *Journal of the Soil Mechanics and Foundations Division 97*(11), 1513–1532.

Harlow, F. H. (1964). The particle-in-cell computing method for fluid dynamics. *Methods in computational physics 3*(3), 319–343.

Harlow, F. H. and M. Evans (1955). A machine calculation method for hydrodynamic problems. Technical report.

Harlow, F. H., M. W. Evans, and E. Bromberg (1957). The particle-in-cell method for hydrodynamic calculations. Technical report, DTIC Document.

Hart, R., P. Cundall, and J. Lemos (1988). Formulation of a three-dimensional distinct element modelpart ii. mechanical calculations for motion and interaction of a system composed of many polyhedral blocks. In *International Journal of Rock Mechanics and Mining Sciences & Geomechanics Abstracts*, Volume 25, pp. 117–125. Elsevier.

Henke, S. Qiu, G. and J. Grabe (2010). A coupled eulerian-lagrangian approach to solve geotechnical problems involving large deformations. In *In 7th European Conference on Numerical Methods in Geotechnical Engineering (NUMGE)*, Trondheim, Norway.

Higo, Y., F. Oka, S. Kimoto, Y. Morinaka, Y. Goto, and Z. Chen (2010). A coupled mpm-fdm analysis method for multi-phase elasto-plastic soils. *Soils and foundations 50*(4), 515–532.

Houlsby, G. (1985). The use of a variable shear modulus in elastic-plastic models for clays. *Computers and Geotechnics 1*(1), 3–13.

Houlsby, G., A. Wheeler, and J. Norbury (1985). Analysis of undrained cone penetration as a steady flow problem. In *Proceedings of the 5th International Conference on Numerical Methods in Geomechanics*, Volume 4, pp. 1767–73.

House, A., J. Oliveira, and M. Randolph (2001). Evaluating the coefficient of consolidation using penetration tests. *International Journal of Physical Modelling in Geotechnics 1*(3), 17–26.

Hrennikoff, A. (1941). Solution of problems of elasticity by the frame-work method. *ASME J. Appl. Mech. 8*, A619A715.

Hu, W. and Z. Chen (2003, August). A multi-mesh MPM for simulating the meshing process of spur gears. *Computers & Structures 81*(20), 1991–2002.

Hu, W. and Z. Chen (2006). Model-based simulation of the synergistic effects of blast and fragmentation on a concrete wall using the mpm. *International journal of impact engineering 32*(12), 2066–2096.

Hu, Y. and M. Randolph (1998). A practical numerical approach for large deformation problems in soil. *International Journal for Numerical and Analytical Methods in Geomechanics 22*(5), 327–350.

Huang, P. and X. Zhang (2011). Contact algorithms for the material point method in impact and penetration simulation. *International Journal for numerical methods in Engineering* (July 2010), 498–517.

Huang, W., D. Sheng, S. Sloan, and H. Yu (2004, October). Finite element analysis of cone penetration in cohesionless soil. *Computers and Geotechnics 31*(7), 517–528.

Idelsohn, S. and E. Oñate (2003). The meshless finite element method. *Internationa Journal for Numerical Methods in Engineering 58*(4), 1–15.

Idelsohn, S., E. Oñate, and F. Del Pin (2003, May). A Lagrangian meshless finite element method applied to fluidstructure interaction problems. *Computers & Structures 81*(8-11), 655–671.

Idelsohn, S., E. Oñate, and F. D. Pin (2004, October). The particle finite element method: a powerful tool to solve incompressible flows with free-surfaces and breaking waves. *International Journal for Numerical Methods in Engineering 61*(7), 964–989.

Idelsohn, S., E. Oñate, F. D. Pin, and N. Calvo (2006, March). Fluidstructure interaction using the particle finite element method. *Computer Methods in Applied Mechanics and Engineering 195*(17-18), 2100–2123.

Ionescu, I., J. Guilkey, M. Berzins, R. M. Kirby, and J. Weiss (2005). Computational simulation of penetrating trauma in biological soft tissues using the material point method. *Studies in health technology and informatics 111*, 213–218.

Iseno, H., H. Kohashi, K. Furumoto, H. Mori, and M. Ohno (2004). Large model tests of levee reinforcement method with toe drain for seepage failure. In *Proc., Annual Symp. of Japanese Geotechnical Society*, Volume 39, pp. 1255–1256.

Jaeger, R., J. DeJong, R. W. Boulanger, H. E. Low, and M. Randolph (2010). Variable penetration rate CPT in an intermediate soil. In Omnipress (Ed.),

Proc., 2nd Int. Symp. on Cone Penetration Testing., Madison.

Janbu, N. and K. Senneset (1974). Effective stress interpretation of in situ static penetration tests. In *Proceedings of the 1st European symposium on penetration testing*, Volume 2, pp. 181–93.

Jassim, I., D. Stolle, and P. Vermeer (2013). Two-phase dynamic analysis by material point method. *International Journal for Numerical and Analytical Methods in Geomechanicsnumerical and analytical methods in Geomechanics 37*, 2502–2522.

Jefferies, M. and K. Been (2006). *Soil liquefaction: a critical state approach*. CRC Press.

Jefferies, M. and M. Davies (1991). Soil classification by the cone penetration test: Discussion. *Canadian Geotechnical Journal 28*(1), 173–176.

Johansson, J. and K. Konagai (2007). Fault induced permanent ground deformations: Experimental verification of wet and dry soil, numerical findings relation to field observations of tunnel damage and implications for design. *Soil Dynamics and Earthquake Engineering 27*(10), 938–956.

Kim, H. Inoue, J. (2007). A stochastic element free seepage flow analysis of heterogeneous subsurface. In S. Pande, G. Pietruszczak (Ed.), *Numerical Models in Geomechanics NUMOG X*, pp. 225–231. Taylor & Francis Group, London.

Kim, K., M. Prezzi, R. Salgado, and W. Lee (2008). Effect of penetration rate on cone penetration resistance in saturated clayey soils. *Journal of Geotechnical and Geoenviromental Engineering* (August), 1142–1153.

Kiousis, P. D., G. Z. Voyiadjis, and M. T. Tumay (1988). A large strain theory and its application in the analysis of the cone penetration mechanism. *International Journal for Numerical and Analytical Methods in Geomechanics 12*(1), 45–60.

Konagai, K. and J. Johansson (2001). Lagrangian Particles for Modeling Large Soil Deformations. In *Proc., Seismic Fault-induced failures*, pp. 101–108.

Konagai, K., J. Johansson, and H. Itoh (2004). Pseudo-three dimensional lagrangian particle finite difference method for modeling earthquake induced soil flows. In *13th World Conference on Earthquake Engineering*, Number 547, Vancouver, B. C: Canada.

Koskinen, M., M. Karstunen, and S. Wheeler (2002). Modelling destructuration and anisotropy of a soft natural clay.

Kouretzis, G. P., D. Sheng, and D. Wang (2014, March). Numerical simulation of cone penetration testing using a new critical state constitutive model for sand. *Computers and Geotechnics 56*, 50–60.

Kurup, P., G. Voyiadjis, and M. Tumay (1994). Calibration chamber studies of piezocone test in cohesive soils. *Journal of Geotechnical Engineering 120*(1), 81–107.

Kutter, B. L. and N. Sathialingam (1992). Elastic-viscoplastic modelling of the rate-dependent dehaviour of clays. *Geotechnique 42*, 427–441.

Ladanyi, B. (1963). Expansion of a cavity in a saturated clay medium. *Journal of the Soil Mechanics and Foundations Division 89*(SM4), 127–161.

Ladanyi, B. and G. Johnston (1974). Behavior of circular footings and plate anchors in permafrost. *Canadian Geotechnical Journal 11*(4), 531–553.

Lehane, B., C. O'Loughlin, M. Randolph, and C. Gaudin (2009, January). Rate effects on penetrometer resistance in kaolin. *Géotechnique 59*(1), 41–52.

Lemos, L. and P. Vaughan (2000). Clay–interface shear resistance. *Geotechnique 50*(1), 55–64.

Levadoux, J.-N. and M. M. Baligh (1980). *Pore pressure dissipation after cone penetration*. Massachusetts Institute of Technology, Department of Civil Engineering, Constructed Facilities Division.

Lewis, R. W. and B. A. Schrefler (1998). *The finite element method in the static and dynamic deformation and consolidation of porous media*. John Wiley.

Lian, Y., X. Zhang, and Y. Liu (2011, November). Coupling of finite element method with material point method by local multi-mesh contact method. *Computer Methods in Applied Mechanics and Engineering 200*(47-48), 3482–3494.

Lian, Y., X. Zhang, and Y. Liu (2012, October). An adaptive finite element material point method and its application in extreme deformation problems. *Computer Methods in Applied Mechanics and Engineering 241-244*, 275–285.

Lian, Y., X. Zhang, X. Zhou, S. Ma, and Y. Zhao (2011). Numerical simulation of explosively driven metal by material point method. *International Journal of Impact Engineering 38*(4), 238–246.

Lim, L., A. Andreykiv, and R. Brinkgreve (2014). On the application of the material point method for offshore foundations. In M. Hicks, Brinkgreve, and A. Rohe (Eds.), *Numerical Methods in geotechnical Engineering*. Taylor and Francis group.

Liu, M. B. and G. R. Liu (2010, February). *Smoothed Particle Hydrodynamics (SPH): an Overview andRecent Developments*, Volume 17.

Love, E. and D. Sulsky (2006, July). An unconditionally stable, energymomentum consistent implementation of the material-point method. *Computer Methods in Applied Mechanics and Engineering 195*(33-36), 3903–3925.

Lu, Q., Y. Hu, M. F. Randolph, and I. C. Bugarski (2004, January). A numerical study of cone penetration in clay. *Géotechnique 54*(4), 257–267.

Lucy, L. B. (1977). A numerical approach to the testing of the fission hypothesis. *The astronomical journal 82*, 1013–1024.

Lunne, T. Robertson, P. and J. Powell (1997). *Cone Penetration Testing in Geotechnical Practice*. Blackie Academic/Chapman & Hall.

Lysmer, J. and R. L. Kuhlemeyer (1969). Finite dynamic model for infinite media. In *Proc. of ASCE*, pp. 859–877.

Ma, J., D. Wang, and M. Randolph (2014). A new contact algorithm in the material point method for geotechnical simulations. *International Journal of Numerical and Analytical Methods in Geomechanics* (March), 1197–1210.

Ma, S., X. Zhang, and X. M. Qiu (2009). Comparison study of mpm and sph in modeling hypervelocity impact problems. *International Journal of Impact Engineering 36*, 272–282.

Martinelli, M. and A. Rohe (2014, December). Soil-water transition with the material point method: the algorithm. MPM-Dredge workshop, Cambridge.

Masin, D. (2005, April). A hypoplastic constitutive model for clays. *International Journal for Numerical and Analytical Methods in Geomechanics 29*(4), 311–336.

Mast, C., P. Mackenzie-Helnwein, P. Arduino, G. Miller, and W. Shin (2012, June). Mitigating kinematic locking in the material point method. *Journal of Computational Physics 231*(16), 5351–5373.

Mayne, P. W. and F. H. Kulhawy (1982). k_0-ocr relationships in soil. *Journal of the Geotechnical Engineering Division 108*(6), 851–872.

Meyerhof, G. (1951). The ultimate bearing capacity of foudations. *Geotechnique 2*(4), 301–332.

Modaressi, H. and L. Laloui (1997). A thermo-viscoplastic constitutive model for clays. *International journal for numerical and analytical methods in geomechanics 21*(5), 313–335.

Monaghan, J. (2012, January). Smoothed Particle Hydrodynamics and Its Diverse Applications. *Annual Review of Fluid Mechanics 44*(1), 323–346.

Monaghan, J. J. (1994). Simulating free surface flows with sph. *J. Comput. Phys.* (110), 399–406.

Moresi, L., F. Dufour, and H.-B. Muhlhaus (2003). A lagrangian integration point finite element method for large deformation modeling of viscoelastic geomaterials. *Journal of Conmputational Physics 184*, 476–497.

Morris, J. P., P. J. Fox, and Y. Zhu (1997). Modeling low reynolds number incompressible flows using sph. *Journal of computational physics 136*(1), 214–226.

Nairn, J. A. (2003). Material point method calculations with explicit cracks. *Computer Modeling in Engineering and Sciences 4*(6), 649–664.

Nazem, M. and D. Sheng (2008). Arbitrary LagrangianEulerian method for largestrain consolidation problems. *International Journal for Numerical and Analytical Methods in Geomechanics 32*(September 2007), 1023–1050.

Numada, M. and K. Konagai (2003). Material point method for run out analysis of earthquake-induced long-traveling soil flows. *JSCE Journal of Earthquake Engineering 27*, 3–6.

Nuygen, P., A. F. van Tol, A. S. K. Elkadi, and A. Rohe (2014). Modelling of pile installation using the material point method (mpm). *Numerical Methods in geotechnical Engineering*, 271.

Oñate, E., M. a. Celigueta, and S. R. Idelsohn (2006, November). Modeling bed erosion in free surface flows by the particle finite element method. *Acta Geotechnica 1*(4), 237–252.

Oñate, E., S. R. Idelsohn, F. Del Pin, and R. Aubry (2004, September). the Particle Finite Element Method an Overview. *International Journal of Computational Methods 01*(02), 267–307.

Oger, L. and S. Savage (1999). Smoothed particle hydrodynamics for cohesive grains. *Computer methods in applied mechanics and engineering 180*(1), 169–183.

Ohta, H. and C. P. Wroth (1976). Anisotropy and stress reorientation in clay under load. In Blacksburg (Ed.), *Proc. 2nd Int. Conf. on Numerical Methods in Geomechanics*, Volume 1, pp. 319–328.

Oliveira, J., M. Almeida, H. Motta, and M. Almeida (2011). Influence of penetration rate on penetrometer resistance. *Journal of Geotechnical and Geoenvironmental Engineering 137*(7), 695–703.

Pastor, M., O. Zienkiewicz, and A. Chan (1990). Generalized plasticity and the modelling of soil behaviour. *International Journal for Numerical and Analytical Methods in Geomechanics 14*(3), 151–190.

Potyondy, J. (1961). Skin friction between various soils and construction materials. *Geotechnique*, 339–353.

Praveen Kumar, R., G. Dodagoudar, and B. Rao (2008). Meshfree modelling of two-dimensional contaminant transport through unsaturated porous media. In D. Toll, C. Augarde, D. Gallipoli, and S. Wheeler (Eds.), *Unsaturated Soils: Advances in Geo-Engineering*, pp. 861866. Taylor & Francis Group, London.

Puzrin, A. M., E. E. Alonso, and N. Pinyol (2010). *Geomechanics of failures*, Chapter 6 - Braced excavation collapse: Nicoll Highway, Singapore, pp. 152–181. Springer Netherlands.

Qiu, G. (2014). Numerical analysis of penetration tests in soils. In J. Grabe (Ed.), *Ports for Container Ships of future generations*, Number 1920, Hamburg, Germany, pp. 183–196.

Qiu, G. and J. Grabe (2011, September). Explicit modeling of cone and strip footing penetration under drained and undrained conditions using a visco-hypoplastic model. *Geotechnik 34*(3), 205–217.

Qiu, G. and J. Grabe (2012, October). Active earth pressure shielding in quay wall constructions: numerical modeling. *Acta Geotechnica 7*(4), 343–355.

Qiu, G. and S. Henke (2011, October). Controlled installation of spudcan foundations on loose sand overlying weak clay. *Marine Structures 24*(4), 528–550.

Qiu, G., S. Henke, and J. Grabe (2011, January). Application of a Coupled EulerianLagrangian approach on geomechanical problems involving large deformations. *Computers and Geotechnics 38*(1), 30–39.

Quek, S. and G. Liu (2003). *Finite Element Method: A Practical Course: A Practical Course*. Butterworth-Heinemann.

Rahman, A. (1964). Correlations in the motion of atoms in liquid argon. *Physical Review 136*(2A), A405.

Randolph, M. (2004). Characterisation of soft sediments for offshore applications. In V. da Fonseca and Mayne (Eds.), *Proc. 2nd Int. Conf. on Site Characterisation, Porto*, Rotterdam, pp. 209–232. Millpress.

Randolph, M., J. Carter, and C. Wroth (1979). Driven piles in claythe effects of installation and subsequent consolidation. *Geotechnique 29*(4), 361–393.

Randolph, M. and S. Hope (2004). Effect of cone velocity on cone resistance and excess pore pressures. In *Proc., Int. Symp. on Engineering Practice and Performance of Soft Deposits*, pp. 147–152. Yodagawa Kogisha Co., Ltd.

Randolph, M. and C. Wroth (1979). An analytical solution for the consolidation around a driven pile. *International Journal for Numerical and Analytical Methods in geomechanics 3*(August 1978), 217–229.

Randolph, M. F. (2003, January). Science and empiricism in pile foundation design. *Géotechnique 53*(10), 847–875.

Robertson, P. (1990). Soil classification using the cone penetration test. *Canadian Geotechnical Journal 27*(1), 151–158.

Robertson, P., J. Sully, D. Woeller, T. Lunne, J. Powell, and D. Gillespie (1992). Estimating coefficient of consolidation from piezocone tests. *Canadian Geotechnical Journal 29*(v), 539–550.

Robertson, P. and C. Wride (1998). Evaluating cyclic liquefaction potential using the cone penetration test. *Canadian Geotechnical Journal 35*(3), 442–459.

Robertson, P. K., R. Campanella, D. Gillespie, and J. Greig (1986). Use of piezometer cone data. In *Use of in situ tests in geotechnical engineering*, pp. 1263–1280. ASCE.

Robinson, J. and J. S. Przemieniecki (1985). *Early FEM pioneers*. Robinson and Associates.

Rohe, A. and P. A. Vermeer (2014, July). Multiphase modelling of large deformations using mpm: Applications in geotechnics and soil-water transition. Colloquium at University of Padova.

Roscoe, K. and J. Burland (1968). *Engineering plasticity*, Chapter On generalised stress strain behaviour of wet clay, pp. 535–609. Cambridge University Press, Cambridge.

Roy, M., R. Blanchet, F. Tavenas, and P. L. Rochelle (1981). Behaviour of a sensitive clay during pile driving. *Canadian Geotechnical Journal 18*(1), 67–85.

Sagaseta, C. and A. Whittle (2001). Prediction of ground movements due to pile driving in clay. *Journal of Geotechnical and Geoenvironmental Engineering* (January), 55–66.

Salgado, R. (1997). Cavity expansion and penetration resistance in sand. *Journal of Geotechnical and Geoenviromental Engineering*, 344–354.

Schanz, T. and P. Vermeer (1998). On the stiffness of sands. *Géotechnique 48*, 383–387.

Schmertmann, J. H. (1978). Guidelines for cone penetration test (performance and design). Technical report.

Schneider, J., B. M. Lehane, and F. Schnaid (2007). Velocity effects on piezocone measurements in normally and over consolidated clays. *International Journal of Physical Modelling in Geotechnics 7*(2), 23–34.

Schneider, J. A., M. F. Randolph, P. W. Mayne, and N. R. Ramsey (2008a). Analysis of factors influencing soil classification using normalized piezocone tip resistance and pore pressure parameters. *Journal of geotechnical and geoenvironmental engineering 134*(11), 1569–1586.

Schneider, J. A., M. F. Randolph, P. W. Mayne, and N. R. Ramsey (2008b). Using Normalized Piezocone Tip Resistance and Pore Pressure Parameters. *Journal of Geotechnical and Geoenvironmental Engineering 134*(November), 1569–1586.

Schofield, A. and P. Wroth (1968). *Critical state soil mechanics*. McGraw-Hill London.

Silva, M., D. White, and M. Bolton (2006). An analytical study of the effect of penetration rate on piezocone tests in clay. *International Journal for numerical and analytical methods in Geomechanics* (30), 501–527.

Silva, M. F. (2005). *Numerical and physical models of rate effects in soil penetration*. Ph. D. thesis, Cambridge University.

Stolle, D., I. Jassim, and P. Vermeer (2010). Simulation of incompressible problems in geomechanics. In *Computer Methods in Mechanics*, pp. 347–361. Springer.

Strang, G. and G. J. Fix (1973). *An analysis of the finite element method*, Volume 212. Prentice-Hall Englewood Cliffs, NJ.

Sulsky, D., Z. Chen, and H. Schreyer (1994). A particle method for history-dependent materials. *Computer Methods in Applied Mechanics and Engineering 118*(1-2), 179–196.

Sulsky, D. and a. Kaul (2004, March). Implicit dynamics in the material-point method. *Computer Methods in Applied Mechanics and Engineering 193*(12-14), 1137–1170.

Sulsky, D. and H. Schreyer (1993a). The particle-in-cell method as a natural impact algorithm. *ASME applied mechanics division publications AMD 180*, 219–219.

Sulsky, D. and H. Schreyer (1993b). A particle method with large rotations applied to the penetration of history-dependent materials. *ASME applied mechanics division publications AMD 171*, 95–95.

Sulsky, D. and H. Schreyer (1996). Axisymmetric form of the material point method with applications to upsetting and Taylor impact problems. *Computer Methods in Applied Mechanics and Engineering 0457825*(96).

Sulsky, D., H. Schreyer, K. Peterson, R. Kwok, and M. Coon (2007). Using the material-point method to model sea ice dynamics. *Journal of Geophysical Research: Oceans (1978–2012) 112*(C2).

Sulsky, D., S.-J. Zhou, and H. L. Schreyer (1995, May). Application of a particle-in-cell method to solid mechanics. *Computer Physics Communications 87*(1-2), 236–252.

Susila, E. and R. D. Hryciw (2003). Large displacement fem modelling of the cone penetration test (cpt) in normally consolidated sand. *International Journal for Numerical and Analytical Methods in Geomechanics 27*(7), 585–602.

Takeda, H., S. M. Miyama, and M. Sekiya (1994). Numerical simulation of viscous flow by smoothed particle hydrodynamics. *Progress of Theoretical Physics 92*(5), 939–960.

Teh, C. and G. Houlsby (1991). An analytical study of the cone penetration test in clay. *Geotechnique 41*(1), 17–34.

Ting, J. M., B. T. Corkum, C. R. Kauffman, and C. Greco (1989). Discrete numerical model for soil mechanics. *Journal of Geotechnical Engineering 115*(3), 379–398.

Tsuji, Y., T. Kawaguchi, and T. Tanaka (1993). Discrete particle simulation of 2-dimensional fluidized-bed. *Powder Technology 77*, 79–87.

Tsuji, Y., T. Tanaka, and T. Ishida (1992). Lagrangian numerical simulation of plug flow of cohesionless particles in a horizontal pipe. *Powder Technology 71*, 239–250.

van den Berg, P. (1994). *Analysis of soil penetration*. Ph. D. thesis, TU Delft, Delft.

van den Berg, P., R. de Borst, and H. Huètink (1996). An Eulerian Finite Element Model For Penetration In Layered Soil. *International Journal for Numerical and Analytical Methods in Geomechanics 20*, 865–886.

van den Berg, P. and P. Vermeer (1988). Undrained shear strenght from cpt and finite element computations. In *Proocedings of the sixth international conference on numerical methods in geomechanics*, Innsbruck, pp. 1095–1100. Balkema, Rotterdam.

van Esch, J., P. Bonnier, and H. Teunissen (2008). Biot consolidation and multiphase subsurface flow.

van Esch, J., D. Stolle, P. Bonnier, and O. C. Lsl (2009). Consideration of Pore Pressures in MPM. In *Computer Methods in Mechanics*, Number May, pp. 1–16.

van Esch, J., D. Stolle, and I. Jassim (2011a). Finite element method for coupled dynamic flow-deformation simulation. In *2nd International Symposium on Computational Geomechanics (COMGEO II), Cavtat-Dubrovnik, Croatia,*.

van Esch, J., D. Stolle, and I. Jassim (2011b). Finite element method for coupled dynamic flow-deformation simulation. In *2nd International Symposium on Computational Geomechanics (COMGEO II)*, Number 1, Cavat-Dubrovnik, Croatia.

Vermeer, P., L. Sittoni, L. Beuth, and Z. Wieckowski (2013). Modeling soil-fluid and fluid-soil transitions with applications to tailings. In *Taylings and Mine waste*, Banff, Alberta, Canada, pp. 305–315.

Vermeer, P. A. (1993). *PLAXIS 2D Reference Manual Version 5*. Balkema, Rotterdam / Brookfield.

Vermeer, P. A., Y. Yuan, L. Beuth, and P. Bonnier (2009). Application of interface elements with the Material Point Method. In *Computer Methods in Mechanics*, Number May, Zielona Gora, Poland.

Verruijt, A. (1996). *Soil dynamics*. Technische Universiteit, Faculteit Civiele Techniek.

Verruijt, A. (2010). *An introduction to soil dynamics*, Volume 24. Springer.

Vesic, A. S. (1972). Expansion of cavities in infinite soil mass. *Journal of Soil Mechanics & Foundations Div 98*(sm3).

Walker, J. and H. S. Yu (2006, April). Adaptive finite element analysis of cone penetration in clay. *Acta Geotechnica 1*(1), 43–57.

Wang, Z., C. Zhao, and L. Dong (2009, January). An approximate springdashpot artificial boundary for transient wave analysis of fluid-saturated porous media. *Computers and Geotechnics 36*(1-2), 199–210.

Wegel, R. and H. Walther (1935). Internal dissipation in solids for small cyclic strains. *Journal of Applied Physics 6*(4), 141–157.

Wheeler, S. (2003). An anisotropic elastoplastic model for soft clays. *Canadian geotechnical journal... 418*(1997), 403–418.

Whittle, A. J. (1993). Evaluation of a constitutive model for overconsolidated clays. *Geotechnique 43*, 289–313.

Wickowski, Z. (2004, October). The material point method in large strain engineering problems. *Computer Methods in Applied Mechanics and Engineering 193*(39-41), 4417–4438.

Wieckowski, Z. (2001). Analysis of granular flow by the Material Point Method. In *European Conference on Computational Mechanics*, Cracow, Poland.

Wieckowski, Z. (2013). Enhancement of the material point method for fluid-structure interaction and erosion. Technical report, Report on EU-FP7 research project Geo Fluid PIEF-GA-2010-274335.

Wieckowski, Z., S.-k. Youn, and J.-h. Yeon (1999). A particle -in-cell solution to the silo discharging problem. *International Journal for Numerical Methods in Engineering 45*(February 1998), 1203–1225.

Wood, D. M. (2003). *Geotechnical modelling*, Volume 1. CRC Press.

Wood, D. M. (2004). *Geotechnical Modelling*. Abingdon, UK: Taylor & Francis.

Xiao-Fei, P., X. Ai-Guo, Z. Guang-Cai, Z. Ping, Z. Jian-Shi, M. Shang, and Z. Xiong (2008). Three-dimensional multi-mesh material point method for solving collision problems. *Communications in Theoretical Physics 49*(5), 1129.

Xie, K. and C. Leo (2004, June). Analytical solutions of one-dimensional large strain consolidation of saturated and homogeneous clays. *Computers and Geotechnics 31*(4), 301–314.

Yerro, A. (2014, December). Mpm for unsaturated soils. MPM-Dredge workshop, Cambridge.

Yerro, A., E. Alonso, and P. N. (2014). Modelling progressive failure with mpm. In M. Hicks, Brinkgreve, and A. Rohe (Eds.), *Numerical modeling in geotechnical engineering*.

Yerro, A., E. Alonso, and N. Pinyol (2013). The Material Point Method: A promising computational tool in Geotechnics. In *proocending of the 18th International Conference on Soil Mechanics and Geotechnical Engineering*, Paris, pp. 853–856.

Yi, J., M. Randolph, S. Goh, and F. Lee (2012, August). A numerical study of cone penetration in fine-grained soils allowing for consolidation effects. *Géotechnique 62*(8), 707–719.

York, A. R., D. Sulsky, and H. L. Schreyer (1999). The material point method for simulation of thin membranes. *International journal for numerical methods in engineering 44*(10), 1429–1456.

Yu, H. (1993). Discussion:singular plastic fields in steady penetration of a rigid cone. *Journal of Applied Mechanics 60*(4), 1061–1062.

Yu, H., L. Herrmann, and R. Boulanger (2000). Analysis of steady cone penetration in clay. *Journal of Geotechnical and Geoenviromental Engineering* (July), 594–605.

Yu, H. and G. Houlsby (1991). Finite cavity expansion in dilatant soils: loading analysis. *Geotechnique 41*(2), 173–183.

Yu, H. and J. Mitchell (1998). Analysis of cone resistance: review of methods. *Journal of Geotechnical and Geoenvironmental Engineering* (February), 140–149.

Yu, H.-S. (2000). *Cavity expansion methods in geomechanics*. Springer.

Yu, H.-S. (2007). *Plasticity and geotechnics*, Volume 13. Springer.

Zhang, D. Z., X. Ma, and P. T. Giguere (2011, July). Material point method enhanced by modified gradient of shape function. *Journal of Computational Physics 230*(16), 6379–6398.

Zhang, D. Z., Q. Zou, W. B. VanderHeyden, and X. Ma (2008, March). Material point method applied to multiphase flows. *Journal of Computational Physics 227*(6), 3159–3173.

Zhang, H., K. Wang, and Z. Chen (2009, April). Material point method for dynamic analysis of saturated porous media under external contact/impact of solid bodies. *Computer Methods in Applied Mechanics and Engineering 198*(17-20), 1456–1472.

Zhang, H., K. Wang, and Z. Zhang (2007). Material point method for numerical simulation of failure phenomena in multiphase porous media. In *Computational Mechanics*, pp. 36–47. Springer.

Zhang, X., K. Sze, and S. Ma (2006). An explicit material point finite element method for hyper-velocity impact. *International Journal for Numerical Methods in Engineering 66*(4), 689–706.

Zhou, S., J. Stormont, and Z. Chen (1999). Simulation of geo- membrane response to settlement in landfills by using the material point method. *Int. J. Numer. Anal. Methods Geomech 23*(15), 1977–1994.

Zhu, H., Z. Zhou, R. Yang, and a.B. Yu (2007, July). Discrete particle simulation of particulate systems: Theoretical developments. *Chemical Engineering Science 62*(13), 3378–3396.

Zienkiewicz, O. (1982). Basic formulation of static and dynamic behaviour of soil and other porous media. In *Numerical methods in geomechanics*, pp. 39–55. Springer.

Zienkiewicz, O., C. Chang, and P. Bettess (1980). Drained, undrained, consolidating and dynamic behaviour assumptions in soils. *Geotechnique 30*(4), 385–395.

Zienkiewicz, O. and D. Naylor (1973). Finite element studies of soils and porous media. *Lect. Finite Elements in Continuum Mechanics*, 459–493.

Zienkiewicz, O. and G. Pande (1977). *Finite elements in Geomechanics*, Chapter Some useful forms of isotropic yield surfaces for soil and rock mechanics, pp. 179–198.

Zienkiewicz, O. and T. Shiomi (1984). Dynamic behaviour of saturated porous media; the generalized Biot formulation and its numerical solution. *International Journal for Numerical and Analytical Methods in Geomechanics 8*, 71–93.

Zienkiewicz, O. C., A. Chan, M. Pastor, B. Schrefler, and T. Shiomi (1999). *Computational geomechanics*. Wiley Chichester.

Zienkiewicz, O. C., a. H. C. Chan, M. Pastor, D. K. Paul, and T. Shiomi (1990, June). Static and Dynamic Behaviour of Soils: A Rational Approach to Quantitative Solutions. I. Fully Saturated Problems. *Proceedings of the Royal Society A: Mathematical, Physical and Engineering Sciences 429*(1877), 285–309.

Zienkiewicz, O. C. and R. L. Taylor (2005). *The finite element method for solid and structural mechanics*. Butterworth-heinemann.